

THE GENERALIZED METHOD OF MOMENTS FOR ELECTROMAGNETIC INTEGRAL
EQUATIONS: NEW FORMULATIONS AND APPLICATIONS

By

Daniel Lawrence Dault

A DISSERTATION

Submitted
to Michigan State University
in partial fulfillment of the requirements
for the degree of

Electrical Engineering – Doctor of Philosophy

2015

ABSTRACT

THE GENERALIZED METHOD OF MOMENTS FOR ELECTROMAGNETIC INTEGRAL EQUATIONS: NEW FORMULATIONS AND APPLICATIONS

By

Daniel Lawrence Dault

The moment method is the predominant approach for the solution of electromagnetic boundary integral equations. Traditional moment method discretizations rely on the projection of solution currents onto basis sets that must satisfy strict continuity properties to model physical currents. The choice of basis sets is further restricted by the tight coupling of traditional functional descriptions to the underlying geometrical approximation of the scattering or radiating body. As a result, the choice of approximation function spaces and geometry discretizations for a given boundary integral equation is significantly limited. A quasi-meshless partition of unity based method called the Generalized Method of Moments (GMM) was recently introduced to overcome some of these limitations. The GMM partition of unity scheme affords automatic continuity of solution currents, and therefore permits the use of a much wider range of basis functions than traditional moment methods. However, prior to the work in this thesis, GMM was limited in practical applicability because it was only formulated for a few geometry types, could not be accurately applied to arbitrary scatterers, e.g. those with mixtures of geometrical features, and was not amenable to traditional acceleration methodologies that would permit its application to electrically large problems.

The primary contribution of this thesis is to introduce several new GMM formulations that significantly expand the capabilities of the method to make it a practical, broadly applicable approach for solving boundary integral equations and overcoming the limitations inherent in traditional moment method discretizations. Additionally, several of the topics covered address continuing open problems in electromagnetic boundary integral equations with applicability beyond GMM. The work comprises five broad contributions. The first is a new GMM formulation capable of mixing both GMM-type basis sets and traditional basis sets in the same discretization. The scheme

handles geometries with mixtures of smooth and sharp features using an expanded range of basis functions classes and geometry representations, thereby permitting the application of GMM to arbitrary scatterers with high fidelity. Second, an acceleration method based on the Multilevel Fast Multipole Algorithm is developed that is equally applicable to GMM and traditional higher order moment methods. The third contribution is an interior penalty integral equation formulation that regularizes GMM surface currents and affords significant savings in computational cost. Fourth, a technique for creating arbitrarily smooth GMM current representations based on conformal mapping is advanced. Finally, a GMM formulation for a new surface description for boundary integral equations, the subdivision surface, is proposed. The resulting subdivision-based method holds promise for optimization and uncertainty quantification of scattering and radiating structures through rapid geometry morphing and subwavelength deformation; furthermore it is readily extensible to traditional moment methods. Taken together, these contributions address several open problems and yield a GMM boundary integral equation solver that is highly accurate, flexible, fast, and applicable to a wide range of electromagnetics engineering problems.

To my wife and children.

ACKNOWLEDGEMENTS

First, I would like to deeply thank Professor Shanker Balasubramaniam for all of the ideas, encouragement, and support over the years of my graduate education. Without your guidance, support, and many insights, both in and beyond the academic sphere, this work would not have been possible.

Next, I would like to thank my committee members, Professors Rothwell and Piermarocchi and Drs. Chahal and Albrecht for their many constructive thoughts and guidance.

No good work is accomplished in a vacuum, and I have been honored to work with an outstanding group of fellow students at Michigan State. I owe a few special mentions. Thank you to Jie Li for the collaboration and many conversations that have spawned new ideas and research directions, and without whose insights this work would have been much poorer. Thank you also to Dr. Naveen V. Nair for his original work on the Generalized Method of Moments and the many conversations and much support in the years since I took up the GMM mantle. Thanks to Dr. Andrew Baczewski for serving as a mentor in my early years as a graduate student. Many thanks also to Andrew Pray and Zane Crawford, Steve Hughey, Scott O’Conner, and Conner Glosser.

A special thank you to Dr. Yiying Tong and his students Beibei Liu and Rundong Zhao for introducing me to subdivision surfaces and helping with some of the initial conceptual work and implementation.

Finally a profound thank you to my family, especially my wife Nicole and my children Maya and James. I could not have done this without your unfailing support and care over the years.

TABLE OF CONTENTS

LIST OF TABLES	ix
LIST OF FIGURES	x
LIST OF ALGORITHMS	xvii
CHAPTER 1 INTRODUCTION AND MATHEMATICAL PRELIMINARIES	1
1.1 Introduction	1
1.2 Introduction to Mathematical Preliminaries	2
1.3 Time Harmonic Maxwell’s Equations in Free Space	3
1.3.1 The Surface Equivalence Principle	5
1.4 Derivation of Electromagnetic Boundary Integral Equations	6
1.5 The Method of Moments	8
1.6 Manifold Theory	10
1.6.1 Definition of a smooth manifold	11
1.6.2 Partitions of unity	12
1.6.3 Tangent and cotangent bundles	13
1.6.4 Embedding in \mathbb{R}^3 and Riemannian manifolds	16
CHAPTER 2 THE GENERALIZED METHOD OF MOMENTS	19
2.1 Introduction	19
2.2 Problem Statement	23
2.3 Formulation	24
2.3.1 Neighborhoods from Point Clouds	25
2.3.2 Partition of Unity	26
2.3.3 Local Geometry Parameterization	26
2.3.3.1 Smooth Polynomial Geometry Parameterization	30
2.3.3.2 Handling of Geometrical Singularities	31
2.3.3.3 Definition of the Tangent Space $T\Omega_i$	31
2.3.3.4 Vector Calculus on Parametric Surfaces	32
2.3.4 Local Basis Functions	34
2.3.4.1 Entire Patch Basis Functions	34
2.3.4.2 Sub-patch Basis Functions	35
2.3.4.3 Default EP/SP Basis	37
2.4 Implementation Details	39
2.4.1 Matrix Elements	40
2.4.2 Automated Patch Construction	41
2.4.2.1 Algorithm for Patch Merging	41
2.4.2.2 Automated Geometry and Basis Assignment	42
2.5 Results	43
2.5.1 Complexity and Matrix Fill Times	51

2.6	Conclusion	54
CHAPTER 3 A MIXED POTENTIAL MLFMA FOR HIGHER ORDER MOMENT METHODS WITH APPLICATIONS TO THE GENERALIZED METHOD OF MOMENTS		
3.1	Introduction	56
3.2	Preliminaries	58
3.2.1	Electromagnetic Problem Statement	58
3.2.2	The Multilevel Fast Multipole Algorithm	60
3.2.3	Application to higher order	61
3.3	Previous Approaches	63
3.4	Point-Based Mixed Potential MLFMA	65
3.4.1	Mixed potential farfield representation	65
3.4.2	Point-based algorithm	66
3.4.3	Mixed potential point-based MLFMA nearfield	67
3.5	Complexity Analysis	68
3.5.1	Computational complexity	70
3.5.2	Memory scaling	71
3.6	Preconditioning	72
3.7	Results	78
3.8	Conclusion	88
CHAPTER 4 AN INTERIOR PENALTY METHOD FOR THE GENERALIZED METHOD OF MOMENTS		
4.1	Introduction	90
4.2	Problem Statement	92
4.2.1	The Generalized Method of Moments	93
4.2.2	Solution errors	94
4.3	Penalty Formulation	95
4.3.1	Implementation details for two dimensions	96
4.4	Spectral Analysis: Two Dimensions	97
4.4.1	Low order analysis	98
4.4.2	Higher order analysis	100
4.5	2D Results	102
4.6	Results in Three Dimensions	107
4.7	Conclusion	111
CHAPTER 5 SCHWARZ-CHRISTOFFEL BASED PARTITIONS OF UNITY FOR THE GENERALIZED METHOD OF MOMENTS		
5.1	Introduction	113
5.2	Problem Statement: Nonsmooth Partitions of Unity	114
5.3	Schwarz-Christoffel Mapping	117
5.4	Schwarz-Christoffel GMM	118
5.5	Evaluation of Field Integrals via Generalized Quadrature	122
5.6	Results	125

5.7	Discussion and Conclusions	129
CHAPTER 6 SUBDIVISION SURFACES FOR THE GENERALIZED METHOD OF		
	MOMENTS	131
6.1	Introduction	131
6.2	Loop Subdivision Surfaces	132
	6.2.1 Evaluation of the Limit Surface and Derivatives	134
6.3	GMM Patches and Local Parameterizations	139
	6.3.1 Merging of Regular Patches	144
6.4	Basis Functions	146
6.5	Partition of Unity	149
6.6	Results	153
6.7	Discussion and Conclusions	158
APPENDIX		159
BIBLIOGRAPHY		166

LIST OF TABLES

Table 2.1	Matrix fill times for CFIE-RWG code.	53
Table 2.2	Matrix fill times for higher order CFIE-GWP & CFIE-GMM codes.	54
Table 3.1	Discretization details for series of plates used in scaling demonstration.	79
Table 3.2	Matrix vector product timings for dyadic kernel for the VFY-218 aircraft, CFIE. .	82
Table 3.3	Matrix vector product timings for mixed potential kernel for the VFY-218 aircraft, CFIE.	82
Table 3.4	Storage for 10λ diameter sphere, $p = 2, h = .8\lambda$	85
Table 3.5	Timings for 10λ diameter sphere, $p = 2, h = .8\lambda$	86
Table 3.6	Storage for 10λ diameter sphere, $p = 7, h = 2\lambda$	86
Table 3.7	Timings for 10λ diameter sphere, $p = 7, h = 2\lambda$	86
Table 3.8	Storage and timings for 15λ ship.	88
Table 3.9	Detailed Matrix Vector Product Timings for 15λ ship.	88
Table 4.1	Iterations to convergence ($\tau = 10^{-3}$) vs. β_J in GMRES solver.	111

LIST OF FIGURES

Figure 1.1	Setup for scattering from a perfectly electrically conducting obstacle in three dimensional free space.	7
Figure 1.2	Manifold Ω , coordinate charts (Ω_1, φ_1) and (Ω_2, φ_2) , and transition maps τ_{12}, τ_{21}	12
Figure 1.3	Tangent bundle for a subset Ω_i of a two-dimensional manifold Ω . The bundle $T\Omega_i$ consists of a collection of copies of \mathbb{R}^2 associated with each pair (u_i^1, u_i^2) in the coordinate chart (Ω_i, φ_i) . Coordinates for the bundle are mapped into \mathbb{R}^4 via the coordinate chart $(\Omega_i \times \mathbb{R}^2, \tilde{\varphi})$, where $\tilde{\varphi}$ maps from the product space $\Omega_i \times \mathbb{R}^2$ into local coordinates in \mathbb{R}^4	15
Figure 2.1	Blending of approximation spaces on overlapping domains via the partition of unity for a 1D signal. (a) A trial function $f(x) = .2(x - 2)^3 + .3$ on the interval $\Omega : 0 \leq x \leq 4$. (b) Interpolation of $f(x)$ using linear interpolatory hat functions $T_i(x) = T(x - .5i)$ on subinterval $\Omega_1 : 0 \leq x \leq 3$ such that $\hat{f}_1(x) = \chi_1(x) \sum_i a_i T_i(x)$, $\chi_1(x) = 1, x \in \Omega_1; 0, x \notin \Omega_1$. (c) Interpolation of $f(x)$ using a third order Legendre polynomial set $P_n(x)$, $n = 0, 1, 2, 3$ on subinterval $\Omega_2 : 2 \leq x \leq 4$ such that $\hat{f}_2(x) = \chi_2(x) \sum_{n=1}^3 a_n P_n(x - 3)$, $\chi_2(x) = 1, x \in \Omega_2, 0; x \notin \Omega_2$. (d) Partitions of unity $\psi_1(x)$ and $\psi_2(x)$. (e) interpolations of $f(x)$ multiplied by partitions of unity as $\hat{f}_1(x)\psi_1(x)$ in Ω_1 and $\hat{f}_2(x)\psi_2(x)$ in Ω_2 . (f) Reconstructed function $\hat{f}(x) = \hat{f}_1(x)\psi_1(x) + \hat{f}_2(x)\psi_2(x)$ (left axis) and absolute reconstruction error (right axis). Through the action of the partition of unity, the representations $\hat{f}_1(x)$ and $\hat{f}_2(x)$ are smoothly blended in the overlap region, $2 \leq x \leq 3$, and the approximation error transitions smoothly between the linear and Legendre interpolations.	27
Figure 2.2	Smooth patch geometry parameterization procedure for patch Ω_i : (note: for clarity, subscripts i are dropped on vector quantities) (a) Start with an oriented point cloud. (b) Define a neighborhood \mathcal{N}_i of nearest neighbors about node i . (c) Define a projection plane Γ_i with normal equal to average of all node normals and specified by a point \mathbf{r}_c that uniquely defines an origin of coordinates. (d) Construct a local orthogonal u^1, u^2, u^3 coordinate system. (e) Take projection of points in \mathcal{N}_i into Γ_i to define the support of the patch in the u^1, u^2 plane. This projection is denoted P_{Γ_i} . (f) Obtain a smooth parameterization to define the local patch surface.	29
Figure 2.3	Tangent and normal vectors associated with a parametric patch surface.	33
Figure 2.4	Entire patch basis function.	35

Figure 2.5	Illustration of sub-patch basis function arrangement with projected PU.	36
Figure 2.6	Design of local RWG basis set with normal continuity across patch boundaries: (a) RWG basis functions associated with internal edges, (b) Additional half-RWG functions associated with exterior patch edges provide a normal component at patch boundary, and (c) Simplex-based partition of unity forces the half-RWG function to zero at patch boundary, removing the line charge.	37
Figure 2.7	Graphical depiction of partitions of unity for overlapped RWG and Legendre patches. (a) Partition of unity ψ_{RWG} and half-RWG basis functions for an RWG patch. (b) Partition of unity ψ_{Leg} for a Legendre patch.	39
Figure 2.8	(a) Graphical representation of $P_{\Gamma_l}(\mathcal{N}_l)$ and (b) construction of triangular integration subdomains. The domain of integration is $D_l = \cup_i T_i$	41
Figure 2.9	Reconstruction error for a function $\mathbf{f}(x,y) = (x - .5)^2 \hat{\mathbf{x}}$ using three different basis sets: all-RWG, all-Legendre, mixed RWG/Legendre. (a) All-RWG discretization, (b) All-RWG reconstruction error, (c) All-Legendre patch discretization (2nd order Legendre polynomials) (d) All-Legendre reconstruction error, (e) Mixed RWG/Legendre discretization (2nd order Legendre Polynomials), (f) Mixed RWG/Legendre reconstruction error.	45
Figure 2.10	Surface currents induced by an incident plane wave on a sphere discretized with (a) overlapping GMM patches supporting a 4th order Legendre basis and (b) an RWG basis for reference. Subfigure (c) shows the patches used to obtain the GMM result. Magnitude of imaginary part of current $\ J_{im}\ $ is shown; $\ J_{re}\ $ yields similar plots.	46
Figure 2.11	GMM discretization of a 4.5λ NASA almond.	47
Figure 2.12	NASA almond bistatic RCS, taken along the $\phi = 0^\circ$ cut.	48
Figure 2.13	GMM discretization of a $1.2\lambda \times .4\lambda \times .4\lambda$ conesphere.	49
Figure 2.14	Bistatic RCS for the conesphere at 300MHz. Incident wave is traveling in the $\theta = 0^\circ, \phi = 0^\circ$ direction with $-x$ -polarization. The RCS is taken along $\phi = 0^\circ$ cut.	49
Figure 2.15	GMM discretization of a $5\lambda \times 1.5\lambda \times .8\lambda$ arrow (a) top view and (b) bottom view.	50
Figure 2.16	Arrow bistatic RCS at 64MHz. Wave is incident in the $\theta_i = 135^\circ, \phi_i = 20^\circ$ direction and is x -polarized relative to incidence direction. The RCS is taken along the $\phi = 0^\circ$ cut.	50
Figure 2.17	GMM discretization of a $4\lambda \times .35\lambda$ Parabolic Reflector (a) top view and (b) side view.	51

Figure 2.18	Parabolic reflector bistatic RCS. Wave is incident in the $\theta_i = 180^\circ, \phi_i = 0^\circ$ direction with x -polarization. The RCS is taken along the $\phi = 0^\circ$ cut.	52
Figure 3.1	Division of a large curvilinear basis function support Ω_n into nearfield and farfield for a source leaf box b_l . Problematic contour integrals appear along the contour Γ between nearfield and farfield regions.	62
Figure 3.2	Illustration of traditional and point-based MLFMA trees. (a) Traditional: MLFMA leaf box size (and therefore tree height) is limited by the size of the largest patch. (b) Point-based/mixed potential: leaf box size and tree height are not limited by patch size, and may be chosen for optimal MLFMA scaling subject to the low frequency limit of MLFMA.	67
Figure 3.3	Point-based MLFMA groupings and nearfield/farfield interaction partitions for interaction between two patches. Only direct interactions between the bold red boxes contribute to Z^N	69
Figure 3.4	Comparison of interactions dyadic and mixed potential MLFMA. (a) Limit on non-point-based dyadic MLFMA leaf box size means that interactions between large patches must be computed directly. (b) For point-based/mixed potential MLFMA, interactions between large patches may be split between nearfield and farfield so that favorable scaling is maintained.	69
Figure 3.5	Local patch trees used to compute preconditioners. Each local tree is a subset of the global MLFMA octree. Interactions between two patches are computed using intersections of the global interaction lists.	74
Figure 3.6	Graphical depiction of the computation of a single column of a preconditioner block \tilde{M}_{lk} . \tilde{M}_{lk}^N consists of the precomputed nearfield interactions and $\mathcal{F}(e_i)$ is an MLFMA product with the i th column of the identity matrix e_i . The summation of the i th column of \tilde{M}_{lk}^N with the $\mathcal{F}(e_i)$ yields the i th column of \tilde{M}_{lk}	74
Figure 3.7	Stencil of overlapped block preconditioner used in preconditioning scaling tests.	76
Figure 3.8	Convergence in relative (Frobenius) error of preconditioning matrix filled using $\mathcal{O}(N_q \log N_q)$ MLFMA-accelerated algorithm vs. $\mathcal{O}(N_q^2)$ direct fill algorithm. Geometry is a 2λ sphere with $p = 4$ and $h = 1\lambda$	76
Figure 3.9	Comparison of MLFMA-accelerated preconditioner fill times with respect to χ for a 2λ sphere with $p = 4$ and $h = 1\lambda$	77
Figure 3.10	Convergence in relative (Frobenius) error of preconditioning matrix filled using $\mathcal{O}(N_q \log N_q)$ MLFMA-accelerated algorithm vs. $\mathcal{O}(N_q^2)$ direct fill algorithm. Geometry is a 2λ sphere with $p = 9$ and $h = 2\lambda$	77

Figure 3.11	Comparison of MLFMA-accelerated preconditioner fill times with respect to χ for a 2λ sphere with $p = 9$ and $h = 2\lambda$	78
Figure 3.12	Scaling of MLFMA matrix vector product timings vs. N_q^{tot} for a series of square plates of size 2λ - 12λ	80
Figure 3.13	Scaling in nearfield and farfield memory for a series of square plates of size 2λ - 12λ	80
Figure 3.14	Scaling of nearfield matrix fill vs. N_q^{tot} for a series of square plates of size 2λ - 12λ	81
Figure 3.15	GMM discretization of VFY-218 aircraft.	82
Figure 3.16	Surface currents for the 30λ VFY-218 aircraft.	83
Figure 3.17	Bistatic RCS for VFY-218 aircraft, $\theta = 90^\circ$ cut.	83
Figure 3.18	Bistatic RCS for 10λ diameter sphere, $\phi = 0$ cut. Two GMM discretizations, disc. 1 ($p = 2, h = .8\lambda$) and disc 2. ($p = 7, h = 2\lambda$) for both the dyadic (“D”) and mixed potential (“MP”) are compared with the analytical Mie series result.	84
Figure 3.19	GMM mixed discretization for 15λ destroyer: 1st order smooth polynomial patches (patch diameter 1λ) and 4th order Legendre basis on smooth regions, triangular tessellation and RWG basis on tips/corners. (Model credit: Nicholas Miller)	87
Figure 3.20	Bistatic RCS for 15λ destroyer, $\theta = 90^\circ$ cut, plane wave incident on bow.	88
Figure 4.1	Patch overlaps γ_k in (a) two and (b) three dimensions.	93
Figure 4.2	Illustration of low and high frequency current errors induced by insufficient quadrature for the TE^z EFIE solution on cylinder of radius $a = .5\lambda$	98
Figure 4.3	Generalized eigenvalues for an $a = .5\lambda$ cylinder.	101
Figure 4.4	High frequency current spectrum of compensated EFIE in visible region for an $a = .5\lambda$ cylinder.	101
Figure 4.5	Current spectrum of compensated EFIE in visible region for an $a = .5\lambda$ cylinder.	102
Figure 4.6	Comparison of analytical and reconstructed current obtained using an 8-point integration rule. (a) $\ \mathbf{J}\ $, $\beta = 0$, (b) RCS, $\beta = 0$, (c) $\ \mathbf{J}\ $, $\beta = 10$, (d) RCS, $\beta = 10$	103
Figure 4.7	Convergence vs β in EFIE solution currents for $a = .5\lambda$ cylinder under TE^z illumination.	104

Figure 4.8	Pointwise absolute error over the cylinder scattering surface.	105
Figure 4.9	Convergence of absolute current error in patch overlaps vs. β	105
Figure 4.10	GMM patches for a teardrop shaped scatterer.	106
Figure 4.11	Comparison of reference ($i = 30$) and reconstructed currents/fields obtained using $i = 10$ rule for the 2λ teardrop scatterer.	106
Figure 4.12	Generalized eigenvalues for the uncompensated and compensated GMM TE^z operator discretized on the teardrop shaped scatterer. Higher order eigenvalues of the compensated operator are shifted, while lower order eigenvalues (inset) are unaffected.	107
Figure 4.13	GMM patches for a $6\lambda \times 2\lambda$ elliptical scatterer.	108
Figure 4.14	Comparison of reference ($i = 30$) and reconstructed currents and RCS obtained using $i = 10$ rule for the $6\lambda \times 2\lambda$ elliptical scatterer.	108
Figure 4.15	Convergence vs. β for a 1λ sphere, $p = 4, i = 5$ case.	109
Figure 4.16	Convergence vs. β for $p = 7, i = 5$ case.	110
Figure 4.17	Comparison of analytical and reconstructed current obtained using 10-point integration rule.	110
Figure 5.1	Two GMM patches and local (u^1, u^2) coordinate systems.	115
Figure 5.2	Image of a triangle T_l under a non-affine transition function τ_{kl}	117
Figure 5.3	Simplex-based PU and derivative with non-affine transition functions.	117
Figure 5.4	Schwarz-Christoffel mapping from canonical disc D to polygon P (plot generated using Matlab SC Toolbox [1]).	119
Figure 5.5	Schwartz-Christoffel mapping in u^1, u^2 plane permits definition of arbitrarily smooth partitions of unity.	119
Figure 5.6	Polynomial sub-partition of unity function.	120
Figure 5.7	Smooth sub-partition of unity mapped from $D(z)$ to projection polygon $P(w)$ via Schwarz-Christoffel map.	120
Figure 5.8	Smooth partition of unity $\psi(u^1, u^2)$, $(u^1, u^2) \in P$ constructed from smooth sub-partitions of unity mapped using Schwarz-Christoffel mapping. (a) Partition of unity ψ . (b) Derivative $\partial\psi/\partial u^1$	121

Figure 5.9	Illustration of reduction in number of quadrature abscissa between adaptive and generalized quadrature schemes. (a) Adaptive quadrature nodes for a patch. Convergence of integrations to relative error of 10^{-5} requires 2148 points. (b) Generalized PU-Chebyshev quadrature nodes for a patch. Only 117 points are required for same accuracy.	124
Figure 5.10	Convergence of integrations of simplex and Schwarz-Christoffel mapped partitions of unity vs. number of quadrature points N_q . (a) Simplex partition of unity and divergence. (b) Schwarz-Christoffel partition of unity ψ_{SC} . (c) $\partial\psi_{SC}/\partial u^1$. (d) $\partial\psi_{SC}/\partial u^2$	126
Figure 5.11	Bistatic RCS ($\phi = 0^\circ$ cut) for a $.5\lambda$ sphere discretized with smooth SC-GMM basis, MFIE solution.	127
Figure 5.12	Bistatic RCS ($\phi = 0^\circ$) for a 1λ sphere, smooth SC-GMM basis, EFIE solution.	127
Figure 5.13	Surface current density ($\ \mathbf{J}\ $) for a 1λ sphere illuminated by an x -polarized plane wave travelling in the $+z$ direction. (a) Mie series solution. (b) SCGMM solution using the EFIE.	128
Figure 5.14	Mixed Schwarz-Christoffel/simplex partition of unity scheme for the 2λ ellipsoid.	129
Figure 5.15	Bistatic RCS ($\phi = 0^\circ$) for the 2λ ellipsoid, MFIE solution.	129
Figure 6.1	Subdivision of a spherical mesh. (a) Primal mesh, (b) $k = 1$, (c) $k = 2$, (d) limit surface ($k = \infty$).	134
Figure 6.2	Neighborhood of a triangle T_l . Vertex \mathbf{v}_1 has a valence of N , vertices $\mathbf{v}_2, \mathbf{v}_{N+1}$ have valence six.	134
Figure 6.3	Recursive subdivision procedure about an irregular vertex \mathbf{v}_0^0 . Each subdivision yields three regular triangles and one irregular triangle.	136
Figure 6.4	Divergent behavior of subdivision surface partial derivatives about an irregular vertex of valence $N = 15$. The (u^1, u^2) coordinate system for this case is defined via direct projection into a common plane that shares the average normal of all triangles incident on the irregular vertex.	139
Figure 6.5	Eigen-neighborhood for a vertex of valence nine. The characteristic map is constructed upon subdivision of this neighborhood.	141
Figure 6.6	Characteristic map for a vertex of valence $N = 5$. (a) Triangulation of an N -gon, (b) a subtriangulation T of the N -gon, (c) a piecewise linear representation of $F(T)$	142

Figure 6.7	Characteristic map for a vertex of valence $N = 6$. (a) Triangulation of an N -gon, (b) a subtriangulation T of the N -gon, (c) a piecewise linear representation of $F(T)$	142
Figure 6.8	Characteristic map for a vertex of valence $N = 15$. (a) Triangulation of an N -gon, (b) a subtriangulation T of the N -gon, (c) a piecewise linear representation of $F(T)$	143
Figure 6.9	Coordinate charts for overlapping irregular (valence 5) and regular GMM patches induced by the characteristic maps $F(\xi^1, \xi^2)$	144
Figure 6.10	Primal mesh (a) and local coordinate domain (b) for a merged regular patch. . .	145
Figure 6.11	Basis functions and divergences for a valence $N = 5$ patch.	148
Figure 6.12	Basis functions and divergences for a valence $N = 15$ patch.	149
Figure 6.13	Subdivision of triangle around irregular vertex \mathbf{v}_0^0 for partition of unity definition.	150
Figure 6.14	Subdivision simplex partition of unity. (a) PU on regular patch with regular neighbors. (b) PU on irregular valence $N = 5$ patch. (c) PU on regular patch neighboring irregular patch (shown schematically for clarity).	152
Figure 6.15	Regular patch support near an irregular vertex.	152
Figure 6.16	Regular patch supports adjacent to an irregular vertex of valence $N = 5$	153
Figure 6.17	Sampled partition of unity $\psi(u^1, u^2)$ on a merged patch adjacent to an irregular vertex.	154
Figure 6.18	Basis function and divergence for a merged regular patch.	154
Figure 6.19	(a) RCS for 1λ subdivision sphere ($\phi = 0^\circ$). (b) RCS for 1λ subdivision sphere with merged patches ($\phi = 0^\circ$).	155
Figure 6.20	Real part of MFIE solution surface currents for 1λ sphere using $h = .5\lambda$ merged patches. Incident plane wave is traveling in $+\hat{\mathbf{z}}$ direction.	155
Figure 6.21	Chmutov surface (a) Coarse primal mesh. (b) Mesh after one subdivision. (b) Limit surface.	156
Figure 6.22	Bistatic RCS for 2λ Chmutov geometry ($\phi = 0^\circ$).	156
Figure 6.23	Torus mesh (a) front view, (b) side view, and twisted torus limit surface (c) front view, (d) side view.	157
Figure 6.24	Bistatic RCS ($\phi = 0^\circ$ cut) for (a) torus and (b) twisted torus geometries.	157

LIST OF ALGORITHMS

Algorithm 2.1	Automated patch merging.	42
Algorithm 2.2	Automated geometry and basis assignment.	43

CHAPTER 1

INTRODUCTION AND MATHEMATICAL PRELIMINARIES

1.1 Introduction

The development of efficient, accurate discretizations for electromagnetic boundary integral equations has been a primary concern for the field of computational electromagnetics since its inception in the middle of the twentieth century. Research in this area has proceeded along three interrelated tracks: the development of integral equation formulations that admit accurate discretization and solution, accurate representation of scattering geometries, and accurate representation of equivalent current densities on scattering boundaries. A fourth area, which has come to the fore in recent decades, is the development of acceleration methodologies to reduce the computational cost of solving electromagnetic integral equations for electrically large scattering bodies. The topic of this thesis is twofold. First, it gives several advances in the Generalized method of moments (GMM), a recently developed discretization method for integral equations that uses a partition of unity to effect blending of surface currents. Second, through the lens of GMM, it addresses some open problems in the four areas of electromagnetic boundary integral equation research. Some of these solutions are specific to GMM, and some, such as acceleration methodologies for higher order moment methods and discretization of currents on novel surface descriptions, may also be applied to address ongoing challenges in the broader context traditional boundary integral equation methods.

The thesis is structured as follows. The remainder of this chapter gives the necessary physical and mathematical preliminaries to define the model physical problem under consideration, and provides the mathematical machinery necessary to define the Generalized Method of Moments. Chapter 2 gives an introduction and context for GMM, and provides a detailed prescription for the construction of GMM discretizations for arbitrary perfectly electrically conducting scatterers that may include curved regions, sharp regions such as corners or tips, regions that are representable

as bodies of revolution, etc. Chapter 3 develops a Multilevel Fast Multipole Algorithm (MLFMA) for GMM that retains optimal scaling for any mixture of low and high order basis functions. The method is directly applicable to the acceleration of other higher order moment methods, which has been a continuing open problem. Chapter 4 proposes an interior penalty method for GMM-type discretizations that provides accurate solutions with significant reductions in the cost of evaluating integrations via numerical quadrature. Chapter 5 gives a formulation for smooth parameterizations of polygonal subdomain supports using the Schwarz-Christoffel map; this method has promise not only for defining smooth GMM discretizations, but also for defining well-behaved local Helmholtz decompositions that are stable to low frequency. Finally, Chapter 6 develops a GMM discretization on subdivision surfaces, a powerful and flexible surface description developed by the computer graphics community that has not been applied to the discretization of electromagnetic integral equations. Several challenges of applying boundary integral equations to subdivision surfaces are solved in the context of GMM. The resulting algorithm is both accurate and flexible, and holds promise for several applications including rapid design optimization via surface morphing. Due to the range of topics covered, this thesis forgoes an extended monolithic introduction and literature review; instead each chapter contains an introductory section that provides context and a literature review specific to the topic at hand.

1.2 Introduction to Mathematical Preliminaries

The remainder of this chapter develops the mathematical and physical concepts required to formulate GMM under specialization to the case of a perfectly electrically conducting (PEC) structures residing in free space, which is the topic of this thesis. It is important to note that GMM itself is not only applicable to the PEC case, and can be applied to a wide array of electromagnetic and acoustic integral equations. Section 1.3 reviews the time harmonic, free space Maxwell's equations and related concepts. Section 1.4 uses these concepts to derive the Electric Field Integral Equation (EFIE) and Magnetic Field Integral Equation (MFIE), the electromagnetic boundary integral equations studied in this work. A formal statement of the method of moments, the most common

solution technique for electromagnetic integral equations, is given in Section 1.5. Finally, the theory of smooth manifolds is introduced in Section 1.6. Manifold theory serves as a framework for understanding various aspects of GMM discretizations throughout this thesis.

1.3 Time Harmonic Maxwell's Equations in Free Space

Consider an unbounded region in \mathbb{R}^3 in which the constitutive parameters are those of isotropic, homogeneous free space, μ_0, ϵ_0 . In the case where all fields are assumed to have time harmonic dependence with angular frequency ω (i.e. all quantities are proportional to $e^{j\omega t}$), the time harmonic Maxwell's equations may be written

$$\nabla \cdot (\epsilon_0 \mathbf{E}(\mathbf{r})) = \rho(\mathbf{r}), \quad (1.1a)$$

$$\nabla \cdot \mathbf{H}(\mathbf{r}) = 0, \quad (1.1b)$$

$$\nabla \times \mathbf{E}(\mathbf{r}) = -j\omega\mu_0\mathbf{H}(\mathbf{r}), \quad (1.1c)$$

$$\nabla \times \mathbf{H}(\mathbf{r}) = \mathbf{J}(\mathbf{r}) + j\omega\epsilon_0\mathbf{E}(\mathbf{r}). \quad (1.1d)$$

Here, $\mathbf{E}(\mathbf{r})$, $\mathbf{H}(\mathbf{r})$ are the electric field and magnetic field, respectively, $\rho(\mathbf{r})$ is the scalar electric charge density, and $\mathbf{J}(\mathbf{r})$ is the vector electric current density. Associated with each of the equations (1.1a)-(1.1d) is a corresponding boundary condition:

$$\hat{\mathbf{n}} \cdot (\mathbf{E}_1(\mathbf{r}) - \mathbf{E}_2(\mathbf{r})) = \frac{\rho_s(\mathbf{r})}{\epsilon_0}, \quad (1.2a)$$

$$\hat{\mathbf{n}} \cdot (\mathbf{H}_1(\mathbf{r}) - \mathbf{H}_2(\mathbf{r})) = 0, \quad (1.2b)$$

$$\hat{\mathbf{n}} \times (\mathbf{E}_1(\mathbf{r}) - \mathbf{E}_2(\mathbf{r})) = 0, \quad (1.2c)$$

$$\hat{\mathbf{n}} \times (\mathbf{H}_1(\mathbf{r}) - \mathbf{H}_2(\mathbf{r})) = \mathbf{J}_s(\mathbf{r}), \quad (1.2d)$$

where $\rho_s(\mathbf{r})$ is the surface electric charge density and $\mathbf{J}_s(\mathbf{r})$ is the surface electric current density. These equations are supplemented by the continuity equation (1.3), which specifies the relation

between the divergence of electric current and the time rate of change (multiplication by $j\omega$ in frequency domain) of the electric charge.

$$\nabla \cdot \mathbf{J}(\mathbf{r}) + j\omega\rho(\mathbf{r}) = 0. \quad (1.3)$$

By taking the curl of (1.1c) and substituting equation (1.1d), the vector Helmholtz equation for the electric field may be obtained as

$$\nabla \times \nabla \times \mathbf{E} - k^2\mathbf{E} = -j\omega\mu_0\mathbf{J}, \quad (1.4)$$

and reversing the substitution, the vector Helmholtz equation for the Magnetic field may be obtained as

$$\nabla \times \nabla \times \mathbf{H} - k^2\mathbf{H} = \nabla \times \mathbf{J}. \quad (1.5)$$

Here, k is the wave number, given by $k = \omega/c$, with $c = \sqrt{\mu_0\epsilon_0}$ the speed of light in free space. Each of these equations may be written in operator notation as $\mathcal{D}\mathbf{E} = -j\omega\mu_0\mathbf{J}$ for (1.4) and $\mathcal{D}\mathbf{H} = \nabla \times \mathbf{J}$. If \mathbf{J} is known, the solution to these partial differential equations corresponds formally to inversion of the operator \mathcal{D} as

$$\begin{aligned} \mathbf{E}(\mathbf{r}) &= \mathcal{D}^{-1}(-j\omega\mu_0\mathbf{J}) \\ \mathbf{H}(\mathbf{r}) &= \mathcal{D}^{-1}(\nabla \times \mathbf{J}). \end{aligned} \quad (1.6)$$

Even if \mathbf{J} is not known, this construction is still useful. The operator \mathcal{D}^{-1} is an integral operator, which will be derived separately for $\mathbf{E}(\mathbf{r})$ and $\mathbf{H}(\mathbf{r})$ below.

The electric and magnetic fields may be expressed in terms of a set of two potentials, the magnetic vector potential $\mathbf{A}(\mathbf{r})$ and the scalar electric potential $\Phi(\mathbf{r})$. These potentials are non-unique, and are only completely fixed by the specification of a gauge. In this work, the usual Lorenz gauge is chosen, which is characterized by the relation

$$\nabla \cdot \mathbf{A}(\mathbf{r}) = \frac{-j\omega}{c^2}\Phi(\mathbf{r}). \quad (1.7)$$

Under the Lorenz gauge, the magnetic field may be expressed in terms of a magnetic vector potential $\mathbf{A}(\mathbf{r})$ as

$$\mathbf{H} = \frac{1}{\mu_0}\nabla \times \mathbf{A}(\mathbf{r}). \quad (1.8)$$

The electric field is also expressible in terms of the vector potential plus the gradient of a scalar potential $\Phi(\mathbf{r})$,

$$\mathbf{E}(\mathbf{r}) = -j\omega\mathbf{A}(\mathbf{r}) - \nabla\Phi(\mathbf{r}). \quad (1.9)$$

The vector and scalar potentials may be obtained in terms of vector and scalar source densities as

$$\mathbf{A}(\mathbf{r}) = \mu_0 \int_{\Omega} G(\mathbf{r}, \mathbf{r}') \mathbf{J}(\mathbf{r}') d\mathbf{r}', \quad (1.10a)$$

$$\Phi(\mathbf{r}) = \frac{1}{\epsilon_0} \int_{\Omega} G(\mathbf{r}, \mathbf{r}') \rho(\mathbf{r}') d\mathbf{r}', \quad (1.10b)$$

where $\mathbf{J}(\mathbf{r})$ is the electric current density, $\rho(\mathbf{r})$ is the electric charge density and Ω is the support of the source domain. The function $G(\mathbf{r}, \mathbf{r}')$ is the free-space Helmholtz Green's function, given by

$$G(\mathbf{r}, \mathbf{r}') = \frac{e^{-jk\|\mathbf{r}-\mathbf{r}'\|}}{4\pi\|\mathbf{r}-\mathbf{r}'\|}. \quad (1.11)$$

Using the continuity equation (1.3), (1.10b) may be rewritten so that the $\rho(\mathbf{r})$ dependence is replaced with a dependence on the divergence of $\mathbf{J}(\mathbf{r})$

$$\Phi(\mathbf{r}) = \frac{j}{\omega\epsilon_0} \int_{\Omega} G(\mathbf{r}, \mathbf{r}') \nabla' \cdot \mathbf{J}(\mathbf{r}') d\mathbf{r}'. \quad (1.12)$$

1.3.1 The Surface Equivalence Principle

The surface equivalence principle is necessary to derive the electromagnetic integral equations treated in this thesis. It is based on tangential boundary conditions at an interface. Given an interface Ω between two domains D_1 and D_2 that is equipped with a unit normal pointing from D_2 into D_1 , assume that the regions D_1 and D_2 respectively support field distributions $\mathbf{E}_1, \mathbf{H}_1$ and $\mathbf{E}_2, \mathbf{H}_2$. Then the surface equivalence principle states that an equivalent problem may be substituted in either region in which additional currents are inserted to provide the same field discontinuities at the interface. These equivalent currents are obtained via the tangential boundary conditions at the interface:

$$\hat{\mathbf{n}} \times (\mathbf{E}_1(\mathbf{r}) - \mathbf{E}_2(\mathbf{r})) = -\mathbf{M}_s(\mathbf{r}), \quad \mathbf{r} \in \Omega, \quad (1.13a)$$

$$\hat{\mathbf{n}} \times (\mathbf{H}_1(\mathbf{r}) - \mathbf{H}_2(\mathbf{r})) = \mathbf{J}_s(\mathbf{r}), \mathbf{r} \in \Omega, \quad (1.13b)$$

where the boundary condition on tangential \mathbf{E} given previously has been augmented with a (fictitious) magnetic surface current $\mathbf{M}_s(\mathbf{r})$. If one is solving a problem in D_1 in the presence of field distributions in D_2 , an equivalent problem may be constructed using a different set of fields $\mathbf{E}'_2, \mathbf{H}'_2$ in D_2 as long as equivalent currents $\mathbf{M}'_s, \mathbf{J}'_s$ are inserted at the interface to maintain the same field distributions $\mathbf{E}_1, \mathbf{H}_1$ in D_1 , i.e. $\mathbf{M}'_s = \mathbf{M}_s + (\mathbf{E}_2 - \mathbf{E}'_2) \times \hat{\mathbf{n}}, \mathbf{J}'_s = \mathbf{J}_s + \hat{\mathbf{n}} \times (\mathbf{H}_2 - \mathbf{H}'_2)$. Uniqueness theorems in electromagnetic theory [2] dictate that only $\hat{\mathbf{n}} \times \mathbf{E}$ or $\hat{\mathbf{n}} \times \mathbf{H}$ need be determined at each point on the interface to uniquely specify fields everywhere, and not both simultaneously. In the case where the interior fields are known to be zero (i.e. the problem of a PEC scatterer), the problem reduces to finding an equivalent current $\mathbf{J}_s = \hat{\mathbf{n}} \times \mathbf{H}_1$ such that $\mathbf{E}_2 = 0, \mathbf{H}_2 = 0$. Applied to scattering from a PEC obstacle, the equivalence principle permits the scattering object to be replaced by a set of equivalent currents residing in free space. The free-space Green's function may therefore be used instead of a Green's function that explicitly accounts for the presence of the scatter; this greatly simplifies the problem as specialized Green's functions that incorporate the presence of arbitrary objects are typically difficult to obtain.

1.4 Derivation of Electromagnetic Boundary Integral Equations

With the above concepts defined, the two electromagnetic integral equations of interest in this study may now be derived. The first, the Electric Field Integral Equation (EFIE) is derived in terms of tangential boundary conditions on the electric field, and the second, the Magnetic Field Integral Equation (MFIE) is defined in terms of boundary conditions on the magnetic field.

Consider a region in unbounded free space containing a perfectly conducting object that is defined by the open volume $D_2 \subset \mathbb{R}^3$ and bounded by the surface Ω , which is equipped with an outward pointing normal $\hat{\mathbf{n}}$. The exterior domain is defined as $D_1 = \mathbb{R}^3 \setminus (D_2 \cup \Omega)$. For this work, the constitutive parameters of the medium in the exterior domain D_1 are assumed to be those of free space. As the fields inside the PEC object are assumed to be zero, the superscripts on $\mathbf{E}^1, \mathbf{H}^1$

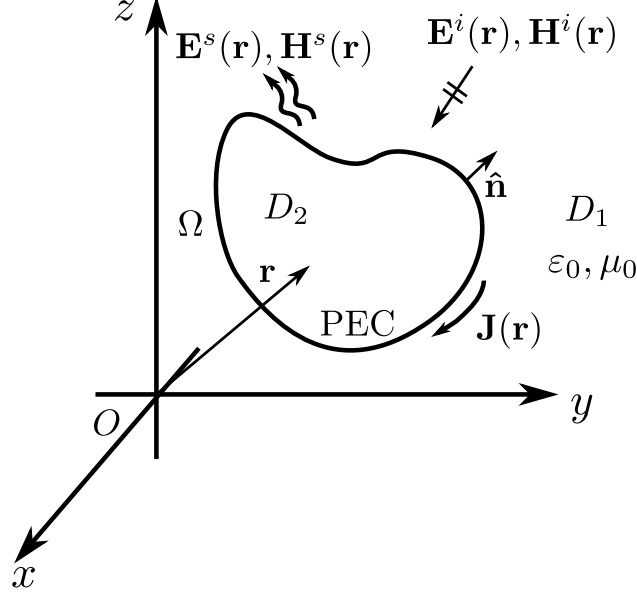


Figure 1.1: Setup for scattering from a perfectly electrically conducting obstacle in three dimensional free space.

will be dropped for the remainder of this section. Assume that an electromagnetic plane wave with associated fields $\mathbf{E}^i(\mathbf{r})$, $\mathbf{H}^i(\mathbf{r})$ is incident upon the scatterer. Fig. 1.1 depicts the setup for this problem.

The goal of solving the EFIE and MFIE is to obtain the equivalent current $\mathbf{J}(\mathbf{r}) = \hat{\mathbf{n}} \times \mathbf{H}(\mathbf{r})$, $\mathbf{r} \in \Omega$. Knowledge of the surface current allows one to use (1.9) with equations (1.10a),(1.12) to obtain the scattered electric field $\mathbf{E}^s(\mathbf{r})$, $\mathbf{r} \in D_1$ due to $\mathbf{E}^i(\mathbf{r})$ impinging on the object. Application of the tangential boundary condition for the electric field at a perfectly conducting interface gives

$$\hat{\mathbf{n}} \times \hat{\mathbf{n}} \times (\mathbf{E}^i(\mathbf{r}) + \mathbf{E}^s(\mathbf{r})) = 0, \quad \mathbf{r} \in \Omega. \quad (1.14)$$

It is customary to include an additional cross product of the unit normal with the usual tangential boundary condition with to directly obtain tangential \mathbf{E} , and to simplify subsequent formulas. Using equations (1.9), (1.10a) and (1.12) and the continuity equation (1.3), (1.14) may be rewritten as

$$\begin{aligned} \hat{\mathbf{n}} \times \hat{\mathbf{n}} \times \mathbf{E}^i(\mathbf{r}) = & -\hat{\mathbf{n}} \times \hat{\mathbf{n}} \times \left[j\omega\mu_0 \int_{\Omega} G(\mathbf{r}, \mathbf{r}') \mathbf{J}(\mathbf{r}') d\mathbf{r}' \right. \\ & \left. - \frac{j}{\omega\epsilon_0} \nabla \int_{\Omega} G(\mathbf{r}, \mathbf{r}') \nabla' \cdot \mathbf{J}(\mathbf{r}') d\mathbf{r}' \right]. \end{aligned} \quad (1.15)$$

This is the EFIE. The MFIE uses tangential magnetic field boundary conditions on a perfect electrical conductor,

$$\hat{\mathbf{n}} \times (\mathbf{H}^i(\mathbf{r}) + \mathbf{H}^s(\mathbf{r})) = \mathbf{J}(\mathbf{r}). \quad (1.16)$$

Substituting (1.10a) into the relation (1.8), equation (1.16) may be rewritten as

$$\hat{\mathbf{n}} \times \mathbf{H}^i(\mathbf{r}) = \mathbf{J}(\mathbf{r}) - \hat{\mathbf{n}} \times \nabla \times \int_{\Omega} G(\mathbf{r}, \mathbf{r}') \mathbf{J}(\mathbf{r}') d\mathbf{r}'. \quad (1.17)$$

Equation (1.17) is the MFIE. The EFIE and MFIE operators by themselves exhibit spurious interior resonances at frequencies corresponding to the cavity modes of closed scattering objects. One common method for removing these resonances is to use a linear combination of the EFIE and MFIE, given by

$$\begin{aligned} \alpha \hat{\mathbf{n}}(\mathbf{r}) \times \hat{\mathbf{n}}(\mathbf{r}) \times \mathbf{E}^i(\mathbf{r}) + (1 - \alpha) \hat{\mathbf{n}}(\mathbf{r}) \times \eta_0 \mathbf{H}^i(\mathbf{r}) = \\ -\alpha \hat{\mathbf{n}}(\mathbf{r}) \times \mathcal{T} \circ \mathbf{J}(\mathbf{r}) + (1 - \alpha) \eta_0 (I - \mathcal{K}) \circ \mathbf{J}(\mathbf{r}). \end{aligned} \quad (1.18)$$

where I is the identity operator, $0 \leq \alpha \leq 1$ is a constant weighting factor, $\eta_0 = \sqrt{\mu_0/\epsilon_0}$ is the intrinsic impedance of free space, and the operators \mathcal{T} and \mathcal{K} are given by

$$\begin{aligned} \mathcal{T} \circ \mathbf{J}(\mathbf{r}) = -\hat{\mathbf{n}}(\mathbf{r}) \times \left[\frac{j}{k} \eta_0 \int_{\Omega} d\mathbf{r}' G(\mathbf{r}, \mathbf{r}') \mathbf{J}(\mathbf{r}') \right. \\ \left. + \frac{j\eta_0}{k} \int_{\Omega} d\mathbf{r}' \nabla \nabla' G(\mathbf{r}, \mathbf{r}') \cdot \mathbf{J}(\mathbf{r}') \right] \\ \mathcal{K} \circ \mathbf{J}(\mathbf{r}) = \hat{\mathbf{n}}(\mathbf{r}) \times \int_{\Omega} d\mathbf{r}' \nabla G(\mathbf{r}, \mathbf{r}') \times \mathbf{J}(\mathbf{r}'). \end{aligned} \quad (1.19)$$

This equation is known as the Combined Field Integral Equation (CFIE). In this thesis the Generalized Method of Moments is applied to solve the CFIE.

1.5 The Method of Moments

The method of moments, or moment method, is the most common approach to solving electromagnetic integral equations of the type defined in the last section. The method of moments may be derived in a variety of ways, using several different mathematical tools [2]. One straightforward

treatment is in terms of projection of solutions onto approximation function spaces. Consider a linear operator L whose operation on some unknown source function f is equal to a known function h . This may be expressed as

$$Lf = h, \quad (1.20)$$

where it is understood that the operator L is acting on f . The operator L can be any linear functional operating on f , e.g. a differential operator or an integral operator. The problem is to find the unknown function f that satisfies the equality, or, formally, to find $f = L^{-1}g$. The moment method is one solution technique for such equations.

To discuss the moment method formulation, it is necessary to first define an inner product between two functions f and g , denoted $\langle f, g \rangle$. Although the choice of inner product is not unique and may be chosen to suit the requirements of the problem, the standard inner product is defined as

$$\langle f, g \rangle = \int_{\Omega} w(x)f(x)g(x)dx, \quad (1.21)$$

where Ω is chosen as a suitable domain and $w(x)$ is a weighting function.

The first step in forming a moment method system is to discretize the unknown function f in terms of a set of approximation functions as

$$f(x) = \sum_{n=1}^N a_n \phi_n(x). \quad (1.22)$$

Here, the set $\{a_n\}$ is a set of unknown coefficients that is presumed to satisfy $\sum_{n=0}^N |a_n|^2 < \infty$, and the set $\{\phi_n\}$ consists of admissible functions, e.g. $\{\phi_n\} \subset L^2$, with L^2 the set of square integrable functions. It is now possible to rewrite (1.20) as

$$\sum_n^N a_n L\phi_n = h. \quad (1.23)$$

If L is an integral operator, interchange of summation and integration is allowed because both the sum and the integral are assumed to converge. The next step in constructing a moment method system is to take inner products with another set of expansion functions $\{w_m\}$:

$$\sum_n^N a_n \langle w_m, L\phi_n \rangle = \langle w_m, h \rangle. \quad (1.24)$$

This procedure is often referred to as “testing” (1.23) with the set $\{w_m\}$, a term that originates in the so-called “reaction” interpretation of the moment method [3], in which the fields due to the equivalent sources $\{\phi_n\}$ are observed, or “tested” by another set of equivalent sources, $\{w_n\}$. Equation (1.24) is a formal statement of the moment method system, and may be solved for the unknown coefficients $\{a_n\}$. It may be rewritten in matrix notation as

$$ZI = V, \quad (1.25)$$

where Z is a matrix with elements $Z_{mn} = \langle w_m, L\phi_n \rangle$, the right hand side $V = [v_1, v_2, v_3, \dots, v_N]^T$, $v_j = \langle w_m, h \rangle$ consists of a vector containing the forcing function tested with each w_m , and $I = [a_1, a_2, a_3, \dots, a_N]^T$ is the vector of unknown scalar (generally complex) coefficients. The solution is obtained by computing $I = Z^{-1}V$ using a matrix inversion procedure, either direct inversion, matrix factorization, or some sort of iterative process. As long as Z_{mn} and v_m can be computed, the unknown coefficients may be solved for and an approximate solution to (1.20) obtained. Discretization and solution of integral equations via the moment method is also subject to different interpretations; e.g. as minimization of an energy functional via a Rayleigh-Ritz procedure [4]. These interpretations will be developed as needed in the chapters below.

1.6 Manifold Theory

The Generalized Method of Moments may be interpreted as a direct application of the modern theory of manifolds to the computational solution of electromagnetic boundary integral equations. This section briefly develops some concepts and nomenclature required to define functions and perform calculus on the manifold structures used in GMM. Discussion here is restricted to smooth manifolds. Some GMM formulations in thesis are rigorously described by smooth manifold theory, and some relax certain conditions required to be classified as globally smooth in the mathematically rigorous sense. Even in these cases, the language and theory of smooth manifolds are still useful conceptual tools for describing GMM discretizations. Additionally, many GMM manifolds

become smooth in the limit that tolerances in geometry representation go to zero. For a comprehensive introduction to manifold theory, see [5].

1.6.1 Definition of a smooth manifold

A smooth manifold is a mathematical entity, denoted in this work by Ω , upon which the operations of calculus may be performed. Heuristically, this means that an n -dimensional (real) manifold looks locally like \mathbb{R}^n , i.e. a copy of n -dimensional real space. To make this definition explicit, and since calculus is done with respect to coordinates, it is necessary to define a notion of coordinates at each point on the manifold. This is done using the mechanism of coordinate charts, which are defined as follows. Given a smooth manifold Ω , for an open (i.e. not containing its boundary) subset $\Omega_i \subset \Omega$, associate a smooth map $\varphi_i : \Omega_i \rightarrow \mathbb{R}^n$ such that each point $p \in \Omega_i$ may be obtained in terms of local coordinates by the inverse map $\varphi_i^{-1}(\mathbf{u}) : \mathbb{R}^n \rightarrow \Omega_i$, $\mathbf{u} \in \mathbb{R}^n \doteq \{u^k\}$, $k = 1, \dots, n$. Throughout this and all subsequent sections, raised indices u^i denote local coordinates. In analogy to a set of local maps covering the earth, the set of all charts $\{(\Omega_i, \varphi_i)\}$ that covers Ω (i.e. $\cup_i \Omega_i = \Omega$) is termed an “atlas” for Ω . The atlas concept provides a means of stitching the coordinate charts $\{\Omega_i\}$ together to obtain the original manifold, and allows locally performed calculus operations to be cast in a global setting. Finally, for a pair of neighborhoods with nonempty intersection, i.e. where $\Omega_i \cap \Omega_j \neq \{\emptyset\}$, “transition maps” are defined between two charts (Ω_i, φ_i) and (Ω_j, φ_j) as $\tau_{ij} : (\Omega_j, \varphi_j) \rightarrow (\Omega_i, \varphi_i) = \varphi_i \circ \varphi_j^{-1}$. The key property of transition maps relevant to GMM is that they allow calculus done on Ω_j to be expressed in terms of calculus performed on Ω_i . These transition maps also carry a significant amount of information about the manifold. Crucially, they may be used to determine whether the manifold is smooth: if the transition maps are smooth up to C^k (i.e. support k bounded derivatives), then the manifold is also C^k smooth. Fig. 1.2 graphically depicts the quantities defined in this section for a two-dimensional manifold. Since GMM is intended to solve electromagnetic scattering problems from two dimensional surfaces in \mathbb{R}^3 , Fig. 1.2 and the remainder of this document will consider only the $n = 2$ case.

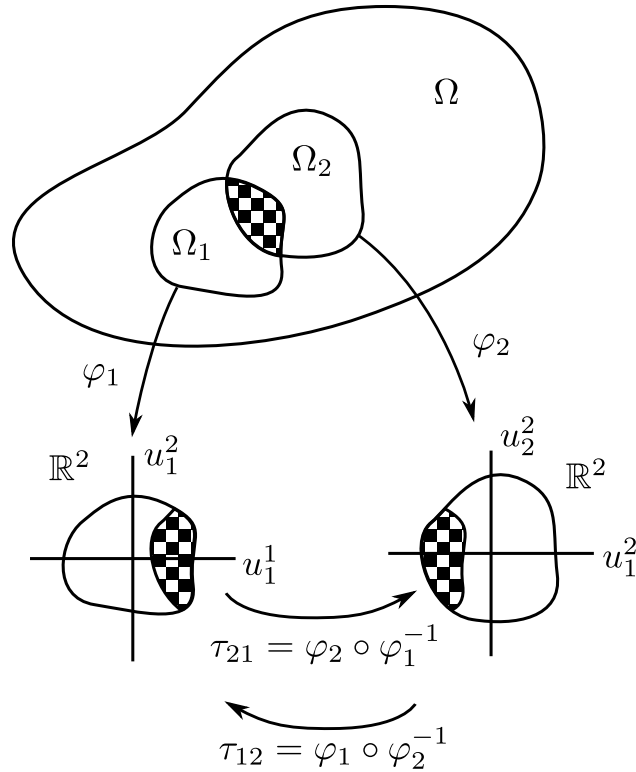


Figure 1.2: Manifold Ω , coordinate charts (Ω_1, φ_1) and (Ω_2, φ_2) , and transition maps τ_{12}, τ_{21} .

1.6.2 Partitions of unity

In general, it is not possible to cover an arbitrary manifold with a single coordinate chart [5]. However, it is possible to stitch together the many coordinate charts (Ω_i, φ_i) , and furthermore to provide smooth transitions between functions defined on different charts. This is accomplished through the construction of a partition of unity, which is defined as follows. Let the set $\{\Omega_i\}$ be an open cover for the manifold Ω . Then subordinate to each open subset $\Omega_i \in \{\Omega_i\}$, define a function ψ_i with the following properties:

1. $0 \leq \psi_i \leq 1$
2. $\text{supp}(\psi_i) \subset \Omega_i$
3. $\sum_i \psi_i = 1$

Then the set of functions $\{\psi_i\}$ is said to form a partition of unity for Ω . The effect of the partition of unity is to allow calculus done in local coordinate systems to be stitched together to cover the entire manifold. Particularly relevant to GMM is that partitions of unity preserve continuity of disparate function descriptions across patch overlaps: for two different functions $f_1 : \Omega_1 \rightarrow \mathbb{R}$ and $f_2 : \Omega_2 \rightarrow \mathbb{R}$ that are not continuous with each other in the overlap region $\Omega_1 \cap \Omega_2$ (i.e. $f_1 + f_2$ is not continuous), the construction $\tilde{f} = \psi_1 f_1 + \psi_2 f_2$ inherits the continuity (and differentiability) of the partitions of unity.

1.6.3 Tangent and cotangent bundles

With each point $p \in \Omega$ on an n -dimensional manifold, there is an associated vector space called the tangent fiber that contains n tangent vectors, and denoted $T_p\Omega$. The entities $X_l(p) \in T_p\Omega$, $l = 1, \dots, n$ that reside in this vector space are referred to as tangent vectors, and are specified with a subscript. As in elementary linear algebra, the notion of tangent vectors naturally gives rise to a dual space, the space of cotangent vectors, with the cotangent fiber at a point p denoted by $T_p^*\Omega$. The cotangent vectors that reside in this this space are denoted by X^l , $l = 1, \dots, n$, and are specified with a superscript. Formally, the cotangent fiber is the space of linear functionals that acts on the space of tangent vectors as $X^j : T_p\Omega \rightarrow \mathbb{R}$. A more concrete way to define the relation between tangent and cotangent vectors is in terms of a basis. For example, let $\{e_i\}$, $i = 1, \dots, n$ be the standard basis in \mathbb{R}^n , and let $\{\varepsilon^j\}$ denote the standard dual basis. Then the dual basis $\{\varepsilon^j\}$ is define through the relation

$$\varepsilon^j e_i = \delta_i^j, \quad (1.26)$$

where δ_i^j is the Kronecker Delta. The collection of all tangent (cotangent) fibers over Ω is called the tangent (cotangent) bundle for the manifold. The tangent bundle is denoted $T\Omega$ and the cotangent bundle is denoted $T^*\Omega$.

A crucial property of the tangent and cotangent bundles is that they are manifolds in their own right, which implies that they may be parameterized in terms of local coordinates in precisely the same manner as the underlying manifold. Additionally, partitions of unity may also be constructed

on $T\Omega$ and $T^*\Omega$, although these partitions of unity are distinct from the partition of unity used on the manifold Ω itself. The surface current spaces used in GMM are constructed using this property.

In order to define computations on $T\Omega$ and $T^*\Omega$ when they are expressed as smooth manifolds, it is necessary to define coordinate charts in a manner analogous to the coordinate charts (Ω_i, φ_i) on Ω . A thorough discussion of the construction of a basis for the tangent and cotangent spaces of an arbitrary manifold is beyond the scope of the current discussion. Instead, it is sufficient to state that there is a standard tangent basis denoted $\{\partial/\partial x^l\}$, $l = 1, \dots, n$ that consists of the set of directional derivatives along the coordinate directions $\{u^l\}$ so that a tangent vector may be expressed as

$$X = \sum_{l=1}^n v^l \frac{\partial}{\partial u^l}. \quad (1.27)$$

In standard three dimensional Euclidean space, the basis $\{\partial/\partial u^l\}$ corresponds exactly to the three canonical coordinate basis vectors with $u^1 = x, u^2 = y, u^3 = z$:

$$\begin{aligned} \frac{\partial}{\partial u^1} &= \frac{\partial}{\partial x} = \hat{\mathbf{x}}, \\ \frac{\partial}{\partial u^2} &= \frac{\partial}{\partial y} = \hat{\mathbf{y}}, \\ \frac{\partial}{\partial u^3} &= \frac{\partial}{\partial z} = \hat{\mathbf{z}}. \end{aligned} \quad (1.28)$$

Thus, in analogy with the familiar Euclidean picture, the coordinates of a vector X^k in the tangent space are $(v^1 \dots v^n) \in \mathbb{R}^n$. The final step necessary of the construction of coordinates for the tangent space (which makes $T\Omega$ a manifold) is to pair the tangent vector coordinates with the local coordinate chart (Ω_i, φ_i) that gives local coordinates for the points $p \in \Omega_i$. This composite coordinate map on the tangent space is defined as $\tilde{\varphi}_i : \Omega_i \times \mathbb{R}^n \rightarrow \mathbb{R}^{2n}$. Using the notation previously defined for coordinate charts, the coordinate charts for the tangent space are $(\Omega_i \times \mathbb{R}^n, \tilde{\varphi}_i)$. The associated transition functions are $\tilde{\tau}_{ij} : \Omega_j \times \mathbb{R}^n \rightarrow \Omega_i \times \mathbb{R}^n$ are given by:

$$\tilde{\tau}_{ij} = \begin{bmatrix} \tau_{ij} & 0 \\ 0 & \sigma_{ij} \end{bmatrix}, \quad (1.29)$$

with the transition map $\sigma_{i,j}$ the $n \times n$ transition matrix between the sets of tangent vectors on $T\Omega_i$ and $T\Omega_j$, which corresponds to the Jacobian of the transition map τ_{ij} . Partitions of unity may

be defined on the open subsets $\Omega_i \times \mathbb{R}^n \subset T\Omega$ in precisely the same way they are on the sets Ω_i . Fig. 1.3 shows the portion of the tangent bundle associated with a subset Ω_i of a two dimensional manifold Ω . In Fig. 1.3, the tangent fibers are visualized as copies of \mathbb{R}^2 ; they are actually vectors expressed as in (1.27), but it can be shown that local tangent bundles $T\Omega_i$ of the type used in GMM may be mapped smoothly onto copies of real space of the same dimension as Ω .

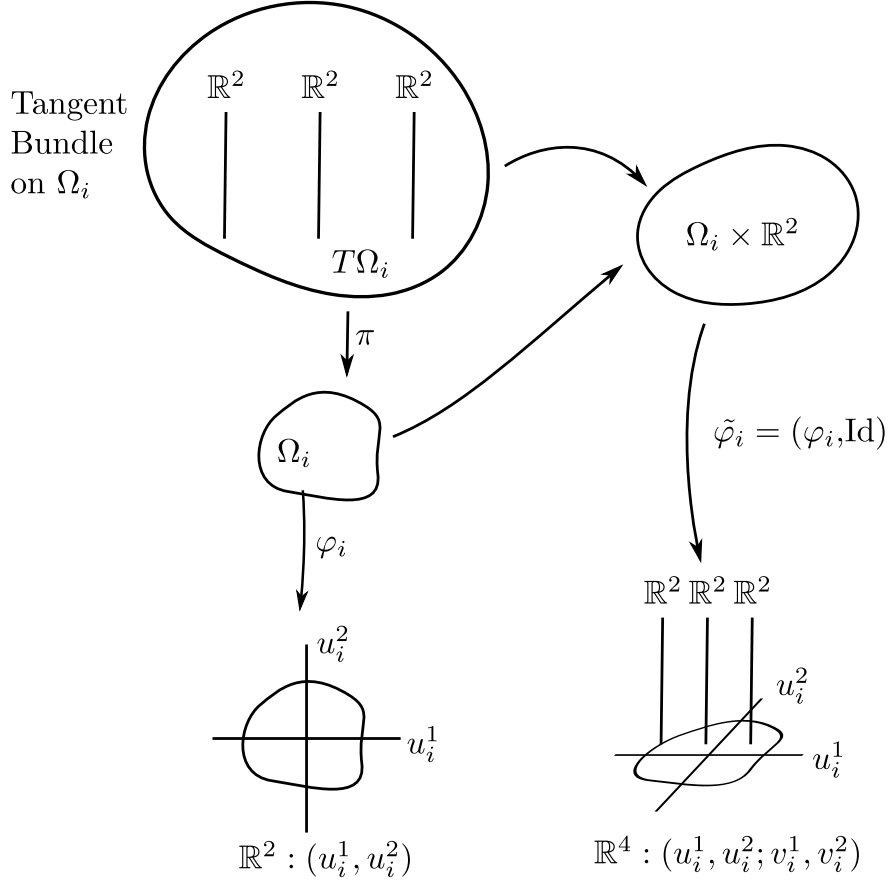


Figure 1.3: Tangent bundle for a subset Ω_i of a two-dimensional manifold Ω . The bundle $T\Omega_i$ consists of a collection of copies of \mathbb{R}^2 associated with each pair (u_i^1, u_i^2) in the coordinate chart (Ω_i, φ_i) . Coordinates for the bundle are mapped into \mathbb{R}^4 via the coordinate chart $(\Omega_i \times \mathbb{R}^2, \tilde{\varphi})$, where $\tilde{\varphi}$ maps from the product space $\Omega_i \times \mathbb{R}^2$ into local coordinates in \mathbb{R}^4 .

The development of a basis for the cotangent space proceeds in a similar manner to that of the tangent bundle basis, with cotangent vectors expressed in the standard cotangent basis $\{du^l\}$ as

$$X^* = \sum_{l=1}^n v_l du^l, \quad (1.30)$$

and $dx^l(\partial/\partial x_k) = \delta_k^l$, as required by duality.

1.6.4 Embedding in \mathbb{R}^3 and Riemannian manifolds

Two final concepts are necessary to describe the Generalized Method of Moments in terms of manifold theory. The first of these is the definition of local parameterizations induced by a smooth embedding of the two dimensional manifolds $\{\Omega_i\}$ into \mathbb{R}^3 . Under this embedding, explicit expressions for the tangent bases may be derived. The second concept is that of a so called ‘‘Riemannian metric’’ g on the manifold, which specifies an inner product on each set Ω_i and allows notions of differential length and area to be concretely defined.

If there is map $F : \Omega \rightarrow \mathbb{R}^3$ that is smooth and invertible, then Ω is said to be a submanifold of \mathbb{R}^3 , \mathbb{R}^3 is said to be the ‘‘ambient manifold’’ for Ω , and the ‘‘codimension’’ of the embedding $\Omega \subset \mathbb{R}^3$ is $\dim \mathbb{R}^3 - \dim \Omega = 1$. This embedding may be naturally extended to the open sets $\{\Omega_i\}$ that cover Ω , and provides the link between the manifold theory discussed in the previous sections and the standard picture of a scatterer bounded by a two dimensional surface residing in \mathbb{R}^3 . Specifically, the mapping of local coordinates on a specific neighborhood Ω_i is of the form $(u_i^1, u_i^2) \mapsto (x, y, z)$. Embedding also facilitates explicit expressions for the manifold tangent vectors $(\partial/\partial u_i^1, \partial/\partial u_i^2)$ in terms of the standard basis on \mathbb{R}^3 via a map $dF : T\Omega_i \rightarrow T\mathbb{R}^3$ as

$$\begin{bmatrix} \frac{\partial}{\partial u_i^1} \\ \frac{\partial}{\partial u_i^2} \end{bmatrix} = \begin{bmatrix} \frac{\partial x}{\partial u_i^1} & \frac{\partial y}{\partial u_i^1} & \frac{\partial z}{\partial u_i^1} \\ \frac{\partial x}{\partial u_i^2} & \frac{\partial y}{\partial u_i^2} & \frac{\partial z}{\partial u_i^2} \end{bmatrix} \begin{bmatrix} \frac{\partial}{\partial x} \\ \frac{\partial}{\partial y} \\ \frac{\partial}{\partial z} \end{bmatrix}. \quad (1.31)$$

Using the identifications from the previous section of $(\partial/\partial x, \partial/\partial y, \partial/\partial z) = (\hat{\mathbf{x}}, \hat{\mathbf{y}}, \hat{\mathbf{z}})$, these relations may be written as

$$\begin{aligned} \frac{\partial}{\partial u_i^1} &= \frac{\partial x}{\partial u_i^1} \hat{\mathbf{x}} + \frac{\partial y}{\partial u_i^1} \hat{\mathbf{y}} + \frac{\partial z}{\partial u_i^1} \hat{\mathbf{z}} = \frac{\partial \mathbf{r}}{\partial u_i^1} \\ \frac{\partial}{\partial u_i^2} &= \frac{\partial x}{\partial u_i^2} \hat{\mathbf{x}} + \frac{\partial y}{\partial u_i^2} \hat{\mathbf{y}} + \frac{\partial z}{\partial u_i^2} \hat{\mathbf{z}} = \frac{\partial \mathbf{r}}{\partial u_i^2}. \end{aligned} \quad (1.32)$$

This basis for the tangent space is utilized to construct current basis function sets in the Generalized Method of Moments.

Finally, we briefly define the Riemannian metric, which provides the necessary structure to compute inner products and other quantities of interest such as gradients, divergences, curls, and integrals on the manifold Ω . A Riemannian metric g in local coordinates is defined as

$$g = g_{kl} du^k du^l. \quad (1.33)$$

i.e. g is a rank two tensor field defined at every point $p \in \Omega$ with respect to the product of the cotangent vectors du^k and du^l . A manifold endowed with a Riemannian metric g is called a Riemannian manifold and is denoted (Ω, g) . Properties of the metric for cases of interest in this work are that it is positive definite ($\text{Det}(g) > 0$) and symmetric ($g_{kl} = g_{lk}$).

The global metric g defined everywhere on Ω is constructed using local metrics on the covering set $\{\Omega_i\}$ using a partition of unity as

$$g = \sum_i \Psi_i g_i. \quad (1.34)$$

The inner product of two vectors $w, v \in T\Omega$ is dictated by the metric

$$\langle w, v \rangle = \sum_{k,l} g_{kl} w^k v^l. \quad (1.35)$$

Although the Riemannian metric may be arbitrarily selected as any rank two covariant tensor field that yields a positive definite inner product, the local parameterizations discussed in previous chapters induce a particular choice of the metric. Explicitly, for a two dimensional manifold embedded in \mathbb{R}^3 , the components of the metric with respect to the basis of the tangent space are

$$g_{kl} = \left\langle \frac{\partial}{\partial u^k}, \frac{\partial}{\partial u^l} \right\rangle, \quad (1.36)$$

which, under the map $F : \Omega \rightarrow \mathbb{R}^3$ may be computed easily using the standard metric on \mathbb{R}^3 , $g_{\mu\nu}^{\mathbb{R}^3} = \delta_{\mu\nu}$, which is the usual vector dot product

$$g_{kl} = \delta_{\mu,\nu} \frac{\partial x^\mu}{\partial u^k} \frac{\partial x^\nu}{\partial u^l} = \frac{\partial \mathbf{r}}{\partial u^k} \cdot \frac{\partial \mathbf{r}}{\partial u^l} \quad (1.37)$$

Because the metric g is defined with respect to the cotangent basis vectors, which act on tangent vectors, it is therefore a covariant tensor. Also important is the contravariant tensor associated

with the metric, and defined as the inverse of g . Traditionally, the components of the contravariant metric tensor are denoted with superscripts as g^{kl} . The contravariant tensor acts on the cotangent vector space, and plays a prominent role in the definition of derivative operators on Riemannian manifolds. Operators of particular interest in this work are

$$\nabla\phi = \sum_{k=1}^2 \sum_{l=1}^2 g^{kl} \frac{\partial\phi}{\partial u^k} \frac{\partial}{\partial u^l} = \sum_{k=1}^2 \frac{\partial\phi}{\partial u^k} du^k \quad (1.38a)$$

$$\nabla \cdot \mathbf{f} = \sum_{k=1}^2 \frac{1}{\sqrt{g}} \frac{\partial}{\partial u^k} (\sqrt{g} f_k), \quad (1.38b)$$

where for a two dimensional manifold Ω , (1.38a) is identified with the surface gradient of scalar functions defined on Ω and (1.38b) is identified with the surface divergence of vector functions defined in the tangent space of Ω . Equation (1.38b) may equivalently be written

$$\nabla \cdot \mathbf{f} = \sum_{k=1}^2 \sum_{l=1}^2 g^{kl} \frac{\partial \mathbf{f}}{\partial u^k} \cdot \frac{\partial}{\partial u^l}. \quad (1.39)$$

With the concepts developed in this chapter, the Generalized Method of Moments for electromagnetic boundary integral equations may be formulated in terms of the theories of classical electromagnetic and manifolds. This formulation is the subject of Chapter 2.

CHAPTER 2

THE GENERALIZED METHOD OF MOMENTS

2.1 Introduction

Significant effort has been exerted in recent years toward constructing discretizations of electromagnetic integral equations that model the underlying continuous problem more closely than traditional low order approaches. The aim of these efforts is to obtain solutions with better fidelity to the continuous solution while significantly reducing the size of the discretized system and realizing commensurate savings in computational cost. Most of the work to these ends has focused on one (or a combination) of three directions: higher order current approximating function spaces that require fewer than the traditional 10 degrees of freedom per wavelength, higher order geometry descriptions that more closely model the true continuous geometry, and mixtures of basis sets, e.g. mixing low order interpolatory basis sets with those derived from asymptotic wave representations.

Moment methods that are higher order in both current approximation spaces and geometry representation have been a subject of intense development in recent years. Methods for higher order current representation have been traditionally based either on hierarchical higher order functions residing in Nedelec Spaces [6–9], or on variations of mapped higher order polynomial tensor products [10–13]. By reducing the number of degrees of freedom per wavelength required to discretize the integral operator, each of these methods realizes reductions in MoM system size. However, the physical requirement that approximation functions must provide current continuity between discretization subdomains places strict limitations on the types of basis functions that may be employed, and means that the boundary integral operators generally must be discretized using a single class of basis function, e.g. only polynomials. Some methods for mixing higher order polynomial bases with other basis classes have been developed (e.g. singularity type bases in [14]), but these also require that the basis set be designed to enforce current continuity.

Closely related to the issue of continuity in basis function set is that of continuity in geometry description. Higher order surface descriptions for moment methods are generally based on smooth polynomial surface parameterizations [15], which have difficulty accurately modeling geometrical singularities such as edges and tips. Recently, representations using Non-rational B-Splines (NURBS) have been developed [16, 17]. A bottleneck with both of these methods is enforcing geometrical continuity at abutting patch edges. As with current approximations, this generally forces the use of the same type approximating function for the parameterization of each subdomain.

GMM is a partition of unity method that decomposes the scatterer surface into overlapping subdomains, termed “patches”. As in the Generalized Finite Element Method [18, 19], the partition of unity serves to decouple approximation function descriptions in neighboring subdomains. Consequentially, GMM is able to easily incorporate higher order basis sets, higher order/mixed geometry descriptions, and arbitrary mixing of approximation function spaces. This flexibility in approximation functions occurs because interpatch continuity is provided not by the approximating functions themselves, but by the partition of unity. This lifting of the continuity constraint on the basis functions permits substantially more freedom in the types of approximation function spaces that may be employed; additionally, it allows mixing of different approximation spaces in adjacent subdomains over the surface of the scattering body. Thus, in GMM, basis sets may be freely chosen to match local current ansatz. The partition of unity scheme also allows blending of different functional geometrical descriptions in the overlap region between subdomains, effectively providing geometrical continuity and permitting the use of distinct geometry parameterizations on neighboring subdomains. This implies that geometry parameterizations from entirely different spaces, e.g. polynomials, conics, and flat tessellations, may be utilized in the same simulation while maintaining effective geometrical continuity.

Although partition of unity methods have been widely employed in finite elements to address some of the challenges in basis function and geometrical continuity [20–23], extension of these methods to integral equations has been limited, in part because defining meaningful partitions of unity on arbitrary two dimensional manifolds residing in \mathbb{R}^3 is a nontrivial problem. Nonetheless,

the Partition of Unity Boundary Element Method (PUBEM) [24] has been developed, primarily for the solution of two dimensional acoustic Helmholtz scattering problems. In PUBEM, traditional interpolating approximation function spaces are enriched with asymptotic plane wave bases for electrically/acoustically large simple scatterers in two dimensions [25, 26], and a sphere in three dimensions [27]. A similar approach is taken in [28, 29], wherein stationary phase methods are applied to acoustics and electromagnetics problems using asymptotic representations on electrically large smooth geometries. The approach in the present paper is significantly more general than these approaches because it applies to vectorial electromagnetics problems on arbitrarily shaped scatterers in three dimensions. The approximation spaces utilized may be arbitrary mixtures of basis functions including, but not restricted to, the plane-wave and asymptotic type expansions employed in the PUBEM and [29].

Finally, we note that the Generalized Method of Moments may be classified as a quasi-meshless method. Meshless methods have traditionally been confined to the finite element community, especially in the field of mechanics and mechanical engineering (e.g. [30, 31]), although there has been increasing interest toward applying such methods to computational electromagnetics, primarily in the context of quasi-static problems [32–34], and generalized finite elements, [35, 36]. To the authors’ knowledge, the only applications of meshless methods to high frequency electromagnetic integral equations, excepting GMM and the references in the preceding paragraph, are implementations of the traditional Moving Least Squares (MLS) method [37, 38] and the work in [39], in which both a MLS-based collocation scheme and an integral transform-based approach are given. The Generalized Method of Moments is distinct from these methods in that it incorporates ideas from mesh-free discretization (node-based primitives, partitions of unity) to effect localization of geometry and approximation functions, but then marries these ideas with the large variety of moment method basis sets that have been developed by the electromagnetics community over the last five decades.

The present work provides a unified prescription for the algorithmic development and implementation of the Generalized Method of Moments for arbitrary PEC scatterers. GMM for electro-

magnetic integral equations was first presented in [40] for piecewise flat tessellations and has been extended to low-order (tessellated) Müller formulations for dielectrics [41, 42] and a higher order smooth formulation for acoustics [43]. In this work, we extend GMM for electromagnetics to geometries composed of mixtures of features including flat regions, tessellations, polynomial smooth patches, sharp tips, bodies of revolution, conic sections, etc. The inclusion of local smooth geometry descriptions removes one major hurdle encountered in the piecewise flat approach in [40], which is the appearance of spurious line charges at boundaries between non-coplanar triangles. By introducing either smooth local geometry parameterizations or subdomain basis sets that cancel line charges by construction, the present work avoids line charges altogether. Preliminary work on smooth local parameterizations and hybridizations with non-smooth geometrical descriptions for GMM is contained in [44, 45], and [46].

Specific contributions of this paper are:

- A framework for arbitrarily mixing different classes of basis functions over the surface of a PEC scatterer.
- A geometrical hybridization scheme wherein various functional geometry descriptions may be combined and blended in a single problem.
- A smooth, higher order geometry representation framework for representing arbitrary curved geometries.
- Hybridization with tessellations and introduction of “sub-patch” basis sets capable of handling geometrical singularities.
- Algorithms for automatically assigning approximation function types and local geometry descriptions based on local physical characteristics of the scattering geometry.
- Results demonstrating the flexibility of the method on several test scattering problems.

The scattering results presented are designed to demonstrate mixing of geometry descriptions and basis function classes, and the corresponding reduction in system size. To address larger problems, the method will be hybridized with the Multilevel Fast Multipole Method [47] in future work.

The remainder of the paper is organized as follows. Section 2.2 briefly outlines the problem under consideration. The formulation of GMM for arbitrary PEC scatterers including construction of patches starting from point clouds, the partitions of unity, local geometry parameterizations, local basis functions, and the evaluation of matrix elements, is detailed in Section 2.3. Results validating the method against a reference code, demonstrating its application to several representative geometries, and comparing matrix fill times for GMM relative to extant higher order methods are presented in section 2.5. Finally, Section 2.6 provides some concluding remarks and future directions.

2.2 Problem Statement

The problem of interest is the computation of the scattered fields $\{\mathbf{E}^s(\mathbf{r}), \mathbf{H}^s(\mathbf{r})\}$ due to a plane wave, characterized by the triad $\{\hat{\mathbf{k}}^i, \mathbf{E}^i(\mathbf{r}), \mathbf{H}^i(\mathbf{r})\}$, impinging on a PEC object residing in free space. The scatterer boundary Ω is equipped with a unit normal $\hat{\mathbf{n}}(\mathbf{r})$ defined for all $\mathbf{r} \in \Omega$ except at a finite number of geometrical singularities (e.g. corners, tips, edges, etc.). The boundary integral formulation we employ is the Combined Field Integral equation (CFIE):

$$\begin{aligned} \alpha \hat{\mathbf{n}}(\mathbf{r}) \times \hat{\mathbf{n}}(\mathbf{r}) \times \mathbf{E}^i(\mathbf{r}) + (1 - \alpha) \hat{\mathbf{n}}(\mathbf{r}) \times \mathbf{H}^i(\mathbf{r}) = \\ -\alpha \hat{\mathbf{n}}(\mathbf{r}) \times \mathcal{T} \circ \mathbf{J}(\mathbf{r}) + (1 - \alpha)(I - \mathcal{K}) \circ \mathbf{J}(\mathbf{r}) \end{aligned} \quad (2.1)$$

where I is the identity operator, $0 \leq \alpha \leq 1$ is a constant weighting factor, and the operators \mathcal{T} and \mathcal{K} are given by:

$$\begin{aligned} \mathcal{T} \circ \mathbf{J}(\mathbf{r}) &= -\hat{\mathbf{n}}(\mathbf{r}) \times \left[jk\eta_0 \int_{\Omega} d\mathbf{r}' g(\mathbf{r}, \mathbf{r}') \mathbf{J}(\mathbf{r}') \right. \\ &\quad \left. + \frac{j\eta_0}{k} \int_{\Omega} d\mathbf{r}' \nabla \nabla' g(\mathbf{r}, \mathbf{r}') \cdot \mathbf{J}(\mathbf{r}') \right] \\ \mathcal{K} \circ \mathbf{J}(\mathbf{r}) &= \hat{\mathbf{n}}(\mathbf{r}) \times \int_{\Omega} d\mathbf{r}' \nabla g(\mathbf{r}, \mathbf{r}') \times \mathbf{J}(\mathbf{r}') \end{aligned} \quad (2.2)$$

Here, $\mathbf{j}(\mathbf{r}) = \hat{\mathbf{n}}(\mathbf{r}) \times \{\mathbf{H}^i(\mathbf{r}) + \mathbf{H}^s(\mathbf{r})\}$ is the induced surface current, $g(\mathbf{r}, \mathbf{r}')$ is the free-space Helmholtz Green's function, k is the propagation constant, and η_0 is the intrinsic impedance of free space. An $e^{j\omega t}$ dependence is assumed and suppressed. To construct a moment method system, the surface current is discretized in terms of a set of basis functions as $\mathbf{j}(\mathbf{r}) = \sum_{n=1}^{N_s} a_n \mathbf{f}_n(\mathbf{r})$ (N_s is the total number of degrees of freedom) and the discretized operators in (2.2) are tested with a set of functions $\{\mathbf{f}_m(\mathbf{r})\}, m \in [1, N_s]$ in the usual fashion.

2.3 Formulation

Although many details of the construction of GMM for piecewise flat tessellation and scalar acoustic equations are given in [40] and [43], we include a detailed discussion here because these techniques have not been developed for electromagnetic integral equations on smooth surfaces, and because the present method differs in several respects from previous work.

GMM is constructed via a decomposition of the manifold Ω into overlapping subdomains, termed ‘‘patches’’, and denoted by the set $\{\Omega_i\}$. Each patch Ω_i is composed of four elements: 1) a set of nodes \mathcal{N}_i , 2) a local geometrical parameterization G_i and associated projection plane Γ_i , 3) a partition of unity ψ_i , and 4) a local approximation function space $\{\mathbf{f}_k(\mathbf{r})\}$. In the following section, we first develop patch definitions and define the partitions of unity, which decouple geometry and approximation functions spaces on neighboring patches. We then describe in some detail the design of the local geometry descriptions and basis sets. The set of patches $\{\Omega_i\}$ may be constructed in

several ways depending on the level of a priori information that is known about the surface. We employ the following approach, which only requires an oriented point cloud as a starting point.

2.3.1 Neighborhoods from Point Clouds

To begin, we require only that Ω be sampled with a discrete set of N_m nodes $\mathcal{N} \doteq \{n_i\}, i = 1, 2, 3, \dots, N_m$ residing in \mathbb{R}^3 and equipped with a connectivity map in the sense of nearest neighbors (note that standard simplicial tessellations implicitly contain this information). Denote by \mathcal{N}_i the neighborhood of the i th node, which is initially defined as the set containing n_i and the set of its nearest neighbors $\overline{\mathcal{N}}_i \doteq \mathcal{N}_i/n_i$ as specified by the connectivity map. Additionally, we require an orientation, specified by a normal defined at each n_i . These normals may be a priori provided, or may be obtained using a classical normal estimation routine, e.g. [48]. In the case where a node occurs at a geometrical singularity such as a tip or corner, the normal is not uniquely defined; in GMM such nodes are flagged as “singular” and are handled using a modified algorithm, which is discussed in a later section. For the remainder of this section, we assume that the geometry is free from singularities.

Given the node list \mathcal{N} and corresponding normals, for each n_i we define a subdomain $\hat{\Omega}_i$ centered on n_i and bounded by $\overline{\mathcal{N}}_i$. Each $\hat{\Omega}_i$ is termed a “patch primitive”. We label the set of patch primitives that neighbor $\hat{\Omega}_i$ as $\hat{\Omega}_{\overline{\mathcal{N}}_i} \doteq \{\hat{\Omega}_j | n_j \in \overline{\mathcal{N}}_i\}$, i.e. $\hat{\Omega}_{\overline{\mathcal{N}}_i}$ is the set of all patch primitives associated with nodes that neighbor n_i , but not including $\hat{\Omega}_i$. By definition each $\hat{\Omega}_i$ overlaps with all patches in $\hat{\Omega}_{\overline{\mathcal{N}}_i}$.

Although the initial set of patches $\{\hat{\Omega}_i\}$ is defined about every node in \mathcal{N} , it is often advantageous to merge neighboring primitives into larger patches, e.g., if the patch primitives are small with respect to the characteristic scale of the problem or form part of the same surface of revolution. We denote the set of merged patches as $\{\Omega_i\}$, with each final patch defined as a union of patch primitives: $\Omega_i \doteq \cup_{k=1}^{N_k} \hat{\Omega}_k$, with $\hat{\Omega}_k$ an N_k -dimensional subset of $\{\hat{\Omega}_i\}$. After merging, the final patches may be associated with much larger collections of nodes, with neighborhoods \mathcal{N}_i and patch neighbor sets $\{\Omega_{\overline{\mathcal{N}}_i}\}$ updated accordingly. As patch merging algorithms depend on local

geometric characteristics, we defer discussion of a sample merging algorithm until section 2.4.2. Because there is no formal distinction between merged patches and patch primitives (they are two instances of the same type of object), we drop the hat notation for the remainder of the paper and use the set $\{\Omega_i\}$ to denote the set of all patches for a given scatterer, primitive or otherwise.

2.3.2 Partition of Unity

Subordinate to each Ω_i , we define a partition of unity function $\psi_i(\mathbf{r})$ with $supp\{\psi_i(\mathbf{r})\} = \Omega_i$ with the property that $\sum_i \psi_i(\mathbf{r}) = 1 \forall \mathbf{r} \in \Omega$. These partitions of unity serve to decouple neighboring patches so that any surface function $\phi(\mathbf{r}), \mathbf{r} \in \Omega$ may be reconstructed as $\phi(\mathbf{r}) = \sum_i \psi_i \phi_i(\mathbf{r})$, where the subsectional functions $\phi_i(\mathbf{r})$ are given by $\phi_i(\mathbf{r}) = \chi_i \phi(\mathbf{r})$, with χ_i the characteristic function of patch Ω_i . In GMM, partition of unity is enforced using an approach based on traditional Shepard Interpolation [49], which takes the form:

$$\psi_i(\mathbf{r}) = \frac{\hat{\psi}_i(\mathbf{r})}{\hat{\psi}_i(\mathbf{r}) + \sum_j \hat{\psi}_j(\mathbf{r})} \quad (2.3)$$

in which $\hat{\psi}_j(\mathbf{r})$ is a local shape function with compact support on patch Ω_j , and $\{\hat{\psi}_j(\mathbf{r})\}$ is the set of local shape functions defined on the set $\Omega_{\mathcal{N}_i}$ of patches that neighbor Ω_i . The choice of local shape function depends on the problem type, and may include simplex type functions, smoothly decaying exponentials, polynomial-based functions, etc. In the present work, a simplex-based partition of unity is utilized. Figure 2.1 illustrates the blending of basis function spaces via the partition of unity in one dimension. These concepts extend directly to functions and patches defined on two dimensional manifolds, and also effectively permit blending of different geometry descriptions in the overlap region between patches.

2.3.3 Local Geometry Parameterization

In this section, we develop methods for constructing local surface geometry descriptions on each patch in $\{\Omega_i\}$. These local surface descriptions are superposed as $\bigcup_i \Omega_i$ to recreate the original

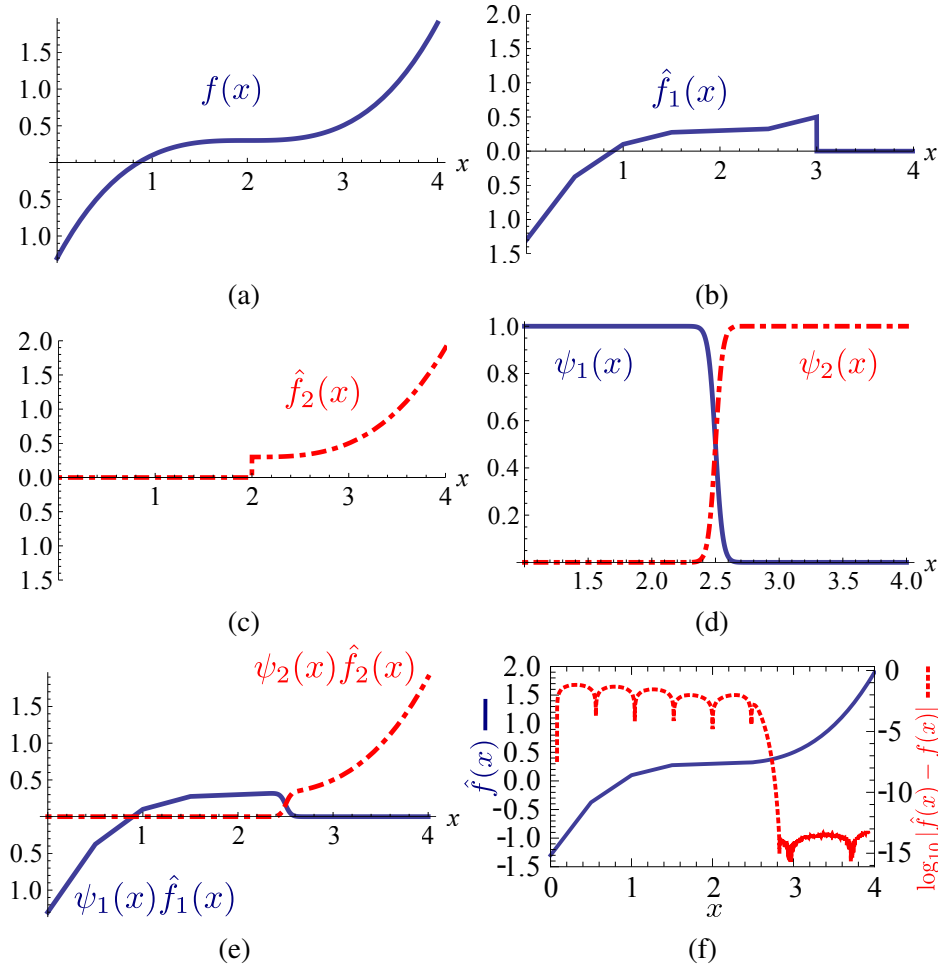


Figure 2.1: Blending of approximation spaces on overlapping domains via the partition of unity for a 1D signal. (a) A trial function $f(x) = .2(x - 2)^3 + .3$ on the interval $\Omega : 0 \leq x \leq 4$. (b) Interpolation of $f(x)$ using linear interpolatory hat functions $T_i(x) = T(x - .5i)$ on subinterval $\Omega_1 : 0 \leq x \leq 3$ such that $\hat{f}_1(x) = \chi_1(x) \sum_i a_i T_i(x)$, $\chi_1(x) = 1, x \in \Omega_1; 0, x \notin \Omega_1$. (c) Interpolation of $f(x)$ using a third order Legendre polynomial set $P_n(x), n = 0, 1, 2, 3$ on subinterval $\Omega_2 : 2 \leq x \leq 4$ such that $\hat{f}_2(x) = \chi_2(x) \sum_{n=1}^3 a_n P_n(x - 3)$, $\chi_2(x) = 1, x \in \Omega_2, 0; x \notin \Omega_2$. (d) Partitions of unity $\psi_1(x)$ and $\psi_2(x)$. (e) interpolations of $f(x)$ multiplied by partitions of unity as $\hat{f}_1(x)\psi_1(x)$ in Ω_1 and $\hat{f}_2(x)\psi_2(x)$ in Ω_2 . (f) Reconstructed function $\hat{f}(x) = \hat{f}_1(x)\psi_1(x) + \hat{f}_2(x)\psi_2(x)$ (left axis) and absolute reconstruction error (right axis). Through the action of the partition of unity, the representations $\hat{f}_1(x)$ and $\hat{f}_2(x)$ are smoothly blended in the overlap region, $2 \leq x \leq 3$, and the approximation error transitions smoothly between the linear and Legendre interpolations.

geometry. This scheme admits a wide variety in the choice of local geometry parameterization. We now describe local geometry construction for both smooth and nonsmooth regions of the scatterer.

From the definition of patches above, each patch Ω_i contains a set of nodes $\mathcal{N}_i = \{n_k\}$ located at positions $\{\mathbf{r}_k\}$ and equipped (in the smooth case) with normals $\{\hat{\mathbf{n}}_k\}$. Local smooth surface parameterization for Ω_i proceeds as a two-step process. First, a ‘‘projection plane’’ Γ_i is defined such that the plane normal $\hat{\mathbf{n}}_i$ is the average of all subordinate node normals:

$$\hat{\mathbf{n}}_i = \frac{\sum_k \hat{\mathbf{n}}_k}{|\sum_k \hat{\mathbf{n}}_k|} \quad (2.4)$$

The plane Γ_i is uniquely defined by its normal and a point \mathbf{r}_{c_i} (defined with respect to the global origin) through which the plane passes; generally, this point is taken as the average of the locations of $\{n_k\}$, although it may be chosen otherwise depending on the requirements of different geometry parameterizations.

Once the plane Γ_i has been defined, a local orthogonal coordinate system (u^1, u^2, u^3) is constructed on Γ_i as follows. First, the altitude direction is taken parallel to $\hat{\mathbf{n}}_i$: $\hat{\mathbf{u}}^3 = \hat{\mathbf{n}}_i$. The $\hat{\mathbf{u}}^1$ direction is defined in the direction of maximum patch dimension, $\max\{|\mathbf{r}_{kb} - \mathbf{r}_{jb}|\}$, where the b subscript indicates a boundary node. The remaining coordinate direction is then defined as $\hat{\mathbf{u}}^2 = \hat{\mathbf{u}}^3 \times \hat{\mathbf{u}}^1$. All local coordinates are defined with respect to a local origin located at \mathbf{r}_{c_i} .

Upon establishment of the local coordinate system, a parameterized manifold Λ_i passing through the nodes $\{n_k\}$ is defined. This parameterization takes the form:

$$\begin{aligned} \Lambda_i &\doteq \{\mathbf{r} \in \mathbb{R}^3 \mid \mathbf{r}(u^1, u^2) = \mathbf{r}_i(u^1, u^2) + \mathbf{r}_{c_i}\}, \\ \mathbf{r}_i(u^1, u^2) &= u^1 \hat{\mathbf{u}}^1 + u^2 \hat{\mathbf{u}}^2 + w_i(u^1, u^2) \hat{\mathbf{u}}^3 \end{aligned} \quad (2.5)$$

where $\mathbf{r}_i(u^1, u^2)$ indicates a local position vector pointing from the (u^1, u^2, u^3) origin to the parameterized surface. The domain of the parameterization is restricted to a polygon in the projection plane Γ_i that bounds the projection $P_{\Gamma_i}(\mathcal{N}_i)$ of the node set \mathcal{N}_i into Γ_i : $u^1, u^2 \in P_{\Gamma_i}(\mathcal{N}_i)$. We denote the type of parameterization on patch Ω_i by G_i . The altitude function $w_i(u^1, u^2)$ may be taken as any well-behaved function of (u^1, u^2) . The conditions for $w_i(u^1, u^2)$ to be well-behaved

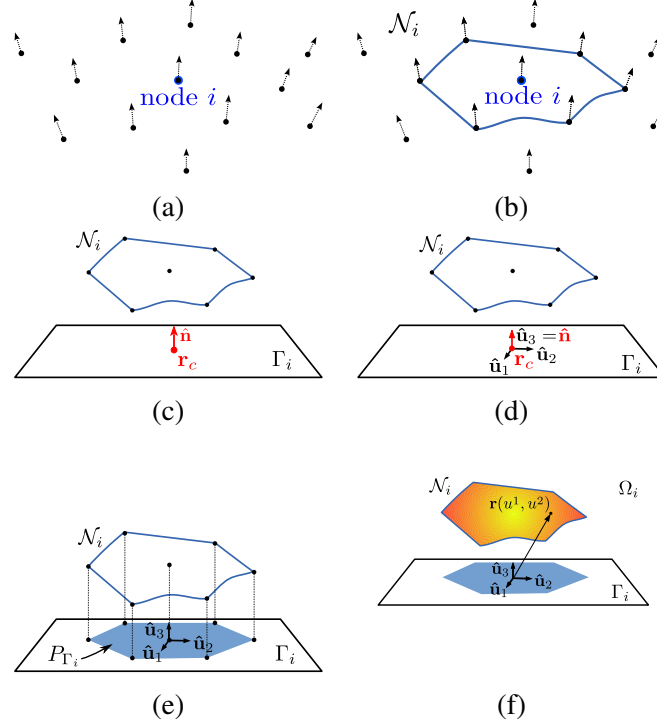


Figure 2.2: Smooth patch geometry parameterization procedure for patch Ω_i : (note: for clarity, subscripts i are dropped on vector quantities) (a) Start with an oriented point cloud. (b) Define a neighborhood \mathcal{N}_i of nearest neighbors about node i . (c) Define a projection plane Γ_i with normal equal to average of all node normals and specified by a point \mathbf{r}_c that uniquely defines an origin of coordinates. (d) Construct a local orthogonal u^1, u^2, u^3 coordinate system. (e) Take projection of points in \mathcal{N}_i into Γ_i to define the support of the patch in the u^1, u^2 plane. This projection is denoted P_{Γ_i} . (f) Obtain a smooth parameterization to define the local patch surface.

are that 1) it is single-valued, 2) its Jacobian is amenable to integration through standard numerical quadrature techniques, and 3) it maintains an appropriate degree of geometrical continuity with neighboring patch descriptions. As long as these conditions are satisfied, different local geometry parameterizations may be used on different patches, and the choice of parameterization G_i may be matched to local geometric features, e.g. a BoR description for rotationally symmetric surface regions, corner elements for edges and tips, Bezier surfaces, etc. The mixing of multiple surface descriptions generalizes the work in [46], which hybridized polygonal tessellations with smooth polynomial surface descriptions. Figure 2.2 summarizes patch neighborhood and local geometry construction for smooth geometries.

To connect the local geometry parameterization process to manifold theory, one can identify

the local parameterization \mathbf{r}_i with a coordinate chart of the form (Ω_i, φ_i) , where $\varphi_i : \Omega_i \rightarrow \mathbb{R}^2$ is a map from the manifold (surface) Ω_i into the (u^1, u^2) plane. This map is the inverse of the mapping \mathbf{r}_i , and is given explicitly with respect to the embedding in \mathbb{R}^3 as:

$$\varphi_i(\mathbf{r}) = (\hat{\mathbf{u}}_1 \cdot (\mathbf{r} - \mathbf{r}_{c_i}), \hat{\mathbf{u}}_2 \cdot (\mathbf{r} - \mathbf{r}_{c_i})) \quad (2.6)$$

i.e. it is the projection of a point \mathbf{r} into the (u^1, u^2) plane associated with the patch. Using the correspondence of $\mathbf{r}_i \leftrightarrow \varphi_i^{-1}$, coordinate changes in overlapping regions between to patches $\mathbf{r} \in \Omega_i \cap \Omega_j$ may be computed using the transition function $\tau_{ij} = \varphi_i \circ \varphi_j^{-1}$ as

$$\tau_{ij} = (\hat{\mathbf{u}}_1^i \cdot (\mathbf{r}_j - \mathbf{r}_{c_i}), \hat{\mathbf{u}}_2^i \cdot (\mathbf{r}_j - \mathbf{r}_{c_i})). \quad (2.7)$$

Note that, if the geometry description is approximate, then the transition functions will τ_{ij} will be approximate as well.

2.3.3.1 Smooth Polynomial Geometry Parameterization

Although any parameterization satisfying the conditions stated in the previous section may be utilized to define patch surfaces, it is desirable to have a default parameterization scheme for surfaces where no a priori surface description is known apart from the node locations and normals. To effect this scheme, following [50] we use a polynomial surface description for the parameterized manifold Λ_i :

$$\mathbf{r}_i(u^1, u^2) = u^1 \hat{\mathbf{u}}^1 + u^2 \hat{\mathbf{u}}^2 + \mathcal{P}_i^g(u^1, u^2) \hat{\mathbf{u}}^3 \quad (2.8)$$

where $\mathcal{P}_i^g(u^1, u^2)$ is as a degree g tensor product of polynomials in u^1 and u^2 :

$$\mathcal{P}_i^g(u^1, u^2) = \sum_{|\alpha| \leq g} c_\alpha (u^1)^{\alpha_1} (u^2)^{\alpha_2} \quad (2.9)$$

Here we have employed standard multi-index notation $\alpha \doteq (\alpha_1, \alpha_2)$, $|\alpha| = \alpha_1 + \alpha_2$ for compactness. The coefficients c_α are obtained via least-squares fit. The geometrical fidelity of Λ_i to the

original node locations is controllable by the degree g and the tolerance in the least squares algorithm. By defining Λ_i as a polynomial function $\mathcal{P}_i^g(u^1, u^2)$, Λ_i is ensured to lie the space C^g of g -differentiable functions. This property is important in evaluating field integrals because basis functions in the GMM scheme inherit the differentiability of the geometry parameterization.

2.3.3.2 Handling of Geometrical Singularities

In the case where a patch contains nodes that lie on geometric singularities, a modified geometry parameterization method is employed. If an analytical description of geometry in the neighborhood of singularity is known, as with a conical tip or straight edge, a custom geometrical description that correctly handles the singularity may be constructed. Alternatively, a standard triangular tessellation may be defined on the set of nodes adjacent to (and including) the singular nodes. Appropriate basis sets are then defined on the tessellation that correctly capture the behavior of currents and charges near the singular feature. Although the design of these functions is outside the scope of this paper, several such basis functions have been developed (the most prevalent being the RWG class of functions) that can be easily incorporated into the GMM framework.

2.3.3.3 Definition of the Tangent Space $T\Omega_i$

The basis functions used to discretize vector current distributions $\mathbf{J}(\mathbf{r})$, $\mathbf{r} \in \Omega$ are defined in the tangent space $T\Omega_i$, or ‘‘Tangent Bundle’’ on each patch Ω_i . Section 1.6.3 of chapter 1 gives a general discussion of the construction of tangent bundles under local parameterizations of the form (2.3), and provides expressions for the tangent basis vectors, which for the local parameterizations developed above are given by:

$$\begin{aligned} \mathbf{r}_{u^1}^i &= \frac{\partial \mathbf{r}_i}{\partial u^1} = \hat{\mathbf{u}}^1 + \frac{\partial w(u^1, u^2)}{\partial u^1} \hat{\mathbf{u}}^3 \\ \mathbf{r}_{u^2}^i &= \frac{\partial \mathbf{r}_i}{\partial u^2} = \hat{\mathbf{u}}^2 + \frac{\partial w(u^1, u^2)}{\partial u^2} \hat{\mathbf{u}}^3 \end{aligned} \tag{2.10}$$

Using this basis, any vector \mathbf{v} in the tangent bundle of the patch Ω_i at a point $\mathbf{r}_i \in \Omega_i$ may be expressed as:

$$\mathbf{v}(u^1, u^2) = v^1(u^1, u^2)\mathbf{r}_{u^1}^i + v^2(u^1, u^2)\mathbf{r}_{u^2}^i \quad (2.11)$$

Thus, the coordinates of the tangent bundle $T\Omega_i$ are given by $(u^1, u^2, v^1, v^2) \in \mathbb{R}^4$, and a coordinate chart $(T\Omega_i, \tilde{\varphi}_i)$ may be defined for the local tangent bundle in the same way that a coordinate chart (Ω_i, φ_i) is associated with each patch Ω_i . Crucially, this also implies that the global tangent bundle may be reconstructed using a partition of unity as:

$$T\Omega = \sum_i \psi_i T\Omega_i \quad (2.12)$$

The ability to subsect the global tangent bundle in this way is the basis for the discretization of currents in GMM.

The map $\tilde{\varphi}_i : T\Omega_i \rightarrow \mathbf{R}^4$ is simply (φ_i, Id_2) , where $\varphi_i : \Omega_i \rightarrow \mathbb{R}^2$ is given by (2.6) and $\text{Id}_2 : \mathbb{R}^2 \rightarrow \mathbb{R}^2$ is the identity map. Finally, transition functions $\tilde{\tau}_{ij} : \mathbb{R}^4 \rightarrow \mathbb{R}^4$ between coordinate charts of the tangent bundles $T\Omega_i, T\Omega_j$ of two overlapping patches Ω_i, Ω_j is given by $\tilde{\tau}_{ij} = \tilde{\varphi}_i \circ \tilde{\varphi}_j^{-1}$ as:

$$\tilde{\tau}_{ij} = \begin{bmatrix} \tau_{ij} & 0 \\ 0 & \sigma_{ij} \end{bmatrix} \quad (2.13)$$

$$\sigma_{ij} = \begin{bmatrix} \mathbf{r}_{u^1}^i \cdot \mathbf{r}_{u^1}^j & \mathbf{r}_{u^1}^i \cdot \mathbf{r}_{u^2}^j \\ \mathbf{r}_{u^2}^i \cdot \mathbf{r}_{u^1}^j & \mathbf{r}_{u^2}^i \cdot \mathbf{r}_{u^2}^j \end{bmatrix} \quad (2.14)$$

2.3.3.4 Vector Calculus on Parametric Surfaces

Here, we briefly define quantities required to do vector calculus on the parametric surface specified by $\mathbf{r}(u^1, u^2)$. Vectors tangential to the surface are expressed as $\mathbf{t} = a\mathbf{r}_{u^1} + b\mathbf{r}_{u^2}$, where a, b are scalar coefficients and the basis vectors \mathbf{r}_{u^j} , $j = 1, 2$ are defined by $\mathbf{r}_{u^j} \doteq \partial\mathbf{r}/\partial u^j$. Note that the tangent

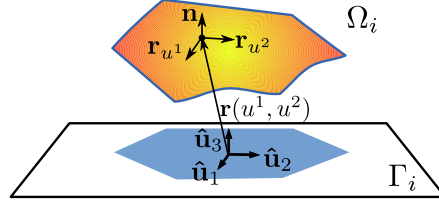


Figure 2.3: Tangent and normal vectors associated with a parametric patch surface.

basis vectors are not normalized, and in general do not need to be orthogonal. For the types of parameterizations used in this paper, the basis vectors are given explicitly by:

$$\begin{aligned}\mathbf{r}_{u^1} &= \hat{\mathbf{u}}^1 + \frac{\partial w(u^1, u^2)}{\partial u^1} \hat{\mathbf{u}}^3 \\ \mathbf{r}_{u^2} &= \hat{\mathbf{u}}^2 + \frac{\partial w(u^1, u^2)}{\partial u^2} \hat{\mathbf{u}}^3\end{aligned}\quad (2.15)$$

The unit normal is given in terms of these tangent basis vectors as $\hat{\mathbf{n}} = (\mathbf{r}_{u^1} \times \mathbf{r}_{u^2}) / \|\mathbf{r}_{u^1} \times \mathbf{r}_{u^2}\|$. Figure 2.3 shows $\mathbf{r}_{u^1}, \mathbf{r}_{u^2}$ and $\hat{\mathbf{n}}$ on the parametric surface.

For the purposes of integrating and taking derivatives with respect to the parametric coordinates (u^1, u^2) , it is necessary to define notions of differential length and area on the parameterized surface. To do so, a transformation matrix called the “metric tensor” is defined as:

$$g = \begin{bmatrix} \mathbf{r}_{u^1} \cdot \mathbf{r}_{u^1} & \mathbf{r}_{u^1} \cdot \mathbf{r}_{u^2} \\ \mathbf{r}_{u^2} \cdot \mathbf{r}_{u^1} & \mathbf{r}_{u^2} \cdot \mathbf{r}_{u^2} \end{bmatrix}.\quad (2.16)$$

Traditionally, components of the metric tensor are indexed using lowered indices g_{ij} . The inverse of the metric tensor g^{-1} is used in expressions involving derivatives, and the components of g^{-1} are referenced using raised indices g^{ij} . The differential surface area element is given by $dS = J d\mathbf{u} = J du^1 du^2$ where the Jacobian is $J = \sqrt{\det(g)}$, with $\det(g)$ the determinate of the metric tensor. Finally, the surface divergence of a vector function $\mathbf{f}(\mathbf{r}(u^1, u^2))$ with respect to the parametric coordinates is:

$$\nabla_s \cdot \mathbf{f}(u^1, u^2) = \sum_{i,j} g^{ij} \frac{\partial \mathbf{f}}{\partial u^i} \cdot \mathbf{r}_{u^j}\quad (2.17)$$

This expression is used to compute the divergences of surface currents required in the \mathcal{T} operator of equation (2.2). For further development of these concepts in the context of electromagnetics, we refer the reader to [51, 52].

2.3.4 Local Basis Functions

Next, we develop local basis function descriptions. GMM patches may incorporate either entire patch (EP) bases with support over the entire patch, or sets of sub patch (SP) bases with support smaller than the entire patch.

2.3.4.1 Entire Patch Basis Functions

The general entire patch vector basis function is given in terms of local coordinates as:

$$\begin{aligned} \mathbf{f}_{i,k}(\mathbf{r}) = & f_{k,1}(u^1, u^2) \mathbf{r}_{u^1}(u^1, u^2) \\ & + f_{k,2}(u^1, u^2) \mathbf{r}_{u^2}(u^1, u^2) \end{aligned} \quad (2.18)$$

so that the unknown surface current on patch Ω_i is expressed as:

$$\mathbf{j}_i(\mathbf{r}) = \psi_i(\mathbf{r}) \sum_{k=1}^{N_i} a_k \mathbf{f}_{i,k}(\mathbf{r}) \quad (2.19)$$

Here, $\psi_i(\mathbf{r})$ is the partition of unity on patch Ω_i , the vectors \mathbf{r}_{u^1} and \mathbf{r}_{u^2} are tangent vectors to the surface as defined in section 2.3.3.4, and the weighting functions $f_{1,k}(u^1, u^2)$ and $f_{2,k}(u^1, u^2)$ may be chosen from any set of functions that lead to convergent integrals on Λ_i . Examples of such functions are hierarchical polynomials, plane waves, body of revolution functions, etc.

To construct EP basis functions, first a canonical minimum bounding shape is defined that encloses the projection P_{Γ_i} of the patch node set \mathcal{N}_i onto the local projection plane Γ_i . The choice of bounding shape depends on the patch type and shape. Rectangles are generally employed for mapped polynomial functions, circles for BoR, etc. Once the appropriate bounding shape is assigned, the component basis functions $f_{k,1}(u^1, u^2)$ and $f_{k,2}(u^1, u^2)$ are defined on its interior and

restricted to the domain included in P_{Γ_i} . Finally, these basis functions are lifted onto the parametric surface as in (2.18). This arrangement is illustrated in figure 2.4.

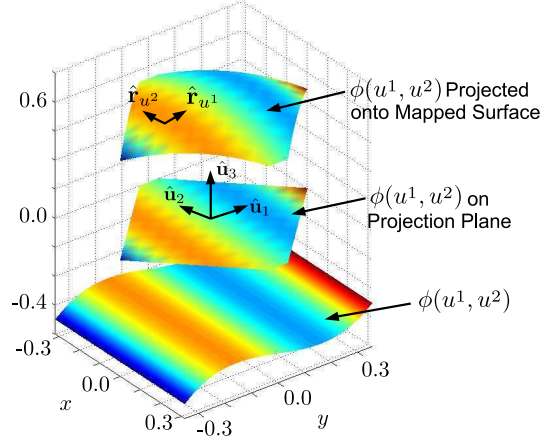


Figure 2.4: Entire patch basis function.

2.3.4.2 Sub-patch Basis Functions

GMM can also easily incorporate multiple basis functions on a single patch with sub-patch support, so called sub-patch (SP) bases. This may be interpreted as defining an EP basis function as $\mathbf{f}(\mathbf{r}) = \sum_j \mathbf{f}_j(\mathbf{r})$, with $\{\mathbf{f}_j(\mathbf{r})\}$ a set of approximation functions with support smaller than $supp\{\Omega_i\}$. The requirements on SP bases are that they introduce no line charges interior to the patch and that they possess a nonzero normal component at the patch edges. Due to the partition of unity, the normal component is only required to be finite, and need not satisfy any explicit continuity constraint across patch boundaries.

Sub-patch bases may be defined on the projection plane and projected onto the parameterized surface as with EP bases; alternatively, SP functions may be defined directly on a tessellation of the point cloud as in a traditional Moment Method discretization. Likewise, the partition of unity is defined either on the projection plane Γ_i and then lifted onto the true surface, or is defined directly on the tessellation itself. Defining sub-patch bases in this way allows most basis function types

from existing tessellation-based Moment Method codes to be directly used in the GMM scheme with minimal alteration. Figure 2.5 shows an example sub-patch tessellation.

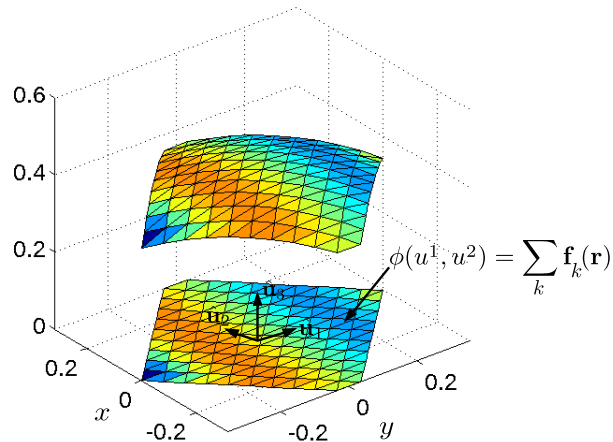


Figure 2.5: Illustration of sub-patch basis function arrangement with projected PU.

To illustrate the manner in which sub-patch bases are implemented in the GMM scheme, we detail the construction of a tessellated patch with Rao-Wilton-Glisson (RWG) [53] basis functions. RWG functions are defined as usual on the tessellated surface, or equivalently, on the projection plane and lifted onto the surface. A simplicial partition of unity fits naturally into the RWG framework and is defined so that it takes a value of unity in all interior triangles and falls linearly to zero in boundary triangles. To provide the necessary normal component at the patch edge, a half-RWG function is defined across exterior patch boundaries. Although half-bases are generally avoided in RWG discretizations because they introduce line charges, this difficulty is avoided in GMM because the PU forces the function to zero at the patch edge. This property of the PU applies to all GMM basis functions, and renders the basis set on a patch charge neutral, regardless of whether the functions are EP or SP. Figure 2.6 shows interior and boundary RWG basis functions, and the removal of the boundary line charge by the PU.

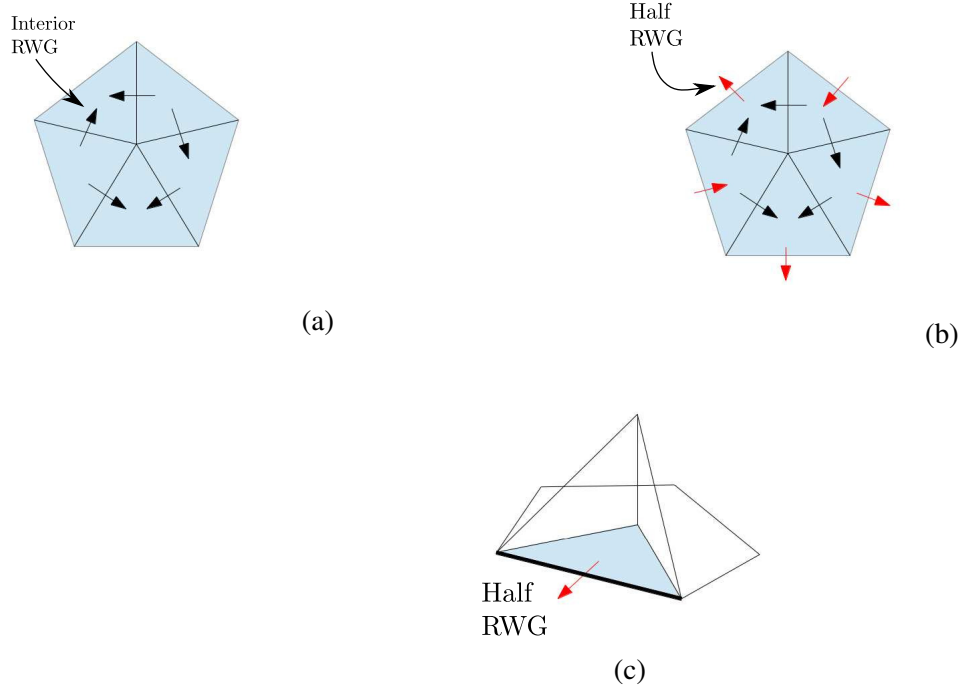


Figure 2.6: Design of local RWG basis set with normal continuity across patch boundaries: (a) RWG basis functions associated with internal edges, (b) Additional half-RWG functions associated with exterior patch edges provide a normal component at patch boundary, and (c) Simplex-based partition of unity forces the half-RWG function to zero at patch boundary, removing the line charge.

2.3.4.3 Default EP/SP Basis

As with local geometry descriptions, it is advantageous to have default basis function types that are utilized when a current ansatz is not available or difficult to obtain. A straightforward choice of an EP basis function is:

$$\begin{aligned}\mathbf{f}_1(u^1, u^2) &= \phi_{\boldsymbol{\beta}}(u^1, u^2) \mathbf{r}_{u^1} \\ \mathbf{f}_2(u^1, u^2) &= \phi_{\boldsymbol{\beta}}(u^1, u^2) \mathbf{r}_{u^2}\end{aligned}\tag{2.20}$$

where $\phi_{\boldsymbol{\beta}}(u^1, u^2) \doteq P_{\beta_1}(u^1)P_{\beta_2}(u^2)$ is a product of two Legendre polynomials of degrees β_1 and β_2 , and the entire p th order representation on patch Ω_i is constructed as:

$$\mathbf{j}_i(\mathbf{r}) = \psi_i(\mathbf{r}) \sum_{l=1}^2 \sum_{|\boldsymbol{\beta}| \leq p} a_{\boldsymbol{\beta}, l} \phi_{\boldsymbol{\beta}}(u^1, u^2) \mathbf{r}_{u_l}\tag{2.21}$$

More complex polynomial bases may be constructed, e.g. one which explicitly enforces a surface Helmholtz decomposition, as in [40]. However, we have found that the minimal tensor product of Legendre polynomials in (2.21) generally provides better matrix conditioning than other choices of polynomial basis functions for the same order. Furthermore, since GMM provides current continuity between patches by design, it is not necessary to use the modified Legendre bases or hierarchical bases often employed in higher order mapped methods [11, 15].

With the influence of the partition of unity, the surface current approximation for the default EP basis spans the space:

$$\begin{aligned} \mathbf{f}_1(u^1, u^2) \in \text{span}\{ & \psi_i(\mathbf{r})(\phi_{\boldsymbol{\beta}}(u^1, u^2)\mathbf{r}_{u1}) \\ & + \psi_i(\mathbf{r})(\phi_{\boldsymbol{\beta}}(u^1, u^2)\mathbf{r}_{u2})\} \\ & |\boldsymbol{\beta}| \leq p \end{aligned} \quad (2.22)$$

As described in section 2.3.3, when geometrical singularities such as sharp tips or edges are present, a smooth geometry parameterization and polynomial EP basis cannot be used. In these situations, we default to a surface tessellation supporting a SP RWG basis as detailed in section 2.3.4.2. The properties of these functions have been extensively developed [53] and are not repeated here.

Finally, we explicitly show how the partitions of unity and half-RWG basis functions are constructed in the case of Legendre (EP-type) and RWG (SP-type) patches that overlap. Figure 2.7(a) shows the partition of unity $\psi_{RWG} = \hat{\psi}_{RWG}/(\hat{\psi}_{RWG} + \hat{\psi}_{Leg})$ and location of half-RWG basis functions for the RWG patch, and Figure 2.7(b) shows the partition of unity $\psi_{Leg} = \hat{\psi}_{Leg}/(\hat{\psi}_{RWG} + \hat{\psi}_{Leg})$ on the Legendre patch. The sub-partition of unity $\hat{\psi}_{RWG}$ on the RWG patch is defined on a triangle-by-triangle basis as:

$$\hat{\psi}_{RWG} = \begin{cases} 1, & n_{bd} = 0 \\ \xi, & n_{bd} = 1 \\ 1 - \xi, & n_{bd} = 2 \end{cases} \quad (2.23)$$

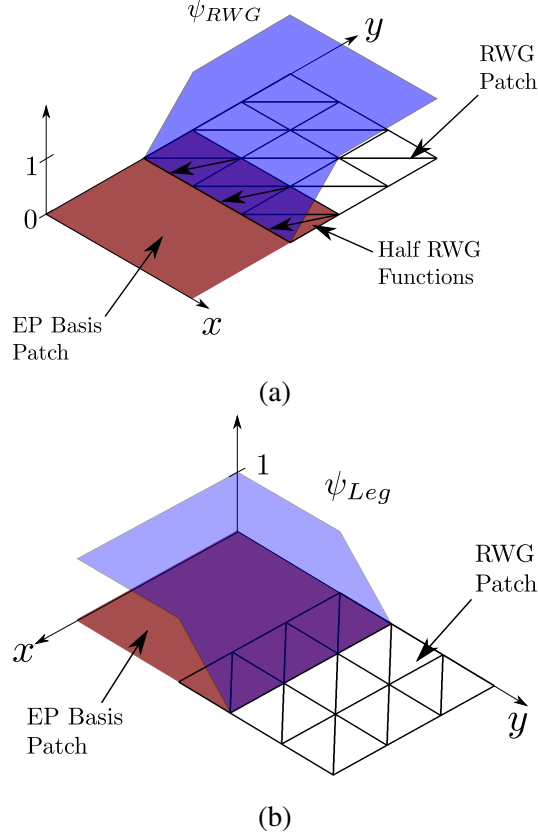


Figure 2.7: Graphical depiction of partitions of unity for overlapped RWG and Legendre patches. (a) Partition of unity ψ_{RWG} and half-RWG basis functions for an RWG patch. (b) Partition of unity ψ_{Leg} for a Legendre patch.

where n_{bd} is the number of triangle nodes on the patch boundary (in the overlap region) and ξ is the simplex coordinate associated with the exterior node if $n_{bd} = 1$ or the interior node if $n_{bd} = 2$.

A similar definition may be used to construct $\hat{\psi}_{Leg}$.

2.4 Implementation Details

In this section, we discuss some practical details of evaluating GMM matrix elements and give sample algorithms for patch merging and basis function assignment. Each of these tasks is non-trivial, and investigations of the most efficient and effective methods for specific types of problems are subjects of ongoing investigation. The integration methodology presented is sufficiently general that it may be used for most GMM discretizations, although more specialized rules could be

developed for specific basis function types. The integrations and algorithms developed here are used to generate all of the results in section 2.5.

2.4.1 Matrix Elements

We devote this section to a brief discussion of the practical evaluation of GMM matrix elements. Using the surface parameterizations from Section 2.3.3 and the differential geometry quantities from Section 2.3.3.4, the tested scattered electric field portion of (2.2) becomes :

$$\begin{aligned}
& -jk\eta_0 \int_{D_i} d\mathbf{u}_i J_i(\mathbf{u}_i) \psi_i(\mathbf{u}_i) \mathbf{f}_{i,m}(\mathbf{u}_i) \\
& \cdot \int_{D_j} d\mathbf{u}'_j J_j(\mathbf{u}'_j) g(\mathbf{r}_i(\mathbf{u}_i), \mathbf{r}_j(\mathbf{u}'_j)) \psi_j(\mathbf{u}_j) \mathbf{f}_{j,n}(\mathbf{u}'_j) \\
& + \frac{j\eta_0}{k} \int_{D_i} d\mathbf{u}_i J_i(\mathbf{u}_i) \nabla_s \cdot (\psi_i(\mathbf{u}_i) \mathbf{f}_{i,m}(\mathbf{u}_i)) \\
& \int_{D_j} d\mathbf{u}'_j J_j(\mathbf{u}'_j) g(\mathbf{r}_i(\mathbf{u}_i), \mathbf{r}'_j(\mathbf{u}'_j)) \nabla'_s \cdot (\psi_j(\mathbf{u}_j) \mathbf{f}_{j,n}(\mathbf{u}'_j))
\end{aligned} \tag{2.24}$$

where we have employed the standard derivative transfers in the Φ portion of the \mathcal{T} operator. The tested magnetic field integral equation portion of (2.2) is:

$$\begin{aligned}
& \int_{D_i} d\mathbf{u}_i J_i(\mathbf{u}_i) \psi_i(\mathbf{u}_i) \mathbf{f}_{i,m}(\mathbf{u}_i) \psi_j(\mathbf{u}_j) \mathbf{f}_{j,n}(\mathbf{u}_j) - \\
& \int_{D_i} d\mathbf{u}_i J_i(\mathbf{u}_i) \mathbf{f}_{i,m}(\mathbf{u}_i) \cdot \hat{\mathbf{n}}(\mathbf{r}(\mathbf{u}_i)) \times \\
& \int_{D_j} d\mathbf{u}'_j J_j(\mathbf{u}'_j) \nabla g(\mathbf{r}_i(\mathbf{u}_i), \mathbf{r}_j(\mathbf{u}'_j)) \times \psi_j(\mathbf{u}_j) \mathbf{f}_{j,n}(\mathbf{u}'_j)
\end{aligned} \tag{2.25}$$

where $\mathbf{u}_l = (u^1, u^2) \in \Gamma_l$ denotes the local transverse coordinates for patch l , J_l is the Jacobian as defined in section 2.3.3.4, and $D_l \in \Gamma_l$ is the domain of integration in the projection plane. If the projection $P_{\Gamma_l}(\mathcal{N}_l)$ of the nodes in \mathcal{N}_l is a canonical integration domain, e.g. a regular polygon, then an appropriate quadrature rule can be used to integrate over the entire projection. For instance, radial/angular rules are used for BoR patches. In the general case where the projection is not bounded by a canonical shape, we perform a triangulation of P_{Γ_l} , e.g. using Delaunay or another

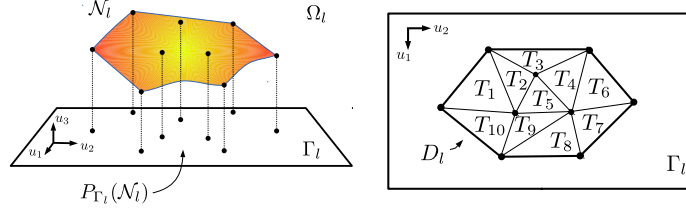


Figure 2.8: (a) Graphical representation of $P_{\Gamma_l}(\mathcal{N}_l)$ and (b) construction of triangular integration subdomains. The domain of integration is $D_l = \cup_i T_i$.

method. Figure 2.8 illustrates this process. Subdividing the domain of integration in this way allows the use of well-developed integration rules for triangles (including singularity rules), and the total integral is the sum of integrations over subtriangles. It is important to note that not every node in P_{Γ_l} needs to be used in defining the triangulation: if the patch is large, some subset of the nodes may be used to lessen the integration cost as long as the patch boundaries are correctly handled.

2.4.2 Automated Patch Construction

For large, complex geometries, it is necessary to automate the processes of patch construction including merging, geometry parameterization, and basis function assignment. The following are two sample algorithms for patch merging and geometry/basis selection.

2.4.2.1 Algorithm for Patch Merging

Using the procedure from section 2.3.1, patch primitives are assigned in the initial pass. To reduce the number of degrees of freedom in the MoM system, it is often advantageous to merge patches if neighboring primitives share common geometrical features, e.g. are part of the same body of revolution or fall on a sufficiently smooth portion of Ω . Given the definition of Ω_i as a collection of nodes, merging and or splitting may be simply done by operating on the sets \mathcal{N}_i . Algorithm 1 illustrates a procedure for merging; splitting may be done in a similar fashion. Criteria for merging are tied both to patch size and patch mean curvature, which is approximated via deviation

```

1: Define maximum normal deviation  $\varepsilon_n$  tolerance
2: Define maximum average normal deviation  $\varepsilon_d$  tolerance
3: Define maximum patch diameter  $D_m$ 
4: for each patch primitive  $\hat{\Omega}_i \in \{\hat{\Omega}_i\}$  do
5:   for each  $n_j \in \mathcal{N}_i$  (corresponding to primitive  $\hat{\Omega}_j$ ) do
6:     if  $\hat{\mathbf{n}}_j \cdot \hat{\mathbf{n}}_i > (1 - \varepsilon_n)$  then
7:       Define candidate merged neighborhood:  $\mathcal{N}_l = \mathcal{N}_i \cup \mathcal{N}_j$ . Designate the
       number of nodes in  $\mathcal{N}_l$  as  $M$ .
8:       Compute new average patch normal  $\hat{\mathbf{n}}_l = (\sum_{k=1}^M \hat{\mathbf{n}}_k) / |\sum_{k=1}^M \hat{\mathbf{n}}_k|$ 
9:       Compute merged patch maximum diameter  $D = \max\{|\mathbf{r}_{n_a} -$ 
        $\mathbf{r}_{n_b}|\}, n_a, n_b \in \mathcal{N}_l$ 
10:      if  $D \leq D_m$  then
11:        Compute average deviation  $\overline{\Delta \hat{\mathbf{n}}}_l$  from patch normal  $\hat{\mathbf{n}}_l$  as:  $\overline{\Delta \hat{\mathbf{n}}}_l \doteq$ 
         $\frac{1}{M} \sum_{k=1}^M \hat{\mathbf{n}}_l \cdot \hat{\mathbf{n}}_k$ 
12:        if  $\overline{\Delta \hat{\mathbf{n}}}_l \leq \varepsilon_d$  then
13:          Merge  $\hat{\Omega}_i, \hat{\Omega}_j$ :
14:           $\mathcal{N}_i \leftarrow \mathcal{N}_l$ 
15:           $\{\hat{\Omega}_i\} \leftarrow \{\hat{\Omega}_i\} \setminus \hat{\Omega}_j$ 
16:        end if
17:      end if
18:    end if
19:  end for
20: end for

```

Algorithm 1: Automated patch merging.

of normals as shown in algorithm 1.

At the end of the merging process, the final set of merged patches is designated $\{\Omega_i\}$. Algorithm 1 is a simplified version of the actual merging algorithm used in the present GMM code. In practice, additional higher level merging conditionals are also used that, for instance, favor convex patch boundaries over concave boundaries, attempt to maintain equal patch sizes over the entire geometry, and group patches with similar characteristics, such as edge singularities or small curvature.

2.4.2.2 Automated Geometry and Basis Assignment

Algorithm 2 illustrates automated assignment of local geometry descriptions G , basis function types b and (where applicable) orders g using tessellations, BoR surfaces, and polynomial

```

1: Define maximum patch normal deviation  $\varepsilon_d$  for smooth surface description
2: Define maximum patch normal deviation for plane wave basis  $\varepsilon_p$ 
3: Define minimum patch diameter for plane wave  $D_p$ 
4: for each final patch  $\Omega_i$  do
5:   Compute average deviation  $\overline{\Delta\hat{\mathbf{n}}}_i$  from average patch normal  $\hat{\mathbf{n}}_i$  as:  $\overline{\Delta\hat{\mathbf{n}}}_i \doteq$ 
6:      $\frac{1}{M} \sum_{k=1}^M \hat{\mathbf{n}}_i \cdot \hat{\mathbf{n}}_k$ 
7:   if  $\overline{\Delta\hat{\mathbf{n}}}_i > \varepsilon_d$  then
8:      $G$ : triangular tessellation
9:      $b$ : RWG Basis
10:  else if Rotationally Symmetric Patch then
11:     $G$ : Axisymmetric BoR representation
12:     $b$ : BoR Basis
13:  else
14:     $G$ : Local smooth approximation to  $\Omega_i$ .
15:    if  $\overline{\Delta\hat{\mathbf{n}}}_i < \varepsilon_p$  &&  $\text{Diam}\{\Omega_i\} > D_p$  then
16:       $b$ : Plane Wave Basis
17:    else
18:       $b$ : Polynomial Basis of order  $g$ 
19:    end if
20:  end if

```

Algorithm 2: Automated geometry and basis assignment.

smooth surfaces for geometry parameterization and RWG, BoR, polynomial, and plane wave bases. Any geometry or basis function class valid for the GMM framework may be included in the algorithm with the proper conditionals. The present code implementing GMM is written in a highly modularized fashion that facilitates easy addition of new geometry and basis function types.

2.5 Results

In this section, we provide results that illustrate hybridization of geometry and basis types and verify the accuracy and flexibility of the method. First, we utilize a representation test to demonstrate the hybridization of multiple basis types in the reconstruction of an analytical function. We then provide several scattering results, each with a different mixture of basis function types and orders defined on patches with varying local geometry descriptions. Throughout the results section, the

algorithms detailed in Section 2.4.2 are used to automatically assign local geometrical descriptions and surface current approximation spaces that are matched to solution ansatzes for the continuous problem. The resulting discretizations give accurate solutions with significant reductions in the numbers of degrees of freedom relative to a reference CFIE-RWG code.

We begin with a representation (Gram) test in which a quadratic vector function $\mathbf{f}(x, y) = (x - .5)^2 \hat{\mathbf{x}}$ is reconstructed on a flat $1\text{m} \times 1\text{m}$ plate using a mixture of a 2nd order Legendre polynomials defined on smooth patches and RWG functions defined on a triangular tessellation. Figure 2.9 shows the discretization and reconstruction error for three cases. Reconstruction error is taken as the pointwise absolute error (abs err) = $|\tilde{\mathbf{f}}(x, y) - \mathbf{f}(x, y)|$, where $\tilde{\mathbf{f}}(x, y)$ is the reconstructed function.

First, as a reference, we interpolate the analytical function $\mathbf{f}(x, y)$ using the standard linear RWG basis on a triangular tessellation with maximum edge length .07m. This discretization is shown in figure 2.9.a. Figure 2.9.b shows the reconstruction error using the all-RWG basis set. As one would expect, the error is highest at the edges where the RWG functions cannot reconstruct the normal component, and lowest where the argument of $\mathbf{f}(x, y)$ goes to zero (at $x = .5\text{m}$). The purpose of this result is to provide a reference error level for RWG discretization for case 3, in which RWG and Legendre bases are mixed.

Figures 2.9.c and 2.9.d show discretization and reconstruction error for an all-Legendre polynomial basis of second order. Because the basis set is polynomial complete to the same order as $\mathbf{f}(x, y)$, the reconstruction is perfect to machine precision everywhere on the plate. Most significantly, the reconstruction is perfect even in the overlap regions between patches where the partition of unity provides the continuity and blending between basis sets on neighboring patches. Without the partition of unity, there would be significant error in the overlap regions.

In figure 2.9.e, a $.25\text{m} \times .25\text{m}$ tessellated patch with RWG functions is placed in the center of the plate, while the outer boundary is discretized using flat patches supporting second order Legendre polynomials. Figure 2.9.f shows the reconstruction error for the mixed RWG/Legendre basis set. In this case, the error in the RWG patch matches that from the center of the plate in figure 2.9.b. Outside of the RWG region, the error falls significantly, although due to the coupling

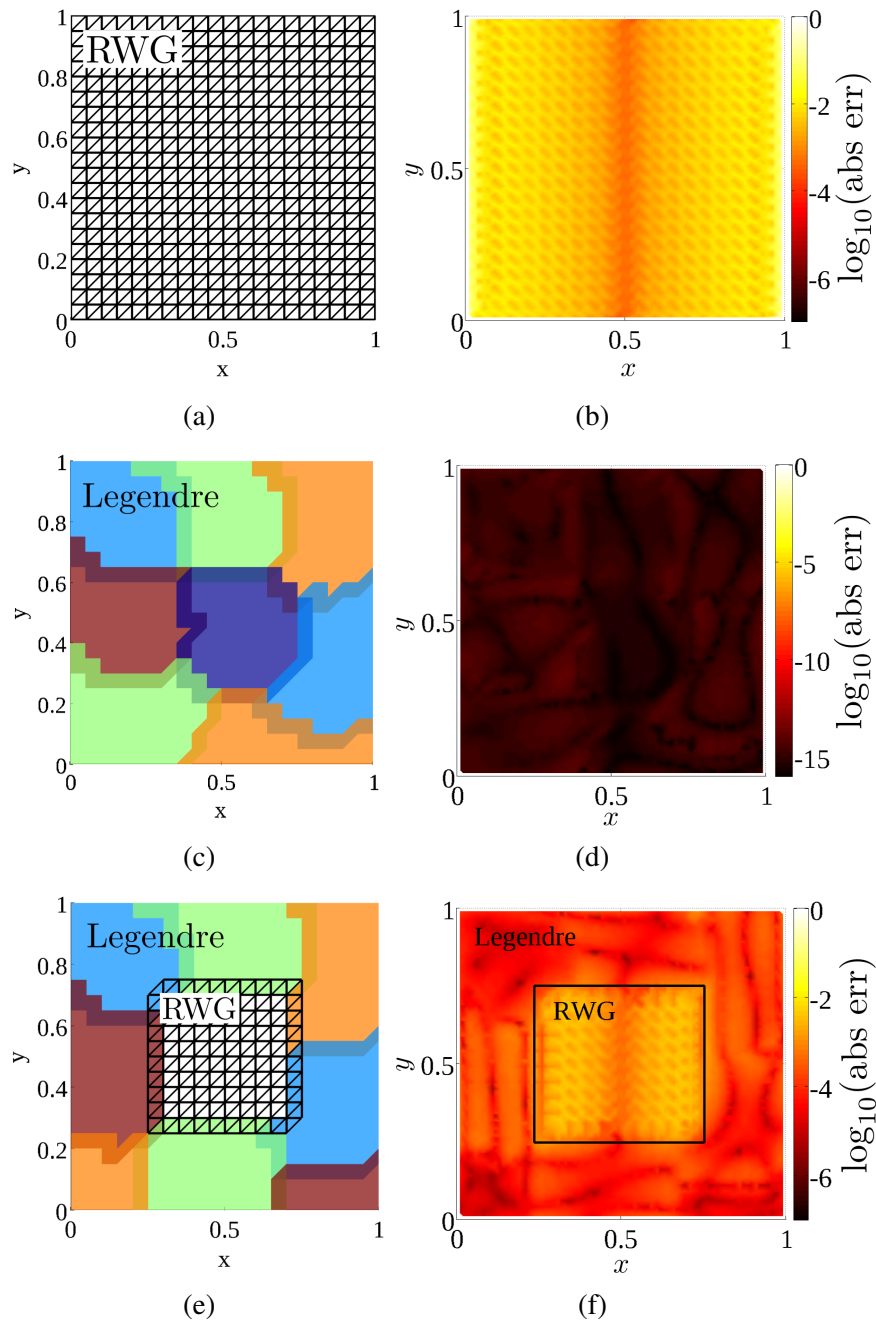


Figure 2.9: Reconstruction error for a function $f(x,y) = (x - .5)^2 \hat{x}$ using three different basis sets: all-RWG, all-Legendre, mixed RWG/Legendre. (a) All-RWG discretization, (b) All-RWG reconstruction error, (c) All-Legendre patch discretization (2nd order Legendre polynomials) (d) All-Legendre reconstruction error, (e) Mixed RWG/Legendre discretization (2nd order Legendre Polynomials), (f) Mixed RWG/Legendre reconstruction error.

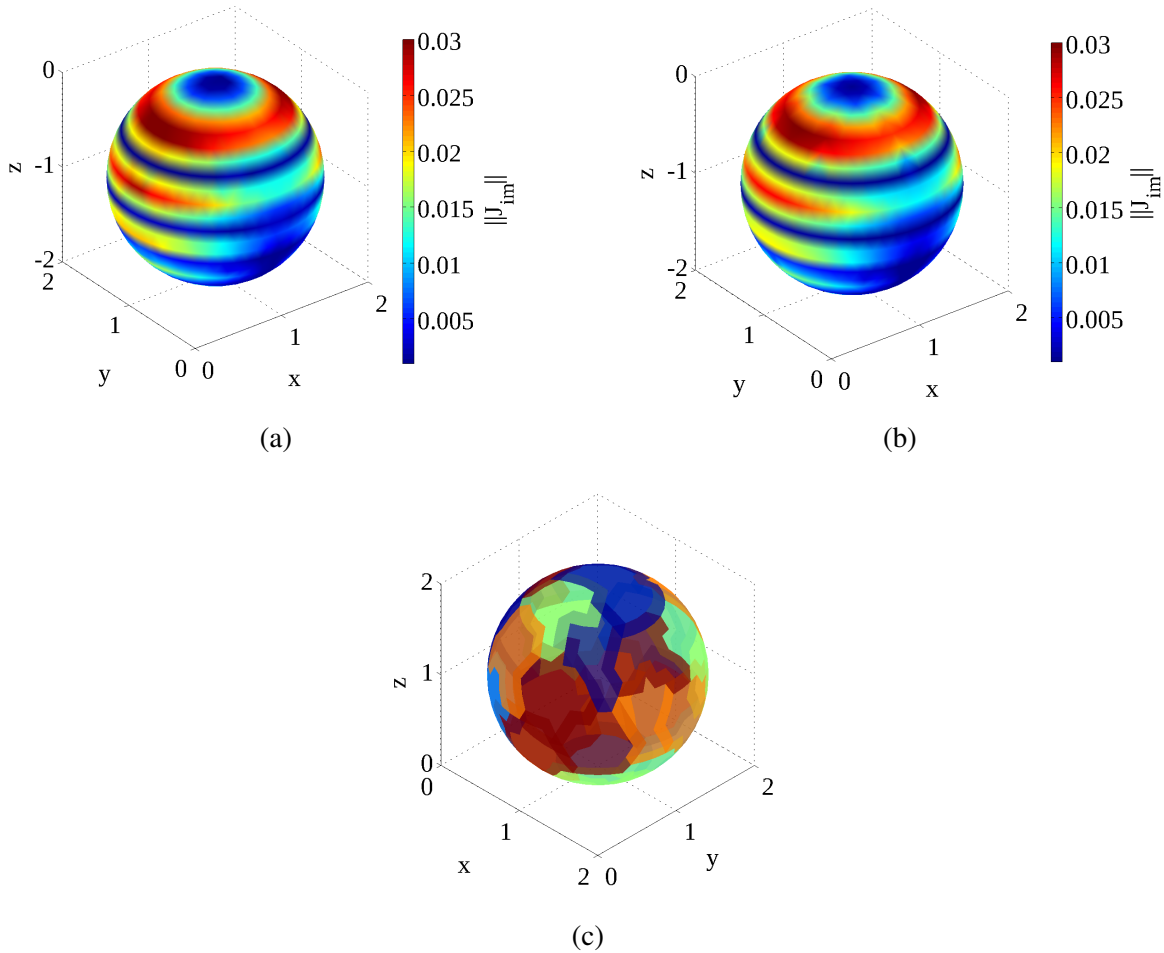


Figure 2.10: Surface currents induced by an incident plane wave on a sphere discretized with (a) overlapping GMM patches supporting a 4th order Legendre basis and (b) an RWG basis for reference. Subfigure (c) shows the patches used to obtain the GMM result. Magnitude of imaginary part of current $\|J_{im}\|$ is shown; $\|J_{re}\|$ yields similar plots.

between the RWG and Legendre patches, it does not decrease to the level of the all-Legendre solution. Crucially, due to the blending effect of the partition of unity, no additional error is introduced in the transition region between the two basis sets.

The next result shows currents induced on a spherical scatterer of radius $a = 1\lambda$ due to an incident x -polarized plane wave propagating in the $-\hat{z}$ direction. Figure 2.10.a shows currents obtained via solving the MFIE using overlapping GMM patches supporting a 4th order Legendre basis, and figure 2.10.b shows the same result using RWG basis functions for reference. Figure 2.10.c shows the overlapping patches used to obtain the GMM result. The current densities

show good agreement, although the higher-order GMM patches give smoother results relative to the RWG discretization. Due to the analytical form of the scatterer, the sphere may be exactly represented using spherical local geometry descriptions in GMM.

The next scattering result demonstrates automated geometry and basis function assignment for a $4.5\lambda \times 1.5\lambda \times .4\lambda$ NASA almond, with the corresponding RCS compared against a well-validated CFIE-RWG reference solution. The almond is illuminated by a unit amplitude x -polarized plane wave of frequency 300MHz incident in the $+z$ direction. Here, a Legendre basis (eq. 2.20) of maximum order $p = 3$ is defined on 2nd order polynomial patches in the smooth regions, which are detected using Algorithm 2. Figure 2.11 shows the discretization of the almond in terms of overlapping smooth and tessellated patches. Tessellated patches supporting RWG basis functions are used to capture regions of high curvature and the geometric singularity at the tip. One could envisage a tip basis function that does not rely on tessellation, but instead captures the tip singularity exactly. While the design of such a basis is outside the scope of this paper, it could be seamlessly integrated into the GMM framework. Figure 2.12 shows the bistatic RCS for the almond, which is taken along the $\phi = 0^\circ$ cut. The number of degrees of freedom for the CFIE-RWG solution is $N_{ref} = 3636$ and the GMM result requires $N_{GMM} = 1861$.

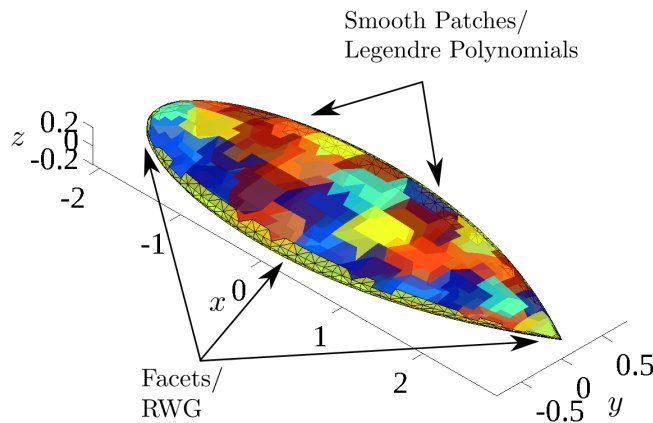


Figure 2.11: GMM discretization of a 4.5λ NASA almond.

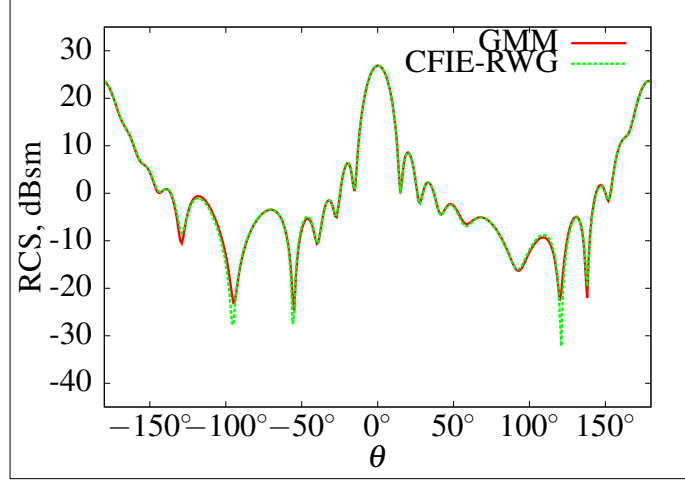


Figure 2.12: NASA almond bistatic RCS, taken along the $\phi = 0^\circ$ cut.

The next result, scattering from a $1.2\lambda \times .4\lambda \times .4\lambda$ diffraction-matched conesphere illuminated by a $-\hat{\mathbf{x}}$ polarized plane wave incident in the $\hat{\mathbf{z}}$ direction, illustrates the high degree of geometrical accuracy that may be obtained when the analytical form of the underlying scatterer is known. Figure 2.13 shows the GMM discretization for the conesphere. The cone portion of the geometry (excluding the tip) is represented exactly through a single BoR patch which supports two types of BoR basis functions, defined as:

$$\begin{aligned} \mathbf{f}_{m,1}(\mathbf{r}) &= aP_n(\rho)e^{jm\phi} \mathbf{r}_\rho(u^1, u^2) \\ \mathbf{f}_{m,2}(\mathbf{r}) &= aP_n(\rho)e^{jm\phi} \mathbf{r}_\phi(u^1, u^2) \end{aligned} \quad (2.26)$$

where $\rho(u^1, u^2) = \sqrt{(u^1)^2 + (u^2)^2}$ and $\phi(u^1, u^2) = \arctan(u^2/u^1)$. To capture the spherical portion of the scatterer to a high degree of precision, 5th order polynomial patches are employed with 3rd order Legendre basis functions. The tip region is modeled with a tessellation and RWG functions. Figure 2.14 shows a comparison of the GMM result against a reference CFIE-RWG result. In this case, the GMM solution uses 126 Legendre functions on the spherical cap, 130 BoR basis functions on the barrel, and 294 RWG functions on the tip, so that the total GMM system size is $N_{GMM} = 550$. The reference RWG solution requires a total of $N_{ref} = 1584$ degrees of freedom. Agreement between the two results is quite good.

To demonstrate the reduction in system size that results from using a polynomial bases on a

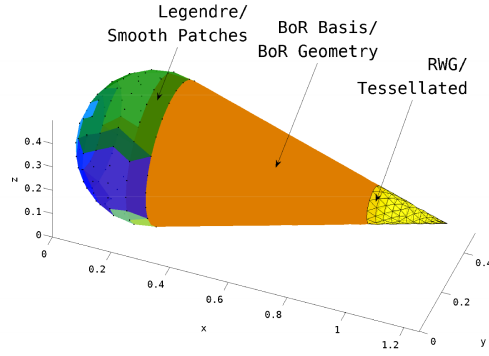


Figure 2.13: GMM discretization of a $1.2\lambda \times .4\lambda \times .4\lambda$ conesphere.

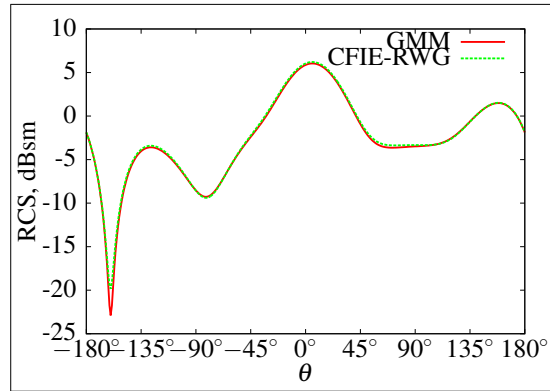
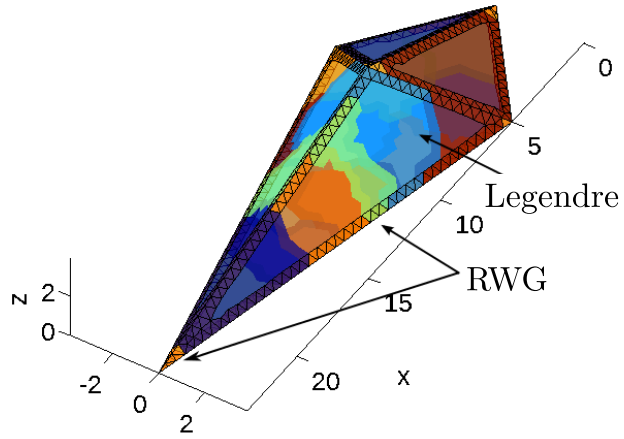


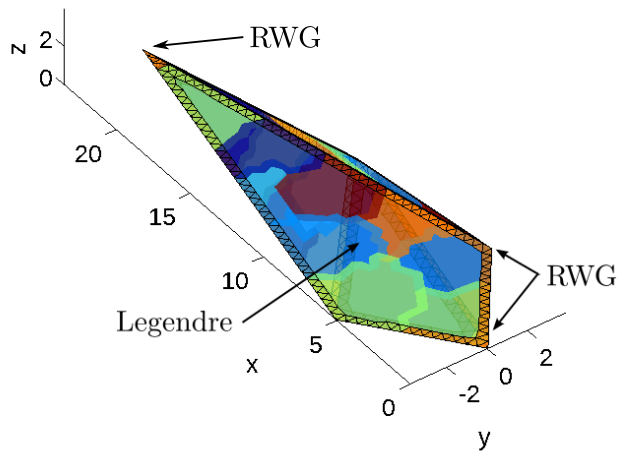
Figure 2.14: Bistatic RCS for the conesphere at 300MHz. Incident wave is traveling in the $\theta = 0^\circ, \phi = 0^\circ$ direction with $-x$ -polarization. The RCS is taken along $\phi = 0^\circ$ cut.

faceted scatterer possessing large flat regions, we present a scattering result from an arrow geometry that possesses several sharp features in addition to large flat faces. The scatter measures $5\lambda \times 1.5\lambda \times .8\lambda$ at 64MHz. In this case the scattering body is discretized with a combination of large flat patches supporting a 4th order Legendre basis on the flat sides and triangular tessellation/RWG on the corners and tips. Figure 2.15 shows the resulting patches and tessellation. The bistatic RCS in Figure 2.16 due to an x -polarized plane wave incident along the $\theta_i = 135^\circ, \phi_i = 20^\circ$ direction was obtained with the CFIE, $\alpha = .5$, and closely matches the reference solution. The number of unknowns is reduced from $N_{ref} = 3549$ for the CFIE-RWG solution to $N_{GMM} = 1830$ using the GMM mixed Legendre/RWG solution.

Finally, we analyze the parabolic reflector in Figure 2.17, which is an open curved structure.



(a)



(b)

Figure 2.15: GMM discretization of a $5\lambda \times 1.5\lambda \times .8\lambda$ arrow (a) top view and (b) bottom view.

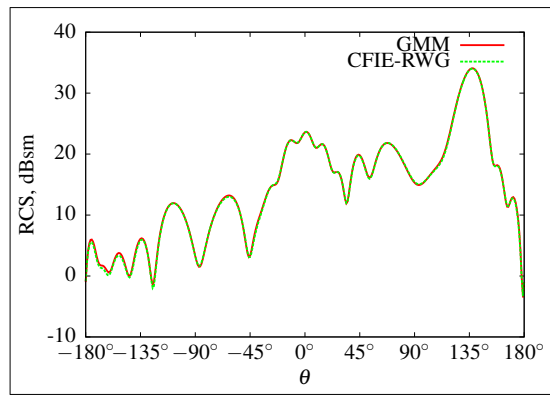


Figure 2.16: Arrow bistatic RCS at 64MHz. Wave is incident in the $\theta_i = 135^\circ, \phi_i = 20^\circ$ direction and is x -polarized relative to incidence direction. The RCS is taken along the $\phi = 0^\circ$ cut.

The smoothly curved interior is modeled using 4th order smooth polynomial patches, and the rim is captured by a piecewise flat triangular tessellation. A 5th order Legendre basis is used on the polynomial patches, and an RWG basis is employed on the tessellated portion. The RCS result in figure 2.18 shows scattering due to an x -polarized plane wave with incidence angles $\theta_i = 180^\circ, \phi_i = 0^\circ$. Again, the agreement in RCS between the reference EFIE-RWG and GMM solutions is excellent. For the reflector, the EFIE-RWG code required $N_{ref} = 4494$ degrees of freedom, and the GMM solution required $N_{GMM} = 1638$ degrees of freedom.

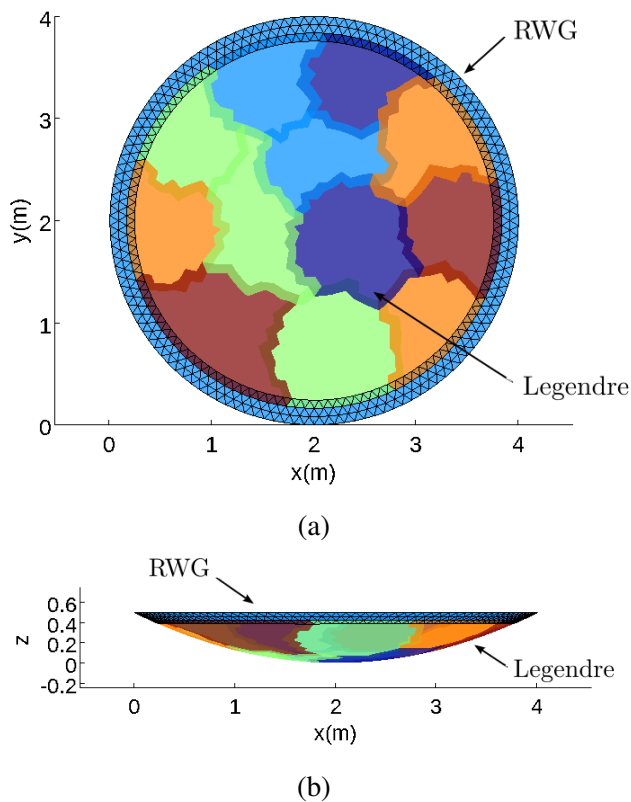


Figure 2.17: GMM discretization of a $4\lambda \times .35\lambda$ Parabolic Reflector (a) top view and (b) side view.

2.5.1 Complexity and Matrix Fill Times

Although the computational costs associated with assembling and solving a GMM system are highly dependent on the particular mixture of basis sets and patch sizes employed, the cost of the

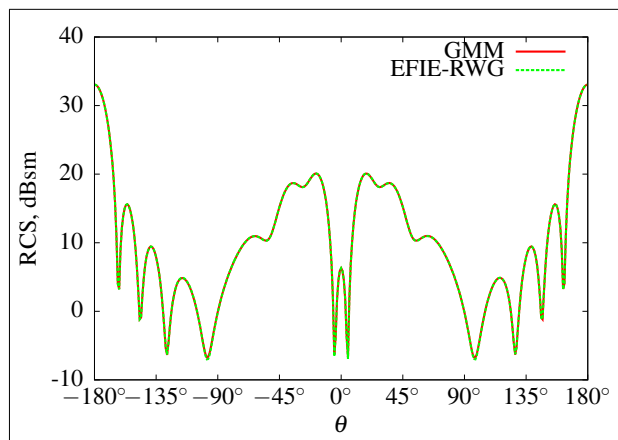


Figure 2.18: Parabolic reflector bistatic RCS. Wave is incident in the $\theta_i = 180^\circ$, $\phi_i = 0^\circ$ direction with x -polarization. The RCS is taken along the $\phi = 0^\circ$ cut.

algorithm in both complexity and storage is similar to that of extant Moment Methods. If currents are predominantly discretized with entire patch basis functions, the cost scales as that of a mapped higher-order Moment Method; alternatively, if sub-patch basis functions are the principle basis type, the cost approaches that of traditional tessellation-based schemes such as RWG or rooftop bases. The only added cost of evaluating matrix elements in GMM relative to traditional Moment Method schemes is that of computing the partition of unity. Since the partition of unity on each patch is non-unity only in the overlaps between patches, its evaluation adds very little to the overall complexity.

To substantiate the qualitative scalings given in the preceding paragraph, we next provide a brief comparison of matrix fill timings for GMM vs. a well-validated reference code that is higher order in geometry and uses a higher order Graglia-Wilton-Peterson (GWP) [8] basis (note that the CFIE-RWG results generated above correspond to a first order geometry with a first order GWP basis). We caution that drawing meaningful comparisons between codes with different implementations is problematic due to variations in code optimizations and the large number of parameters that may be tuned, e.g. surface order, basis function order, discretization rate, quadrature rule, etc. Furthermore, it is difficult to directly compare low and high order codes because each solves the problem on a fundamentally different surface with a different fidelity to the true surface, and total

Table 2.1: Matrix fill times for CFIE-RWG code.

N_s	l_2 err	Fill Time (s)
576	6.21e-02	6.052
1296	2.66e-02	28.954
2304	1.47e-02	100.164
3600	9.30e-03	221.999
5184	6.40e-03	457.722
7056	4.68e-03	842.440
11664	2.81e-03	2301.787
14400	2.27e-03	3523.760

error in an observable is a composite of both geometrical and functional representation errors. To ensure as fair a comparison as possible, we analyze scattering from a 1λ sphere due to an x -polarized plane wave traveling in the $+\hat{z}$ direction. The sphere is selected because it is one of the few geometries that admits comparison against an analytical solution. Both codes solve the CFIE ($\alpha = .5$). We fix the order of the basis function and geometry representation, and then find the largest patch size that yields a solution convergent below an l_2 relative error tolerance of 2.5×10^{-3} vs. the canonical Mie series solution in farfield data for an observation plane along the $\phi = 0^\circ$ cut. All timings were run on a single 1.6GHz core of a Dell Optiplex 9010 8-core workstation with 16GB of RAM, and solutions were obtained using the TFQMR iterative algorithm with a convergence tolerance of 10^{-5} .

First, as a reference and to demonstrate typical convergence behavior of a lower order method, we examine the time to fill the MoM impedance matrix for the CFIE-RWG case. Table 2.1 gives convergence data and timings for a 1λ sphere at various discretization rates. To reach the desired error tolerance, it is necessary to use $N_s = 14400$ degrees of freedom, with a matrix fill time of almost 1 hour. The slow convergence is a primarily due to the poor fidelity of the low order mesh to the true sphere.

Next we compare timings for the 1λ sphere using the higher order reference code with 3rd order geometry and a 2nd order GWP basis compared with a corresponding GMM setup using a 3rd order polynomial local surface description and a 2nd order Legendre basis. Table 2.2 shows the results for both GMM and the reference GWP code. The GWP result illustrates the reductions

Table 2.2: Matrix fill times for higher order CFIE-GWP & CFIE-GMM codes.

Code	N_s	l_2 err	Fill Time (s)
GWP	4320	1.17e-03	729.336
GMM, All Leg	4488	1.95e-03	435.107
GMM, Mixed	11532	4.57e-03	1790.287

in numbers of unknowns and fill time that is generally afforded by higher order Moment Methods for a given accuracy. The first GMM result uses an all-Legendre basis set with patches sized to give approximately the same number of degrees of freedom as the CFIE-GWP code, and exhibits significantly faster fill time than the GWP code with comparable solution accuracy. To demonstrate timings for a mixed GMM case, the third result in Table 2.2 is discretized with RWG on the top half and the 2nd order Legendre basis on the bottom half. The same patch sizes, basis orders, and integration rules as in the previous all-RWG and all-Legendre examples are utilized. The slightly higher error in the mixed result is due to the use of the same integration rules as in the homogeneous discretization examples; a slightly higher integration rule in the PU overlap region for the RWG basis would be required to reach the prescribed tolerance. As expected, the fill time is between that of the all-RWG and all-Legendre discretizations. These results demonstrate that GMM is quite competitive in fill time with a comparable higher order code for the same solution accuracy and support the qualitative scalings discussed above.

We do not include matrix-vector product timings or memory scalings in these tests as all matrices were fully computed without recourse to acceleration techniques such as MLFMA. Both the matrix-vector product and storage costs therefore scale as N_s^2 for all examples, and the relative costs of different discretizations may be directly inferred from the reported numbers of degrees of freedom.

2.6 Conclusion

This work extends the scope of the Generalized Method of Moments to include multiple geometry representations and mixed current approximation spaces on PEC scatterers. Decomposition

of the scatter surface via overlapping patches and the partition of unity allow local geometry descriptions capable of handling geometrical features including smooth regions, regions for which a priori functional description is known or can be easily extracted, and regions with geometrical singularities. Furthermore, the partition of unity permits mixtures of multiple classes of Entire Patch and/or Sub Patch basis sets within a single simulation. In particular, the introduction of subpatch basis sets on traditional tessellations allows straightforward handling of geometrical singularities, even in problems with smooth higher order geometry descriptions. Finally, the entire process of geometry and basis assignment can be automated for complex structures. The resulting method permits discretization the underlying integral operators in a manner that more closely matches the physics and may result in significant reductions in the number of degrees of freedom required for a given problem relative to traditional moment method solvers.

Future investigations will expand the types of basis functions and local geometry parameterizations used in GMM and apply GMM to dielectric problems. One interesting possibility is to investigate GMM in the context of a domain decomposition method (DDM). GMM is distinct from DDM in that it is a discretization method that stitches together different basis and geometry descriptions to form a Moment Method system, whereas DDM is a solution method in which the Moment Method system is solved by breaking the overall problem into subproblems and solving each smaller problem individually, subject to global consistency constraints. The two methods therefore address different aspects of the discretization and solution of electromagnetic integral equations, and could naturally complement each other. Using a GMM discretization in a domain decomposition framework would yield a method in which individual subdomains could be solved independently as in [54] or the Equivalence Principle Algorithm in [55], but where continuous transitions between non-conformal subdomains are provided by the partition of unity.

This chapter ©2014 reprinted, with permission, from Dault, D.L.; Nair, N.V.; Jie Li; Shanker, B., "The Generalized Method of Moments for Electromagnetic Boundary Integral Equations," *Antennas and Propagation, IEEE Transactions on*, June 2014.

CHAPTER 3

A MIXED POTENTIAL MLFMA FOR HIGHER ORDER MOMENT METHODS WITH APPLICATIONS TO THE GENERALIZED METHOD OF MOMENTS

3.1 Introduction

Higher order moment method discretizations are attractive alternatives to lower order moment methods due to the potential reduction in number of degrees of freedom and higher order convergence afforded by higher order current representations. However, the practical application of higher (and mixed) order discretizations to practical electrically large structures has been hampered by the difficulty of accelerating higher order moment method representations using traditional acceleration methodologies. As the support of basis functions in higher order moment methods becomes large with respect to a wavelength, the scaling of traditional implementations of the Multilevel Fast Multipole Algorithm (MLFMA) [52] rapidly degrades both in memory and in the cost of computing MLFMA-accelerated matrix vector products.

The poor scaling of traditional MLFMA for higher order is caused by three main problems:

1. The larger support of higher order basis functions cannot be subdivided, which places restriction on leaf box size and severely limits the height of the MLFMA tree.
2. Because of the large leaf box size, the cost of filling the nearfield matrix can be as large or greater than the solution time.
3. Large patches may not align well with large leaf level boxes, causing increased error in MLFMA representation.

Additionally, traditional scaling analyses with respect to the number of basis functions can obscure the true costs and scalings of MLFMA for higher order algorithms. Taken together, these issues significantly hamper the application of MLFMA to the many higher order moment method for-

mulations that have been advanced over recent decades. The challenges become even more acute when attempting to accelerate the recently developed Generalized Method of Moments [56], a new moment method discretization scheme that permits mixtures of basis function types with supports that may range from subwavelength up to many wavelengths.

This chapter presents an MLFMA implementation that maintains favorable MLFMA scaling and precomputation time for any mixture of basis function orders and supports; moreover, MLFMA is used to accelerate filling of algebraic preconditioners, which are necessary for convergence in iterative solvers. We apply the method to solving large scattering problems using the Generalized Method of Moments, although the method is equally applicable to other moment methods using higher or lower order geometry and current representations.

Specific contributions of this chapter are:

- A mixed potential MLFMA formulation that retains optimal scaling for any mixture of basis function types, orders, and patch sizes.
- An MLFMA-accelerated scheme for precomputing preconditioners that is significantly faster than direct preconditioner fill, especially with large patches.
- Scaling analysis of the mixed potential MLFMA relative to extant methods.
- Results validating the scaling and accuracy of both the MLFMA and preconditioning schemes applied to scattering problems discretized using the Generalized Method of Moments.

The remainder of this chapter is organized as follows. Section 3.2 gives preliminaries including the electromagnetic problem statement, a short review of the dyadic form of MLFMA, and a brief description of the Generalized Method of Moments, which serves as the test case for the scaling of the mixed potential higher order MLFMA. Section 3.3 examines the challenges above in detail and past approaches. Section 3.4 describes the mixed potential MLFMA formulation. Section 3.5 provides a complexity analysis of the new approach and compares it to past approaches. Section 3.6 gives an MLFMA-accelerated strategy for preconditioning higher order moment methods, and fi-

nally section 3.7 gives results demonstrating the scaling and efficiency of the MLFMA-accelerated solution and preconditioning schemes.

3.2 Preliminaries

3.2.1 Electromagnetic Problem Statement

We seek to compute the scattered fields $\{\mathbf{E}^s(\mathbf{r}), \mathbf{H}^s(\mathbf{r})\}$ due to a plane wave given by $\{\hat{\mathbf{k}}^i, \mathbf{E}^i(\mathbf{r}), \mathbf{H}^i(\mathbf{r})\}$ that is incident on a perfectly electrically conducting scattering body residing in free space. The scatterer boundary is defined by a two-dimensional bounding surface Ω embedded in \mathbb{R}^3 , and is equipped with a unit normal $\hat{\mathbf{n}}(\mathbf{r})$ defined for all points $\mathbf{r} \in \Omega$ except a finite number of geometrically singular points (e.g. corners, tips, edges, etc.). The induced surface current may be obtained via solution of the Combined Field Integral equation (CFIE):

$$\begin{aligned} \alpha \hat{\mathbf{n}}(\mathbf{r}) \times \hat{\mathbf{n}}(\mathbf{r}) \times \mathbf{E}^i(\mathbf{r}) + (1 - \alpha) \eta_0 \hat{\mathbf{n}}(\mathbf{r}) \times \mathbf{H}^i(\mathbf{r}) = \\ -\alpha \hat{\mathbf{n}}(\mathbf{r}) \times \mathcal{T} \circ \mathbf{J}(\mathbf{r}) + (1 - \alpha) \eta_0 \left(\frac{1}{2} I - \mathcal{K} \right) \circ \mathbf{J}(\mathbf{r}) \end{aligned} \quad (3.1)$$

with I the identity operator, η_0 the impedance of free space, $0 \leq \alpha \leq 1$ a constant weighting factor, and the operators \mathcal{T} and \mathcal{K} given by

$$\begin{aligned} \mathcal{T} \circ \mathbf{J}(\mathbf{r}) &= -\hat{\mathbf{n}}(\mathbf{r}) \times jk\eta_0 \int_{\Omega} d\mathbf{r}' \left[\underline{\underline{\mathbf{I}}} + \frac{\nabla \nabla}{k^2} \right] G(\mathbf{r}, \mathbf{r}') \mathbf{J}(\mathbf{r}') \\ \mathcal{K} \circ \mathbf{J}(\mathbf{r}) &= \hat{\mathbf{n}}(\mathbf{r}) \times \int_{\Omega} d\mathbf{r}' \nabla G(\mathbf{r}, \mathbf{r}') \times \mathbf{J}(\mathbf{r}') \end{aligned} \quad (3.2)$$

Here, $\mathbf{J}(\mathbf{r}) = \hat{\mathbf{n}}(\mathbf{r}) \times \{\mathbf{H}^i(\mathbf{r}) + \mathbf{H}^s(\mathbf{r})\}$ is the induced surface current, $G(\mathbf{r}, \mathbf{r}')$ is the free-space Helmholtz Green's function, k is the propagation constant, $\underline{\underline{\mathbf{I}}}$ is the identity dyad, and the integral in the \mathcal{K} operator is taken in the Cauchy principal value sense. An $e^{j\omega t}$ dependence is assumed and suppressed. To construct a moment method system, the surface current is discretized in terms of a set of basis functions as $\mathbf{J}(\mathbf{r}) = \sum_{n=1}^{N_s} a_n \mathbf{f}_n(\mathbf{r})$ and the discretized operators in (3.2) are tested with a set of functions $\{\mathbf{f}_m(\mathbf{r})\}, m \in [1, N_s]$ in the usual fashion to obtain a matrix equation $ZI = V$, where $V = [V_1 V_2 \dots V_{N_s}]^T$, with $V_m = \langle \mathbf{f}_m, \hat{\mathbf{n}} \times \hat{\mathbf{n}} \times \mathbf{E}^i \rangle$ and $I = [a_1, a_2, \dots, a_{N_s}]^T$ the vector of unknown coefficients.

Although the method developed in this chapter works equally well for both the electric field integral equation (EFIE) and the magnetic field equation (MFIE), the primary focus of the current work is efficient acceleration of the EFIE, i.e. the \mathcal{T} operator in (3.2); focus is therefore restricted to the case where $\alpha = 1$. In the results section CFIE solutions are presented that combine both the MFIE and EFIE. In the case where $\alpha = 1$, the elements of the matrix Z (after application of standard derivative transfers) are given by

$$Z_{mn} = I_{mn}^S + I_{mn}^L, \quad (3.3)$$

where the two components I_{mn}^S and I_{mn}^L are

$$I_{mn}^S = \int_{\Omega_m} d\mathbf{r} \mathbf{f}_m(\mathbf{r}) \cdot \int_{\Omega_n} G(\mathbf{r}, \mathbf{r}') \mathbf{f}_n(\mathbf{r}') d\mathbf{r}' - \frac{1}{k^2} \int_{\Omega_m} d\mathbf{r} \nabla \cdot \mathbf{f}_m(\mathbf{r}) \int_{\Omega_n} G(\mathbf{r}, \mathbf{r}') \nabla' \cdot \mathbf{f}_n(\mathbf{r}') d\mathbf{r}' \quad (3.4)$$

$$I_{mn}^L = \frac{1}{k^2} \oint_{\gamma_m} dl \hat{\mathbf{n}}_{\gamma_m}(\mathbf{r}) \cdot \mathbf{f}_m(\mathbf{r}) \int_{\Omega_n} G(\mathbf{r}, \mathbf{r}') \nabla' \cdot \mathbf{f}_n(\mathbf{r}') d\mathbf{r}' - \frac{1}{k^2} \int_{\Omega_m} d\mathbf{r} \nabla \cdot \mathbf{f}_m(\mathbf{r}) \oint_{\gamma_n} G(\mathbf{r}, \mathbf{r}') \hat{\mathbf{n}}'_{\gamma_n}(\mathbf{r}') \cdot \mathbf{f}_n(\mathbf{r}') dl' - \frac{1}{k^2} \oint_{\gamma_m} dl \hat{\mathbf{n}}_{\gamma_m}(\mathbf{r}) \cdot \mathbf{f}_m(\mathbf{r}) \oint_{\gamma_n} G(\mathbf{r}, \mathbf{r}') \hat{\mathbf{n}}'_{\gamma_n}(\mathbf{r}') \cdot \mathbf{f}_n(\mathbf{r}') dl', \quad (3.5)$$

where Ω_m is the support of \mathbf{f}_m , $\gamma_m = \partial\Omega_m$ is the boundary of the support of $\mathbf{f}_m(\mathbf{r})$ and $\hat{\mathbf{n}}_{\gamma_m}$ is a outward pointing normal to γ_m that is tangent to Ω_m . The I_{mn}^S term consists of surface source and testing integrals, and the I_{mn}^L term contains integrals in which at least one of the source and testing integrations is a contour integral. Contour integral terms in higher order moment methods are problematic for two primary reasons. First, they may be difficult to parameterize and integrate on higher order surfaces, and second, the term in which both the source and testing integrations are contour integrals cannot be integrated if the contours γ_m and γ_n are coincident. The usual remedy for these issues is to design the basis sets $\{\mathbf{f}_m\}$, $\{\mathbf{f}_n\}$ so that 1) $\hat{\mathbf{n}}_{\gamma_{m,n}} \cdot \mathbf{f}_{m,n} = 0$ everywhere on the boundary of $\Omega_{m,n}$ and 2) any contour integrals arising at discontinuities in surface normals interior to $\Omega_{m,n}$ are explicitly canceled. As shown below, this places strict limitations on the implementation of the MLFMA when patch sizes grow to be large relative to a wavelength.

3.2.2 The Multilevel Fast Multipole Algorithm

This section provides a brief review of MLFMA and establish the nomenclature that will be used throughout the rest of the chapter. MLFMA relies on the partitioning of the moment method system as:

$$ZI = (Z^N + Z^F)I = V, \quad (3.6)$$

where Z^N consists of all “near” interactions, and Z^F consists of all “far” interactions. Precise definition of near and far interactions relies on a hierarchical partitioning of the problem domain as follows. Consider a cubical domain B^L that completely encloses the scattering surface Ω . This box is termed the “root level” box. The root level box is recursively subdivided L times, with boxes at the finest level termed the “leaf” boxes. The edge length of a single leaf box is denoted Δx_0 , and the edge length of the root level box B^L is $2^{L-1}\Delta x_0$. Interactions between source functions \mathbf{f}_n and testing functions \mathbf{f}_m that reside in boxes sharing a vertex are termed “nearfield”; all other interactions are termed “farfield”. Nearfield interactions are computed directly using (3.4), where it is assumed that the basis function is defined in such a way that the line integrals are canceled or go to zero. Farfield interactions are computed using the MLFMA farfield representation:

$$Z_{mn} = \int_S d\hat{\mathbf{k}}^2 \mathbf{V}_{mj}^*(\hat{\mathbf{k}}) \cdot T(\hat{\mathbf{k}}, \mathbf{r}_{ij}) \mathbf{V}_{ni}(\hat{\mathbf{k}}), \quad (3.7)$$

where $\mathbf{r}_i, \mathbf{r}_j$ respectively denote the centers of the source and observer boxes, $\mathbf{r}_{ij} = \mathbf{r}_j - \mathbf{r}_i$ is the vector between the box centers, S is the unit sphere in k -space, and $T_{N^l}(\hat{\mathbf{k}}, \mathbf{r}_{ij})$ is the translation operator [57], given by

$$T_{N^l}(\hat{\mathbf{k}}, \mathbf{r}_{ij}) = \sum_{r=0}^{N^l} (-j)^r (2l+1) h_r^{(2)}(k|\mathbf{r}_{ij}|) P_r(\hat{\mathbf{k}} \cdot \hat{\mathbf{r}}_{ij}) \quad (3.8)$$

where $h_r^{(2)}(\cdot)$ is an r th order spherical Hankel function of the second kind and $P_r(\cdot)$ the r th degree Legendre polynomial. A key parameter is N^l , the truncation order of the addition theorem, which must be chosen large enough to ensure that (3.8) converges to a desired accuracy for boxes at level

l in the tree. The source (observer) multipoles (local expansions) are given by:

$$\mathbf{V}_{r,q} = \int_{\Omega_r} d\mathbf{r} e^{-j\mathbf{k}\cdot(\mathbf{r}-\mathbf{r}_q)} [\underline{\mathbf{I}} - \hat{\mathbf{k}}\hat{\mathbf{k}}] \cdot \mathbf{f}_r(\mathbf{r}). \quad (3.9)$$

We designate (3.7) as the “dyadic” version of MLFMA because the dyad $[\underline{\mathbf{I}} - \hat{\mathbf{k}}\hat{\mathbf{k}}]$ appears in the equation. Due to the inherent separability of the exponential terms appearing in (3.9), multipoles may be recursively aggregated about box centers at higher levels of the MLFMA tree. Using this hierarchical structure, the MLFMA algorithm is divided into five steps:

1. Source to multipole (S2M) aggregation of sources into multipoles about leaf level box centers ,
2. Multipole to multipole (M2M) recursive interpolation of lower level multipoles into higher level multipoles,
3. Multipole to local (M2L) translation using the translation operator,
4. Local to local (L2L) recursive interpolation of higher level terms in terms of lower level multipoles,
5. Local to observer (L2O) evaluation of potentials at observation locations due to local expansions residing at leaf box centers.

In dyadic MLFMA, the multipoles/local expansions $\mathbf{V}_{r,q}$ have two components, and each matrix vector product requires two tree traversals.

3.2.3 Application to higher order

The challenge in using the dyadic MLFMA kernel with boxes sized smaller than a patch is illustrated by the following example (the terms “patch” and “basis function support” are used interchangeably in the following discussion). Consider a self-interaction Z_{nn} for a single higher order basis function \mathbf{f}_n with diameter of support $\text{Diam}(\Omega_n) > 2\Delta x_0$. For a given source leaf box b_s , define the partial matrix element Z_{nn}^s that results from evaluation of interactions between the source

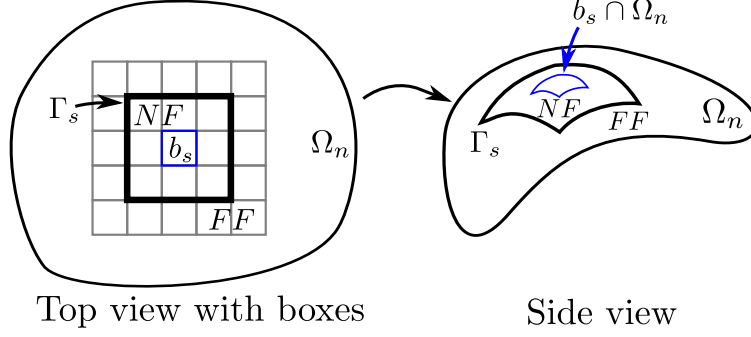


Figure 3.1: Division of a large curvilinear basis function support Ω_n into nearfield and farfield for a source leaf box b_l . Problematic contour integrals appear along the contour Γ between nearfield and farfield regions.

\mathbf{f}_n localized to $\Omega_n \cap b_s$ and observed by \mathbf{f}_n over its full support. Partition the element in the usual MLFMA manner as $Z_{nn}^s = Z_{nn}^{s,F} + Z_{nn}^{s,N}$ and denote by Γ_s the contour defined by the intersection of the box faces delineating nearfield and farfield regions, with $\hat{\mathbf{n}}_{\Gamma_s}^{NF}$ defined as the normal to Γ_s pointing out of the nearfield region. Fig. 3.1 shows a schematic representation of the contour Γ_s induced by the split between nearfield and farfield. Summing over all source boxes with $b_s \cap \Omega_n \neq \emptyset$, the full matrix element is obtained as

$$\begin{aligned} Z_{nn} &= Z_{nn}^N + Z_{nn}^F, \\ Z_{nn}^N &= \sum_s Z_{nn}^{s,N}, \quad Z_{nn}^F = \sum_s Z_{nn}^{s,F}. \end{aligned} \quad (3.10)$$

Using the nomenclature of section 3.2.1, the interactions Z_{nn}^N and Z_{nn}^F can be further partitioned as

$$\begin{aligned} Z_{nn}^N &= I_{nn}^{S,N} + I_{nn}^{L,N} \\ Z_{nn}^F &= I_{nn}^{S,F} + I_{nn}^{L,F}, \end{aligned} \quad (3.11)$$

where the contour terms $I_{nn}^{L,F}$, $I_{nn}^{L,N}$ are aggregations of all line integrals along contours Γ_s and

$$I_{nn}^{L,F} = -I_{nn}^{L,N} \quad (3.12)$$

because $\hat{\mathbf{n}}_{\Gamma_s}^{NF} = -\hat{\mathbf{n}}_{\Gamma_s}^{FF}$ for all s . The equality (3.12) allows one to write $Z_{nn} = I_{nn}^{S,N} + I_{nn}^{S,F}$ provided the terms $I_{nn}^{L,F}$ and $I_{nn}^{L,N}$ are correctly canceled.

Since both $I_{nn}^{S,F}$ and $I_{nn}^{L,F}$ are implicit in the dyadic MLFMA kernel and cannot be independently extracted, the terms $I_{nn}^{L,N}$ must be explicitly computed to correctly recover Z_{nn} ; otherwise

the equivalent interaction is $I_{nn}^{S,N} + I_{nn}^{S,F} + I_{nn}^{L,F} \neq Z_{nn}$. The same situation occurs for any Z_{mn} in which some portion of Ω_m and Ω_n fall within each others' spatial nearfield. For higher order surfaces, integrations along the contours Γ_s become quite difficult to parameterize and computationally burdensome to compute.

Due to these challenges, leaf boxes sizes in traditional MLFMA implementations cannot be smaller than the size of the largest basis function supports so that each basis function is associated with a single leaf box. For lower order bases with small supports relative to a wavelength, the basis function size is generally smaller than the limit on leaf box size imposed by the low-frequency breakdown of MLFMA and no splitting between nearfield and farfield occurs.

3.3 Previous Approaches

Before introducing the mixed potential MLFMA formulation, this section reviews previous approaches to accelerating higher order moment method problems with MLFMA. These fall into two broad categories. The first type of approach maintains the large leaf box size and limited tree height forced by large basis function supports, and uses a variety of strategies to ameliorate the various costs in runtime and storage for different parts of the algorithm. One method [58–60] is to use spherical harmonic expansions (SHE) to reduce storage at the leaf level. Recently, [61] adopted this approach and introduced additional shifts at the leaf level to overcome the overlap problem. Investigations of a similar approach was carried out in [62], which concluded that basis function order and support were limited in higher order MLFMA implementations. In [63], an extended tree was utilized in which the additional non-translating leaf levels were added to the MLFMA octree to reduce storage costs and speed up the aggregation and disaggregation of multipoles at the leaf level. While these approaches can reduce storage and computation time for aggregation and disaggregation steps, they do not address the fundamental limitations of the high cost of nearfield fill or limited tree height.

The second approach is the point-based method of [64], [65,66], which treats samples of basis

functions at quadrature abscissa as individual radiating dipoles. MLFMA groupings and interaction lists are defined based on the locations of these equivalent dipoles. This approach permits MLFMA leaf box size to be much smaller than the support of a single higher order basis function, thereby permitting the use of more levels the MLFMA tree and maintaining more favorable scaling of the MLFMA algorithm. To avoid the problematic contour integrals that arise in dyadic MLFMA, [64] defines nearfield matrix elements using the following subtraction scheme:

$$Z_{mn}^N = Z_{mn} - Z_{mn}^{FF} \quad (3.13)$$

where Z_{mn} is computed directly and the Z_{mn}^{FF} correction term, which may be computed directly or using MLFMA, uses the dyadic kernel. Although the number of nearfield interactions may be less than with the non-point-based approaches due to the reduced box size, (3.13) can still be costly to compute since it requires 1) the full direct computation of entire patch-patch interactions for Z_{mn} and 2) the farfield subtraction step. As shown in the results section, for some configurations the cost of these steps can dominate the overall cost of the algorithm at runtime, and furthermore, the cost of the correction step can be approximately as costly as the direct evaluation of Z_{mn} .

The algorithm presented in this work is related to the point-based MLFMA approach of [64] in that the lowest level MLFMA groupings are indexed to discrete quadrature abscissas, and not basis functions supports, with the result that the diameter leaf-level box size can be much smaller than the extent of a basis function support. Instead of the dyadic Green's function, a mixed potential form of the EFIE is employed that does not suffer from the contour integration problem of the dyadic Green's function at box edges. The resulting algorithm is free of the overlap problem, maintains MLFMA scaling regardless of basis function support size, and permits Z^N to be filled solely on the basis of a spatial nearfield criterion. To the authors' knowledge, the only works that have been published on mixed potential MLFMA in the context of high frequency electromagnetics are [67], where it was applied to efficient representation using the SHE method applied to low order discretizations, [68], where its accuracy was compared with that of the dyadic representation using large leaf box sizes, and [69], where it was employed in a hybrid MLFMA-FFT method. None of

these works applied the mixed potential formulation to higher order MLFMA in the context of a point-based method for higher order functions as is done in the present work.

An MLFMA implementation was developed for GMM in the conference work [50] using a tree with non-uniform leaf box sizes. However, that work was based on a traditional dyadic MLFMA implementation and suffered from the problems of large leaf box size, limited tree height, and the overlap problem, although the latter problem was somewhat ameliorated by the non-uniform tree employed.

3.4 Point-Based Mixed Potential MLFMA

3.4.1 Mixed potential farfield representation

As stated above, the bottleneck in accelerating the higher order moment method solution of the EFIE using MLFMA is the appearance of uncompensated contour integrals at the boundaries between mixed potential nearfield and dyadic farfield representations. To remove this obstacle, the mixed potential formulation (3.3)-(3.5) is used for both the MLFMA farfield interactions and the nearfield interactions. Doing so permits the $I^{L,N}$, $I^{L,S}$ integrals defined in the last section to be analytically extracted and canceled so that the farfield portion of Z_{mn} contains only the $I^{S,F}$ term and the nearfield portion contains only the $I^{S,N}$ term. The mixed potential integral $I^{S,F}$ may then be accelerated using MLFMA.

Equation (3.4) contains four independent terms that must be computed in the inner integral: three corresponding to the vector potential, and one corresponding to the scalar potential. Each basis function \mathbf{f}_k may therefore be identified with a four-component vector function:

$$\tilde{\mathbf{f}}_k = [f_k^1, f_k^2, f_k^3, \frac{j}{k} \nabla \cdot \mathbf{f}_k]^T, \quad (3.14)$$

where $[f_k^1, f_k^2, f_k^3]$ are the x, y, z components of the basis function. Likewise, the potentials $\Phi(\mathbf{r})$ and $\mathbf{A}(\mathbf{r})$ may be combined into a four-component potential vector as

$$\tilde{\mathbf{S}} = [A^1, A^2, A^3, \Phi]. \quad (3.15)$$

One may now compactly write

$$Z_{mn} = \langle \tilde{\mathbf{f}}_m, \tilde{\mathbf{S}}(\tilde{\mathbf{f}}_n) \rangle = \sum_l \int_{\Omega_m} d\mathbf{r} \tilde{f}_m^l S^l(\tilde{f}_n^l) \quad (3.16)$$

where

$$S^l(\tilde{f}_n^l) = -jk\eta_0 \int_{\Omega_n} d\mathbf{r}' G(\mathbf{r}, \mathbf{r}') \tilde{f}_n^l(\mathbf{r}'). \quad (3.17)$$

Equation (3.17) is nothing but the I^S term defined in (3.4). Employing the MLFMA farfield representation on each of the four components, one may write

$$\int_{\Omega_n} d\mathbf{r} \tilde{\mathbf{f}}(\mathbf{r}) \cdot \tilde{\mathbf{S}}(\mathbf{r}) = \int_S d\hat{\mathbf{k}}^2 \tilde{\mathbf{V}}_{mj}^*(\mathbf{k}) \cdot T(\hat{\mathbf{k}} \cdot \mathbf{r}_{ij}) \tilde{\mathbf{V}}_{ni}(\mathbf{k}), \quad (3.18)$$

with the new multipoles defined as

$$\tilde{\mathbf{V}}_{r,q}(\mathbf{k}) = \int_{\Omega_r} d\mathbf{r} e^{-j\mathbf{k} \cdot (\mathbf{r} - \mathbf{r}_q)} \tilde{\mathbf{f}}_r(\mathbf{r}). \quad (3.19)$$

Since the representation in the farfield is now identical to that in the nearfield and the problematic contour integrals $I^{L,N}$, $I^{L,F}$ analytically cancel, it is possible to arbitrarily subdivide the support of a basis function into nearfield and farfield regions. The result is that the leaf box size may be much smaller than the patch size, and discretizations containing any arbitrary mixture of patch sizes may be accelerated without affecting the scaling of the method. Furthermore, as with the dyadic point-based method, removal of the restrictions on box size permits the height of the MLFMA tree to be chosen for optimal scaling, and not based on the diameter of the largest patch. Fig. 3.2b illustrates these advantages.

3.4.2 Point-based algorithm

Practical evaluation of the spatial integrals in (3.16) for full patches is effected through numerical quadrature as

$$Z_{mn} \approx -jk\eta_0 \sum_{t=1}^{N_{qm}} \sum_{s=1}^{N_{qn}} w_s w_t \tilde{\mathbf{f}}_m(\mathbf{r}_t) \cdot G(\mathbf{r}_t, \mathbf{r}_s) \tilde{\mathbf{f}}_n(\mathbf{r}_s) \quad (3.20)$$

with w_s the s th source quadrature weight, \mathbf{r}_s the location of the s th source quadrature abscissa in \mathbb{R}^3 , and N_{qn} is the total number of quadrature points over Ω_n , with corresponding definitions for

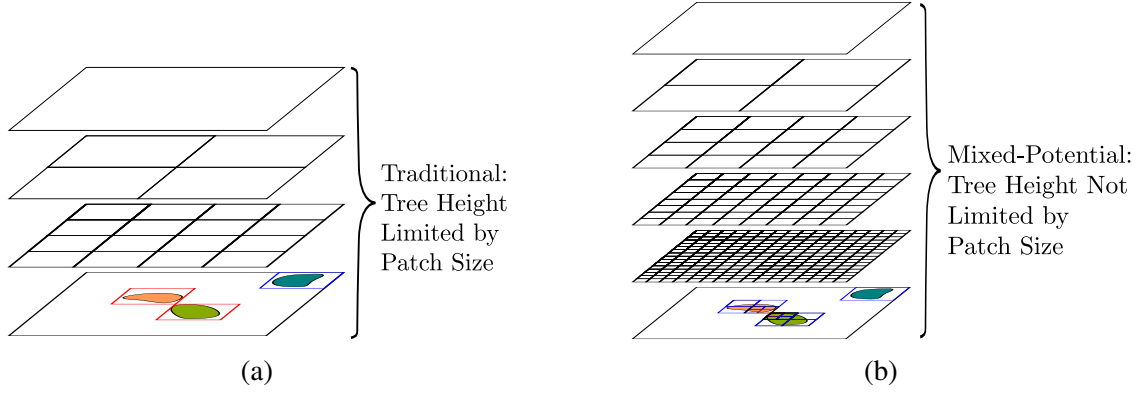


Figure 3.2: Illustration of traditional and point-based MLFMA trees. (a) Traditional: MLFMA leaf box size (and therefore tree height) is limited by the size of the largest patch. (b) Point-based/mixed potential: leaf box size and tree height are not limited by patch size, and may be chosen for optimal MLFMA scaling subject to the low frequency limit of MLFMA.

the testing quadrature. Similar to the approach in [64], each source sample $w_s \tilde{\mathbf{f}}_n(\mathbf{r}_s)$ is interpreted as an independent radiating dipole and each testing sample $w_t \tilde{\mathbf{f}}_m(\mathbf{r}_t)$ as an independent observing dipole. These source/observer dipoles are then grouped into leaf level boxes in the usual fashion.

The source multipole for a single leaf box b_q is given by:

$$\tilde{\mathbf{V}}_{r,q}(\mathbf{k}) = \sum_{s \in \Lambda_q} w_s e^{-j\mathbf{k} \cdot (\mathbf{r}_s - \mathbf{r}_q)} \tilde{\mathbf{f}}_r(\mathbf{r}_s), \quad (3.21)$$

where Λ_q is defined as the set of quadrature points with $\mathbf{r}_s \in b_q$. For a patch Ω_r that is large with respect to the leaf box size Δx_0 , $\dim(\Lambda_q) \ll N_{qr}$. Fig. 3.3 depicts the point-based grouping scheme and interactions for two GMM patches, and Fig. 3.4 shows the interaction levels between patches with various separations for traditional dyadic and point-based MLFMA. The point-based mixed potential scheme permits MLFMA accelerated computation of (3.16) even for the case where $\Omega_m = \Omega_n$, as long as the singular and near integrations are carefully handled.

3.4.3 Mixed potential point-based MLFMA nearfield

In the mixed potential point-based MLFMA, the entries of Z_{mn}^N are defined differently than in traditional and dyadic point-based MLFMA. If the support of $\tilde{\mathbf{f}}_n(\mathbf{r})$ is Ω_n , denote as B_n the set of leaf boxes indices such that $b_l \cap \Omega_n \neq \emptyset$, and assume that B_n contains K_n boxes. The set B_m for the

testing function $\tilde{\mathbf{f}}_m(\mathbf{r})$ with support Ω_m is defined analogously. For each source leaf box $b_n, n \in B_n$, define Θ_n as the set of indices $m \in B_m$ of boxes with which b_n experiences a nearfield interaction. The nearfield element Z_{mn}^N is then given by

$$-jk\eta_0 \sum_{k \in B_n} \sum_{l \in \Theta_n} \int_{\Omega_m \cap b_l} d\mathbf{r} \tilde{\mathbf{f}}_m(\mathbf{r}) \cdot \int_{\Omega_m \cap b_k} d\mathbf{r}' G(\mathbf{r}, \mathbf{r}') \tilde{\mathbf{f}}_n(\mathbf{r}'). \quad (3.22)$$

For patches with diameter $D > 2\Delta x_0$, the set $\{\Theta_{n_1}, \Theta_{n_2}, \dots, \Theta_{n_{K_n}}\}$, $n_i \in B_n$, is smaller than $B_n \times B_m$, sometimes considerably so if the patches are large. This implies that Z_{mn}^N is only partially filled, with the remaining interactions accounted for in Z_{mn}^F . The subtraction scheme of [64] effects a similar partial filling of Z_{mn}^N , but with the (often considerable) extra work of computing the full matrix element and then subtracting the MLFMA farfield contribution.

Evaluation of the partial integrations in (3.22) requires local self, near, and nonself source quadrature rules, with the particular rule selected based on the proximity of a given interacting box pair b_l, b_k . For instance, in the case that $l = k$, an appropriate singular integration rule is required. In GMM, source integrations are defined on a subtriangulation of the patch support [56], with the subtriangles generally smaller than the MLFMA leaf box size. Localized singular and near integrations are therefore easily handled without modification to the GMM integration scheme. The mixed potential MLFMA is also readily applicable to other higher order moment methods that use similar subdivisions to compute near and self interactions [12, 15]. Schemes that use whole-patch self rules over large patches, e.g. those in [11], do not fit immediately into the mixed potential framework and would have to use modified quadrature schemes.

3.5 Complexity Analysis

Obtaining an accurate sense of scaling for GMM (and other higher order methods in general) is somewhat more difficult than for lower order methods due to the potential collocation of many higher order basis functions, as well as the relatively large spatial extent of basis function support. Furthermore, while asymptotic scaling is generally the metric of choice when discussing fast methods, the constants that appear in front of the asymptotic scalings are often significantly larger

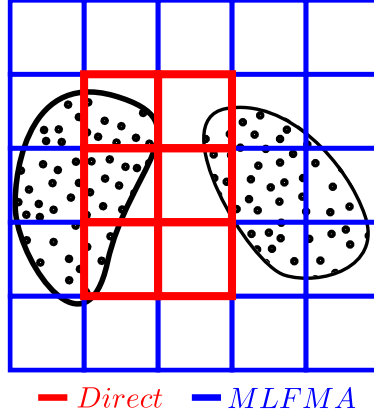


Figure 3.3: Point-based MLFMA groupings and nearfield/farfield interaction partitions for interaction between two patches. Only direct interactions between the bold red boxes contribute to Z^N .

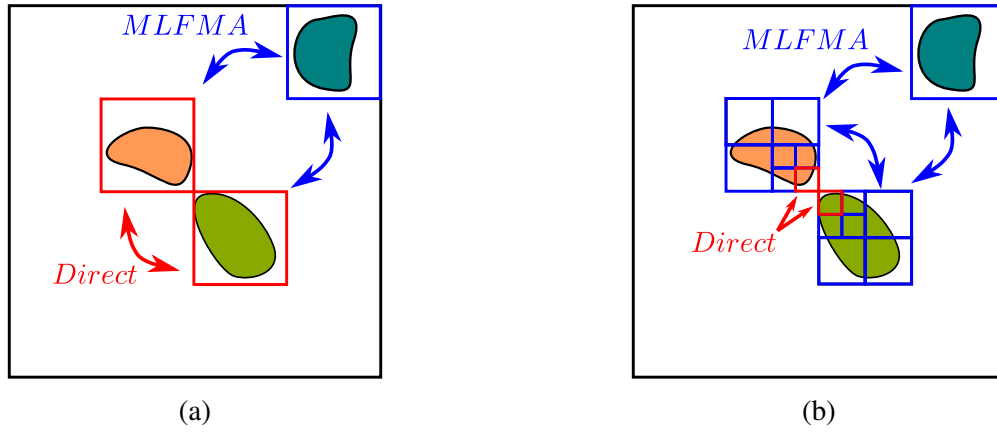


Figure 3.4: Comparison of interactions dyadic and mixed potential MLFMA. (a) Limit on non-point-based dyadic MLFMA leaf box size means that interactions between large patches must be computed directly. (b) For point-based/mixed potential MLFMA, interactions between large patches may be split between nearfield and farfield so that favorable scaling is maintained.

for higher order methods than for lower order methods, and can have a more pronounced impact on the relative cost of different formulations. Inspired by the point-based nature of the present algorithm, the present scaling discussion is cast in terms of N_q^{tot} , the total number of unique dipole locations, and N_{dip} , the total number of dipoles that must be evaluated, instead of the traditional measure in terms of the total number of basis functions N_s , which can obscure the true cost of setup and execution time. Denoting the number of basis functions and quadrature abscissa on patch Ω_r

as N_b^r and N_q^r respectively, one obtains:

$$\begin{aligned} N_q^{tot} &= \sum_{r=1}^{N_p} N_q^r, \\ N_{dip} &= \sum_{r=1}^{N_p} N_q^r N_b^r, \end{aligned} \tag{3.23}$$

with N_p the total number of patches. For a discretization with the same number of basis functions N_b per patch, $N_{dip} = N_q^{tot} N_b$, i.e. N_b appears only as a scaling factor.

Using these definitions, the cost of directly evaluating the interaction between two patches Ω_r and Ω_k is $N_b^r N_q^r N_b^k N_q^k$. (We exclude self-rules for the case $r = k$ from this analysis since they are restricted to a local neighborhood and scale linearly with respect to patch diameter.) When a discretization is heterogeneous in the patch size and number of basis functions per patch, as is often the case in GMM, determining scalings is quite complex; the following discussion assumes that all patches are of approximately the same size and support the same numbers of basis functions (N_b) and quadrature points (N_q).

3.5.1 Computational complexity

Using the metric of N_q^{tot} , the cost of filling the entire impedance matrix scales as $\mathcal{O}(N_b N_p N_q)^2 = \mathcal{O}(N_b N_q^{tot})^2$. When MLFMA is employed using both the traditional and point-based dyadic methods, the cost of filling the nearfield matrix instead scales as $C_1 N_p (N_b N_q)^2 = C_1 N_q N_b^2 N_q^{tot}$, where the constant C_1 is determined by the number of nearfield interactions between patches, and the scaling proportional to N_b^2 occurs because multiple basis functions must be evaluated at each quadrature point. For a dyadic method based on a traditional tree such as the SHE-based method in [58], C_1 may be quite large due to the large leaf box size and correspondingly large number of nearfield interactions. For the point-based dyadic method, the smaller leaf box size can reduce the number of interactions classified as nearfield, so C_1 may be slightly smaller relative to the traditional method. For the mixed potential point-based method, only interactions between quadrature points in each others' spatial nearfield must be evaluated, and the cost of filling the nearfield matrix scales proportional to $\tilde{N}_q N_b^2 N_q^{tot}$, with \tilde{N}_q the average number of quadrature points in each leaf box. For patches

with diameter $D > 2\Delta x_0$, $\tilde{N}_q \ll C_1 N_q$ for the mixed potential method relative to the point-based dyadic method.

At runtime, the cost of the nearfield portion of a matrix vector product for the mixed potential formulation and the dyadic point-based formulation are identical because both generate an identical nonzero pattern for Z^N . For the traditional dyadic MLFMA, the nearfield portion of the matrix vector product is larger than the point-based method due to the higher density of Z^N .

The dominant scaling of the farfield portion of a matrix vector product for both the mixed potential and dyadic point-based methods is $\mathcal{O}(C_2 N_{dip} \log_2 N_{dip} + C_3 N_{dip})$. Here, C_2 is a constant related to the number of tree traversals and the truncation limit of the translation operator (3.8), and C_3 is related to cost of aggregation/disaggregation of multipoles/local expansions at the leaf level. Both the linear and logarithmic scalings are retained because in higher order discretizations where many basis functions are evaluated at each quadrature point, it is often the case that $C_2 N_{dip} \log_2 N_{dip} \leq C_3 N_{dip}$ for reasonably sized octrees. The scaling of the traditional dyadic method degrades from $N_{dip} \log_2 N_{dip}$ as patch size grows because only a few levels in the tree are used due to the restrictions on leaf box size. Denoting by C_k^{MP} and C_k^{DPB} , $k = 1, 2$ the constants for the mixed potential and dyadic point-based algorithms, one finds that $C_2^{MP} \approx 2C_2^{DPB}$ because the mixed potential algorithm requires four MLFMA tree traversals instead of the two required for dyadic MLFMA. However, as shown in the results section, $C_3^{MP} < C_3^{DPB}$ because the mixed potential algorithm actually requires fewer flops per dipole in the aggregation/disaggregation steps. The total time to compute a matrix vector product for higher order discretizations using the mixed potential and dyadic point-based formulations is therefore often comparable.

3.5.2 Memory scaling

As partial matrix elements are computed for the nearfield in the mixed potential MLFMA, nearfield storage for the point-based and mixed potential MLFMA implementations is the same and scales as $N_p N_b^2$, where N_p is the number of patches in a discretization. Nearfield storage for traditional approaches such as the SHE method can be higher because of the larger number of nearfield in-

teractions. Farfield memory requirements for the SHE method is less than that for the point-based methods since the SHE affords both more efficient storage at the leaf level and also entails fewer levels in the tree due to restrictions on leaf box size [58]. For the point-based and mixed potential formulations, the farfield storage is $\mathcal{O}(C_2 N_{dip} \log N_{dip})$, where again $C_2^{MP} = 2C_2^{DPB}$.

From the scaling analysis presented here it is evident that for discretizations with large patches, the mixed potential formulation provides speedups in precomputation time relative to both the traditional and point-based dyadic formulations, while solution time is often comparable. As is demonstrated in the results in section 3.7, the savings can be significant for mixed discretizations commonly encountered in GMM, or for higher order methods when the patches are large.

3.6 Preconditioning

Practical implementation of MLFMA for the EFIE (and CFIE) requires preconditioning to speed up convergence in iterative solvers; for example the MLFMA matrix vector product using a right preconditioner M becomes

$$(Z^F + Z^N)M^{-1}MI = V. \quad (3.24)$$

For good convergence, it is necessary that the elements of M be “fully” computed in the sense that all quadrature points corresponding to a matrix element of M must be summed over. Failure to do so generally destroys the benefit of the preconditioner and leads to poor convergence in iterative solvers. In traditional MLFMA, the elements of M are generally taken as subsets of Z^N , since these elements are precomputed. The mixed potential Z^N only stores partial matrix elements, so entries of Z^N are not immediately suitable for preconditioning. Depending on the stencil of the preconditioner, direct evaluation of the missing interactions between quadrature points can substantially erase the cost gains from the partial fill of Z^N . Instead, the mixed potential MLFMA is exploited to rapidly precompute elements of the preconditioner M in the following manner, which works for algebraic preconditioners built on any stencil, e.g. diagonal, block diagonal, ILU, etc.

Higher order basis sets from a source patch Ω_l and observer patch Ω_k whose interactions are included in M contribute to a submatrix \tilde{M}_{lk} of dimension $N_b^k \times N_b^l$ which may be full or sparse depending on the selected preconditioning strategy. Each subblock is separated into spatial nearfield and farfield contributions as

$$\tilde{M}_{lk} = \tilde{M}_{lk}^N + \tilde{M}_{lk}^F, \quad (3.25)$$

where \tilde{M}_{lk}^N contains the contributions from quadrature points that are in each others' spatial nearfield as specified by the global MLFMA interaction lists, and \tilde{M}_{lk}^F contains the complementary farfield interactions. For basis functions with small support, $\tilde{M}_{lk} = \tilde{M}_{lk}^N$ as in traditional MLFMA. We begin by inserting into M the relevant portions of the precomputed Z^N matrix that fall onto the selected preconditioning stencil, i.e. \tilde{M}_{lk} is filled up for all interacting l, k . To complete the farfield contributions of M , for each patch Ω_l define T_l , a subset of the global MLFMA tree that completely encloses the patch. The local patch tree T_l extends only up only to the first level containing a box that entirely circumscribes the patch. Fig. 3.5 shows patch trees for two patches that contribute to the preconditioner and experience both near and farfield interactions. Associated with each patch tree is a corresponding list τ_l of all translations in which boxes in the patch tree participate. For patches Ω_l, Ω_k that contribute to M , take an intersection of the translation lists on each patch $\tau_{lk} = \tau_l \cap \tau_k$. Using precomputed global translation operators indexed to the translations contained in τ_{lk} , \tilde{M}_{lk} is completed by computing

$$\tilde{M}_{lk}(:, i) = \tilde{M}_{lk}^N(:, i) + \mathcal{F}_{lk}(e_i), \quad i = 1, N_b^l, \quad (3.26)$$

where e_i is the i th column of the $N_b^l \times N_b^l$ identity matrix and the notation $\mathcal{F}_{lk}(e_i)$ indicates the MLFMA-accelerated portion of the contributions, which equivalent to the matrix vector product $\tilde{M}_{lk}^F e_i$. For patches that are included in the preconditioner but who are completely in each others' spatial farfield, $\tilde{M}_{lk} = \tilde{M}_{lk}^F$, and the submatrix is filled exclusively using MLFMA, often with only one or a small number of translations. Fig. 3.6 depicts the manner in which fill of a preconditioner block is split between nearfield and farfield computations.

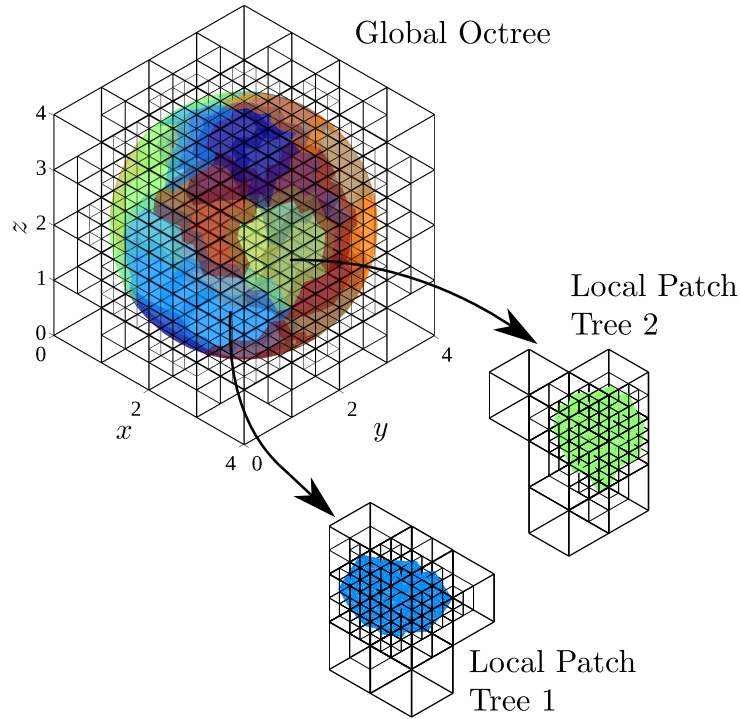


Figure 3.5: Local patch trees used to compute preconditioners. Each local tree is a subset of the global MLFMA octree. Interactions between two patches are computed using intersections of the global interaction lists.

$$\begin{array}{c}
 \begin{array}{c} \tilde{M}_{lk}^F \\ \left[\begin{array}{c} \color{red}{\rule{0.5cm}{0.4pt}} \end{array} \right] \\ \mathcal{F}(e_i) = \tilde{M}_{lk}^F(:, i) \end{array} \\
 + \\
 \begin{array}{c} \tilde{M}_{lk}^N \\ \left[\begin{array}{c} \color{blue}{\rule{0.5cm}{0.4pt}} \end{array} \right] \\ \tilde{M}_{lk}^N(:, i) \end{array} \\
 = \\
 \begin{array}{c} \tilde{M}_{lk} \\ \left[\begin{array}{c} \color{purple}{\rule{0.5cm}{0.4pt}} \end{array} \right] \\ \tilde{M}_{lk}(:, i) \end{array}
 \end{array}$$

Figure 3.6: Graphical depiction of the computation of a single column of a preconditioner block \tilde{M}_{lk} . \tilde{M}_{lk}^N consists of the precomputed nearfield interactions and $\mathcal{F}(e_i)$ is an MLFMA product with the i th column of the identity matrix e_i . The summation of the i th column of \tilde{M}_{lk}^N with the $\mathcal{F}(e_i)$ yields the i th column of \tilde{M}_{lk} .

It is often sufficient (and even desirable) that the elements of a preconditioner only approximate those of the moment method impedance matrix; however, for a robust and reliable preconditioning strategy it is necessary that the approximation error be controllable. To verify that a preconditioner filled using MLFMA-accelerated patch-patch interactions has controllable accuracy, the accuracy of an overlapped block diagonal preconditioner is compared for a 2-lambda sphere filled directly vs. using acceleration in Figs. 3.8-3.11. The preconditioner M is overlapped in the sense that, in addition to the diagonal block, nonself blocks on the superdiagonal and subdiagonal are also computed. The accuracy of the matrix fill is controlled by the parameter χ , which specifies the truncation order N^l in the addition theorem for the MLFMA translation operator at level l so that $N^l = \chi ka^l$, where $a^l = 2^{(l-1)}\Delta x_0$ is the radius of the smallest sphere that completely encloses a box at level l . For all preconditioning results, the discretization is chosen to produce an error in the bistatic RCS of $\epsilon_{l_2} \leq 5 \times 10^{-3}$, where ϵ_{l_2} is the relative l_2 error, defined as

$$\epsilon_{l_2} = \frac{\|\tilde{\mathbf{E}} - \mathbf{E}_{\text{Mie}}\|}{\|\mathbf{E}_{\text{Mie}}\|}, \quad (3.27)$$

with $\|\cdot\|$ the l_2 norm, $\tilde{\mathbf{E}}$ the solution radiation field, and \mathbf{E}_{Mie} the analytical radiation field obtained from the Mie Series. Convergence is computed as $\epsilon_{Fro} = \|\tilde{M} - M_{Dir}\|_F / \|M_{Dir}\|_F$, where $\|\cdot\|_F$ is the Frobenius norm, \tilde{M} is the preconditioner obtained using the mixed potential formulation with MLFMA acceleration, and M_{Dir} is the preconditioner obtained through direct computation. All timings in this and the results section were performed on a single core of a Dell Precision T7600 workstation operating at 1.2 GHz with 12GB of RAM.

Figs. 3.8-3.9 show convergence and computation time for computing \tilde{M} relative to the time to compute M_{Dir} . For this test, the sphere is discretized using $N_p = 65$ GMM patches of diameter $h = 1\lambda$, each of which supports a $p = 4$ Legendre basis ($N_s = 4950$), for a range of Δx_0 . Comparison of the two figures reveals that an accuracy of $\epsilon_{Fro} \approx 10^{-3}$ may be obtained using MLFMA in approximately one half the time of a direct fill. The slower convergence for smaller Δx_0 in Fig. 3.8 is a manifestation of the low frequency breakdown of MLFMA. We note that the convergence for small leaf boxes could be significantly improved through hybridization with low frequency MLFMA [70] or the method of Accelerated Cartesian Expansions (ACE) [71], which

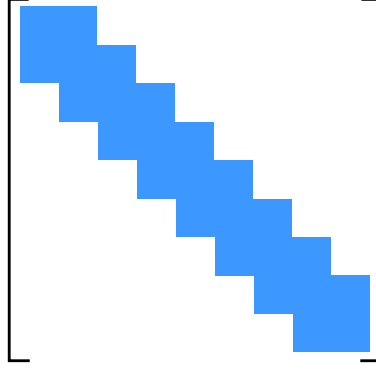


Figure 3.7: Stencil of overlapped block preconditioner used in preconditioning scaling tests.

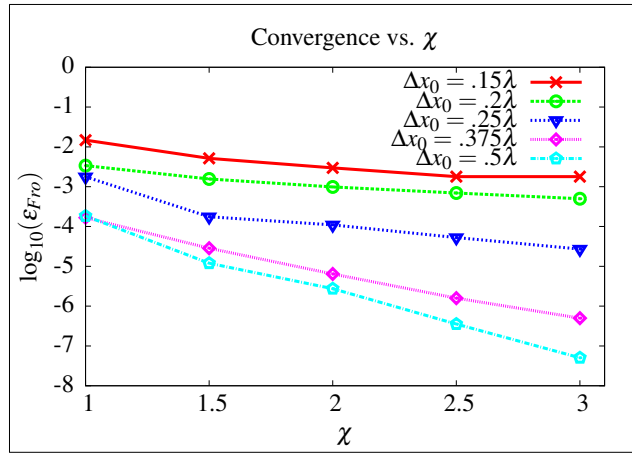


Figure 3.8: Convergence in relative (Frobenius) error of preconditioning matrix filled using $\mathcal{O}(N_q \log N_q)$ MLFMA-accelerated algorithm vs. $\mathcal{O}(N_q^2)$ direct fill algorithm. Geometry is a 2λ sphere with $p = 4$ and $h = 1\lambda$.

are low frequency methods complementary to high frequency MLFMA. Because the mixed potential MLFMA contains four components, it maps directly onto ACE, which uses the same mixed potential formulation.

Figs. 3.10-3.11 show convergence and timings for the same 2λ sphere with a $p = 9$, $h = 2\lambda$ discretization which yields $N_p = 28$, $N_s = 3080$. Computation of M for larger patches clearly shows the advantage of using the mixed potential MLFMA formulation to precompute preconditioners. For all values Δx_0 , the computation of \tilde{M} is faster than direct computation, and accuracies of $\epsilon_{Fro} \approx 10^{-4}$ can be obtained with a speedup of approximately 10 times over the direct fill time.

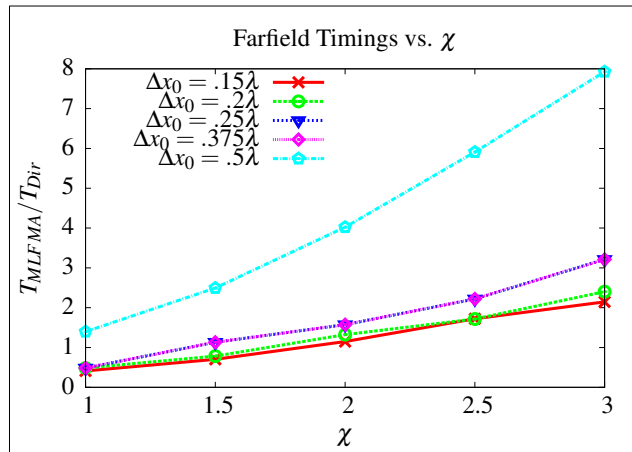


Figure 3.9: Comparison of MLFMA-accelerated preconditioner fill times with respect to χ for a 2λ sphere with $p = 4$ and $h = 1\lambda$.

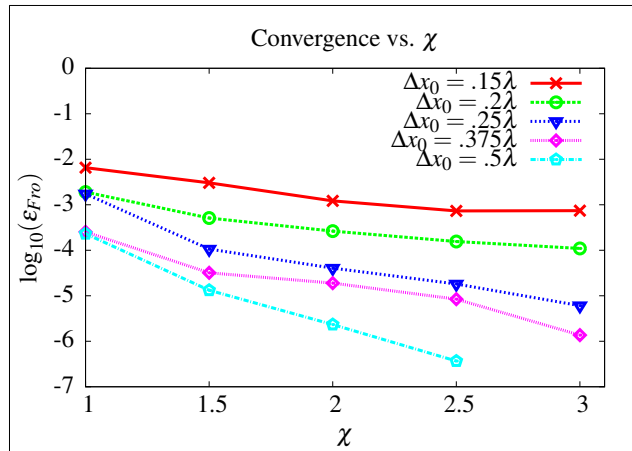


Figure 3.10: Convergence in relative (Frobenius) error of preconditioning matrix filled using $\mathcal{O}(N_q \log N_q)$ MLFMA-accelerated algorithm vs. $\mathcal{O}(N_q^2)$ direct fill algorithm. Geometry is a 2λ sphere with $p = 9$ and $h = 2\lambda$.

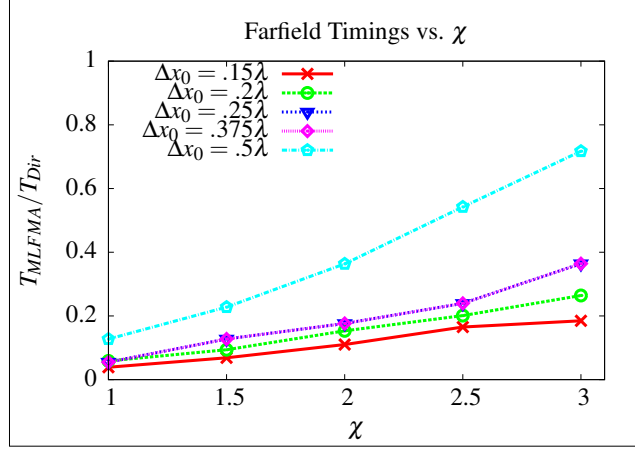


Figure 3.11: Comparison of MLFMA-accelerated preconditioner fill times with respect to χ for a 2λ sphere with $p = 9$ and $h = 2\lambda$.

3.7 Results

This section presents results validating the scaling and accuracy of the mixed potential MLFMA scheme. We also apply it to some relevant scattering geometries discretized with the Generalized Method of Moments using all-higher order discretizations and mixed high and low-order discretizations. In all tests, the MLFMA leaf box size is fixed to $\Delta x_0 = .25\lambda$, the incident field is a plane wave, and all RCS measurements are bistatic. For details on how GMM integrals are evaluated, see [56].

The first set of results in Figs. 3.12-3.14 validates the theoretical scalings vs. the total number of quadrature points N_q^{tot} (in this case $N_{dip} = N_b N_q^{tot}$, and scalings in N_{dip} and N_q^{tot} are interchangeable). The scaling tests are performed for a series of square plates of side length $a = 2\lambda$ to $a = 12\lambda$ residing in xy plane. Plates are chosen because they represent a worst-case scenario for the scaling of MLFMA. The patch size is fixed at $h = 1\lambda$ and a $p = 4$ tensor product Legendre basis (30 basis functions/patch) is utilized. Table 3.1 lists the numbers of basis functions, patches, and N_q^{tot} for the series of plates.

Fig. 3.12 shows the scaling of matrix vector product timings for the series of plates using the mixed potential MLFMA. The scaling is quite close to linear, with a slope of $m = 1.018$. Careful checks were made to ensure that the primary scaling came from the farfield part of the matrix vector

Table 3.1: Discretization details for series of plates used in scaling demonstration.

a/λ	N_s	N_p	N_q^{tot}
2	450	15	112140
3	900	30	251685
4	1560	52	449505
5	2430	81	708435
6	3540	118	1026585
7	4650	155	1392720
8	6060	202	1823640
9	7590	253	2311050
10	9450	315	2860305
11	11430	381	3468150
12	13410	447	4118520

product. As shown below, this scaling is due to the dominant cost of the multipole aggregation and local disaggregation steps, typical of higher order discretizations with many collocated basis functions. Since these steps scale linearly with respect to the number of dipoles, the overall scaling appears close to linear.

Scalings in storage for both Z^N and the MLFMA tree are shown in Fig. 3.13. As expected, the nearfield memory scales linearly, and the farfield memory scales as $N_q^{tot} \log N_q^{tot}$. Note that the jumps in the farfield memory correspond to the addition of a new level of the tree as the plate size grows larger than $(2^n)\Delta x_0$, where n is an integer. For the same number of levels in the tree the scaling is as predicted by theory. The final scaling result for the plate geometries is shown in Fig. 3.14, which demonstrates that the fill time of the nearfield impedance matrix Z^N scales linearly with the number of quadrature points N_q^{tot} , as expected.

The second result demonstrates that for a given geometry, because the leaf box size may be fixed independent of the patch size or basis order, the only change in the cost of the farfield portion of a matrix vector product for varying h and p occurs at the aggregation and disaggregation (S2M and L2O) steps, which scale linearly in both the number of quadrature points N_q^{tot} and the number of basis functions per patch N_b . Fig. 3.15 shows a GMM discretization of a representative scattering geometry, a 15m VFY-218 aircraft discretized at 600 MHz using a mixture of higher order

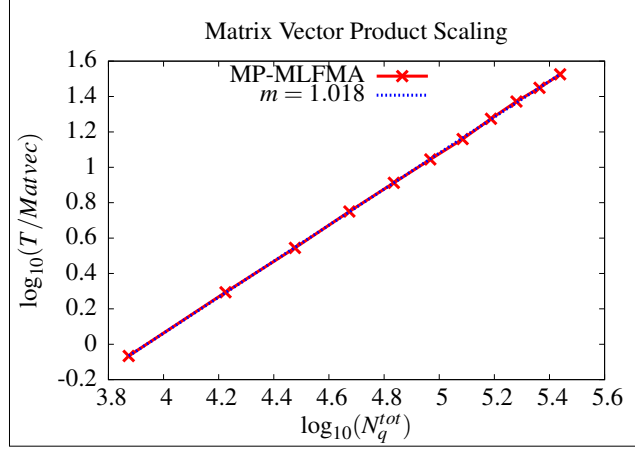


Figure 3.12: Scaling of MLFMA matrix vector product timings vs. N_q^{tot} for a series of square plates of size 2λ - 12λ .

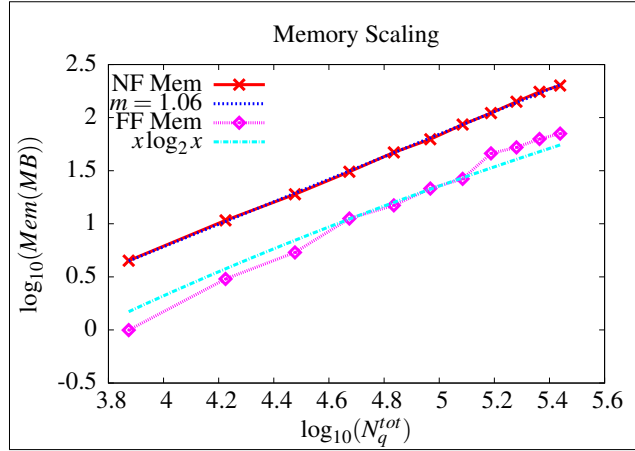


Figure 3.13: Scaling in nearfield and farfield memory for a series of square plates of size 2λ - 12λ .

patches and tessellations on edges/tips. The leaf box size is fixed at $\Delta x_0 = .25\lambda$, and h and p are varied in tandem. Tables 3.2 and 3.3 show the timings for each step of the MLFMA matrix vector product $V^F = Z^F I$ for the mixed potential and dyadic point-based kernels, for a CFIE solution with the coefficient $\alpha = .5$. For both the dyadic and mixed potential kernels the MLFMA truncation factor is fixed at $\chi = 1.4$. We note that it was shown in [72] that the translation operator scalar Green's function can be truncated at one fewer harmonics than the dyadic translation operator; however, because of the curl operator in the MFIE and the higher spectral content of the divergence of the basis function [69] required in the scalar potential contribution of the mixed potential

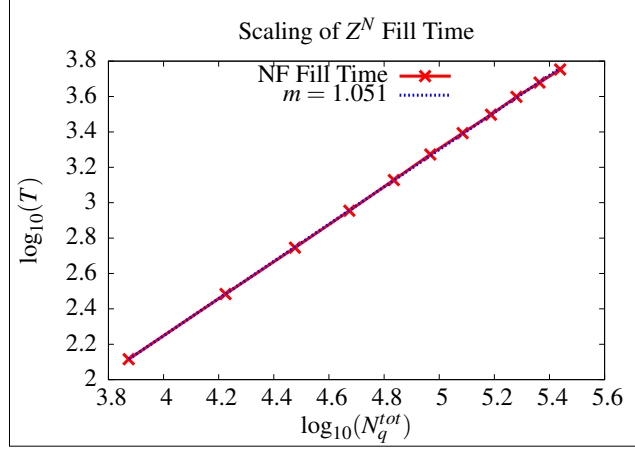


Figure 3.14: Scaling of nearfield matrix fill vs. N_q^{tot} for a series of square plates of size $2\lambda - 12\lambda$.

EFIE operator, the same number of harmonics is used for both.

Although the overall time to compute a mixed potential matrix vector product is slower, (as expected) for the CFIE result, it is still quite competitive with dyadic kernel. The reason for this is the number of floating point operations (flops) required to compute the aggregation/disaggregation steps, which are the most costly steps in the algorithm. The innermost loop for evaluating the dyadic multipole (3.9) at the i th sample point on the k -sphere requires computation of the terms $\exp[j\mathbf{k}^i \cdot (\mathbf{r} - \mathbf{r}_q)] \hat{\mathbf{k}}_\theta^i \cdot \mathbf{f}_n(\mathbf{r})$ and $\exp[j\mathbf{k}^i \cdot (\mathbf{r} - \mathbf{r}_q)] \hat{\mathbf{k}}_\phi^i \cdot \mathbf{f}_m(\mathbf{r})$, for a total of $2 \times 4 = 8$ flops at each sampling point on the k -sphere, where it assumed that the exponential term is computed in an outer loop and therefore only introduces a single multiplication (additions are neglected). The scalar kernel, on the other hand, does not contain dot products of the basis function with unit k vectors, and therefore requires only 4 multiplications with the exponential term per sample point on the k -sphere. The result is that, although the dyadic MLFMA is twice as fast above the leaf level, the faster evaluation of multipole and local expansions in the mixed potential MLFMA renders that matrix vector product only slightly slower.

Fig. 3.17 shows the RCS compared to a well-validated low-order RWG result for the VFY illuminated by a $\hat{\mathbf{z}}$ -polarized plane wave traveling in the $+\hat{\mathbf{y}}$ direction. The GMM result used the mixed potential CFIE algorithm with the $p = 3$ Legendre basis defined on $h = .8\lambda$ patches from Table 3.3. Fig. 3.16 shows the surface currents for the GMM result.

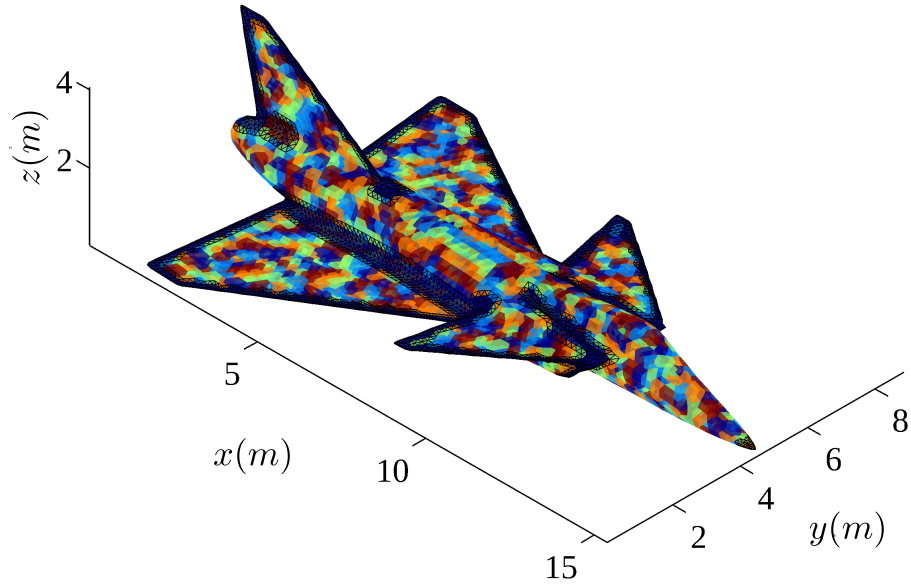


Figure 3.15: GMM discretization of VFY-218 aircraft.

Table 3.2: Matrix vector product timings for dyadic kernel for the VFY-218 aircraft, CFIE.

p	h/λ	N_{dip}	Ag.	Int.	Tr.	Ant.	Dis.	Total
1	0.30	2722734	6.97s	3.08s	0.68s	4.12s	8.65s	23.53s
2	0.60	4643982	7.87s	3.09s	0.68s	4.12s	10.78s	26.59s
3	0.80	6386674	8.53s	3.09s	0.67s	4.12s	12.41s	28.87s
4	1.0	8340864	9.60s	3.09s	0.67s	4.12s	14.70s	32.23s
5	1.25	10397394	10.86s	3.09s	0.67s	4.12s	17.44s	36.23s
6	1.5	12660410	12.37s	3.09s	0.67s	4.12s	20.05s	40.35s

Table 3.3: Matrix vector product timings for mixed potential kernel for the VFY-218 aircraft, CFIE.

p	h/λ	N_{dip}	Ag.	Int.	Tr.	Ant.	Dis.	Total
1	0.30	2722734	6.88s	4.99s	1.21s	5.90s	8.41s	27.46s
2	0.60	4643982	7.73s	5.01s	1.22s	5.92s	10.33s	30.28s
3	0.80	6386674	8.31s	5.00s	1.21s	5.92s	11.93s	32.44s
4	1.0	8340864	9.32s	5.01s	1.22s	5.90s	14.01s	35.53s
5	1.25	10397394	10.58s	5.01s	1.22s	5.90s	17.00s	39.77s
6	1.5	12660410	12.02s	4.99s	1.22s	5.90s	19.08s	43.27s

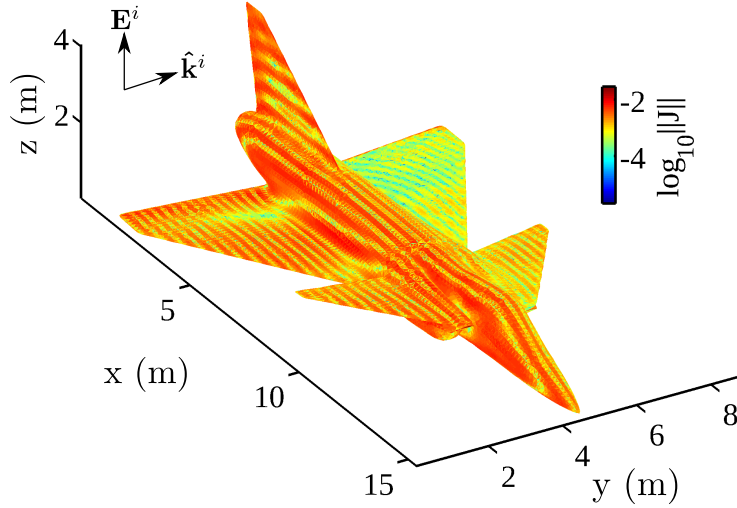


Figure 3.16: Surface currents for the 30λ VFY-218 aircraft.

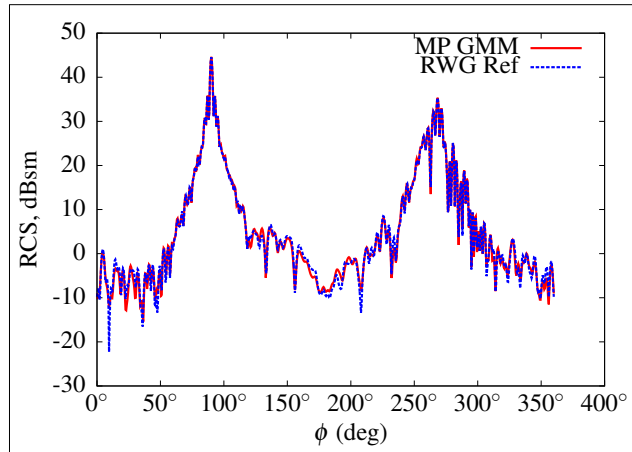


Figure 3.17: Bistatic RCS for VFY-218 aircraft, $\theta = 90^\circ$ cut.

The next result directly compares timings and storage for the mixed potential and dyadic point-based approaches in solving for scattering from a diameter 10λ sphere due to an \hat{x} -polarized plane wave incident along the \hat{z} direction. A leaf box size of $\Delta x_0 = .25\lambda$ yielded a 10 level MLFMA tree, and $\chi = 1.4$ was used as the MLFMA truncation parameter. Throughout the remainder of the results section, the abbreviations “D” and “MP” respectively denote the dyadic and mixed potential point-based kernels. Two discretizations are examined. The first divides the sphere into 1785 patches (average patch diameter $h = .8\lambda$), each of which supports a $p = 2$ Legendre basis, yielding at total of $N_s = 21,240$ basis functions, and the second has 210 patches (average patch

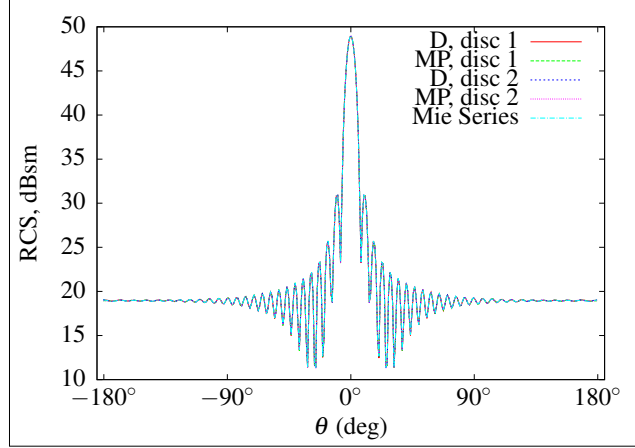


Figure 3.18: Bistatic RCS for 10λ diameter sphere, $\phi = 0$ cut. Two GMM discretizations, disc. 1 ($p = 2$, $h = .8\lambda$) and disc 2. ($p = 7$, $h = 2\lambda$) for both the dyadic (“D”) and mixed potential (“MP”) are compared with the analytical Mie series result.

diameter $h = 2.0\lambda$), each of which supports a $p = 7$ Legendre basis. Fig. 3.18 shows the bistatic RCS obtained from both the dyadic and point-based methods compared to the analytical Mie series result.

For the $p = 2$ discretization, storage and timings for various stages of the algorithm are given in tables 3.4, 3.5. Both solutions converged in 80 steps of the FGMRES [73] iterative solver using a block diagonal preconditioner, with each block corresponding to the interactions between all basis functions on a given patch. Note that timings are only reported for for the costliest portions of the algorithm; times for all other pre/post-computation steps such as geometry initialization, MLFMA tree definition, RCS computation, etc. are common to both algorithms and are insignificant relative to the steps shown.

Storage for Z^N is the same since both methods use the same nearfield stencil. MLFMA storage for the mixed potential algorithm is roughly double that of the dyadic potential since it requires twice the number of MLFMA trees. However, fill time for Z^N is considerably shorter for the mixed potential algorithm because it only computes partial nearfield matrix elements, and furthermore, the mixed potential approach avoids the farfield correction step, the costliest step for the dyadic kernel. In the dyadic approach, full matrix elements of the block diagonal preconditioner are read-

Table 3.4: Storage for 10λ diameter sphere, $p = 2$, $h = .8\lambda$.

Kernel	Z^N mem.	MLFMA mem.
D	72.85MB	80.35MB
MP	72.85MB	160.69MB

ily available from the nearfield matrix, but the mixed potential algorithm requires the additional step to complete these matrix elements, incurring an additional cost of 756s. Because both algorithms converged in the same number of steps in the FGMRES solver, comparison of solution time is meaningful. Here, the dyadic kernel has a slight advantage due to its only having two trees. The total time to solution for the mixed potential algorithm is roughly one half that of the point-based algorithm.

Finally, tables 3.6 and 3.7 show memory and timings for the same sphere discretized with . Table 3.6 shows that, relative to the previous result, storage for Z^N increases the same amount with both methods due to the larger number of collocated basis functions on each patch, but MLFMA storage stays the same since the MLFMA octree does not change. Because of the large patch size and the necessity of directly computing complete nearfield matrix elements, the times required to fill Z^N and compute the farfield correction become very large and dominate the cost of the dyadic point-based algorithm. Note that the farfield correction step was accelerated using the dyadic MLFMA kernel for this discretization.

For the mixed potential point-based algorithm, the times to compute the nearfield matrix elements and farfield portion of the preconditioner grows far more modestly relative to the $p = 2$ result. Although solution time for the mixed potential algorithm is slightly higher than for the dyadic algorithm, total time for the mixed potential algorithm is almost one order of magnitude less than for the dyadic algorithm.

The final set of results, scattering from a mockup next generation navy destroyer, illustrates the overall speedup in fill time for Z^N and the block preconditioner that may be obtained using the mixed potential MLFMA algorithm over direct evaluation and evaluation of MLFMA using large boxes on the order of a wavelength, as in traditional MLFMA. The ship is 15λ in its longest

Table 3.5: Timings for 10λ diameter sphere, $p = 2$, $h = .8\lambda$.

Kernel	Z^N fill	FF Corr.	Prec. FF	Avg. Matvec	Soln.	Total
D	1,603s	2,403s	–	14.34s	1177s	5,204s
MP	442s	–	756s	16.58s	1359s	2,557s

Table 3.6: Storage for 10λ diameter sphere, $p = 7$, $h = 2\lambda$.

Kernel	Z^N mem.	MLFMA mem.
D	336.18MB	80.35MB
MP	336.18MB	160.69MB

Table 3.7: Timings for 10λ diameter sphere, $p = 7$, $h = 2\lambda$.

Kernel	Z^N fill	FF Corr.	Prec. FF	Avg. Matvec	Soln.	Total
D	61,599s	15,712s	–	32.26s	2,002s	79,313s
MP	4,129s	–	2,248s	33.83s	2,065s	8,442s

dimension. A total of 2 RWG patches and 162 smooth polynomial patches ($h = 1\lambda$) supporting a $p = 4$ Legendre basis are used to discretize the problem, and the CFIE is solved with $\alpha = .5$. Note that each RWG patch supports many RWG functions. The resulting discretization, which has a total of $N_s = 25266$ basis functions ($N_{RWG} = 25255$, $N_{Leg} = 4860$) is shown in Fig. 3.19. Three configurations are compared: fill and solution of the full moment method system, MLFMA with $\Delta x_0 = 1\lambda$, and MLFMA with $\Delta x_0 = .25\lambda$. The mixed potential algorithm was used for both the $\Delta x_0 = 1\lambda$ and $\Delta x_0 = .25\lambda$ cases. All results converged to a relative residual error of 5.0×10^{-3} in 34 steps of the FGMRES iterative solver with a Sparse Approximate Inverse (SAI) [74] preconditioner in the inner solver. Memory costs and timings are summarized in Table 3.8.

Direct fill time of the GMM matrix took 189,469s (52.6hr) and solution time of the full system was 141s. For the $\Delta x_0 = 1\lambda$ result, the fill time for Z^N was 26,977s (7.49h) and solution time was 4436s. This illustrates one of the challenges of using MLFMA for GMM, in that the leaf box size dictated by the large Legendre patches is deeply suboptimal for the RWG functions. Even without the RWG functions, in higher order methods with large boxes much of the MLFMA cost can be

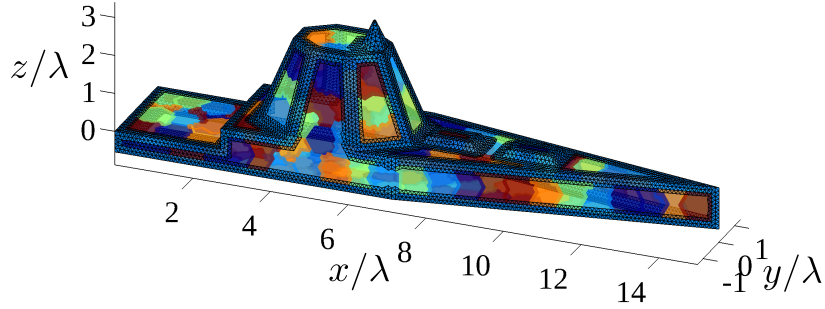


Figure 3.19: GMM mixed discretization for 15λ destroyer: 1st order smooth polynomial patches (patch diameter 1λ) and 4th order Legendre basis on smooth regions, triangular tessellation and RWG basis on tips/corners. (Model credit: Nicholas Miller)

shifted to precomputation of the nearfield. Using the mixed potential MLFMA formulation with a leaf box size of $\Delta x_0 = .25\lambda$, the fill time for Z^N was 1842s (30.7min) and matrix solution time was 440s (7.3min). The restricted spatial extent of the nearfield region for the $\Delta x_0 = .25\lambda$ solution also gives significant savings in memory storage for Z^N relative to the $\Delta x_0 = 1\lambda$ solution, which contains many more nearfield interactions. Memory used for the MLFMA tree for $\Delta x_0 = 1\lambda$ was approximately half that used for the $\Delta x_0 = .25\lambda$ solution. The reduced farfield storage for the $\Delta x_0 = 1\lambda$ result is due to the smaller number of levels in the tree is smaller which means that fewer radiation patterns and translation operators have to be stored.

Table 3.9 gives detailed matrix vector product timings for the three solution methods. The matrix vector product for the direct approach is particularly fast since the final system size is not large. However, as shown in table 3.8, faster solution time is far outweighed by the large setup time. For the $\Delta x_0 = 1\lambda$ MLFMA solution, the dominant cost (by approximately two orders of magnitude) is in the aggregation/disaggregation steps at the leaf level. This is characteristic of MLFMA with large boxes applied to higher order discretizations. Finally, although the aggregation/disaggregation steps are still the costliest part of the matrix vector product for the $\Delta x_0 = .25\lambda$ solution, they are greatly reduced relative to the $\Delta x_0 = 1\lambda$ result due the smaller number of basis functions per box and the smaller number of sampling points on the k -sphere afforded by the smaller box size. Even with the larger farfield storage cost, the smaller box size wins in setup time, solution time, and storage over the $\Delta x_0 = 1\lambda$ result; furthermore, both MLFMA results are

Table 3.8: Storage and timings for 15λ ship.

System type	Z^N storage	MLFMA storage	Z^N fill	Precond FF	Avg. Matvec	Solution Time	Total Time
Full Z	9760MB	–	189,469s	–	3.7s	141s	191,688s
$\Delta x_0 = 1\lambda$	1921MB	18.52MB	26,977s	31s	122s	4436s	31,444s
$\Delta x_0 = .25\lambda$	142MB	39.33MB	1842s	276s	12s	440s	2,118s

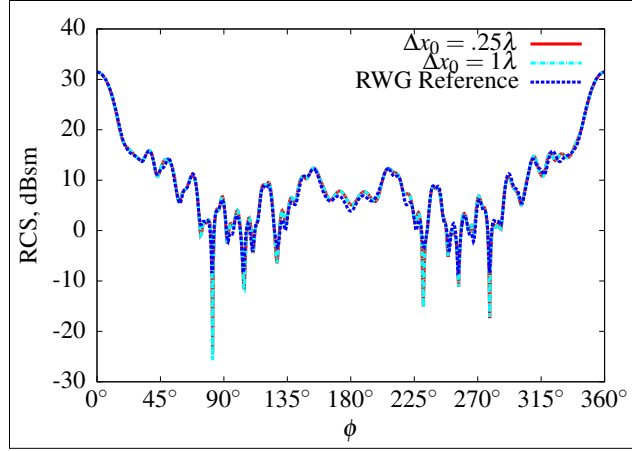


Figure 3.20: Bistatic RCS for 15λ destroyer, $\theta = 90^\circ$ cut, plane wave incident on bow.

Table 3.9: Detailed Matrix Vector Product Timings for 15λ ship.

System type	Z^N	Ag.	Int.	Tr.	Ant.	Dis.	Total
Full Z	3.70s	–	–	–	–	–	3.70s
$\Delta x_0 = 1\lambda$	9.38e-1s	44.33s	2.20e-1s	2.35e-2s	2.71e-1s	76.42s	122.20s
$\Delta x_0 = .25\lambda$	7.77e-2s	3.84s	7.31e-1s	1.17e-1s	8.08e-1s	6.48s	12.05s

significantly faster than the full matrix fill approach.

3.8 Conclusion

This chapter has detailed a mixed potential MLFMA formulation that has the advantage that the large support of higher order basis functions may be arbitrarily subdivided down to the theoretical limit of high frequency MLFMA. As a consequence, height of the MLFMA tree is not limited by the patch size, as it is when traditional dyadic MLFMA is applied to higher order moment methods, but is only limited by the low frequency breakdown of MLFMA. Furthermore, because the farfield

and nearfield integral formulations are the same, nearfield matrix elements can be only partially filled based only on a spatial nearfield criterion, with the remaining farfield contributions completed through the MLFMA tree. This leads to far better efficiency in the cost of nearfield matrix fill than previous point-based methods. We have also leveraged the scheme to effect MLFMA-accelerated precomputation of algebraic preconditioners. The overall method retains optimal MLFMA scaling for any mixture of basis function support size and order from low order discretizations up through extremely high order and asymptotic-type basis functions. Several results with mixed discretizations using the Generalized Method of Moments demonstrated the scaling and accuracy of the method.

In this chapter, only the high frequency variant of mixed potential MLFMA was developed. However, the method is ideally suited to hybridization with the ACE method, which will extend the accuracy and convergence into the low-frequency regime. Also, the SHE expansions in [58] could be used to decrease the memory cost at the lowest level of the MLFMA tree. Finally, although this work utilized relatively simple preconditioning strategies, it can be readily applied to more sophisticated strategies such as the spectral method in [75]. Investigations of these avenues will be the subjects of future publications.

CHAPTER 4

AN INTERIOR PENALTY METHOD FOR THE GENERALIZED METHOD OF MOMENTS

4.1 Introduction

The GMM partition of unity-based representation provides smooth transitions of basis sets from patch to patch. However, because partitions of unity are generally rational functions, integral equation formulations that require derivatives of the basis set can be difficult to integrate. The quality of the GMM solution therefore depends on (i) whether derivatives of basis functions (and therefore of partitions of unity) are necessary in the integral equation formulation, (ii) the order of the numerical integration rules used and (iii) the metric used to measure quality. For example, the electric field integral equation (EFIE) requires derivatives of the basis functions whereas the magnetic field integral equation (MFIE) does not, implying that accurate nearfield solutions for the EFIE require higher order numerical integration rules than for the MFIE. Additionally, it is well known that metrics that rely on farfield data (for instance, radar scattering cross-section) can give high accuracy when compared to those that use nearfield data (for instance, impedance) for the same level of error in the solution current. To reduce the computational burden associated with high order quadrature for GMM discretizations of the EFIE, this chapter proposes the addition of a penalty constraint to the usual integral operators to enforce smoothness of solutions between overlapping patches. With the addition of the penalty term, smooth, accurate solutions may be obtained with significantly lower order numerical quadrature than with the unmodified operator.

Although constraint methods such as Lagrange Multiplier and penalty-type formulations have been widely used in the context of finite element methods [76, 77], they have received relatively little attention from the integral equation community. This is primarily because many integral operators of interest do not satisfy the classical saddlepoint conditions [77, 78] that form the basis for convergence proofs traditionally used for finite elements. Recently, a few formulations that im-

pose solution constraints for some low-order discretizations have been advanced. Both a Lagrange multiplier and a penalty (Nitsche-type) method were developed in [79], [80] for a provably elliptic hypersingular integral equation associated with the Laplacian. Both of these approaches were extended without proof to three dimensional electromagnetic scattering problems in a penalty method for the three dimensional EFIE and MFIE [81] and a mortar element approach for the EFIE [82].

Although the discretized EFIE operator has not been proven to be stationary for all basis sets admissible in the GMM framework, the discretized integral operators used in this chapter satisfy a saddlepoint condition away from resonant frequencies because the scattering surfaces are everywhere smooth and the smooth divergence-conforming basis sets employed admit a local Helmholtz decomposition [83, 84]. If the Moment Method solution to the EFIE is interpreted as the Rayleigh-Ritz algorithm that correctly minimizes the associated functional in the variational sense [85], the addition of a penalty constraint to the original functional should have the effect of driving the minimization toward a constrained solution that possesses the desired characteristics.

This work shows the effects of the penalty formulation on through analysis of the spectrum of the discretized operator on a circular cylinder. This analysis shows that the primary function of the penalty method is to regularize high frequency surface current modes on the scatterer. The analysis is far more straightforward and illuminating in two dimensions, and therefore restricted to the two dimensional EFIE under TE^z excitation. Results are furnished that show the same behavior in three dimensions.

The content of this chapter is as follows. Section 4.2 formulates the electromagnetic scattering problem in two and three dimensions, give a brief statement of the GMM discretization, and state the problem addressed in this work. Section 4.3 furnishes details of the proposed penalty function formulation, and section 4.4 provides a spectral analysis of effect of the operator on the discretized operator. Finally, section 4.5 gives results showing convergence of solutions obtained using the stabilized two dimensional EFIE operator, and section 4.6 shows results in three dimensions.

4.2 Problem Statement

We develop the penalty method in both two and three dimensions. The d dimensional model problem is that of the scattering of an incident electromagnetic plane wave due to a perfect electrically conducting (PEC) object residing in \mathbb{R}^d . In what follows, the notation $\mathbf{r}_d \in \mathbb{R}^d$ refers to the position vector; unless the dimensionality of the domain is not clear from the context, the subscript is dropped on the position vector. The incident plane wave is given by $\mathbf{E}_2^i(\mathbf{r}) = \mathbf{E}_{0,2}e^{-j\mathbf{k}^i \cdot \mathbf{r}}$ for $d = 2$ and $\mathbf{E}_3^i(\mathbf{r}) = \mathbf{E}_{0,3}e^{-j\mathbf{k}^i \cdot \mathbf{r}}$, where $\mathbf{E}_{0,d}$ is a constant vector, and $\mathbf{k} = k\hat{\mathbf{k}}^i$ with $k = \omega/c$ (ω is the angular frequency and c is the ambient wave speed), and $\hat{\mathbf{k}}^i$ the direction of propagation. Throughout this chapter, an $e^{j\omega t}$ time dependence is assumed and suppressed. We denote the scattering surface by $\Omega^d \subset \mathbb{R}^d$, and assume that an outward pointing normal $\hat{\mathbf{n}}(\mathbf{r})$ is defined $\forall \mathbf{r} \in \Omega^d$. Using the boundary conditions for tangential electric field at a PEC interface, the standard EFIE may be written as:

$$\mathcal{T}_d(\mathbf{J}(\mathbf{r})) = \mathbf{g}^i(\mathbf{r}) \quad (4.1)$$

with the \mathcal{T}_d operators for $d = 2$ and $d = 3$ given by

$$\begin{aligned} \mathcal{T}_2(\mathbf{J}(\mathbf{r})) = & \hat{\mathbf{n}}(\mathbf{r}) \times \hat{\mathbf{n}}(\mathbf{r}) \times \left[jk\eta_0 \int_{\Omega} d\mathbf{r}' G(\mathbf{r}, \mathbf{r}') \mathbf{J}(\mathbf{r}') \right. \\ & \left. + \frac{j\eta_0}{k} \nabla \int_{\Omega} d\mathbf{r}' G_d(\mathbf{r}, \mathbf{r}') \nabla' \cdot \mathbf{J}(\mathbf{r}') \right], \end{aligned} \quad (4.2)$$

$$\begin{aligned} \mathcal{T}_3(\mathbf{J}(\mathbf{r})) = & -\hat{\mathbf{n}}(\mathbf{r}) \times \left[\frac{jk\eta_0}{4\pi} \int_{\Omega} d\mathbf{r}' G(\mathbf{r}, \mathbf{r}') \mathbf{J}(\mathbf{r}') \right. \\ & \left. + \frac{j\eta_0}{4\pi k} \int_{\Omega} d\mathbf{r}' \nabla \nabla' G_d(\mathbf{r}, \mathbf{r}') \cdot \mathbf{J}(\mathbf{r}') \right] \end{aligned}$$

$$\mathbf{g}^i(\mathbf{r}) = \hat{\mathbf{n}}(\mathbf{r}) \times \hat{\mathbf{n}}(\mathbf{r}) \times \mathbf{E}_d^i(\mathbf{r}). \quad (4.3)$$

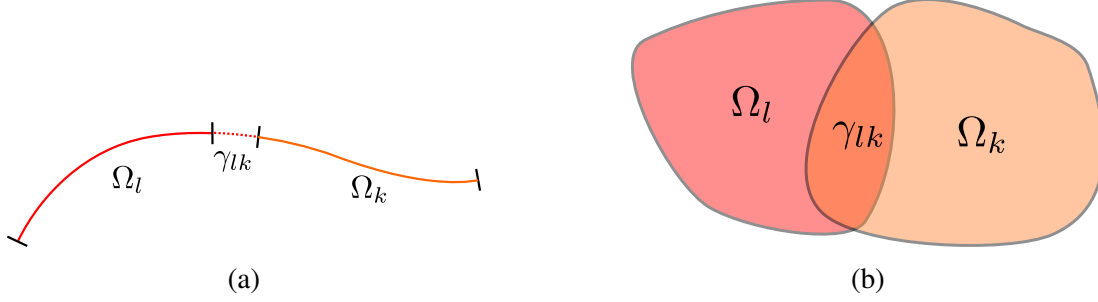


Figure 4.1: Patch overlaps γ_{lk} in (a) two and (b) three dimensions.

where it has been implicitly assumed that \mathbf{J} accrues no contour charges on the boundary of Ω . In (4.2), η_0 is the intrinsic impedance of free space and the Green's functions $G_d(\mathbf{r}, \mathbf{r}')$ are given by

$$\begin{aligned}
 G_2(\mathbf{r}, \mathbf{r}') &= \frac{j}{4} H_0^{(2)}(k \|\mathbf{r} - \mathbf{r}'\|), \\
 G_3(\mathbf{r}, \mathbf{r}') &= \frac{e^{-jk \|\mathbf{r} - \mathbf{r}'\|}}{4\pi \|\mathbf{r} - \mathbf{r}'\|}.
 \end{aligned} \tag{4.4}$$

In (4.4), $H_0^{(2)}(\cdot)$ is the zeroth order Hankel function of the second kind and $\|\cdot\|$ denotes the standard L^2 norm.

4.2.1 The Generalized Method of Moments

This section introduces some slightly altered notation for the Generalized Method of Moments to facilitate statement of the penalty formulation. The scattering surface Ω is subdivided into a set of N_p overlapping patches $\{\Omega_l\}$ such that $\cup_l \Omega_l = \Omega$. The set of patch overlaps $\Omega_l \cap \Omega_j \neq \emptyset$ is denoted by $\gamma = \{\gamma_{lk} : \mathbf{r} \in \Omega_l \cap \Omega_j, l > k\}$. Note that the last inequality removes the redundancy of the form $\gamma_{lk} = \gamma_{kl}$ and also excludes the case of a patch overlapping itself. In the case where three patches overlap the same region of Ω the three dimensional problem, the overlaps γ_{lk} are taken pairwise. Figure Over the set Ω_l , a partition of unity $\{\psi_l\}$ is defined with the properties that $0 \leq \psi_l \leq 1$, $\text{supp}(\psi_l) \subset \Omega_l$, and $\sum_l \psi_l = 1$.

Using the partition of unity, the surface current may be expanded as $\mathbf{J}(\mathbf{r}) = \sum_l \psi_l \mathbf{J}_l(\mathbf{r})$, where $\mathbf{J}_l(\mathbf{r})$, $\mathbf{r} \in \Omega_l$ is the portion of the global current \mathbf{J} that is localized to patch Ω_l via the action of the partition of unity. Each local $\mathbf{J}_l(\mathbf{r})$ is expressed in terms of a set of local approximating functions

as $\mathbf{J}_l(\mathbf{r}) = \sum_{n=1}^{N_l} a_{ln} \mathbf{f}_{ln}(\mathbf{r})$. Discretization with this set of approximating functions and testing (4.1) with a set of suitable similarly constructed functions yields a moment method system

$$\sum_{\Lambda} a_{ln} \langle \psi_k \mathbf{f}_{km}, \mathcal{T}(\psi_l \mathbf{f}_{ln}) \rangle = \langle \psi_k \mathbf{f}_{km}, \mathbf{g}^i(\mathbf{r}) \rangle, \quad (4.5)$$

where $k, l = 1, \dots, N_p$ and for each $k, m = 1, \dots, N_k$, for each $l, n = 1, \dots, N_l$, and Λ is an appropriate index set.

4.2.2 Solution errors

In GMM, ideally the solution currents and charges (reconstructed via the appropriate basis sets) on two overlapping patches should be identical in the region of their mutual overlap, thus enabling the recovery of the current description in all of Ω . In practice, when solving (4.5), the degree to which this condition is realized is determined by the accuracy to which the integrations of products of the basis functions with the partitions of unity can be evaluated. While the integrals involving the current are well behaved and easily evaluated, those involving its derivative (i.e. charge) are significantly more difficult to evaluate and require much higher numerical integration rules. Insufficient numerical integration of these terms leads to solution errors in the patch overlaps. The fundamental cause of this difficulty is easily understood by examining the divergence of the current in (4.6), which consists of a desirable term given by the divergence of the current localized by the partition of unity, and the second an undesirable term involving the gradient of the PU function:

$$\nabla \cdot \mathbf{J}(\mathbf{r}) = \underbrace{\sum_l \psi_l(\mathbf{r}) \nabla \cdot \mathbf{J}_l(\mathbf{r})}_{\text{Desired Term}} + \underbrace{\sum_l \nabla \psi_l(\mathbf{r}) \cdot \mathbf{J}_l(\mathbf{r})}_{\text{Undesirable Term}}. \quad (4.6)$$

If $\mathbf{J}_l(\mathbf{r}) = \mathbf{J}_k(\mathbf{r})$, $\mathbf{r} \in \gamma_{kl}$, then the second term vanishes by the property that $\nabla \sum_l \psi_l(\mathbf{r}) = 0$. However, if the reconstruction is not perfect, then upon summation of the currents, if the derivative of the partition of unity is large (which may be the case), the difference $\mathbf{J}_l(\mathbf{r}) - \mathbf{J}_k(\mathbf{r})$ may be greatly magnified in the solution, leading to spurious features in the solution currents. It is therefore de-

sirable to minimize the discrepancy in the overlaps by enforcing the condition that

$$\mathbf{J}_l(\mathbf{r}) - \mathbf{J}_k(\mathbf{r}) = 0. \quad (4.7)$$

In the limit that (4.7) is satisfied, any errors due to insufficient integration of the gradient of the partition of unity are antisymmetric between the overlapping patches, and consequently precisely cancel in the reconstructed solution.

4.3 Penalty Formulation

Given the origin of the spurious current features associated with the divergence of $\psi_l \mathbf{J}_l$, a formulation is desirable that will minimize the discrepancy $\mathbf{J}_l(\mathbf{r}) - \mathbf{J}_k(\mathbf{r})$, $\mathbf{r} \in \gamma_{kl}$, $\forall \gamma_{kl} \in \gamma$. To do so, recall that according to the reactance principle [3], (4.1) may be cast as a variational problem where the functional of interest is given by

$$I(\mathbf{J}, \mathbf{J}^t) = \langle \mathbf{J}^t, \mathbf{g}^i \rangle_\Omega + \langle \mathbf{J}, \mathbf{g}^* \rangle_\Omega - \langle \mathbf{J}^t, \mathcal{T}(\mathbf{J}) \rangle_\Omega \quad (4.8)$$

In (4.8), $\mathbf{g}^* = \hat{\mathbf{n}} \times \hat{\mathbf{n}} \times \mathbf{E}^*$ is the tangential trace of a plane wave propagating away from the scatterer, the current \mathbf{J}^t is the solution to the adjoint equation, and $\langle \cdot, \cdot \rangle_\Omega$ is an inner product over Ω . A minimization of (4.8) may be performed via discretization with the GMM basis set and the usual Rayleigh-Ritz procedure. To enforce the constraint (4.7), the modified functional

$$\begin{aligned} \tilde{I}(\mathbf{J}, \mathbf{J}^t) = & \langle \mathbf{J}^t, \mathbf{g}^i \rangle_\Omega + \langle \mathbf{J}, \mathbf{g}^* \rangle_\Omega \\ & - \langle \mathbf{J}^t, \mathcal{T}(\mathbf{J}) \rangle_\Omega + \beta \langle [[\mathbf{J}^t]], [[\mathbf{J}]] \rangle_\gamma \end{aligned} \quad (4.9)$$

is proposed, where $[[\mathbf{J}^t]], [[\mathbf{J}]]$ are the jumps in the testing (adjoint) and source current distributions as defined by (4.7), $\beta \geq 0$ is a real number, and $\langle \cdot, \cdot \rangle_\gamma$ denotes the inner product taken over the set of patch overlaps. The purpose of the additional term in (4.9) is to penalize discrepancies between patch currents in the overlap regions. Upon discretization with the functions given in section 4.2.1 and application of the Rayleigh-Ritz procedure, the following formulation of the discretized EFIE

is obtained.

$$\begin{aligned} & \sum_{\Lambda} a_{ln} \left[\langle \psi_k \mathbf{f}_{km}, \mathcal{F}(\psi_l \mathbf{f}_{ln}) \rangle_{\Omega_k} \right. \\ & \left. - \beta \sum_{kl} \sum_{mn} \langle [[\mathbf{f}_{klm}]]_{kl}, [[\mathbf{f}_{kln}]]_{kl} \rangle_{\gamma_{kl}} \right] = \\ & \langle \psi_k \mathbf{f}_{km}, \mathbf{g}^i \rangle_{\Omega_k}, \end{aligned} \quad (4.10)$$

where the notation $[[\mathbf{f}_{kl\alpha}]]_{kl}$ is understood to refer to the jumps in the testing ($\alpha = m$) or source ($\alpha = n$) basis sets between patches Ω_k and Ω_l . We shall refer to (4.10) as the ‘‘compensated’’ form of the discretized EFIE, and (4.1) as the ‘‘uncompensated’’ form. Equation (4.10) may be written in matrix form as:

$$\tilde{Z} = (Z^{MoM} - \beta Z^P)I = V, \quad (4.11)$$

where Z^{MoM} is the uncompensated moment method matrix, Z^P is a (block) tridiagonal matrix corresponding to the penalty term, I is the vector of unknown coefficients, and V is the tested forcing function.

4.3.1 Implementation details for two dimensions

The necessary general implementation details for three dimensional GMM has been developed in Chapters 2 and 5. All two dimensional examples in this chapter are implemented using the following general scheme. A scattering body is subdivided into N_p patches of width W , and width of the overlap region between patches is $W/10$. The partition of unity on patch Ω_l is given by

$$\psi_l(\xi_l) = \frac{\hat{\psi}_l(\xi)}{\hat{\psi}_{l-1}(\xi) + \hat{\psi}_l(\xi) + \hat{\psi}_{l+1}(\xi)}, \quad (4.12)$$

with $\xi \in [-1, 1]$ a local coordinate frame on patch Ω_l . The sub-partition of unity functions are given by $\hat{\psi}(\xi) = e^{\frac{-1}{1-(\xi)^2}}$. Each patch supports a basis set of Legendre polynomials of order p .

To accurately evaluate the required integrations in (4.10), a 3-part composite integration rule is constructed on each patch as follows. First, each patch Ω_l is split into three regions: two overlap regions $\Omega_l^+ \doteq \Omega_l \cap \gamma_{l,l+1}$, $\Omega_l^- \doteq \Omega_l \cap \gamma_{l,l-1}$, and the patch interior $\Omega_l^I \doteq \Omega_l \setminus (\Omega_l^+ \cup \Omega_l^-)$. In Ω_l^I , where the value of the partition of unity ψ_l is 1, an order i point rule Gauss-Legendre is defined.

In each of the overlap regions, a Gauss-Legendre rule of order $i + 1$ is defined, where the higher order is used because of the higher order behavior of ψ_l in patch overlaps. Finally, the three rules are concatenated to form an integration rule for the entire patch. We have found that rules constructed in this manner are far superior to a single Gauss-Legendre rule over the full patch. In the subsequent discussion, a composite rule so constructed is referred to as an “ i th order rule”, where i is indexed to the rule defined in Ω_l^I . For singular integrals, a lin-log rule [86] is substituted for one of the Gauss rules in the appropriate patch region. Integrations of the penalty term of (4.10) use only the portion of the composite rule restricted to the patch overlaps.

4.4 Spectral Analysis: Two Dimensions

This section analyzes the spectral properties of the compensated and uncompensated EFIE operators in two dimensions. The two dimensional problem admits significantly clearer analysis than the three dimensional case, which is far less tractable. This investigation demonstrates that insufficient integration gives rise to both low and high frequency errors in the solution current, and that the effect of the penalty function is to suppress the high frequency errors and correct low frequency errors by smoothing lower order current modes. To simplify the discussion and admit analytical treatment, the present analysis is restricted to a circular cylinder of radius a .

The effect of insufficient integration is shown in Fig. 4.2, where the solution currents are obtained using the uncompensated operator discretized with a $p = 3$ order Legendre basis set. The first trace shows the current obtained using a low-order integration rule ($i = 8$), the second shows the current obtained using a high-order rules ($i = 30$), and the third shows the analytical Mie series solution. The $i = 30$ rule sufficiently integrates the partition of unity and matches very closely with the analytical solution. It is apparent that the low order $i = 8$ rule introduces two types of errors: low frequency anomalies that corrupt the solution everywhere in the patch, and high frequency errors that are manifested as sharp features in the patch overlaps.

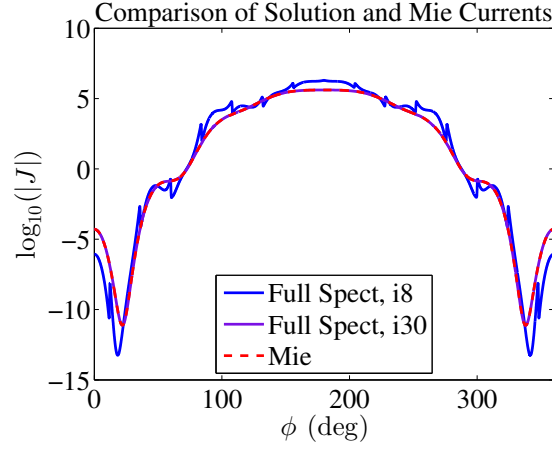


Figure 4.2: Illustration of low and high frequency current errors induced by insufficient quadrature for the TE^z EFIE solution on cylinder of radius $a = .5\lambda$.

4.4.1 Low order analysis

We begin our analysis with a low order discretization in which each patch supports a single basis function, so that the total current discretization is given by $\mathbf{J}(\mathbf{r}) = \sum_n \psi_n(\phi) f_n(\phi) \hat{\phi}$. The exact form of the basis function is not necessary for this analysis, but it is required that $f_n(\phi)$ be shift invariant, so that $f_n(\phi) = f(\phi - n\phi_0)$, where $\phi_0 = 2\pi/N_s$ and $n\phi_0$ is the center of the n th patch. If Galerkin testing is used, the resulting impedance matrix of the uncompensated EFIE operator Z^{MoM} is circulant, implying that its eigenvectors are sampled complex exponentials of the form $\mathbf{v}_q = [1, e^{jq\phi_0}, e^{j2q\phi_0} \dots e^{j(N_s-1)q\phi_0}]$. Using this property and following [87] the eigenvalues λ_q^{MoM} , $q = 0, \dots, N_s - 1$ of the discretized TE^z EFIE operator on a cylinder of radius a may be obtained as

$$\lambda_q^{MoM} = \frac{2\pi\eta_0ka}{2N_s} \sum_{s=-\infty}^{\infty} J'_{q+sN_s}(ka) H_{q+sN_s}^{(2)'}(ka) |F_{q+sN_s}|^2, \quad (4.13)$$

where $J'_k(\cdot), H_k^{(2)'}(\cdot)$ are the derivatives of a k th order Bessel function of the first kind and a k th order Hankel function of the second kind, respectively, and F_k is the k th Fourier coefficient of the product of the partition of unity and the basis function $\psi(\phi)f(\phi)$. Because the patches are evenly spaced and because the penalty term is only nonzero in the overlaps of neighboring patches, the

penalty function matrix is also circulant. Using analysis similar to that of the moment method matrix, one can obtain a formula for the q th eigenvalue λ_q^P of the penalty matrix:

$$\lambda_q^P = C_1 - C_2 \cos(p\phi_0), \quad (4.14)$$

where

$$\begin{aligned} C_1 &= 4\pi a \sum_{p=-\infty}^{\infty} |\tilde{F}_p|^2, \\ C_2 &= 4\pi a \sum_{p=-\infty}^{\infty} |\tilde{F}_p|^2 \cos(q\phi_0), \end{aligned} \quad (4.15)$$

with \tilde{F}_p is the p th Fourier coefficient of the $\mathbf{f}(\phi)$ restricted to the patch overlap. It can be shown that although $C_2 \leq C_1$, generally $C_2 \approx C_1$. The eigenvalues of the penalty matrix therefore behave as

$$\lambda_q^P \sim 2C_1(\sin^2(q\phi_0/2)) + \delta_q(\phi_0), \quad (4.16)$$

with $|\delta_q(\phi_0)| = |(C_1 - C_2) \cos(q\phi_0)/C_1| \ll |C_1|, |C_2|$. From the leading term in (4.16), it is evident that for small q , the values of λ_q^P are small, and then grow with increasing q until they reach their maximum at $q = N_s/2$. This property is key to the regularizing effect of the penalty function on the high frequency spectrum of the solution current, as is now demonstrated.

Because both Z^{MoM} and Z^P are circulant matrices of dimension N_s , they share the same eigenvector basis (sampled complex exponentials), and the eigenvalues of the compensated system \tilde{Z} may be obtained through direct summation as $\tilde{\lambda}_q = \lambda_q^{MoM} - \beta \lambda_q^P$. If the elements of V are expanded in the eigenbasis of \tilde{Z} , one obtains a spectral representation of the solution current as

$$\mathbf{J}(\phi) = \hat{\phi} \sum_{q=-\infty}^{\infty} \frac{b_q e^{jq\phi}}{\lambda_q^{MoM} - \beta \lambda_q^P} \quad (4.17)$$

$$b_q = a\eta_0 \sum_{l=-\infty}^{\infty} F_{-(q-lN_s)} j^{-(q-lN_s+1)} J'_{q-lN_s}(ka). \quad (4.18)$$

Due to the spectral behavior of λ_q^P , for large q and sufficiently large values of β , $|\beta \lambda_q^P| \gg |\lambda_q^{MoM}|$ and $|\beta \lambda_q^P| \gg |b_q|$. The penalty term therefore regularizes high order current modes by driving the

higher order current coefficients toward zero, significantly damping the spurious high frequency features in the current.

4.4.2 Higher order analysis

When a higher order basis set is used with multiple basis functions per patch, both Z^{MoM} and Z^P become block-circulant matrices and the analysis becomes considerably more involved. Nonetheless, similar spectral results hold as in the low order case. To demonstrate this, a numerical approach is employed in which the generalized eigenvalue problem

$$\tilde{Z}\tilde{\mathbf{v}}_q = \tilde{\lambda}_q Z^G, \quad (4.19)$$

is solved, where Z^G is the gram matrix of the basis set and $\{\tilde{\lambda}_q, \tilde{\mathbf{v}}_q\}$ are the q th eigenvalue and eigenvector. The geometry is the $a = .5\lambda$ cylinder discretized with $N_p = 15$ patches, each of which supports a $p = 3$ Legendre basis set.

Figure 4.3 shows a comparison of the uncompensated and compensated ($\beta = .01$) eigenvalues with the analytical eigenvalues of the continuous operator obtained via the Mie series. Two trends are evident. First, it is clear that both the uncompensated and compensated systems correctly capture most of the lower order eigenvalues. Second, the effect of the penalty function for the higher order basis set is the same as that obtained analytically for the lower order basis set, i.e. to add a significant real part to the higher order eigenvalues. In Fig 4.3, $\beta = .01$ is shown for plotting purposes; in practice $\beta \approx 10$ is used, which shifts the real part of the largest eigenvalues by $\approx 10^4$, driving the higher order current coefficients to values many orders of magnitude lower than the lower order current coefficients.

Figures 4.4 and 4.5 show the corrective action of the penalty function on the spectrum of the current when an $i = 9$ quadrature rule is used. Figure 4.4 shows the complete spectrum of the uncompensated and compensated solutions out to very high frequency. The effect of the penalty function with increasing β is to suppress the side lobes that introduce the spurious high frequency components into the solution. Figure 4.5 shows the “visible spectrum” of the analytical current,

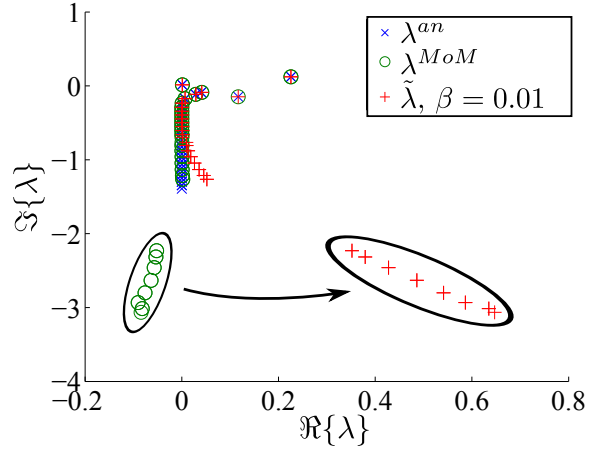


Figure 4.3: Generalized eigenvalues for an $a = .5\lambda$ cylinder.

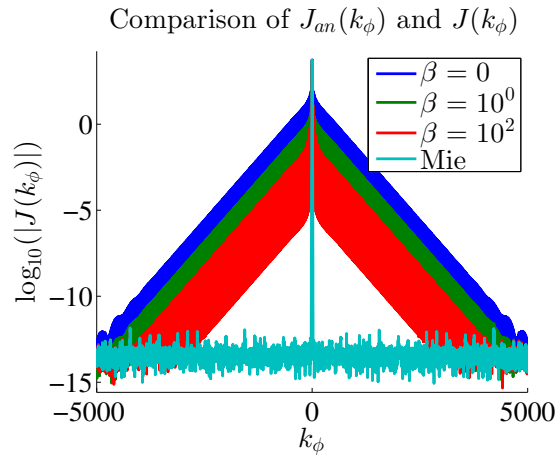


Figure 4.4: High frequency current spectrum of compensated EFIE in visible region for an $a = .5\lambda$ cylinder.

i.e. harmonics that fall within the limit of $q \lesssim ka + 5$. The effect of the penalty function within the visible region is to correct the erroneous eigenvalue corresponding to a low-order mode by removing high frequency content that is aliased to the low order eigenmodes, thereby smoothing the resulting modes and correcting their corresponding eigenvalues.

While the analysis in this section has been specialized to current solutions on a circular cylinder, the results section shows that the same regularizing behavior occurs for eigenvalues of the compensated EFIE on arbitrarily shaped scatterers discretized with nonuniformly sized patches.

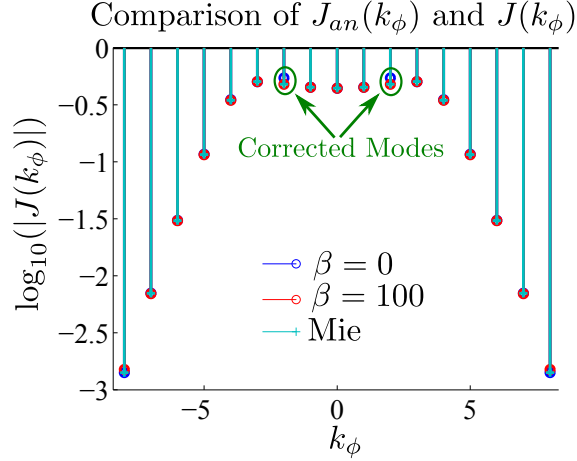


Figure 4.5: Current spectrum of compensated EFIE in visible region for an $a = .5\lambda$ cylinder.

4.5 2D Results

This section presents results demonstrating convergence of solutions using the penalty function formulation. For all results, the exciting field is a $-\hat{y}$ -polarized plane wave traveling in the $+x$ direction, and the solution current is obtained using (4.10).

The first result in Fig. 4.6 shows the current for the circular $a = .5\lambda$ cylinder with $N_p = 15$ patches, each of which supports a $p = 3$ Legendre basis set. All integrals are evaluated with an $i = 8$ point integration rule. The solution currents and bistatic radar cross section (RCS) for two cases, $\beta = 0$ and $\beta = 10$, are shown. As in Fig 4.2, the currents with $\beta = 0$ exhibit spurious high and low frequency features. In contrast, the RCS is quite smooth and accurate even for $\beta = 0$. This highlights an important point: if the target metric is farfield computation, a low order integration rule may suffice. If, however, the target metric is surface current (or a derived quantity such as impedance that depends on surface current), then the low order integration rule is wholly insufficient. When the same configuration is solved with $\beta = 10$ and a low order quadrature, the solution matches the analytical current extremely well.

Next, convergence of the current error vs. β is investigated for the $a = .5\lambda$ cylinder. Figure 4.7 shows l_2 relative error of the solution obtained using GMM vs. the analytical Mie Series solution for three integration rules, $i = 8$, $i = 10$, and $i = 30$. The error is computed as $\|\mathbf{J}_{GMM} -$

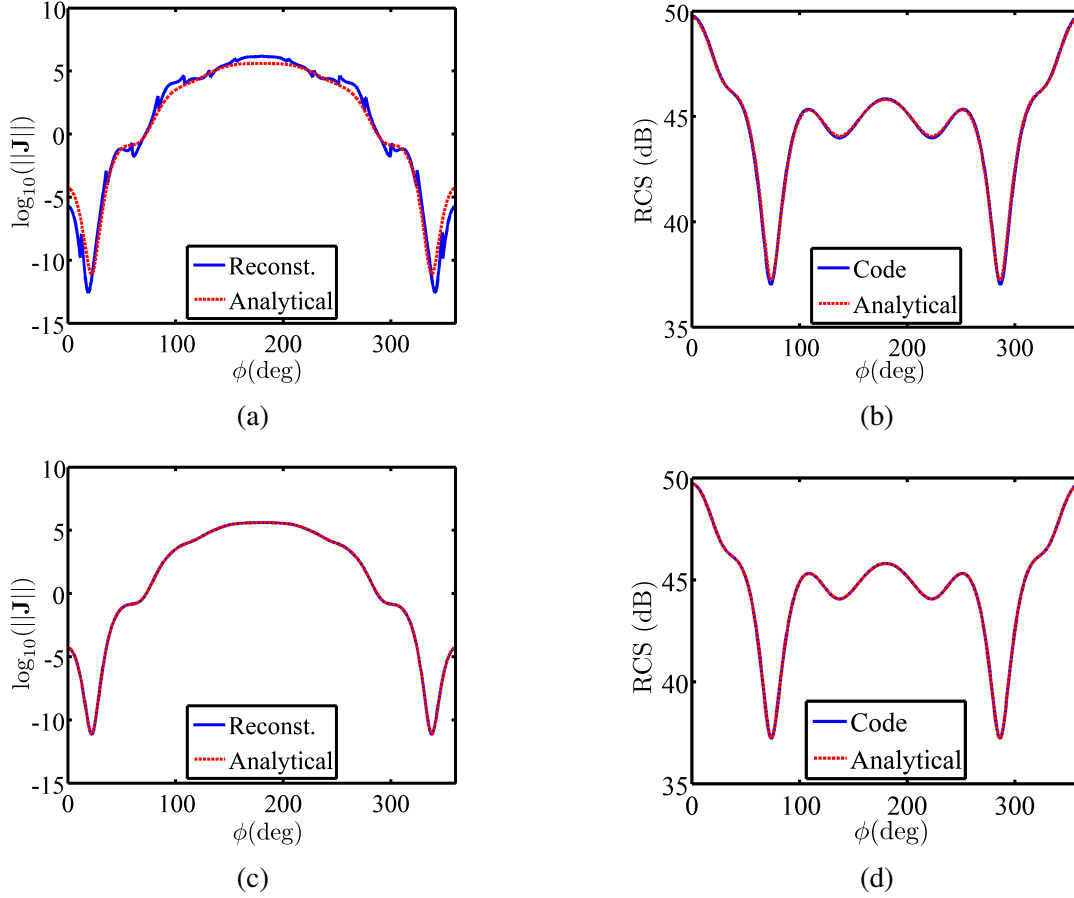


Figure 4.6: Comparison of analytical and reconstructed current obtained using an 8-point integration rule. (a) $\|\mathbf{J}\|$, $\beta = 0$, (b) RCS, $\beta = 0$, (c) $\|\mathbf{J}\|$, $\beta = 10$, (d) RCS, $\beta = 10$.

$\mathbf{J}_{Mie}/\|\mathbf{J}_{Mie}\|$. For the $i = 30$ rule, nothing is gained by addition of the penalty term; in fact, the error deteriorates as β is increased. For both the $i = 8$ and $i = 10$ rules, the solution error converges until $\beta \approx 10^2$, and then diverges. The nonmonotonic convergence can be understood by the spectral analysis in section 4.4. Initially, as β is increased, the higher order current modes are suppressed and the solution is perturbed toward the smooth (correct) solution. Once β reaches $\approx 10^2$, however, the magnitude of the penalty term is on par with that of the operator, and lower order eigenvalues of $\tilde{\mathbf{Z}}$ begin to be perturbed from their correct values.

Figure 4.8 shows pointwise absolute error $\|\mathbf{J}_{GMM}(\phi) - \mathbf{J}_{Mie}(\phi)\|$ of the compensated solution vs. the analytical Mie solution for the $i = 8$ rule. As β is increased, the modified operator produces successively smoother solutions. At $\beta \approx 10^2$, the penalty term begins to dominate the EFIE opera-

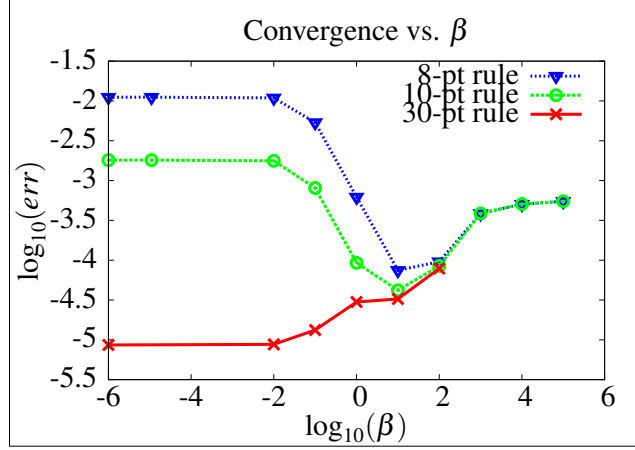


Figure 4.7: Convergence vs β in EFIE solution currents for $a = .5\lambda$ cylinder under TE^z illumination.

tor, and enforces a solution that is *too* smooth, i.e. sacrifices global error for continuity of currents between patches.

To further confirm the efficacy of the penalty function, the error between current expansions in patch overlaps for neighboring patches is examined next. Figure 4.9 shows convergence of the average absolute overlap error, defined as $\|\sum \gamma_{lk}(\mathbf{J}_l(\phi) - \mathbf{J}_k(\phi))\|/(N_{samp}N_p)$, $\forall \gamma_{lk} \in \gamma$, where N_{samp} is the total number of points used to sample the error in a single overlap and N_p is the total number of patches. In this test, $N_{samp} = 100$ was used. Unlike the total relative l_2 error shown in Fig. 4.7, convergence of the overlap error is monotonic. This further confirms that the action of the penalty function is to perturb the solution of the compensated EFIE variational problem toward a result that enforces continuity in patch overlaps.

Next, it is verified that the eigenvalues of the compensated moment method system follow the same trend for a non-canonical scatterer as for the canonical circular cylinder. To do so, scattering is computed from the $3\lambda \times 1.25\lambda$ teardrop-shaped scatterer shown in Fig. 4.10, demonstrates that the penalty method produces smoothed current solutions for non-canonical structures. The teardrop is discretized with $N_p = 25$ patches, each of which supports a $p = 5$ Legendre basis set. Figures 4.11(a),(b) show the surface current and RCS obtained using the uncompensated operator with an $i = 10$, and 4.11(c),(d) shows the same results for the compensated operator with $\beta = 10$.

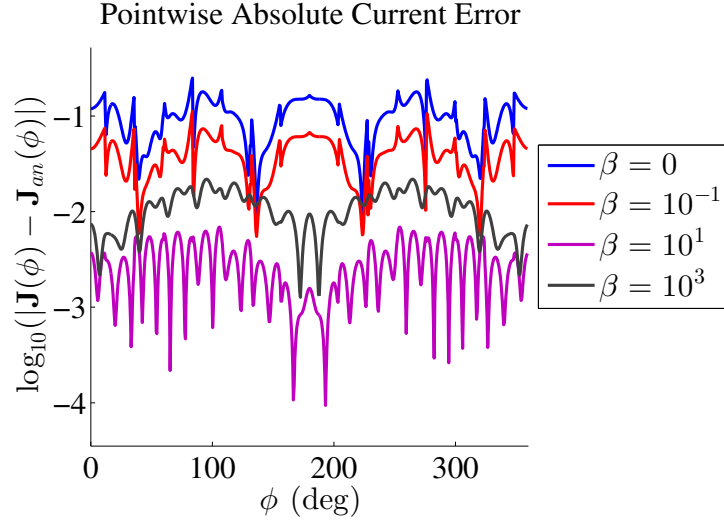


Figure 4.8: Pointwise absolute error over the cylinder scattering surface.

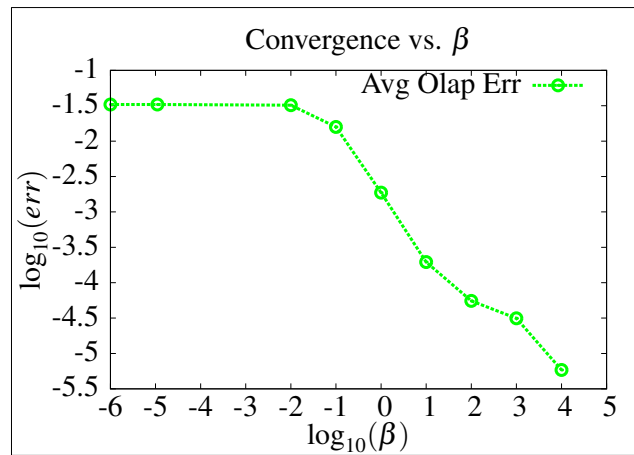


Figure 4.9: Convergence of absolute current error in patch overlaps vs. β .

The reference result is obtained using the same discretization with a high order ($i = 30$) rule that accurately integrates derivatives of the partition of unity. As with the circular cylinder result, the uncompensated operator with the $i = 10$ rule gives erroneous surface currents that exhibit spurious high and low frequency features, while the compensated operator gives results that are significantly smoother and more accurate.

Figure 4.12 shows generalized eigenvalues for the uncompensated and compensated GMM TE^z EFIE operator discretized on the teardrop shaped scatterer. As in the cylindrical case, the higher

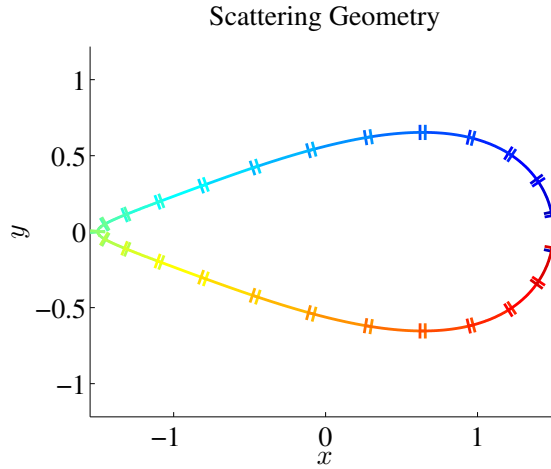


Figure 4.10: GMM patches for a teardrop shaped scatterer.

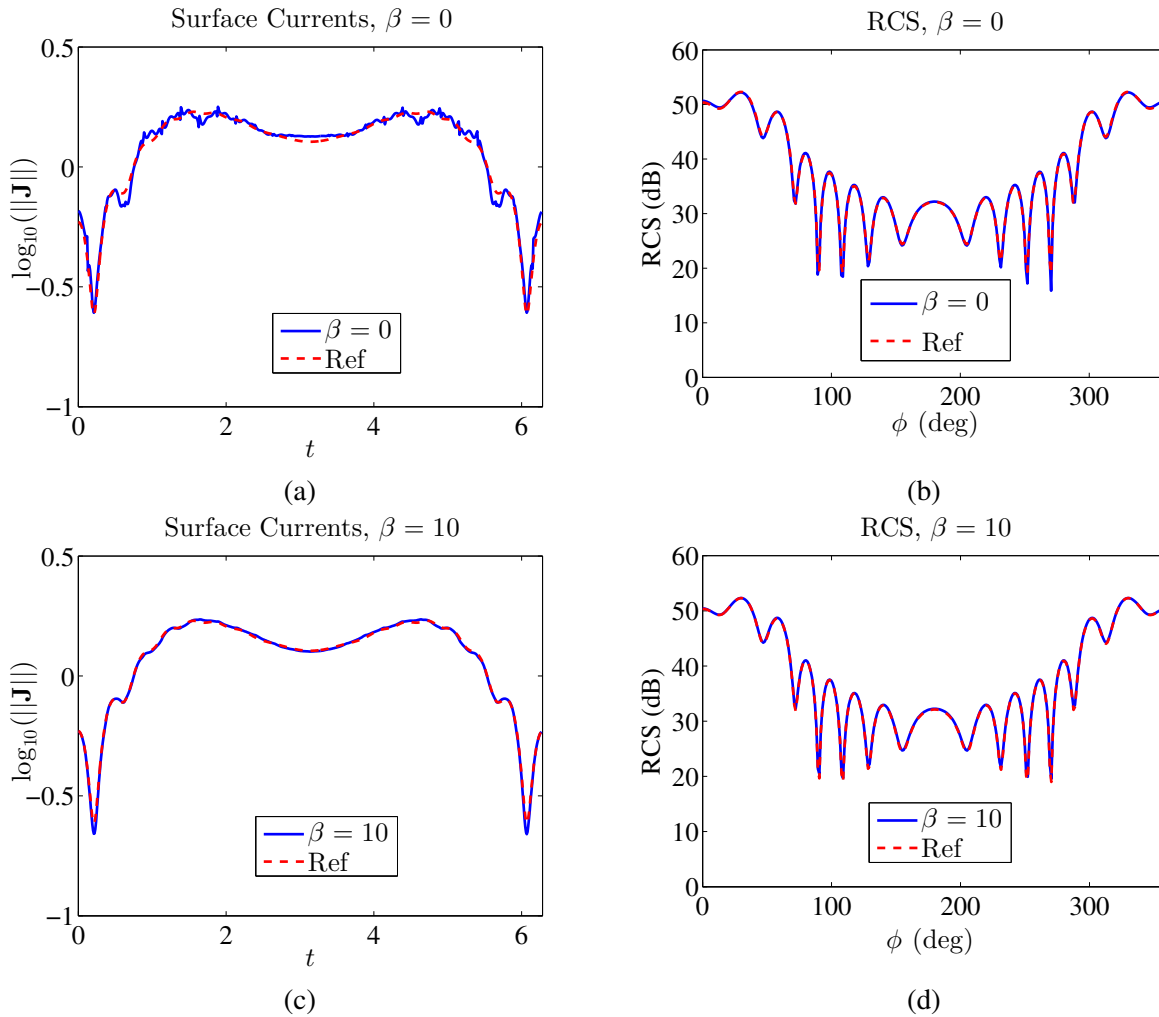


Figure 4.11: Comparison of reference ($i = 30$) and reconstructed currents/fields obtained using $i = 10$ rule for the 2λ teardrop scatterer.

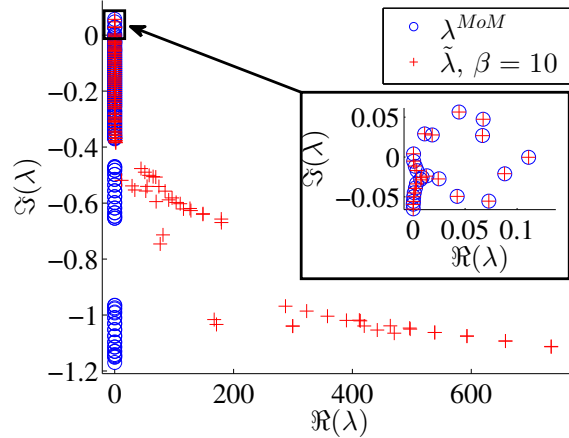


Figure 4.12: Generalized eigenvalues for the uncompensated and compensated GMM TE^z operator discretized on the teardrop shaped scatterer. Higher order eigenvalues of the compensated operator are shifted, while lower order eigenvalues (inset) are unaffected.

order eigenvalues of the uncompensated operator are significantly shifted by the penalty function, while the low order eigenvalues are quite stable (inset). The shifted eigenvalues effect the same regularization of currents for the arbitrarily shaped scatterer as for the canonical circular scatterer.

The final result, scattering from a $6\lambda \times 2\lambda$ ellipse, demonstrates that the penalty function formulation works for larger scatterers as well as the relatively small examples treated so far. The ellipse is discretized with 25 patches, each of which supports a $p = 5$ basis set. Figure 4.13 shows the patch discretization, and Fig. 4.14 shows the solution currents and RCS for the uncompensated and compensated operators. The solution of the compensated system shows considerably better matching in the currents and a more accurate RCS than does the uncompensated system.

4.6 Results in Three Dimensions

The conclusion that the penalty function compensates for insufficient integration is especially important when GMM is extended to the three dimensional case. This is because, in GMM, the transition maps between patches $\tau_{kl} : \Omega_l \rightarrow \Omega_k$ that are necessary to compute the partition of unity are nonlinear for curvilinear scattering geometries, and are therefore much harder to integrate [56]. As the results in this section show, application of the penalty function to the three dimensional

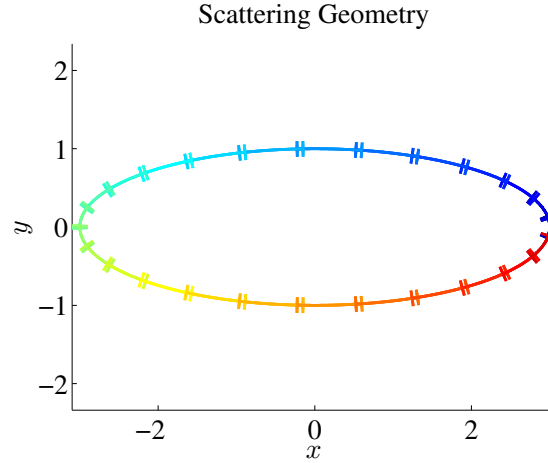


Figure 4.13: GMM patches for a $6\lambda \times 2\lambda$ elliptical scatterer.

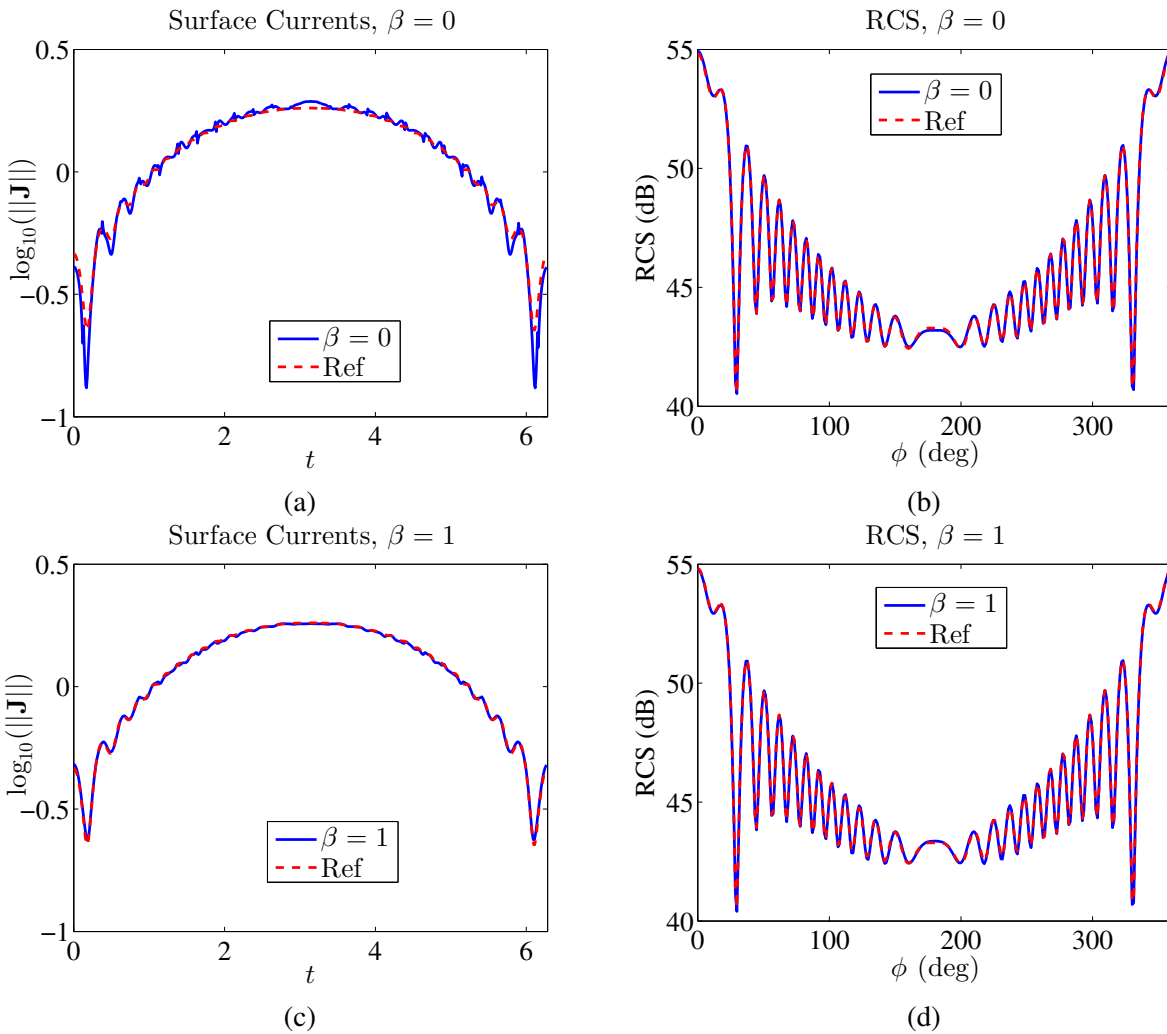


Figure 4.14: Comparison of reference ($i = 30$) and reconstructed currents and RCS obtained using $i = 10$ rule for the $6\lambda \times 2\lambda$ elliptical scatterer.

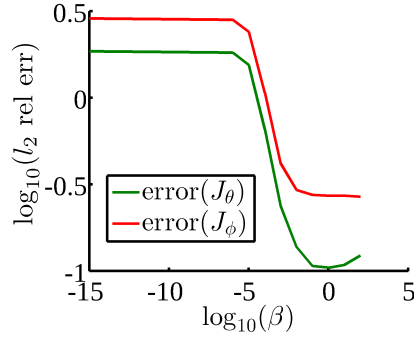


Figure 4.15: Convergence vs. β for a 1λ sphere, $p = 4$, $i = 5$ case.

case yields solutions that are both smoother and more accurate than for the EFIE alone. Investigation of the effect of the penalty function is performed for scattering from a sphere of radius 1λ discretized with $N_p = 43$ patches. Figure 4.15 shows convergence of surface current components vs. β compared with the analytical Mie series solution for the case where each patch supports a $p = 4$ Legendre basis set. The effect of the penalty constraint is clearly to drive the solution toward the continuous analytical solution, however, as in the two dimensional case the convergence is not monotonic. At approximately $\beta = 10$, the solution begins to diverge as the effect of the penalty matrix dominates that of the original moment method system. Figure 4.16 shows convergence for the same sphere, but with each patch supporting a $p = 7$ basis set. The penalty function again drives the GMM solution currents toward the analytical currents, but is able to obtain higher accuracy due to the higher order basis employed. Interestingly, the divergence of the solution happens at a higher value of β for the $p = 7$ case than for the $p = 4$ case.

The radiation from the spurious current features is negligible, as demonstrated the behavior of fields in the very near-field region of a scattering sphere discretized with a $p = 2$ Legendre basis. Figure 4.17 shows surface currents for the compensated GMM solution with $\beta = .1$ next to the analytical Mie series solution currents, as well as a comparison of analytical and numerically obtained fields at a height of $d = .1\lambda$ above the surface of the sphere. The numerical fields are computed using currents obtained via solution of the EFIE with $\beta = 0$ and $\beta = .1$. It is clear that the fields are essentially the same, although the uncompensated result does show some slight

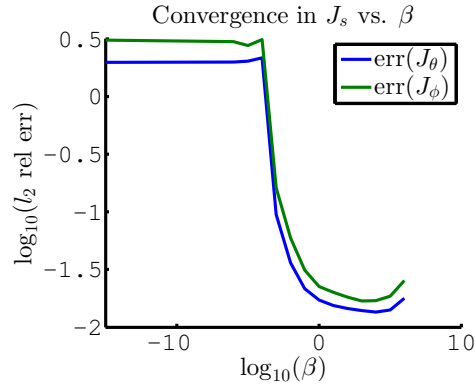


Figure 4.16: Convergence vs. β for $p = 7, i = 5$ case.

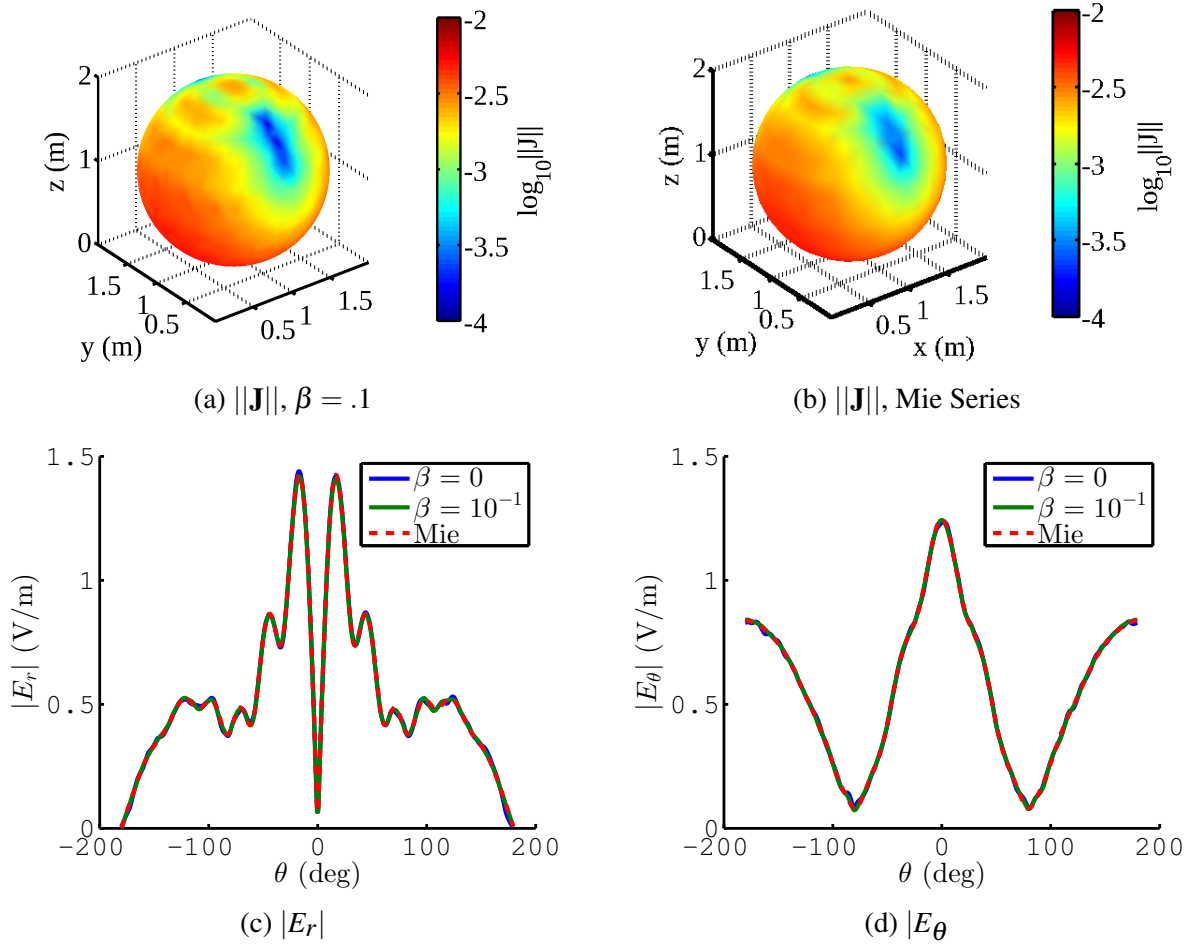


Figure 4.17: Comparison of analytical and reconstructed current obtained using 10-point integration rule.

Table 4.1: Iterations to convergence ($\tau = 10^{-3}$) vs. β_J in GMRES solver.

β_J	Iterations
0	183
10^{-1}	18
10^0	7
10^1	10
10^2	40

variation. This variation is, however, much smaller than the error in solution currents for the uncompensated operator (cf. Figs. 4.15,4.16). So, while the apparent errors in surface currents may be high, fields due to these errors are extremely tightly bound to the scatterer and effects on fields even in the extreme nearfield of the scatterer are minimal. Thus, if one is only interested in fields, especially fields in the far zone, the uncompensated operator may suffice, while if one is interested in current-dependent quantities such as feedpoint impedance, the addition of the penalty term is necessary.

Not only does the regularization of the penalty function give better accuracy in surface currents, it can also significantly reduce the number of iterations required for convergence in iterative solvers. To illustrate this, the EFIE was solved for a 1λ sphere with a high-order basis set of $p = 8$ Legendre polynomials on 47 patches for a total of 4230 basis functions, illuminated by an $\hat{\mathbf{x}}$ -polarized plane wave traveling in the $+\hat{\mathbf{z}}$ direction. Table 4.1 shows convergence in unpreconditioned GMRES (with convergence tolerance set to $\tau = 10^{-3}$) for various values of β_J . The penalty function clearly influences the number of iterations, although, as with error convergence there is a region of maximum benefit, in this case around $\beta = 1$.

4.7 Conclusion

The Generalized Method of Moments is a promising technique for discretizing electromagnetic and acoustic integral equations, but some operators, particularly those containing derivatives of the basis set, require high numerical quadrature orders. This chapter has investigated the effects of insufficient numerical quadrature on GMM solutions, and have proposed a penalty function

constraint that gives smooth, accurate solutions with significantly lower order quadrature rules than would otherwise be required. Through analytical and numerical examples, the effect of the penalty function on the operator has been detailed. The analysis in this chapter has been restricted to two dimensions to enable transparent analytical and numerical analysis, although the penalty method exhibits the same regularizing behavior in three dimensions as well. As is evident from the results presented above, the approach works for a range of problem sizes from sub-wavelength to many wavelengths. It seems that there is some dependence of the value of β on the wavelength, and although the development of theory to explain the relationship between β , k , and patch size is outside the scope of this chapter, it is a topic for future work. Other topics of future work include investigation of the interior penalty method for mixed discretizations and on large practical scattering targets using the Multilevel Fast Multipole Algorithm developed in Chapter 3, as well as a detailed study of the effect of the penalty term on convergence of iterative solvers.

CHAPTER 5

SCHWARZ-CHRISTOFFEL BASED PARTITIONS OF UNITY FOR THE GENERALIZED METHOD OF MOMENTS

5.1 Introduction

Past implementations of GMM have relied on nonsmooth partitions of unity that possess discontinuous derivatives. On curved surfaces, such nonsmooth partitions of unity lead to complicated piecewise continuous domains that are difficult to integrate; furthermore, the limited smoothness precludes the use of some basis sets (e.g. certain Helmholtz decompositions). This chapter proposes a means of defining arbitrarily smooth partitions of unity in the context of GMM through the use of Schwarz-Christoffel mapping, a method for conformal mapping between the unit disk and an arbitrary planar polygon.

Schwarz-Christoffel mapping is a classical technique first developed in the 1800s [88] for mapping between the half plane and regions bounded by a polygonal contour in the complex plane. Only a few Schwarz-Christoffel maps can be evaluated analytically, and it was not until the advent of robust numerical methods for evaluating Schwarz-Christoffel mappings [89] that Schwarz-Christoffel maps could be widely employed. Since then, the technique has been used to solve a range of problems in areas as varied as electrostatics [90], design of resistors with arbitrary polygonal cross-section [91], and fluid dynamics [92–94]. Recently, Schwarz-Christoffel mapping has been employed to evaluate integrations over irregular polygonal domains [95] with applications to crack interface problems in the Extended Finite Element Method [96].

Nonsmooth partitions of unity have been required in past GMM implementations because GMM patches are generally defined as projections from polygonal regions in a plane onto a higher order surface. The vertices of the polygonal domain of support are geometrically singular, which for the purposes of this chapter is defined as having a radius of curvature of $\rho = 0$. It is not generally possible to directly define smooth functions on a domain with a non-smooth boundary, so

GMM partitions of unity have hitherto been defined in a piecewise-smooth manner such that they exhibit discontinuous derivatives on a finite number of contours interior to the polygonal support. Schwarz-Christoffel mapping takes a function defined on a canonical smooth domain (in this case the unit disc) into a polygon with n vertices, and is smooth everywhere on the open disk. This property permits smooth partition of unity functions defined on the open unit disk to be taken smoothly into the polygonal support of GMM basis sets, yielding partitions of unity with continuous, smooth derivatives up to any desired degree. In this chapter, a Schwarz-Christoffel mapping is employed to effect smooth partitions of unity in the Generalized Method of Moments to solve both the Electric Field Integral Equation (EFIE) and Magnetic Field Integral Equation (MFIE) for electromagnetic scattering from arbitrary perfectly conducting objects. Because the EFIE discretized via GMM includes derivatives of the GMM basis set, the smooth partitions of unity are particularly useful.

The rest of the chapter is structured as follows. Section 5.2 gives a formal statement of the problem. Section 5.3 defines the Schwarz-Christoffel map, which is then used in a new a GMM formulation with arbitrarily smooth partitions of unity in section 5.4. Section 5.5 gives a generalized integration scheme that permits efficient evaluation of field integrals involving the smooth local partition of unity functions. Results demonstrating and validating the method are presented in section 2.5, and finally section 5.7 gives some concluding discussion and further directions.

5.2 Problem Statement: Nonsmooth Partitions of Unity

For reference, figure 5.1 recalls definitions and notations from Chapters 1 and 2 for the local coordinate systems, projection polygons, and transition maps. The partitions of unity employed in GMM are based on Shepard interpolation [49], in which the partition of unity on patch Ω_l is given by

$$\psi_l = \frac{\hat{\psi}_l}{\sum_{k \in \Lambda_l} \hat{\psi}_k} \quad (5.1)$$

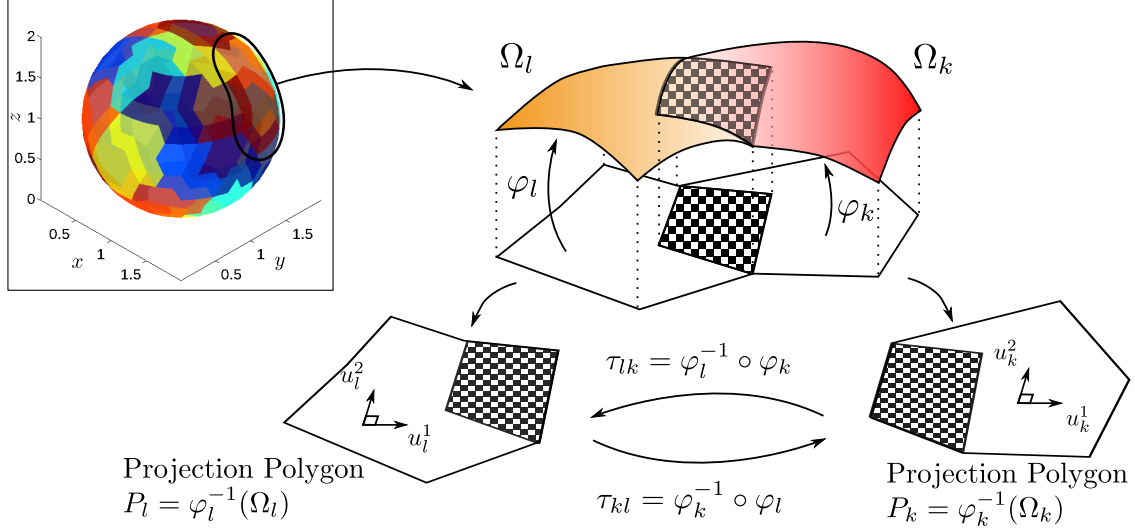


Figure 5.1: Two GMM patches and local (u^1, u^2) coordinate systems.

with Λ_l an index set containing all patches that intersect Ω_l , and $\hat{\psi}_k$ a local “sub-partition of unity” function (sub-PU) on patch Ω_k . In previous versions of GMM (cf. Chapter 2), these sub-partitions of unity were chosen to be linear nodal shape functions defined on a triangulation of the patch support. These functions have the property that they are zero at all exterior nodes and unity at all interior nodes, with linear variation from the edge to the first ring of interior nodes. Although such functions are smooth within each triangle, they are nonsmooth between triangles, and their derivatives are therefore discontinuous.

For the purpose of numerically integrating simplex partitions of unity, it is desirable that triangulations of overlapping patches are consistent in the sense that the image of one triangle under the transition function between the patches coincides exactly with a triangle in the overlapping patch. More formally, given two overlapping patches Ω_l and Ω_k , define a triangulation \mathcal{T}_l in the reference domain P_l and \mathcal{T}_k in the reference domain P_k . Then for a triangle $T_{li} \in \mathcal{T}_l$, it is desirable that the following condition hold:

$$\tau_{lk} \circ T_{li} = T_{jk}, \quad T_{jk} \in \mathcal{T}_k, \quad (5.2)$$

i.e. a triangle in \mathcal{T}_l maps exactly onto some triangle in \mathcal{T}_k . If φ_l and φ_k are GMM-style projection mappings, condition (5.2) can in general only be satisfied if the transition functions are affine

maps, e.g. they maintain straight lines and points. In GMM, the transition functions are only affine if 1) the normals of the projection planes P_l and P_k coincide (i.e. $\hat{\mathbf{n}}_l = \hat{\mathbf{n}}_k$), or if 2) the surface defined by φ_l is itself a triangulation consisting of piecewise flat triangles. When higher order surface parameterizations are used to define φ , the transition functions are in general not affine, and $\tau_{lk} \circ T_{il} \neq T_{jk}$.

Non-affine transition functions in GMM are problematic because the simple piecewise linear sub-partitions of unity exhibit complex non-smooth behavior when (5.1) is computed. To illustrate, consider figure 5.2, which shows the image of the triangle T_l under a non-affine transition mapping τ_{kl} . Because $\hat{\psi}_k(\mathbf{u}_k)$ is not smooth on the boundaries between triangles in \mathcal{T}_k , $\hat{\psi}_k(\tau_{lk} \circ T_l)$ is also non-smooth. The contours that define the non-smooth region in P_l are not linear, leading to a function $\psi_l(\mathbf{u}_l)$ that is practically impossible to numerically integrate using standard Gauss-type rules over the triangle T_l . The problem is particularly pronounced in the derivative of the partition of unity, which is required when solving the EFIE. Figure 5.3 illustrates the non-smooth derivatives that result from a nonlinear transition function.

If the transition maps are nonlinear but close to affine, then they may be approximated by affine maps with reasonable control over error. Past implementations of GMM that employed higher order surfaces utilized this approximation, i.e. that the higher order surface could be sufficiently approximated by a low order surface so that the non-affine transition functions could be replaced by approximate affine transition functions. If such a level of approximation is not permissible given either the desired accuracy in solution or because the surface description in the vicinity of a patch overlap is highly nonlinear, then the full nonlinear transition functions must be employed. In this case it is not possible to utilize simple piecewise linear sub-partitions of unity due to their nonsmooth behavior, and a means of defining smooth partitions of unity must be found. The main contribution of this chapter is to develop globally smooth sub-partitions of unity that remain smooth under any smooth transition mapping.

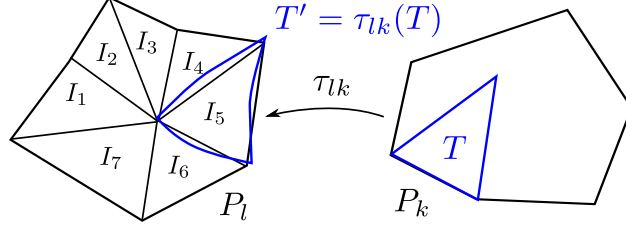


Figure 5.2: Image of a triangle T_l under a non-affine transition function τ_{kl} .

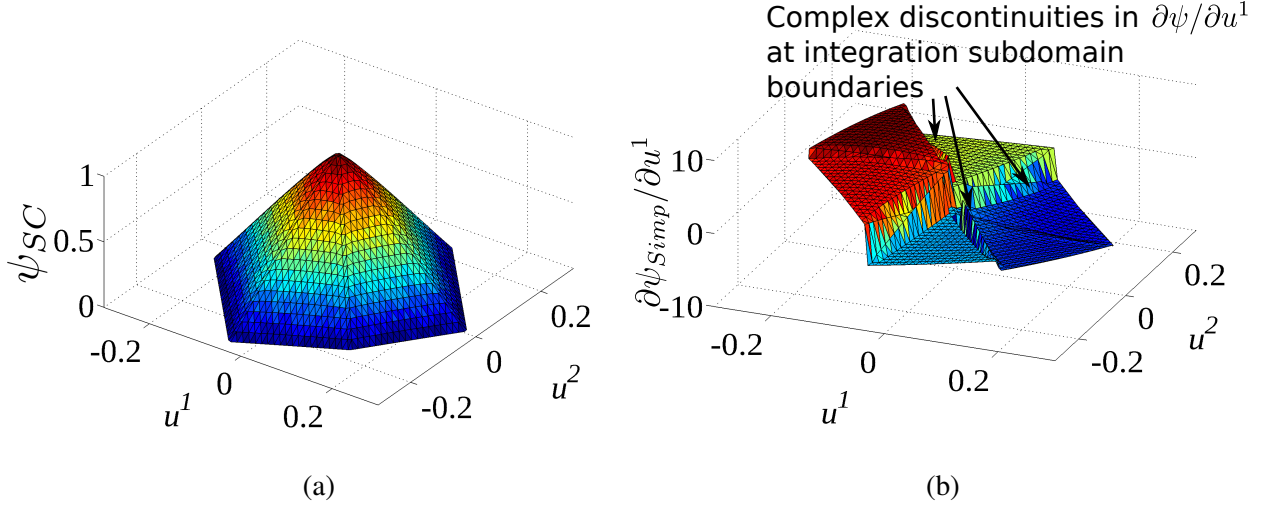


Figure 5.3: Simplex-based PU and derivative with non-affine transition functions.

5.3 Schwarz-Christoffel Mapping

Due to the polygonal shape of the reference domain, P_l , it is not possible to directly define functions that are smooth everywhere away from the polygon vertices. Instead, an additional mapping is introduced for the purposes of defining smooth sub-partitions of unity $\hat{\psi}_l$, namely the Schwarz-Christoffel map. A Schwarz-Christoffel map is a conformal mapping from a canonical domain (e.g. the upper half plane or the unit disk) to a polygon P in the complex plane defined by set of vertices $\{w_k\}$, $k = 1, \dots, n$, with $w = u^1 + ju^2$. This work utilizes the closed unit disk \bar{D} as the canonical domain in the complex z , for which the Schwarz-Christoffel map $w = f(z)$ is written as:

$$w(z) = f(z) = C \int_{z_0}^z \prod_{k=1}^n \left(1 - \frac{\zeta}{z_k}\right)^{1-\alpha_k-1} d\zeta, \quad (5.3)$$

where C is a complex constant, $z_0 \in \bar{D}$ is an arbitrary starting point, and the set of prevertices $\{z_k\}$ are the preimages of the vertices w_k , i.e. $f(z_k) = w_k$. The prevertices reside on the boundary of

the closed unit disk. Each of the terms α_k in the exponents of (5.3) is defined as ϕ_k/π , with ϕ_k the interior angle formed by the two polygon sides incident upon the vertex w_k . For the polygons that appear in GMM discretizations, $0 < \alpha_k < 2$; i.e polygons with degenerate sides or vertices at infinity do not occur. Furthermore, since GMM polygonal domains are closed,

$$\sum_{n=1}^n (1 - \alpha_k) = 2. \quad (5.4)$$

Since the $\{\alpha_k\}$ are in general not integers, the integrand of (5.3) contains branch-point singularities at the prevertices $\{z_k\}$; specialized Gauss-Jacobi quadrature rules have been developed to handle the evaluation of (5.3) in the vicinity of these singularities [89]. For all but a few canonically shaped polygons, a nonlinear optimization problem (the “parameter problem”) must be solved once to extract the prevertex locations. Once the prevertices are obtained, they may be stored for use in all subsequent evaluations of (5.3).

Also necessary for implementation in GMM is the inverse Schwarz-Christoffel map $z = f^{-1}(w)$, which is obtained by solving

$$\frac{dz}{dw} = \frac{1}{C} \prod_{k=1}^n \left(1 - \frac{z}{z_k}\right)^{1-\alpha_k}. \quad (5.5)$$

Equation (5.5) is a nonlinear ordinary differential equation. Efficient, stable numerical techniques for evaluating (5.3), (5.5), and the parameter problem are well known [88] and implemented in the software libraries SCPACK [89] for Fortran and the SC-Toolbox [1] in Matlab. Implementation of the Schwarz-Christoffel map in this chapter is built upon a modified version of [89]. Figure 5.4 shows an example Schwarz-Christoffel mapping from the unit disk to a polygonal domain.

5.4 Schwarz-Christoffel GMM

The key property of the Schwarz-Christoffel for GMM is that it is conformal, and is therefore analytic everywhere in the open unit disk D . Branch points occur at the prevertex locations $\{z_k\}$, but these are restricted to the boundary of \bar{D} , and are therefore outside of the domain of GMM basis functions as long as the partition of unity and its first derivative are zero on the boundary of \bar{D} . The branch cuts corresponding to the branch points located at $\{z_k\}$ are taken so that they do not

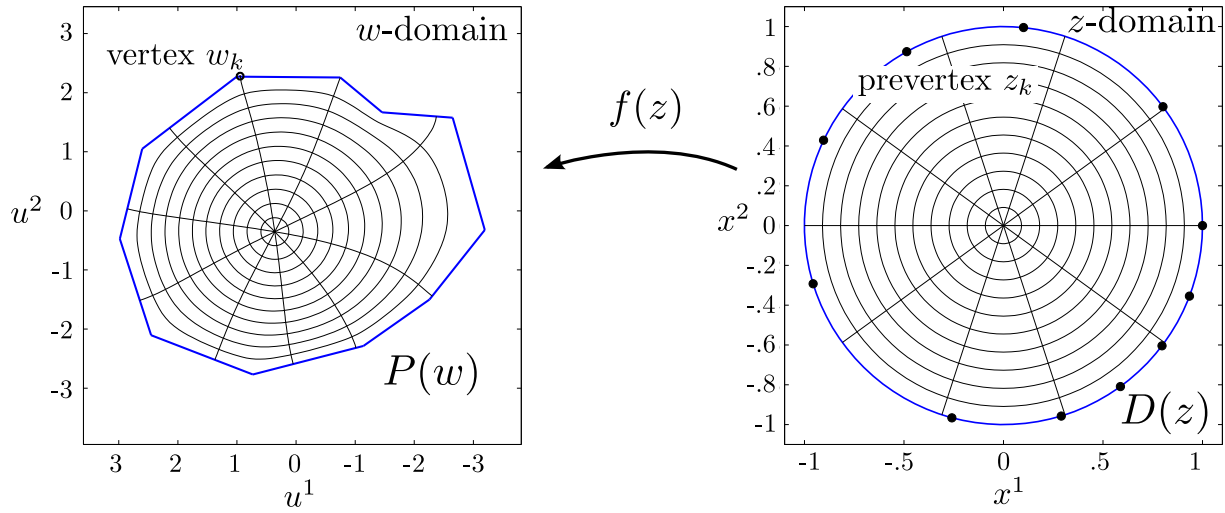


Figure 5.4: Schwarz-Christoffel mapping from canonical disc D to polygon P (plot generated using Matlab SC Toolbox [1]).

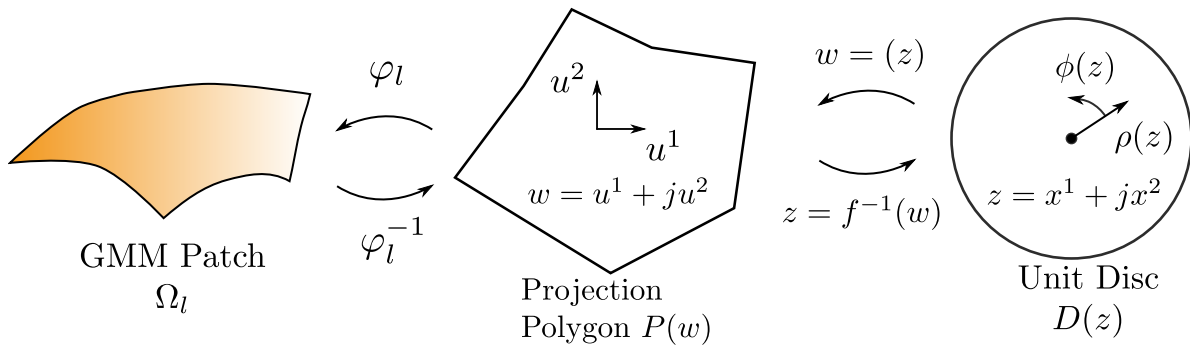


Figure 5.5: Schwartz-Christoffel mapping in u^1, u^2 plane permits definition of arbitrarily smooth partitions of unity.

intersect D . Due to the analyticity of the Schwarz-Christoffel map, any smooth function defined on D (instead of \bar{D}) retains its smoothness under the Schwarz-Christoffel mapping. This property allows the construction of a GMM based on arbitrarily smooth partitions of unity.

Smooth partitions of unity are defined using smooth sub-partitions of unity as follows. For a patch Ω_l with associated polygonal reference domain P_l , a Schwarz-Christoffel mapping is defined from the open unit disk D to P_l . Figure 5.5 illustrates the composition of maps. A function $\tilde{\psi}(\rho)$, $\rho = |z|$ with local support and the desired degree of smoothness (up to k) derivatives is defined in D . Any smooth function with local support may be utilized. The two functions used in this chapter are a polynomial sub-partition of unity $\tilde{\psi}(\rho) = h(\rho)$, with $h(t)$ defined as

$$h(t) = \begin{cases} (1-t^{\beta_1})^{\beta_2}, & 0 \leq t < 1, \beta_1, \beta_2 \in \mathbb{Z} \\ 0, & t \geq 1. \end{cases} \quad (5.6)$$

and a sub-partition of unity based on the exponentially decaying “bump function” $\tilde{\psi}(\rho) = g(\rho)$, defined as:

$$g(t) = e^{\frac{1}{1-(t)^2}+1}, \quad |t| \leq 1 \quad (5.7)$$

In this work, (5.6) is primarily used, although (5.7) is included for completeness in convergence tests in the results section. A plot of (5.6) with $\beta_1 = 5, \beta_2 = 4$ is shown in figure 5.6. Figure 5.7 shows the smooth sub-PU $h(\rho)$ mapped from D to a polygonal domain $P(w)$.

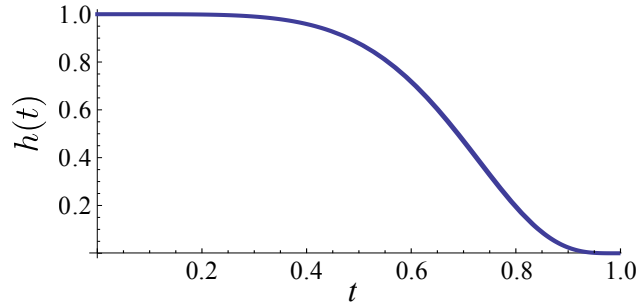


Figure 5.6: Polynomial sub-partition of unity function.

In GMM the approximation function spaces, geometrical parameterization, and integration rules are computed with respect to the (u^1, u^2) coordinate system. It is therefore necessary evaluate

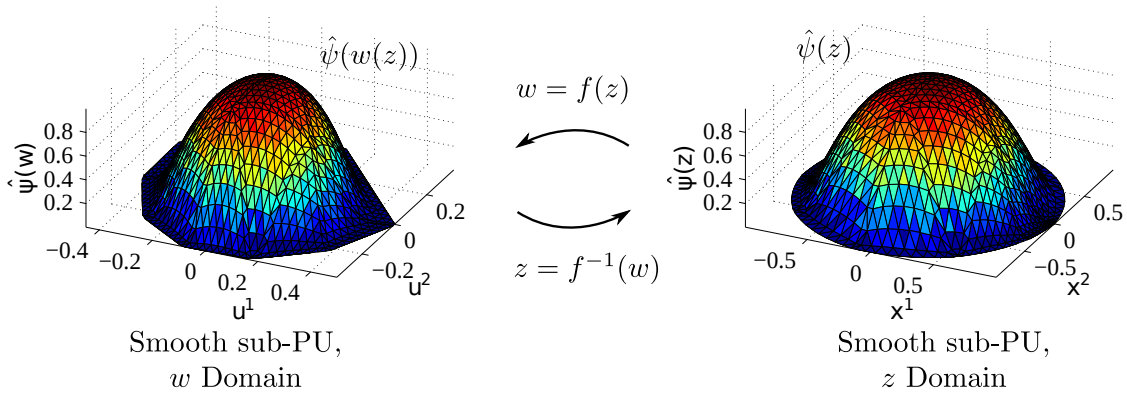


Figure 5.7: Smooth sub-partition of unity mapped from $D(z)$ to projection polygon $P(w)$ via Schwarz-Christoffel map.

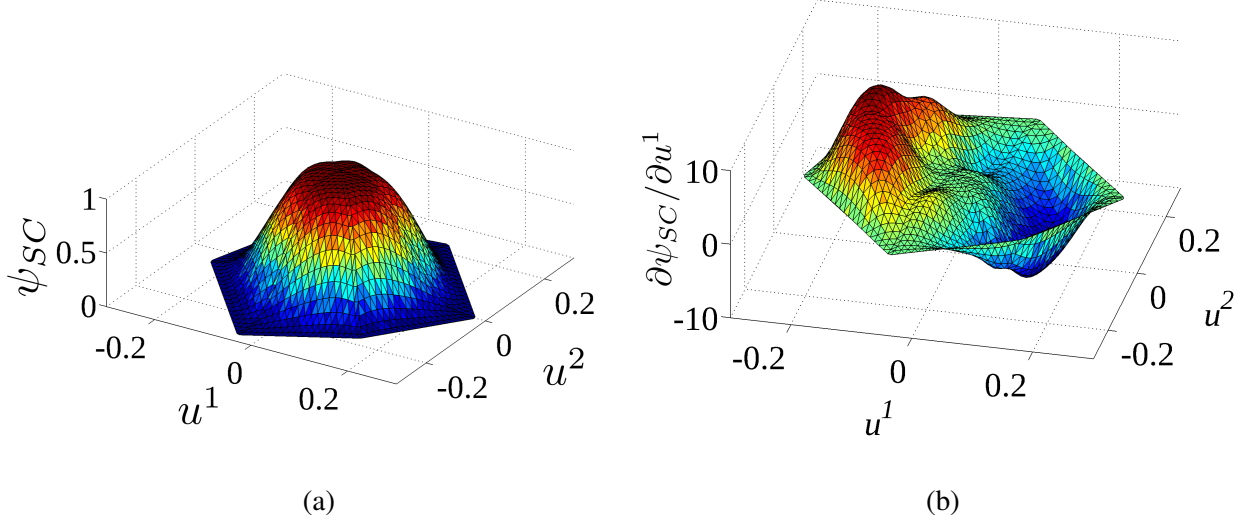


Figure 5.8: Smooth partition of unity $\psi(u^1, u^2)$, $(u^1, u^2) \in P$ constructed from smooth sub-partitions of unity mapped using Schwarz-Christoffel mapping. (a) Partition of unity ψ . (b) Derivative $\partial\psi/\partial u^1$.

the partitions of unity as:

$$\psi(u^1, u^2) = \psi(\rho(u^1, u^2)), \quad (5.8)$$

where $\rho(u^1, u^2) = |z(w)|$, with $z(w)$ obtained through the numerical solution of (5.5). While transition functions for the main GMM algorithm remain unchanged, augmented transition functions for the partition of unity are given by:

$$\tau_{\psi, lk} = f_l^{-1} \circ \tau_{lk} \circ f_k. \quad (5.9)$$

The \mathcal{T} operator in (1.19) requires derivatives of the basis set, which must be evaluated with respect to the u^1, u^2 coordinate system. Derivatives of the partition of unity are constructed using a quotient rule applied to (5.1), which requires derivatives of the sub-partitions given by:

$$\begin{bmatrix} \frac{\partial \hat{\psi}}{\partial u^1} \\ \frac{\partial \hat{\psi}}{\partial u^2} \end{bmatrix} = \tilde{J} \begin{bmatrix} \frac{x}{\rho} \\ \frac{y}{\rho} \end{bmatrix} \frac{\partial \hat{\psi}(\rho)}{\partial \rho} \quad (5.10a)$$

where \tilde{J} is the Jacobian of the Schwarz-Christoffel map. Full evaluation of derivatives on the scattering surface with respect to (u^1, u^2) requires additional Jacobians of the mapping ϕ_l as well

as of the transition functions τ_{lk} between patches; these have been addressed in [56], and are omitted here for clarity. The Jacobian \tilde{J} of the Schwarz-Christoffel map is given explicitly by:

$$\tilde{J} = \begin{bmatrix} \frac{\partial x}{\partial u^1} & \frac{\partial y}{\partial u^1} \\ \frac{\partial x}{\partial u^2} & \frac{\partial y}{\partial u^2} \end{bmatrix} = \frac{1}{\left|\frac{\partial w}{\partial z}\right|^2} \begin{bmatrix} \Re\left\{\frac{\partial w}{\partial z}\right\} & \Im\left\{\frac{\partial w}{\partial z}\right\} \\ -\Im\left\{\frac{\partial w}{\partial z}\right\} & \Re\left\{\frac{\partial w}{\partial z}\right\} \end{bmatrix}, \quad (5.11)$$

where $\partial w/\partial z$ is the integrand of (5.3). The formula (5.11) may be verified using the Cauchy-Riemann relations [4] applied to the derivatives of (5.3). Although the derivatives $\partial w/\partial z$ in (5.11) exhibit branch-type singularities and may be unbounded in modulus near irregular vertices, it can be shown that as long as either (5.6) with $\beta_1, \beta_2 > 0$ or (5.7) is used as the sub-partition of unity, (5.11) is nonsingular. Since any practical implementation of the method uses $\beta_1, \beta_2 > 1$, the derivatives of the Schwarz-Christoffel partitions of unity are well-behaved everywhere on the open unit disk D for all cases of interest.

Practical implementation of Schwarz-Christoffel GMM requires a precomputation step that identifies patches with highly nonlinear transition functions and definition of the Schwarz-Christoffel maps. A unique Schwarz-Christoffel map f_l is constructed for each designated patch, including solution of the parameter problem and storing the prevertices $\{z_k\}$, the exponents $\{a_k\}$ and the constant C . At run time, these parameters are recalled and passed to the appropriate SCPACK routines to compute either the map or its inverse.

5.5 Evaluation of Field Integrals via Generalized Quadrature

The procedure outlined in the preceding section produces partitions of unity that are smooth, and therefore integrable. However, because the partition of unity is a ratio of nonlinear functions, and because the sub-partitions of unity are not polynomial with respect to the (u^1, u^2) coordinate system (due to the Schwarz-Christoffel mapping), (5.1) can be costly to integrate using traditional Gauss-Legendre integration. To remedy this problem, the present method adopts a modified approach based on [97] and [98] to precompute generalized quadrature rules on a patch-by-patch basis.

Here the algorithm is briefly sketched; see [97] for more details for the 1 dimensional case. For each triangle $T_{il} \subset P_l$, first compute an adaptive quadrature rule for functions of the form $\psi_l \phi_i(u^1, u^2)$, with $\phi_i = (u^1)^m (u^2)^n$, $m = 0, \dots, M$, $n = 0, \dots, N$ and M, N are chosen so that the elementary monomials $(u^1)^m (u^2)^n$ interpolate the integrands in (1.19) of non-self integrations to prescribed accuracy. For basis functions of non-polynomial classes, different elementary functions may be chosen as appropriate. The adaptive rule is constructed by defining successively higher order Gauss-Legendre rules on T_{il} up to some maximum order N_{max} , after which the triangle is subdivided into four subtriangles and the procedure is repeated recursively on each subtriangle until the desired convergence is obtained. Fig. 5.9(a) shows an adaptive rule defined for a patch tessellated with 13 triangles. The adaptive rule converged to a relative error of $\varepsilon = 10^{-5}$, with $\varepsilon = (I_k - I_{k-1})/I_{k-1}$ for the k th refinement step. The total order of the adaptive quadrature rule over the patch is $N_{adapt} = 2148$.

To extract the generalized quadrature rule, the generalized Vandermonde matrix is constructed from the elementary functions as

$$V_{ij} = \sqrt{w_j} \phi_i(u_j^1, u_j^2) \psi(u_j^1, u_j^2), \quad k = 1, 2. \quad (5.12)$$

with (u_j^1, u_j^2) and w_j the j th quadrature abscissa and weight, respectively. Because the dimension of V is $N_{adapt} \times k$, (with $k = M \times N$), the matrix V contains at most $M \times N$ linearly independent rows, which implies that a quadrature rule of order $M \times N$ may be constructed that yields precisely the same result as the high order quadrature rule. In practice, this rule is extracted using a QR decomposition [97]. It is possible to further reduce the dimension of this quadrature rule using nonlinear optimization [97], but the savings are substantial enough using only the QR factorization that implementation of the optimization step is unnecessary. Using the QR-based approach, the number of quadrature points for the example in figure 5.9 is reduced from 2218 for the adaptive rule to 117 (9/triangle) for the generalized quadrature rule with $M, N = 3$. For a given solution, these quadrature rules are precomputed and stored for each triangle, and then accessed at run time. If the EFIE is being solved it is necessary to repeat the procedure for the derivatives of the partition of unity, i.e. rules must be computed using the Vandermonde matrices with entries

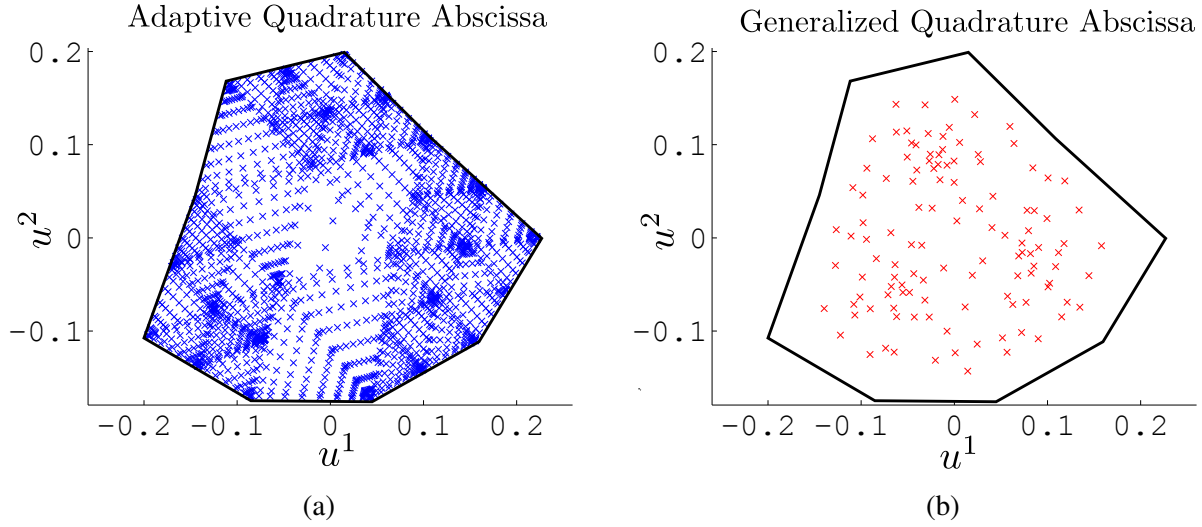


Figure 5.9: Illustration of reduction in number of quadrature abscissa between adaptive and generalized quadrature schemes. (a) Adaptive quadrature nodes for a patch. Convergence of integrations to relative error of 10^{-5} requires 2148 points. (b) Generalized PU-Chebyshev quadrature nodes for a patch. Only 117 points are required for same accuracy.

$$\tilde{V}_{ij}^k = \sqrt{w_j} \phi_i(u_j^1, u_j^2) \frac{\partial \psi(u_j^1, u_j^2)}{\partial u^k}, \quad k = 1, 2. \quad (5.13)$$

Forming the generalized quadrature rules on a triangle-by-triangle basis permits the use of standard triangle-based GMM integration strategies for singular self and near integrations [99, 100]. The cost of computing singular rules scales as $\mathcal{O}(N)$ in the number of basis functions, and is therefore the same as the cost of computing generalized quadrature rules, so there is no advantage to precomputing singular rules; furthermore, the storage for singular rules would be prohibitive. Singular integrations are therefore performed at run time without recourse to generalized quadrature for source integrations, and generalized quadrature rules are used for testing integrals and for non-self source interactions. When singularity cancellation techniques that require subdivision of a triangle about the projection of testing point are used, the precomputed generalized testing rules afford a significant benefit due to the large reduction in the number of testing points that must be projected, which greatly reduces the number of singular rules that must be computed at run time.

5.6 Results

This section gives results demonstrating the proposed method for a variety of scattering geometries and examining convergence of the generalized quadrature scheme relative to direct and adaptive schemes. For all scattering results, the excitation is a unit amplitude x -polarized plane wave traveling in the $+z$ direction.

The first set of results motivates the need for the smooth partition of unity by demonstrating the failure of quadrature rules to correctly integrate the simplex partition of unity. Figure 5.10a shows convergence in relative error in the integration of the partition of unity and its derivatives (taken for the i th step as $(I_i - I_{i-1})/I_i$), with I_i the integral of the partition of unity or one of its derivatives with rule i , which is indexed to the total number of quadrature points N_q . Integrations are performed on a single patch comprised of 10 triangles that resides on the south pole of a 1λ sphere, and the tensor product type rules from [101] were employed. Although the integrations initially appear to converge, as the order is increased, the integrations diverge at approximately 40-50 abscissas/triangle (i.e. a 6-7th order integration rule). The divergence occurs because of the nonsmooth behavior of the partition of unity near the edges of the triangles; this behavior is missed by the lower order rules, but is detected by the higher order rules with points close to the edges of the triangles. The effect is particularly marked in the derivatives of the partition of unity, which are completely corrupted by the discontinuities in the simplex partition of unity derivatives.

Figures 5.10b, 5.10c and 5.10d show the same test for the Schwarz-Christoffel based partition of unity. Although convergence is slower for the smooth partition of unity and there is some oscillation in convergence, there is overall no divergence of the integral value as the quadrature rule is increased to the same orders as in the simplex partition of unity test. Several different orders of polynomial sub-partitions of unity are used in this study as well as a partition of unity based on the bump function. In practice, the use of generalized quadrature rules based on adaptive rules greatly reduces the number of integration points required for field integrations to N points per triangle (with N the number of basis functions supported on the triangle), so the total number of quadrature points used in practice is significantly less than that used in figures 5.10b-5.10d.

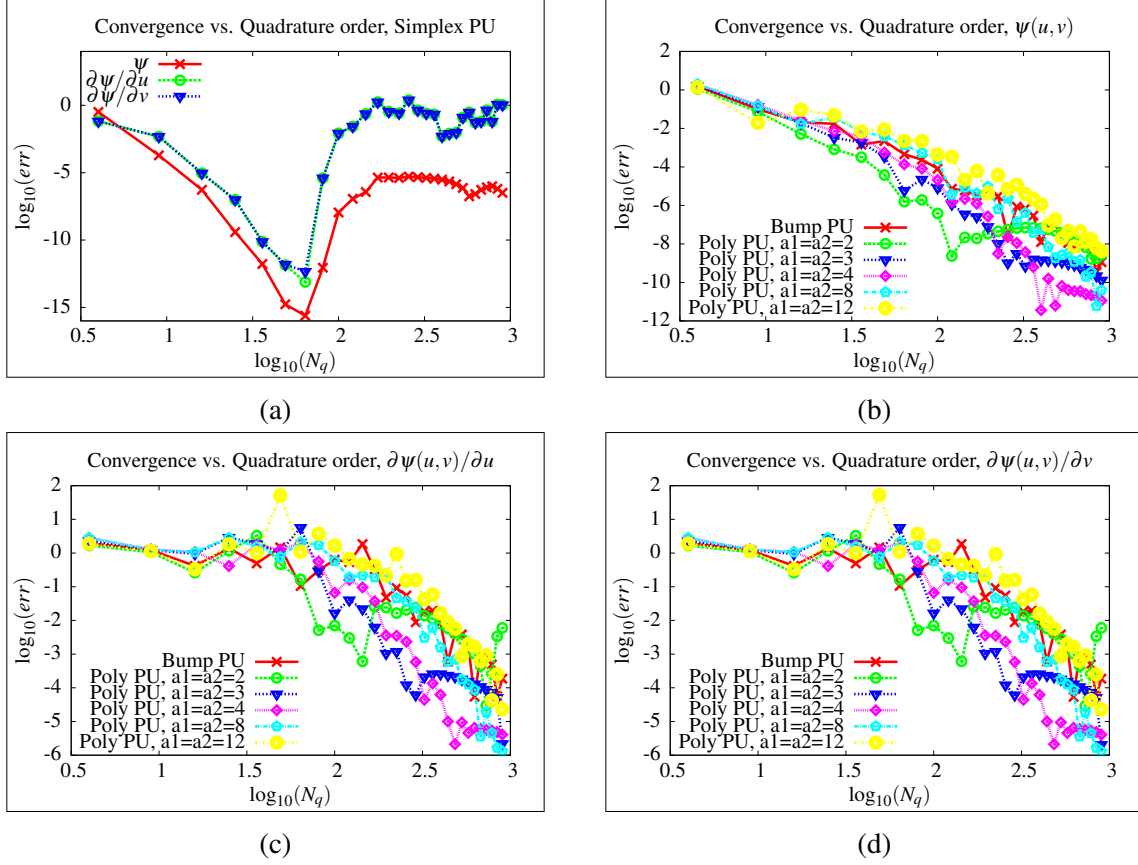


Figure 5.10: Convergence of integrations of simplex and Schwarz-Christoffel mapped partitions of unity vs. number of quadrature points N_q . (a) Simplex partition of unity and divergence. (b) Schwarz-Christoffel partition of unity ψ_{SC} . (c) $\partial\psi_{SC}/\partial u^1$. (d) $\partial\psi_{SC}/\partial u^2$.

The first result is scattering from a $.5\lambda$ sphere computed using the MFIE ($\alpha = 0.0$ in (1.18)). The sphere is discretized with $.3\lambda$ spherical sector patches (so that the geometry is a perfect sphere), each of which supports a $p = 2$ Legendre basis. The RCS shown in figure 5.11 is taken in the $\phi = 0^\circ$ cut. The RCS obtained using Schwarz-Christoffel GMM exhibits good matching with the analytical Mie series result. Generalized quadrature is used for this result; the original adaptive rule required 291654 points, while the total number of generalized quadrature points is 16272, a reduction of 94.42%.

Figure 5.12 shows the bistatic RCS for a 1λ sphere computed using the EFIE ($\alpha = 1.0$ in (1.18)), and figure 5.13 shows a comparison of the analytical and numerically obtained surface currents. In this case, the sphere was discretized using 306 patches and a $p = 2$ Legendre basis.

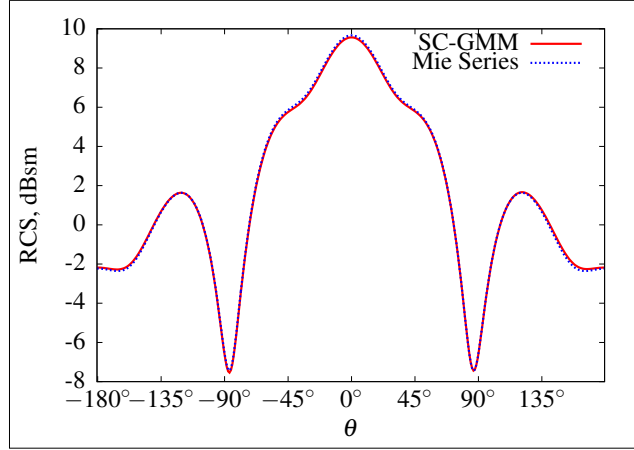


Figure 5.11: Bistatic RCS ($\phi = 0^\circ$ cut) for a $.5\lambda$ sphere discretized with smooth SC-GMM basis, MFIE solution.

Instead of utilizing generalized quadrature rules, this solution instead employs high-order Gauss-Legendre tensor product rules (256 points/triangle) and the constraint scheme developed in chapter 4 with a penalty factor $\beta = 1$ to smooth currents. Matching is again quite good between analytical and the numerical result in both bistatic RCS (Fig. 5.12) and surface currents (Fig. 5.13). Total l_2 relative error in the currents is $\epsilon_{\text{rel}} = 5.39 \times 10^{-2}$, with $\epsilon_{\text{rel}} = \|\mathbf{J}_{GMM} - \mathbf{J}_{\text{Mie}}\| / \|\mathbf{J}_{\text{Mie}}\|$.

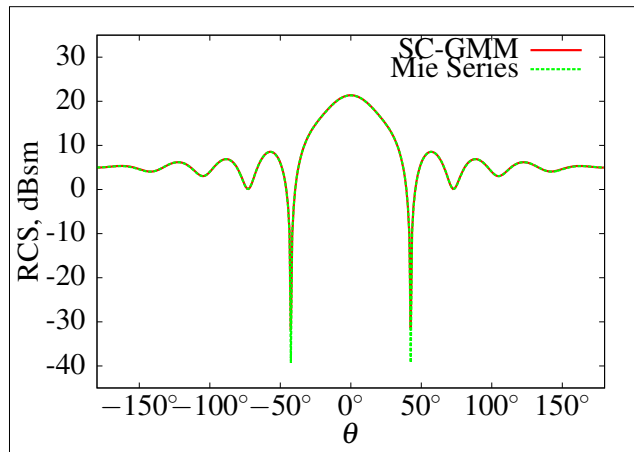


Figure 5.12: Bistatic RCS ($\phi = 0^\circ$) for a 1λ sphere, smooth SC-GMM basis, EFIE solution.

The final scattering result is scattering from $2\lambda \times 1\lambda \times .5\lambda$ PEC ellipsoid, which contains regions of higher curvature on the sides and the ends. The solution was obtained using the MFIE, and the GMM discretization of the ellipsoid contains 147 3rd order polynomial patches, each of

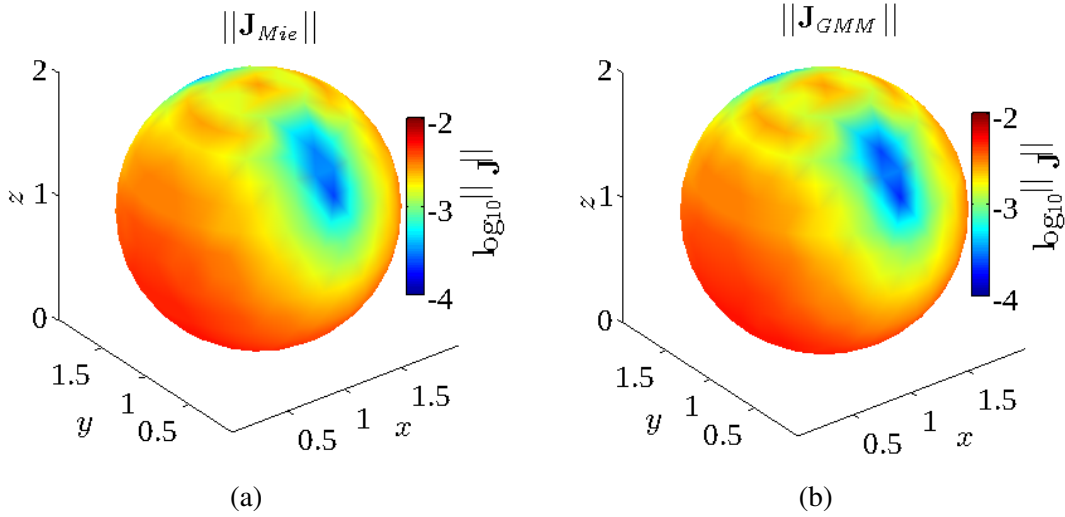


Figure 5.13: Surface current density ($\|\mathbf{J}\|$) for a 1λ sphere illuminated by an x -polarized plane wave travelling in the $+z$ direction. (a) Mie series solution. (b) SCGMM solution using the EFIE.

which supports a $p = 2$ Legendre basis. Two partition of unity configurations are used. The first uses the Schwarz-Christoffel mapping everywhere on the scatterer, with 17,307 generalized points required to accurately integrate the partition of unity to six significant digits, versus 305,613 points for the adaptive rule. The second configuration uses a mixed partition of unity, with simplex partitions of unity utilized on the flatter portions and Schwarz-Christoffel partitions of unity on the curved sides and ends. Fig. 5.14 shows the locations of GMM patches with the different partition of unity types for the mixed result. The mixed result uses a standard 12-point Gauss-Legendre rule on patches that only overlapped simplex patches, and generalized rules on all other patches. With a 43,488 standard + 6,435 generalized = 49923 total quadrature points, the mixed result uses approximately three times the number of points for the all Schwarz-Christoffel partition of unity. However, the time to precompute quadrature rules for the mixed scheme was 247s vs. 749s for the all Schwarz-Christoffel discretization.

Fig. 5.15 shows the bistatic RCS for both GMM partition of unity configurations and an RWG reference result. The matching is quite good, and it is evident that the mixed discretization introduces no additional error into the solution.

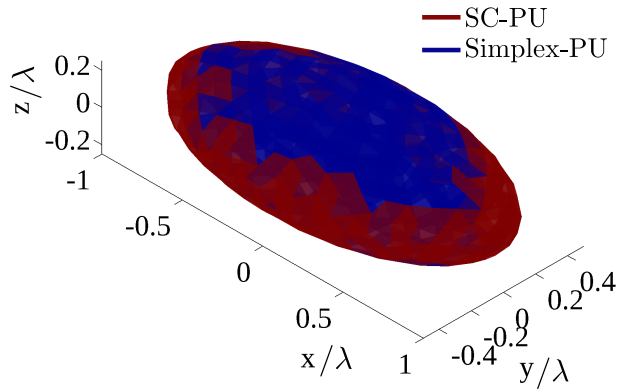


Figure 5.14: Mixed Schwarz-Christoffel/simplex partition of unity scheme for the 2λ ellipsoid.

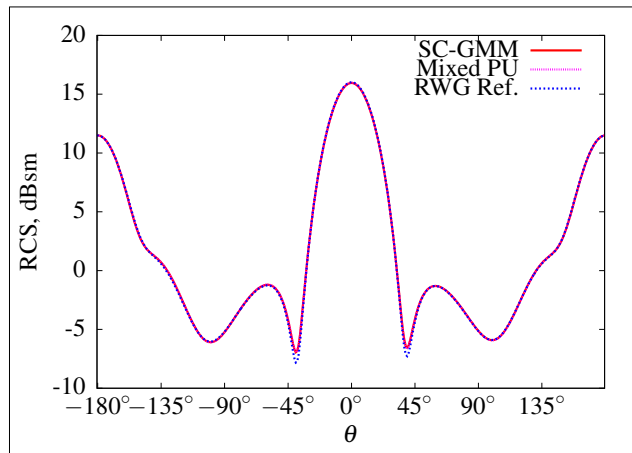


Figure 5.15: Bistatic RCS ($\phi = 0^\circ$) for the 2λ ellipsoid, MFIE solution.

5.7 Discussion and Conclusions

When GMM transition maps are highly non-linear, and in particular, far from affine, integrals of piecewise smooth partitions of unity are extremely difficult to evaluate using standard numerical quadrature. This chapter has proposed the use of Schwarz-Christoffel maps to define partitions of unity with any desired degree of smoothness. Results show that the method is capable of accurately solving both the MFIE and the EFIE on PEC scattering targets; however, the method is quite general and can be used for any integral equation formulation that admits a GMM discretization. The cost of evaluating the smooth partitions of unity is necessarily somewhat higher than the

cost of the simplex partition of unity due to evaluation of the Schwarz-Christoffel mapping. This suggests that the simplex-based partition of unity should be used when possible, and the Schwarz-Christoffel partition of unity only where the curvature of the surface is high. Although these new partitions of unity are smooth and therefore theoretically integrable using numerical quadrature, in practice their rational form and nonlinearity require very high order quadrature rules for accurate integration. To reduce this cost, generalized quadrature rules were employed that intrinsically integrate the partition of unity to desired precision. These rules may themselves be relatively costly to compute since they rely on an initial adaptive quadrature rule that can be quite dense. However, the computation of the generalized rules scales linearly with the number of patches, and therefore is asymptotically far less costly than using the dense quadrature rules to compute field elements, which scales quadratically in both the number of patches and the number of basis functions. If a mixed Schwarz-Christoffel/simplex partition of unity approach is adopted, the setup cost is further reduced. It is possible that the cost of precomputing the rules could be significantly reduced through hierarchical rule aggregation; this is a topic of future research.

CHAPTER 6

SUBDIVISION SURFACES FOR THE GENERALIZED METHOD OF MOMENTS

6.1 Introduction

The topic of this chapter is the formulation of the Generalized Method of Moments on subdivision surfaces. Subdivision surfaces are widely used in the computer graphics community to construct globally smooth, easily deformable and intrinsically refinable surfaces, e.g. for character animation (Pixar's *Toy Story 2*, *Cars*, etc.). Several characteristics of subdivision surfaces are of interest in constructing boundary integral equation discretizations. First, subdivision surfaces provide an efficient means for constructing higher order surfaces directly from low order meshes without the need for additional interpolation points; furthermore, the resulting surface is globally smooth to second order everywhere but a small number of vertices. Subdivision surfaces do not suffer from problems with watertightness, can easily handle topologically complex geometries, can be easily deformed, and can also handle sharp edges and tips where desired. Because of these properties, subdivision surfaces hold promise for electromagnetics in optimization problems, uncertainty quantification, analysis of deformable scatters, etc. The subdivision approach has been used in thin-shell deformation problems [102] and a boundary element method for elastics [103], but not for electromagnetic or acoustic boundary integral equations. One reason for this is that subdivision surfaces present some unique challenges in constructing well-behaved basis sets near so-called "irregular" vertices that arise in subdivision parameterizations of arbitrary meshes. This chapter solves these problems in the context of the GMM and gives a formulation for a boundary integral equation discretization on subdivision surfaces that can be readily hybridized with more traditional moment method discretizations. Furthermore, the continuity properties of subdivision surfaces paired with carefully chosen local parameterizations and basis sets near irregular vertices yield a GMM discretization that is significantly easier to integrate than for arbitrary surface descrip-

tions. Subdivision-based GMM is also free from the problem of noncongruent overlaps between integration domains discussed in Chapter 5 and admits the use of a relatively simple partition of unity. Specific contributions of this chapter are:

- Definition of a Generalized Method of Moments parameterization of the subdivision surface tangent space.
- Development of subdivision vector basis functions that are well behaved and suitable for representing physical currents everywhere over the subdivision surface, including in the vicinity of irregular vertices.
- A simplified, efficient partition of unity based on first order box splines and corresponding integration scheme.
- A prescription for merging of GMM patches on subdivision surfaces.

The remainder of the chapter is structured as follows. Section 6.2 defines the Loop subdivision surface [104] utilized in this work. Section 6.3 develops a local parameterization of subdivision surfaces suitable for GMM, and Sections 6.4 and 6.5 respectively detail the construction of basis functions and partitions of unity in subdivision GMM. Finally, 6.6 gives results and 6.7 gives discussion and concluding remarks.

6.2 Loop Subdivision Surfaces

Subdivision surfaces are defined through recursive refinement of an initial first order “primal” mesh, denoted in this work by \mathcal{M}^0 . The primal mesh contains a collection of vertices $\{\mathbf{v}_i^0\}$, $i = 1, \dots, N_v^0$ as well as an associated collection of faces $\{T_l^0\}$, $l = 1, \dots, N_f^0$. The initial mesh \mathcal{M}^0 is refined into the \mathcal{M}^1 mesh by application of a subdivision rule, which adds additional vertices and faces and repositions the original set of vertices to create new sets $\{\mathbf{v}_i^1\}$, $i = 1, \dots, N_v^1$ and $\{T_l^1\}$, $l = 1, \dots, N_f^1$. This process may be applied recursively k times, and in the limit that $k \rightarrow \infty$, a

smooth “limit surface” is obtained. The properties of the limit surface depend on the type of initial mesh and the choice of refinement rules.

This work focuses on the Loop subdivision scheme [104], which is constructed upon primal meshes with triangular faces; other element types such as quadrilaterals may also be treated [105]. Surfaces generated through Loop subdivision fall under the class of “approximating” subdivision surfaces. Unlike “interpolating” subdivision schemes, approximating subdivision surfaces do not exactly interpolate their original generating mesh [102]. However, approximating schemes such as Loop, Catmull-Clark, and Doo-Sabin [106] are C^2 almost everywhere while interpolating subdivision schemes are at best C^1 [107], [108]. For certain discretizations of electromagnetic boundary integral equations, the higher degree of continuity is of interest; furthermore approximating subdivision surfaces can be fitted to a desired sampled surface [109, 110]. Loop subdivision is chosen for GMM because it yields surfaces with C^2 continuity and, since the primal mesh elements are triangles, the subdivision may be directly applied to existing low order meshes without the need for remeshing or the insertion of additional interpolation nodes as is required in Lagrange-type interpolation.

Some additional concepts are necessary to precisely describe the Loop subdivision process. Each vertex \mathbf{v}_i^0 in \mathcal{M}^0 possesses a neighborhood called a “one-ring”, defined as the set of vertices with which \mathbf{v}_i^0 shares an edge. A key characteristic of each vertex is its valence N , which is defined as the number of vertices in its one-ring. The valence plays a prominent role in the choice of subdivision rules in the neighborhood of a vertex. Practical meshes contain a mixture of “regular” vertices ($N = 6$), and a small number of “irregular” vertices ($N \neq 6$).

In the Loop scheme, subdivision of a level k mesh to a level $k + 1$ mesh about a vertex \mathbf{v}_0^k proceeds by inserting one new vertex on each edge incident on \mathbf{v}_0^k and recomputing the vertex positions, with the new level k vertex positions given by

$$\mathbf{v}_i^{k+1} = (3\mathbf{v}_0^k + \mathbf{v}_{i-1}^k + 3\mathbf{v}_i^k + \mathbf{v}_{i+1}^k)/8 \quad (6.1)$$

for the new vertices, and

$$\mathbf{v}_0^{k+1} = (1 - Nw)\mathbf{v}_0^k + w\mathbf{v}_1^k + \cdots + w\mathbf{v}_1^k \quad (6.2)$$

for vertex \mathbf{v}_0^k , where $w = (10 - (3/2 + \cos(2\pi/N))^2)/(16N)$. This choice of rules produces a limit surface that is C^2 everywhere but at irregular vertices, where it is C^1 [104]. Figure 6.1 shows a coarse sphere primal mesh, two successive subdivisions, and the limit surface ($k \rightarrow \infty$).

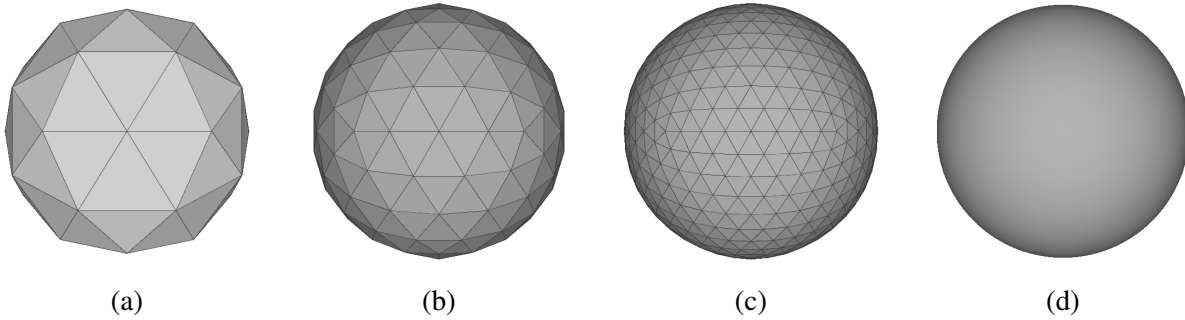


Figure 6.1: Subdivision of a spherical mesh. (a) Primal mesh, (b) $k = 1$, (c) $k = 2$, (d) limit surface ($k = \infty$).

6.2.1 Evaluation of the Limit Surface and Derivatives

Since the computation of any point on the limit surface is accomplished through an infinite number of subdivisions, it is clearly not feasible to evaluate the limit surface using the subdivision procedure. Fortunately, it has been established that the Loop subdivision limit surface may be exactly parameterized about regular vertices by a set of smooth quartic box spline functions [104], and may therefore be directly evaluated without recourse to recursive subdivision. Near irregular vertices,

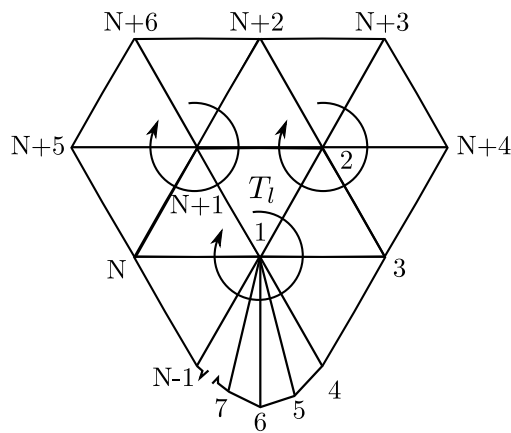


Figure 6.2: Neighborhood of a triangle T_l . Vertex \mathbf{v}_1 has a valence of N , vertices $\mathbf{v}_2, \mathbf{v}_{N+1}$ have valence six.

a modified procedure is used. The following discussion elucidates the evaluation procedures for both regular and irregular vertices, and identifies that challenge of defining well-behaved tangent spaces near irregular vertices that is relevant to the discretization of boundary integral equations.

For a triangle $T^0 \in \mathcal{M}^0$ with $K = N + 6$ vertices in its neighborhood, the Loop subdivision limit surface can be evaluated as:

$$\mathbf{S}(\xi^1, \xi^2) = \sum_{i=1}^K b_i(\xi^1, \xi^2) \mathbf{v}_i \quad (6.3)$$

where $b_i(\xi^1, \xi^2)$ are a set of smooth functions and $\mathbf{v}_i, i = 1, \dots, K$ are the K vertices in the neighborhood \mathbf{V}^0 of T^0 . Figure 6.2 shows the neighborhood and indexing scheme for an arbitrary triangle T_l with two regular vertices and one irregular vertex of valence N . Since the subdivision process preserves local mesh topology, the irregular vertex will be incident upon N triangles at any level of subdivision refinement. For conciseness, (6.3) may be written in the following notation:

$$\mathbf{S}(\xi^1, \xi^2) = (\mathbf{b}_K(\xi^1, \xi^2))^T \mathbf{V}^0 \quad (6.4)$$

with $\mathbf{b}_K(\xi^1, \xi^2) = [b_1(\xi^1, \xi^2), b_2(\xi^1, \xi^2), \dots, b_K(\xi^1, \xi^2)]^T$. In the case that $K = 12$ (i.e. all vertices in \mathbf{V}^0 are regular), the functions $b_i(\xi^1, \xi^2)$ are box splines [104]. For irregular vertices, the functions \mathbf{b}_K are not analytically available, and a modified subdivision procedure is adopted.

Subdivision of the mesh \mathcal{M}^0 once into the mesh \mathcal{M}^1 for the triangle T^0 can be expressed as the action of a matrix \bar{A} upon \mathbf{V}^0 , the neighborhood of T^0 in the primal mesh as

$$\mathbf{V}^1 = \bar{A} \mathbf{V}^0, \quad (6.5)$$

where the rows of the matrix \bar{A} contain appropriately shifted versions of the Loop subdivision rules (6.1) and (6.2). The result of this operation is a new set of L vertices, subsets of which define level $k = 1$ neighborhoods of the 4 new subtriangles $T_l^1, l = 1, \dots, 4$ within to the original triangle T^0 . These subsets are obtained by the application of “picking matrices” P_l that select only vertices in the neighborhood of T_l^1 , so that \mathbf{V}_l^1 , the level $k = 1$ neighborhood of triangle T_l^1 , is given by:

$$\mathbf{V}_l^1 = P_l \bar{A} \mathbf{V}^0, \quad (6.6)$$

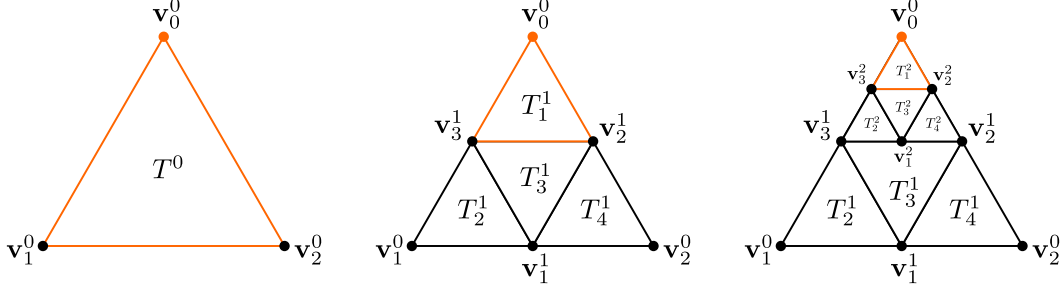


Figure 6.3: Recursive subdivision procedure about an irregular vertex \mathbf{v}_0^0 . Each subdivision yields three regular triangles and one irregular triangle.

and the limit surface in each subtriangle is given by:

$$\begin{aligned} \mathbf{S}(\xi^1, \xi^2)|_{T_l^1} &= (\mathbf{b}_K(f_l^1(\xi^1, \xi^2)))^T P_l \mathbf{V}^1 \\ &= (\mathbf{b}_K(f_l^1(\xi^1, \xi^2)))^T P_l \bar{A} \mathbf{V}^0 \end{aligned} \quad (6.7)$$

where $f_l^1(\xi^1, \xi^2)$ transforms from barycentric coordinates on the parent triangle to barycentric coordinates on T_l^1 . For a triangle with one irregular vertex (it is assumed that the mesh has been subdivided at least once to ensure that each triangle has at most one irregular vertex), three of the subtriangles T_2^1, T_3^1, T_4^1 have regular neighborhoods and may therefore be evaluated in closed form using box splines; only T_1^1 possesses a neighborhood with an irregular vertex. T_1^1 may again be subdivided, yielding four more subtriangles, three of which have regular neighborhoods and one of which retains the irregular valence. Since only T_1^1 has to be subdivided, it is useful to define the $K \times K$ matrix $A = P_1 \bar{A}$. Then the limit surface within T_1^1 may be evaluated as:

$$\mathbf{S}(\xi^1, \xi^2)|_{T_l^2} = \begin{cases} (\mathbf{b}_K(f_l^2(\xi^1, \xi^2)))^T A^2 \mathbf{V}^0, & l = 1 \\ (\mathbf{b}_{12}(f_l^2(\xi^1, \xi^2)))^T P_l \bar{A} A \mathbf{V}^0, & l = 2, 3, 4, \end{cases} \quad (6.8)$$

Since the limit surface cannot be evaluated in closed form for T_1^1 , the process is again repeated, yielding three more regular triangles T_l^2 , $l = 2, 3, 4$, and on irregular triangle T_1^2 . Fig. 6.3 illustrates the first two levels of the subdivision process near an irregular vertex \mathbf{v}_0^0 . Generalizing to k subdivisions, the limit surface in the vicinity of the irregular vertex may be parameterized as:

$$\mathbf{S}(\xi^1, \xi^2)|_{T_l^k} = \begin{cases} (\mathbf{b}_K(f_l^k(\xi^1, \xi^2)))^T A^k \mathbf{V}^0, & l = 1 \\ (\mathbf{b}_{12}(f_l^k(\xi^1, \xi^2)))^T P_l \bar{A} A^{k-1} \mathbf{V}^0, & l = 2, 3, 4 \end{cases} \quad (6.9)$$

To reach the irregular vertex, it is necessary to take A^k , $k \rightarrow \infty$, which is not computationally feasible. Stam [111] solved this problem by turning to eigenanalysis, where he defined:

$$A = C\Lambda C^{-1}, \quad (6.10)$$

with $\Lambda = \text{diag}(\lambda_1, \lambda_2, \dots, \lambda_K)$ a diagonal matrix containing the eigenvalues of A , and $C = [\mathbf{c}_1, \mathbf{c}_2, \dots, \mathbf{c}_K]$ a matrix whose columns \mathbf{c}_i form a basis for the eigenspace of A . Explicit formulas for the eigenvalues of A have been derived [111]. Using (6.10), (6.9) may be rewritten as

$$\mathbf{S}(\xi^1, \xi^2)|_{T_l^k} = \begin{cases} \sum_{i=1}^K (\mathbf{b}_K(f_l^k(\xi^1, \xi^2)))^T \mathbf{c}_i \lambda_i^k C^{-1} \mathbf{V}^0, & l = 1 \\ \sum_{i=1}^{12} (\mathbf{b}_{12}(f_l^k(\xi^1, \xi^2)))^T P_l \bar{A} \mathbf{c}_i \lambda_i^{k-1} C^{-1} \mathbf{V}^0, & l = 2, 3, 4 \end{cases} \quad (6.11)$$

which may be evaluated much more rapidly since it involves only powers of a diagonal matrix. To further simplify 6.11, define $\hat{\mathbf{V}} = C^{-1} \mathbf{V}^0$. Since $\hat{\mathbf{V}} = [C^{-1} \mathbf{v}_1, C^{-1} \mathbf{v}_2, \dots, C^{-1} \mathbf{v}_K]^T$ has the form of a triangle neighborhood, it is designated the ‘‘eigen-neighborhood’’ of T^0 , and the formula for the limit surface in terms of $\hat{\mathbf{V}}$ is:

$$\mathbf{S}(\xi^1, \xi^2)|_{T_l^k} = \begin{cases} \sum_{i=1}^K (\mathbf{b}_K(f_l^k(\xi^1, \xi^2)))^T \mathbf{c}_i \lambda_i^k C^{-1} \hat{\mathbf{v}}_i, & l = 1 \\ \sum_{i=1}^{12} (\mathbf{b}_{12}(f_l^k(\xi^1, \xi^2)))^T P_l \bar{A} \mathbf{c}_i \lambda_i^{k-1} \hat{\mathbf{v}}_i, & l = 2, 3, 4 \end{cases} \quad (6.12)$$

Final simplifications may be found by examining the properties of the eigenvectors and eigenvalues of the matrix A . It has been shown [112] that if the eigenvalues are ordered so that $|\lambda_1| > |\lambda_2| \geq \dots \geq |\lambda_K|$, $\lambda_1 = 1$. Indeed, if this were not the case, (6.12) shows that in the limit $k \rightarrow \infty$ the value of \mathbf{S} at the irregular vertex would be zero. Additionally, it can be shown that $|\lambda_2| = |\lambda_3|$ [111], and the first eigenvector corresponding to λ_1 is $\mathbf{v}_1 = [1, 1, \dots, 1]^T$ [112]. Because of this and the fact that the box splines $\mathbf{b}_{12}(\xi^1, \xi^2)$ form a partition of unity, $\hat{\mathbf{v}}_1$ may be extracted from the sum in (6.12) to give

$$\mathbf{S}(\xi^1, \xi^2)|_{T_l^k} = \begin{cases} \hat{\mathbf{v}}_1 + \sum_{i=2}^K (\mathbf{b}_K(f_l^k(\xi^1, \xi^2)))^T \mathbf{c}_i \lambda_i^k C^{-1} \hat{\mathbf{v}}_i, & l = 1 \\ \hat{\mathbf{v}}_1 + \sum_{i=2}^{12} (\mathbf{b}_{12}(f_l^k(\xi^1, \xi^2)))^T P_l \bar{\mathbf{A}} \mathbf{c}_i \lambda_i^{k-1} \hat{\mathbf{v}}_i, & l = 2, 3, 4 \end{cases} \quad (6.13)$$

Due to the condition that $\lambda_1 = 1$ is the largest eigenvalue, it is clear that the limit surface converges to $\hat{\mathbf{v}}_1$ at the irregular vertex.

Definition of a basis set on \mathbf{S} that is suitable for discretization of electromagnetic boundary integral equations requires parameterizations of the local tangent vectors in the neighborhood of the irregular vertex. The partial derivatives of (6.13) yield expressions for the tangent vectors:

$$\begin{aligned} \mathbf{S}(\xi^1, \xi^2)_{\xi^j}|_{T_l^k} = \\ \frac{\partial f_l^k(\xi^1, \xi^2)}{\partial \xi^j} \sum_{i=2}^{12} (\mathbf{b}'_{12}(f_l^k(\xi^1, \xi^2)))^T P_l \bar{\mathbf{A}} \mathbf{c}_i \lambda_i^{k-1} \hat{\mathbf{v}}_i, \quad l = 2, 3, 4, j = 1, 2 \end{aligned} \quad (6.14)$$

where the first sum in (6.13) has been omitted as it cannot be analytically evaluated except at the irregular vertex. The transformation f_l^k is given by:

$$f_l^k(\xi^1, \xi^2) = \begin{cases} (2^k \xi^1 - 1, 2^k \xi^2), & l = 2 \\ (1 - 2^k \xi^1, 1 - 2^k \xi^2), & l = 3 \\ (2^k \xi^1, 2^k \xi^2 - 1), & l = 4. \end{cases} \quad (6.15)$$

Taken together with (6.14), (6.15) shows that the leading term of \mathbf{S}_{ξ_j} scales as $2(2\lambda_2)^{(k-1)}$. Therefore, if $\lambda_2 > 1/2$, which is the case for triangles with neighborhoods of size $K > 12$ [111], the magnitudes of the non-normalized tangent vectors tends to infinity in the limit $k \rightarrow \infty$, i.e. as the irregular vertex is approached. Likewise, if $\lambda_2 < 1/2$, as it is for neighborhoods with $K < 12$, the magnitudes of the non-normalized tangent vectors tend to zero. Fig. 6.4 shows the divergent behavior of the subdivision Jacobian $J = \|\partial \mathbf{S} / \partial \xi^1 \times \partial \mathbf{S} / \partial \xi^2\|$ of the subdivision surface about a valence $N = 15$ vertex.

The only stable case is $K = 12$, for which $\lambda_2 = 1/2$, which in the $k \rightarrow \infty$ limit gives $(2\lambda_2)^{k-1} = 1$. The divergent behavior of the tangent vectors in the neighborhood of irregular vertices makes

them unsuitable for representation of physical vector current quantities. Normalization would lead to better behavior of the tangent vectors themselves, but yields divergent higher order derivatives of \mathbf{S} , which are required for evaluation of divergences of basis functions. It is therefore necessary to reparameterize the subdivision surface in the neighborhood of the irregular vertex in a way that exactly compensates for the behavior of f_l^k . Fortunately the GMM discretization, which is built upon local coordinate charts defined on subsets of the mesh, permits the seamless inclusion of such a reparameterization.

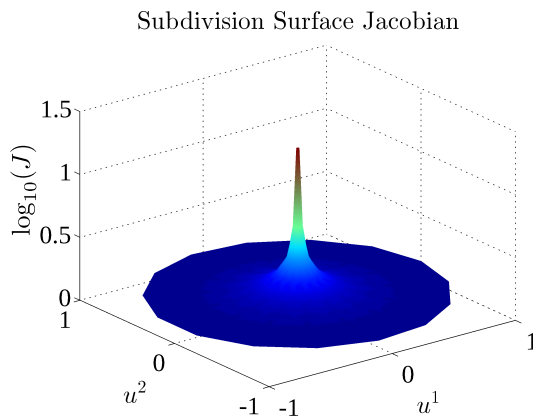


Figure 6.4: Divergent behavior of subdivision surface partial derivatives about an irregular vertex of valence $N = 15$. The (u^1, u^2) coordinate system for this case is defined via direct projection into a common plane that shares the average normal of all triangles incident on the irregular vertex.

6.3 GMM Patches and Local Parameterizations

Definition of a GMM discretization on the subdivision surface first requires the division of the surface into overlapping subdomains Ω_k , termed patches, and appropriate parameterizations of the surface and tangent space within each patch. For a subdivision surface, an initial primitive patch Ω_l is identified with a single vertex \mathbf{v}_l^0 on the primal mesh, such that the number of patches is N_V^0 . The domain of the patch Ω_l is taken as the union of the set of primal faces, denoted \mathcal{T}_l , incident on \mathbf{v}_l^0 . The solution may be constructed in terms of these primitive patches directly, or they may be merged into larger patches as discussed below.

Although subdivision surfaces admit a natural parameterization of the surface Ω_l in terms of the barycentric (ξ^1, ξ^2) coordinates on each face, in general this parameterization is only higher order smooth within a face, and exhibits only C^0 smoothness between faces [113] (note that the surface itself parameterized in terms of barycentric coordinates is C^2 almost everywhere). The only case in which parameterization in terms of (ξ^1, ξ^2) is higher order continuous between triangles is the case where all triangles are equilateral, which occurs only when all triangles are coplanar and the vertex \mathbf{v}_l^0 has valence six. For regular vertices, such a parameterization can be constructed by a piecewise linear mapping of the triangles into a regular hexagon in the (u^1, u^2) plane via the maps $\varphi_r : T_r \rightarrow \Gamma_l$, with Γ_l the regular hexagon with all vertices placed on the unit circle.

For vertices with valence $N \neq 6$, a linear piecewise mapping is not sufficient for higher order continuity between triangles in the unit N -gon. Several possible maps can be used, for example the conformal maps defined in [114], which are by definition C^∞ . However, for reasons that will become apparent below, this work uses the so-called characteristic map parameterization.

The characteristic map $F : \mathbb{R}^2 \rightarrow \mathbb{R}^2, (\xi^1, \xi^2) \mapsto (u^1, u^2)$ is defined by performing subdivision on an “eigen-neighborhood” of the irregular vertex. The coordinates of eigen-neighborhood vertices are given by $\tilde{\mathbf{v}}_2, \tilde{\mathbf{v}}_3$, the subdominant eigenvectors of the subdivision matrix B_N about a vertex of valence N . The matrix B_N , which is related to but distinct from the matrix A above, is formed by tabulating the Loop subdivision rules (6.1), (6.2) for a vertex \mathbf{v}_l^0 and all triangles incident on its one- and two-rings (collectively referred to as the “two-neighborhood” of the vertex) such that the application of B_N upon \mathbf{v}_l^0 and its two-neighborhood yields the vertex \mathbf{v}_l^1 with a topologically similar two-neighborhood at the $k = 1$ subdivision level. Details of construction and analytical expressions for the eigenvalues of B_N are given in [115].

Characteristic maps have been a primary analysis tool for subdivision surfaces and play a key role in smoothness proofs for subdivision schemes about irregular vertices [112, 115, 116]. They have been utilized for local reparameterizations leading to curvature continuous surfaces in [117, 118] for Catmull Clark and [113] for Loop subdivision schemes. For all cases of interest to this work, it has been shown that the Loop subdivision characteristic map is C^2 everywhere but at the

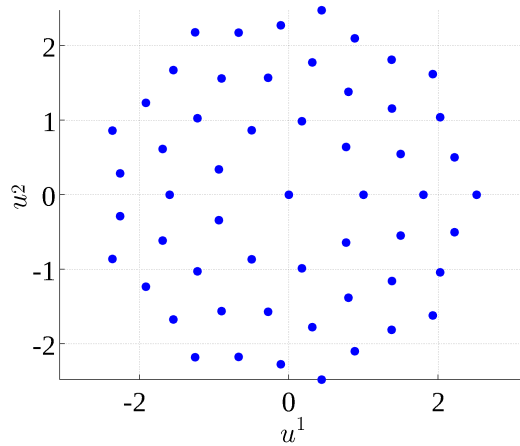


Figure 6.5: Eigen-neighborhood for a vertex of valence nine. The characteristic map is constructed upon subdivision of this neighborhood.

irregular vertex, where it is C^1 [115]. Figure 6.5 shows the (normalized) eigen-neighborhood for a vertex of valence nine, where the (u^1, u^2) coordinates are defined by $[\tilde{\mathbf{v}}_2, \tilde{\mathbf{v}}_3]$, the subdominant eigenvector pair for the B_9 subdivision matrix. The inner ring of the eigen-neighborhood for a vertex of valence N is always a regular N -gon.

Since the characteristic map is defined via a Loop subdivision procedure, its limiting values can be obtained by the same evaluation procedure outlined in section 6.2.1 as

$$[u^1, u^2] = \mathbf{b}_K^T(\xi^1, \xi^2)[\tilde{\mathbf{v}}_2, \tilde{\mathbf{v}}_3]; \quad (6.16)$$

specifically, the same recursive eigen-based approach illustrated in Fig. 6.3 is used to compute the limit position in the (u^1, u^2) plane. Figs. 6.6-6.8 show primal triangulations, subtriangulations, and images of the subtriangulations under the characteristic map for valences five, six, and fifteen. For valence six the characteristic map is the regular hexagon.

The key property of the characteristic map for this work is that it is defined using the same subdivision procedure as for the surface. This means that the partial derivatives of the characteristic map with respect to (ξ^1, ξ^2) contain the same dependence on f_l^k (equation (6.15)) as do derivatives of the subdivision surface \mathbf{S} . We exploit this property below to construct well-behaved basis sets near irregular vertices.

The local coordinate chart for each GMM patch primitive Ω_l is constructed using the character-

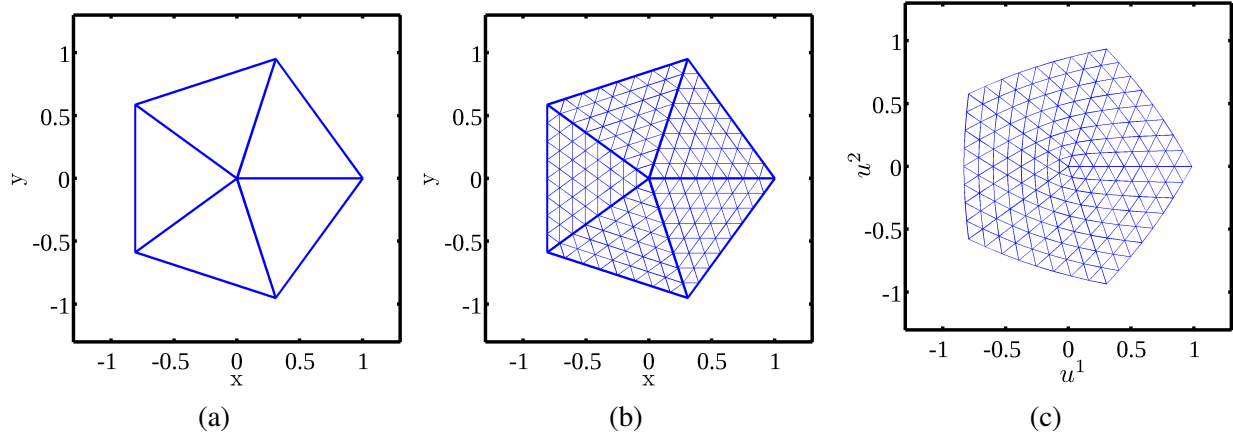


Figure 6.6: Characteristic map for a vertex of valence $N = 5$. (a) Triangulation of an N -gon, (b) a subtriangulation T of the N -gon, (c) a piecewise linear representation of $F(T)$.

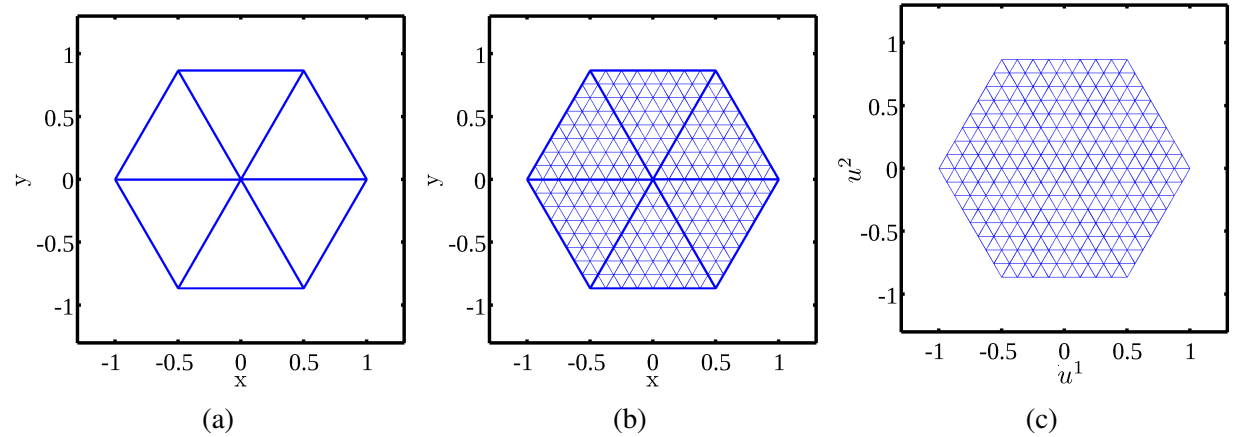


Figure 6.7: Characteristic map for a vertex of valence $N = 6$. (a) Triangulation of an N -gon, (b) a subtriangulation T of the N -gon, (c) a piecewise linear representation of $F(T)$.

istic map F_l of the appropriate valence that maps from the subdivision surface into the local (u^1, u^2) coordinate domain. Figure 6.9 shows the local coordinate charts defined by the characteristic maps for overlapping patches of valence five and six. The global subdivision surface is completely described by the atlas (see Chapter 1) made up of the union of the patches $\Omega_l, l = 1 \dots N_v^0$ and their corresponding local coordinate charts defined via the characteristic maps.

The final consideration in constructing GMM parameterizations is the continuity and behavior of the transition functions τ_{lk} between local coordinate charts $F_l(\Omega_l), F_k(\Omega_k), \Omega_l \cap \Omega_k \neq \emptyset$. For characteristic parameterizations on Loop subdivision surfaces, the transition functions are defined

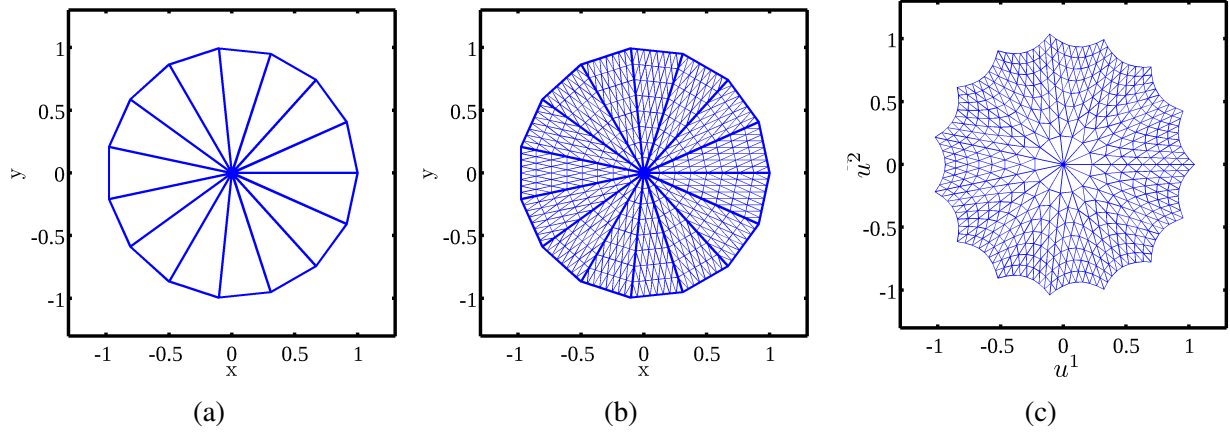


Figure 6.8: Characteristic map for a vertex of valence $N = 15$. (a) Triangulation of an N -gon, (b) a subtriangulation T of the N -gon, (c) a piecewise linear representation of $F(T)$.

as $\tau_{lk} \doteq F_l \circ F_k^{-1}$, with F_q the characteristic map associated with vertex \mathbf{v}_q . Since both F_l and F_q are C^2 (C^1 at an irregular vertex) and invertible, the transition function τ_{lk} is also C^2 (C^1 at an irregular vertex). The continuity of the characteristic map and transition functions between triangles permits the definition of partitions of unity and basis sets with support larger than a single triangle that have well-behaved (bounded) derivatives, a key characteristic for discretization electromagnetic integral equations.

Evaluation of F_k^{-1} , the inverse of the characteristic map, is practically quite difficult. To avoid this difficulty, practical implementations of GMM on subdivision surfaces are expressed entirely in terms of the barycentric coordinates (ξ^1, ξ^2) , so that F_k^{-1} need never be explicitly evaluated. Another feature of particular importance for GMM is that, given a triangle $T_r \in \mathcal{T}_l \cap \mathcal{T}_k$, the images $F_l(T_r), F_k(T_r)$ map precisely to a single “wedge” in their respective local (u^1, u^2) coordinate systems regardless of the valence of the two patches. GMM discretizations on subdivision surfaces therefore completely avoid the noncongruent overlap problem identified in Chapter 5 and the associated integration issues.

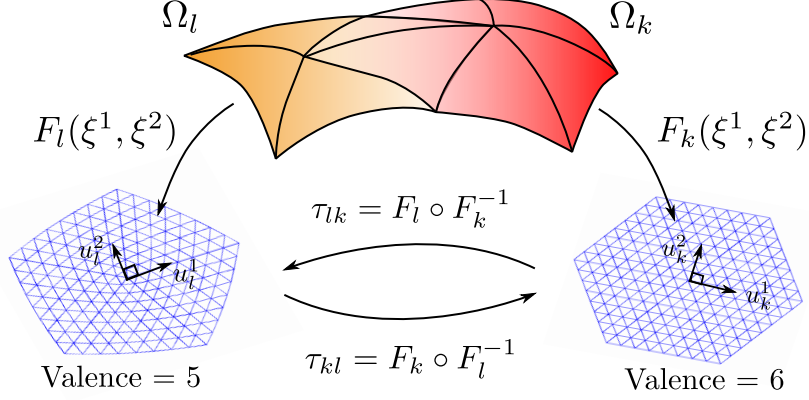


Figure 6.9: Coordinate charts for overlapping irregular (valence 5) and regular GMM patches induced by the characteristic maps $F(\xi^1, \xi^2)$.

6.3.1 Merging of Regular Patches

Defining an individual patch about every vertex in the primal mesh can lead to over-discretization for large, dense meshes. Furthermore, many GMM basis sets, such as plane wave-type functions, are designed for patches with large support. To employ such bases, and to reduce the number of unknowns, it is desirable to merge the initial primitive patches into larger patches in the manner of Chapter 2. For regular vertices, the regularity of the characteristic map yields transition functions that are isometric, i.e. images of equilateral triangles under the transition map between two regular patches is identity up to a rotation. It is therefore possible to merge the local coordinate systems of overlapping regular patches into larger regions with common support. Patches defined about irregular vertices, however, cannot in general be merged with neighboring patches since the transition functions are not isometric. Specifically, merging can only be performed under one of two conditions. Either 1) both patches are regular, or 2) parameterization of a merged irregular patch with a regular patch is performed using the characteristic map of the irregular patch, with appropriate expansion of the irregular patch parameterization domain to include the regular patch. In this work, only the first case is considered as it is by far the most common. The second is of less interest because merging is limited to only the two ring of the irregular vertex and therefore does not afford much benefit in terms of larger patch support. Irregular patches in the current formulation are never merged.

Given a group of overlapping regular patches, the merging algorithm proceeds as follows. First, the patch associated with the vertex nearest the geometrical center of the grouping is selected as the reference vertex. The origin of the corresponding (u^1, u^2) local coordinate system is fixed as the merged patch origin. The transition functions between the remaining overlapping patches are then recursively traversed, starting with the nearest neighbors of the reference patch. The local coordinate system of each successive patch is assigned both a translational and a rotational offset with respect to the coordinate system of the reference patch. Using the translational offsets, each interior node on the merged patch is assigned a location in (u^1, u^2) space relative to the origin, and its coordinate system is rotated appropriately to align with the reference coordinate system. Since all patches are regular and all primal coordinate domains are regular hexagons, the resulting parameterization domain is a regular hexagonal lattice. The function defined by these translations and rotations in (u^1, u^2) space yields a local coordinate chart, designated \tilde{F}_l , for the merged patch Ω_l .

Figure 6.10 shows the geometry and local parameterization domain of a merged patch. In this case the reference origin is taken as vertex nine; after merging the local origin may be redefined arbitrarily, e.g. as the geometric center of the (u^1, u^2) parameterization domain.

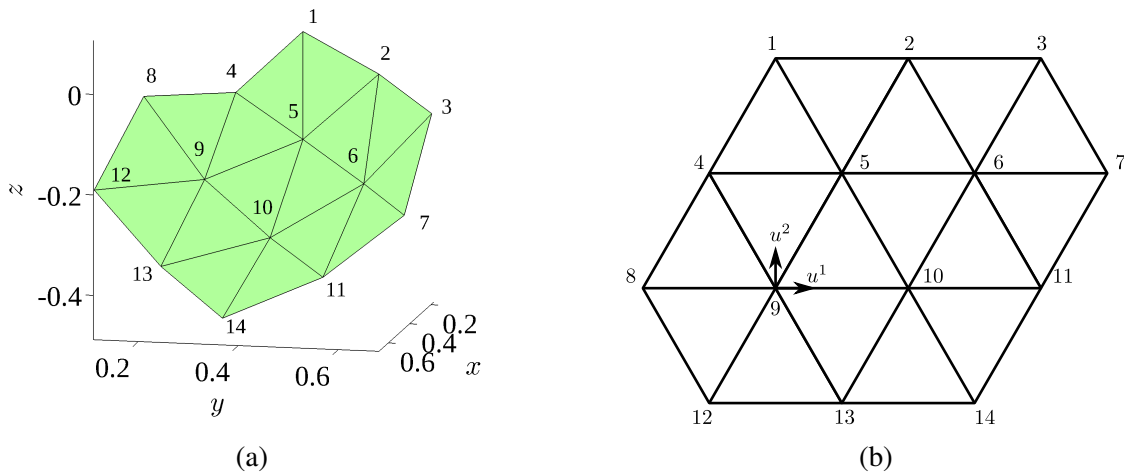


Figure 6.10: Primal mesh (a) and local coordinate domain (b) for a merged regular patch.

Care must be taken when merging regular patches in the vicinity of irregular vertices. Although

the regular and irregular patches are never merged, if several regular patches adjacent to the irregular vertex are allowed to merge, self-intersections of the local coordinate system may result. This is specifically a problem for irregular vertices with valence greater than six. Since all triangles in the merged regular patch domain are equilateral and therefore have interior angles of $\pi/3$ if the number of regular patches about an irregular vertex is allowed to be more than five, the coordinate system wraps back upon itself and the map \tilde{F}_l becomes non-unique. To avoid this complication, no more than five regular primitive patches are allowed to merge into a single patch around any irregular vertex.

6.4 Basis Functions

Basis sets for GMM are defined on the tangent space of the surface with respect to the local (u^1, u^2) coordinate system. Expressed purely in terms of local coordinates, a basis function defined on patch Ω_l may be written

$$\mathbf{f} = f_1(u^1, u^2) \frac{\partial \mathbf{S}}{\partial u^1} + f_2(u^1, u^2) \frac{\partial \mathbf{S}}{\partial u^2}. \quad (6.17)$$

However, because integrations are carried out with respect to the local (ξ^1, ξ^2) coordinates, it is more convenient to express the basis sets as

$$\mathbf{f}(\xi^1, \xi^2) = f_1(F_l(\xi^1, \xi^2)) \frac{\partial \mathbf{S}}{\partial \xi^1} + f_2(F_l(\xi^1, \xi^2)) \frac{\partial \mathbf{S}}{\partial \xi^2}, \quad (6.18)$$

with $F_l(\xi^1, \xi^2)$ the characteristic map associated with patch Ω_l . This expression is also more efficient to compute since the partial derivatives of the subdivision surface are expressed directly in terms of (ξ^1, ξ^2) . The regularity of the partial derivatives $\partial \mathbf{S} / \partial \xi^i$ about regular vertices means that basis sets defined on regular patches may be chosen with the usual freedom permitted by the GMM scheme. As shown in section 6.2.1, the partial derivatives of the surface about irregular vertices become singular in the limit that the irregular vertex is approached. Representation of physical currents in the neighborhood of irregular vertices therefore requires carefully designed basis sets that are smooth and non-singular regardless of valence.

Based on the conclusions of section 6.2.1, the partial derivatives of the subdivision surface \mathbf{S} behave as $\mathcal{O}((2\lambda)^k)$, with λ the subdominant eigenvalue of the subdivision matrix and $k \propto \log_2(\rho)$, ρ the radial distance from the irregular vertex. A well-behaved basis set therefore requires that the coefficient functions f_1, f_2 in 6.18 behave as $\mathcal{O}(2\lambda)^{-k}$ as the irregular vertex is approached. To effect this behavior, the basis set around the irregular vertex is defined in terms of the surface gradient of a scalar function

$$\mathbf{f} = \nabla\phi(u^1, u^2). \quad (6.19)$$

Recalling the explicit form of the surface gradient from Chapter 1, (6.19) expressed in terms of the ξ^1, ξ^2 coordinate system is

$$\sum_{i=1}^2 \sum_{j=1}^2 g^{ij} \frac{\partial\phi(F(\xi^1, \xi^2))}{\partial\xi^i} \frac{\partial\mathbf{S}}{\partial\xi^j}, \quad (6.20)$$

where g^{ij} is the (i, j) th component of the inverse of the metric tensor g . Components of g^{-1} are proportional to $(\text{Det}(g))^{-1/2} = J^{-1} = \|\partial\mathbf{S}/\partial\xi^1 \times \partial\mathbf{S}/\partial\xi^2\|^{-1} \sim \mathcal{O}((2\lambda)^{-2k})$. Because the characteristic map uses the same subdivision scheme as the surface, $\partial\phi/\partial\xi^i = (\partial F/\partial\xi^i)\phi'(F(\xi^1, \xi^2)) \sim \mathcal{O}((2\lambda)^k)$. The overall scaling of each term in $\nabla\phi$ is therefore $\mathcal{O}(1)$ for patches of any valence.

A complete basis set is defined by including, in addition to the curl-free function $\nabla\phi$, the divergence-free function

$$\mathbf{f}_i = \hat{\mathbf{n}} \times \nabla\phi_i. \quad (6.21)$$

The combined basis set forms a local surface Helmholtz decomposition on the patch. In this work, a p th order basis is constructed using the scalar functions

$$\phi_{mn}(u^1, u^2) = P_n(u^1)P_m(u^2), \quad 0 < m + n \leq p + 1 \quad (6.22)$$

with $P_q(\cdot)$ a q th degree Legendre polynomial, although any suitably well behaved set of scalar functions may be employed. Figs. 6.11 and 6.12 show a set of $p = 2$ basis functions and their divergences for a valence 5 and a valence 15 patch. Because $\hat{\mathbf{n}} \times \nabla\phi$ is divergence free, divergences are only shown for the $\nabla\phi$ functions. For the cases of irregular vertices both $N < 6$ and $N > 6$, the basis functions are smooth everywhere across the patch, and the divergence is continuous everywhere except the irregular vertex. This is a consequence of the continuity of the subdivision

surface and characteristic map, which are C^2 everywhere but at the irregular vertex, where they are C^1 .

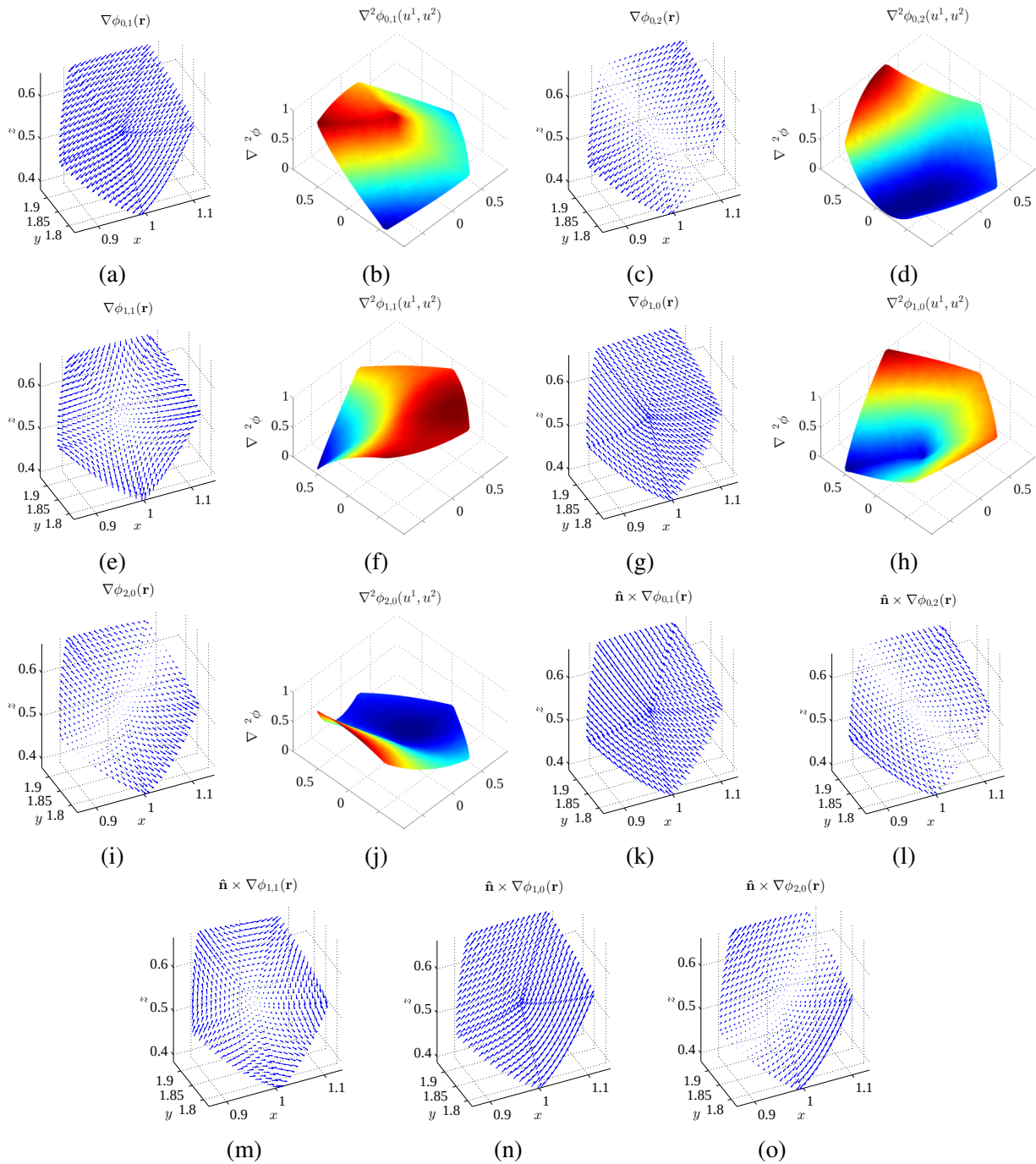


Figure 6.11: Basis functions and divergences for a valence $N = 5$ patch.

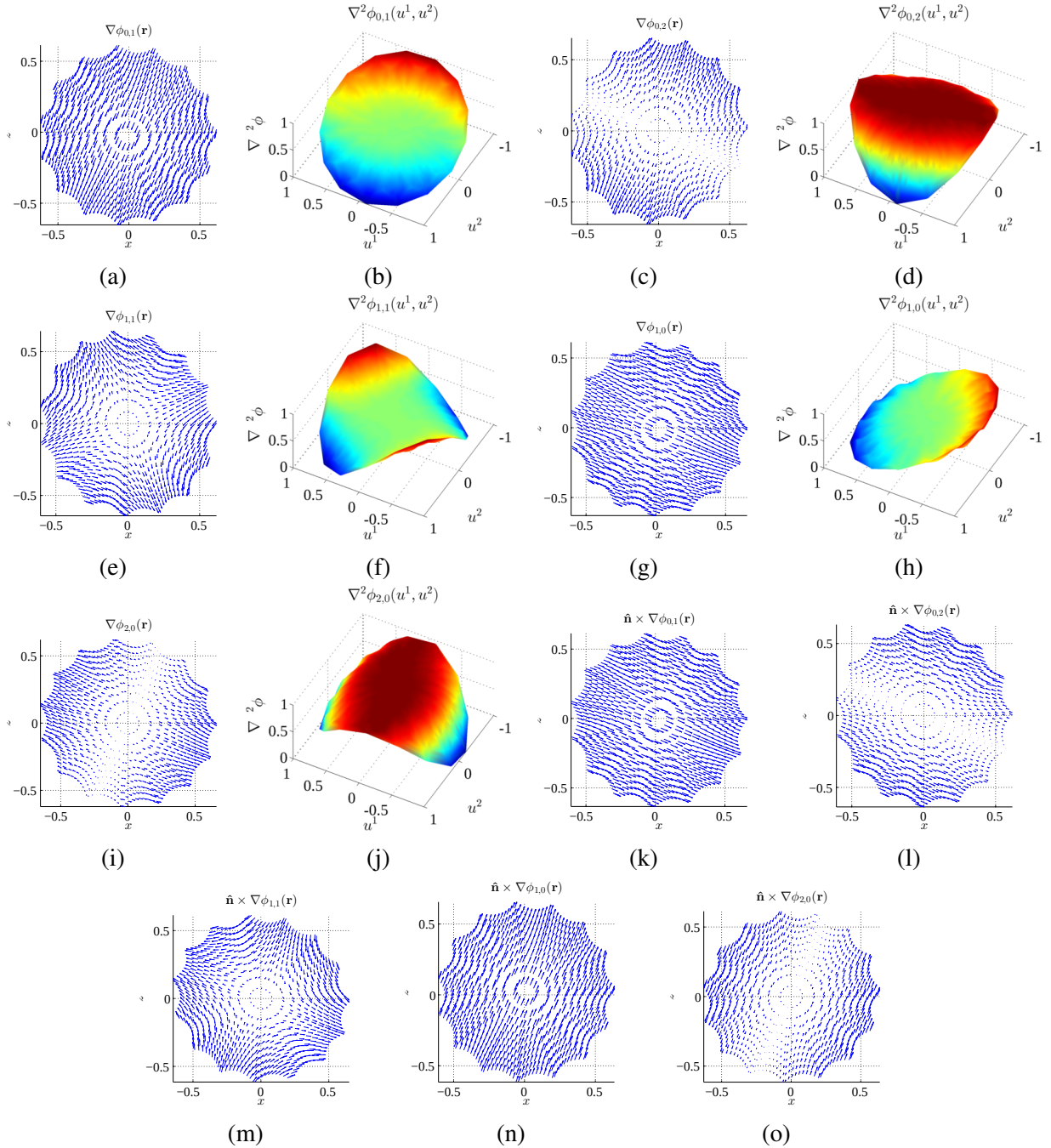


Figure 6.12: Basis functions and divergences for a valence $N = 15$ patch.

6.5 Partition of Unity

A key feature of the GMM discretization is that the basis set on each patch is multiplied by a partition of unity that provides automatic current continuity between patches. The partition of unity permits the use of different types of basis functions in the same discretization. For smooth non-

subdivision surface representations, the partition of unity is based on Shepard interpolation [49]. The local parameterization and patch definitions introduced in section 6.3 for Loop subdivision surfaces admit the use of a partition of unity based on first order box spline for regular patches, which are C^0 functions that naturally form a partition of unity. Fig. 6.14(a) shows a first order box spline about a regular vertex. In terms of the local barycentric coordinates in each triangle, the box spline for a regular patch Ω_l is simply defined as

$$\phi_l = \xi_l, \quad (6.23)$$

with ξ_l the barycentric coordinate corresponding to vertex \mathbf{v}_l . This first order spline partition of unity may be identified with the simplex partition of unity of Chapter 2.

In the vicinity of an irregular vertex, the partition of unity must be modified to ensure that basis sets on neighboring regular patches are well behaved as the irregular vertex is approached. The reason for this is that basis functions about regular vertices are parameterized with respect to a regular parametric map, which does not provide adequate compensation for the divergent behavior of the surface partial derivatives at the irregular vertex. Furthermore, unless the partition of unity is expressed as a function of the (u^1, u^2) coordinates generated by the irregular characteristic map, its gradient will also diverge at the irregular vertex. To circumvent these issues, the partition of unity is defined as follows.

First, the triangles in the 1-neighborhood of the irregular primal vertex \mathbf{v}_0^0 are subdivided once as shown in Fig. 6.13. For the patch Ω_l associated with the irregular vertex \mathbf{v}_0 in Fig. 6.13, the

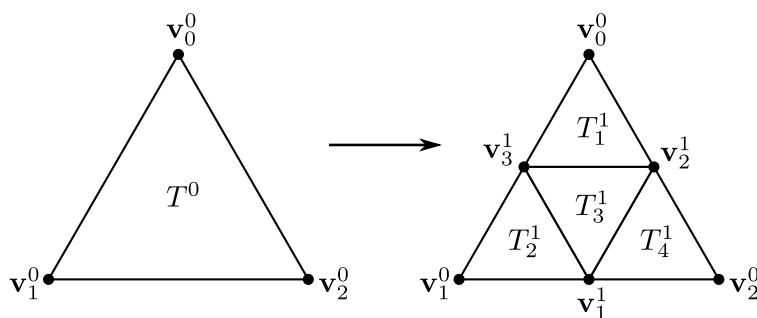


Figure 6.13: Subdivision of triangle around irregular vertex \mathbf{v}_0^0 for partition of unity definition.

partition of unity is defined at a point p as

$$\psi_0 = \begin{cases} 2\xi_0^0 & , p \in T_0 \setminus T_1^1 \\ 1 & , p \in T_1^1 \\ 0 & , \text{O.W.} \end{cases} \quad (6.24)$$

where the barycentric coordinate ξ_0^0 is associated with the \mathbf{v}_0^0 node in Fig. 6.13. This definition ensures that the derivative of the partition of unity is identically zero near the irregular vertex, leading to a partition of unity with a well-defined gradient that, while discontinuous, is non-divergent and easily integrable over the entire support of the patch. Fig. 6.14(b) shows the partition of unity function for a valence five vertex plotted versus (u^1, u^2) .

Finally, the partition of unity for the regular patch associated with vertex \mathbf{v}_1^0 a regular patch overlapping the irregular patch is given by

$$\psi_1 = \begin{cases} \xi_1^0 + .5\xi_1^1, & p \in T_2^1 \\ .5\xi_1^1, & p \in T_3^1 \\ .5\xi_1^1, & p \in T_4^1 \\ 0, & \text{O.W.,} \end{cases} \quad (6.25)$$

where the barycentric coordinate labels match the subdivided vertex labels in Fig. 6.13 and the barycentric coordinates are associated with the subdivided (not primal) triangles. The appropriate reflection of (6.25) gives the partition of unity function ψ_2 for the regular patch associated with \mathbf{v}_2^0 . The definition (6.25) ensures that gradient of the partition of unity is well-defined and non-divergent over its support. Furthermore, the partition of unity restricts the support of the basis set defined on the regular patch with respect to the regular characteristic map so that the basis function is well-behaved everywhere the partition of unity is nonzero. It can be readily verified that, for a triangle T^0 with one irregular vertex and the functions ψ_l identified with vertices \mathbf{v}_l , $l = 0, 1, 2$, the summation $\psi_0 + \psi_1 + \psi_2 = 1$ everywhere in T^0 .

Fig. 6.14(c) shows a schematic depiction of the resulting partition of unity functions on a regular patch neighboring an irregular patch. Fig. 6.15 shows the effective support of the partition

of unity for the regular patch, and Fig. 6.16 shows the effective supports of all regular patches neighboring a valence five irregular vertex. In triangles shared with regular patches the usual first order linear box spline partition of unity is used, but for triangles adjacent to the irregular vertex (6.25) is used.

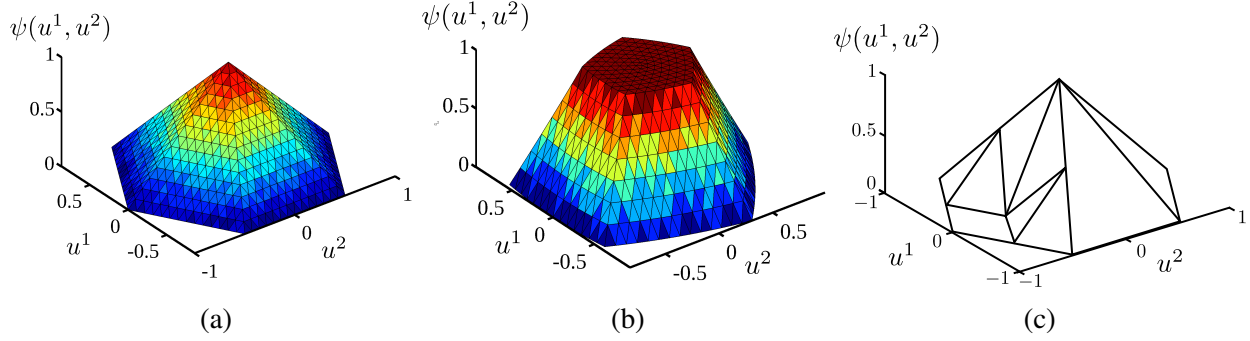


Figure 6.14: Subdivision simplex partition of unity. (a) PU on regular patch with regular neighbors. (b) PU on irregular valence $N = 5$ patch. (c) PU on regular patch neighboring irregular patch (shown schematically for clarity).

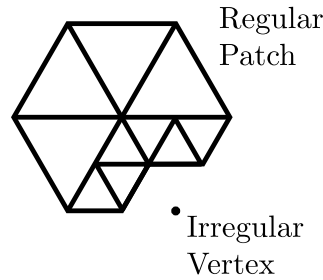


Figure 6.15: Regular patch support near an irregular vertex.

To accurately integrate the partition of unity in the neighborhood of an irregular vertex, it is necessary to define triangular Gauss quadrature rules on each level 1 subtriangle in Fig. 6.13. This incurs little extra cost since the subdivided integration rules need to be used only in triangles incident on an irregular vertex. Using the partition of unity described in this section, the final GMM basis set for patch Ω_l is

$$\begin{aligned} \psi_l \mathbf{f}_{lmn, \text{div}}(\mathbf{r}) &= \psi_l \nabla \phi_{mn} \\ \psi_l \mathbf{f}_{lmn, \text{rot}}(\mathbf{r}) &= \hat{\mathbf{n}} \times \psi_l \nabla \phi_{mn}, \end{aligned} \quad (6.26)$$

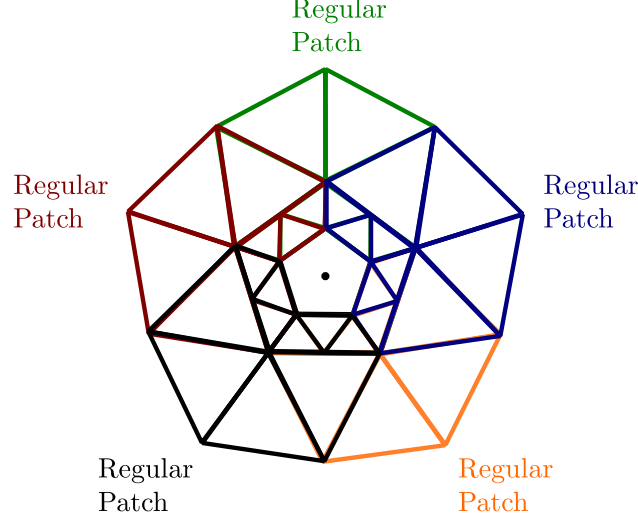


Figure 6.16: Regular patch supports adjacent to an irregular vertex of valence $N = 5$.

and the divergences are given by

$$\begin{aligned}\nabla \cdot (\psi_l \mathbf{f}_{lmn, \text{div}}(\mathbf{r})) &= \nabla \psi_l \cdot \nabla \phi_{mn} + \psi_l \nabla^2 \phi_{mn} \\ \nabla \cdot (\psi_l \mathbf{f}_{lmn, \text{rot}}(\mathbf{r})) &= \nabla \psi_l \cdot (\hat{\mathbf{n}} \times \nabla \phi_{mn}).\end{aligned}\tag{6.27}$$

In this work, the basis set (6.26) is used for both unmerged regular and irregular patches. For merged regular patches, the Legendre basis set defined in Chapter 2 is utilized as there is no issue with divergence of the subdivision tangent space on regular patches. A sampled partition of unity on a merged patch next to an irregular vertex is shown in figure 6.17. The total partition of unity over the patch is the summation of the local partitions of unity defined about each interior vertex. Figure 6.18 shows for the same patch a basis function in \mathbb{R}^3 and its divergence in the local (u^1, u^2) coordinate domain (shown *sans* partition of unity for clarity). Note the restriction of support for both functions in the vicinity of the regular vertex.

6.6 Results

This section provides results demonstrating the viability and accuracy of the subdivision for some electromagnetic scattering problems. The first result is scattering from a 1λ sphere due to an $\hat{\mathbf{x}}$ -polarized plane wave incident along the $+\hat{\mathbf{z}}$ direction. No patch merging was employed and a $p = 1$

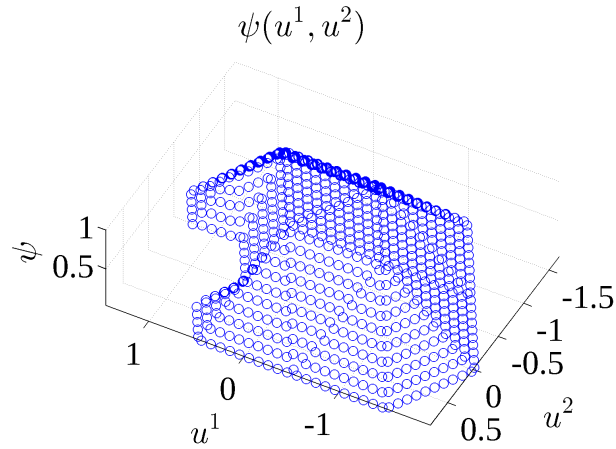


Figure 6.17: Sampled partition of unity $\psi(u^1, u^2)$ on a merged patch adjacent to an irregular vertex.

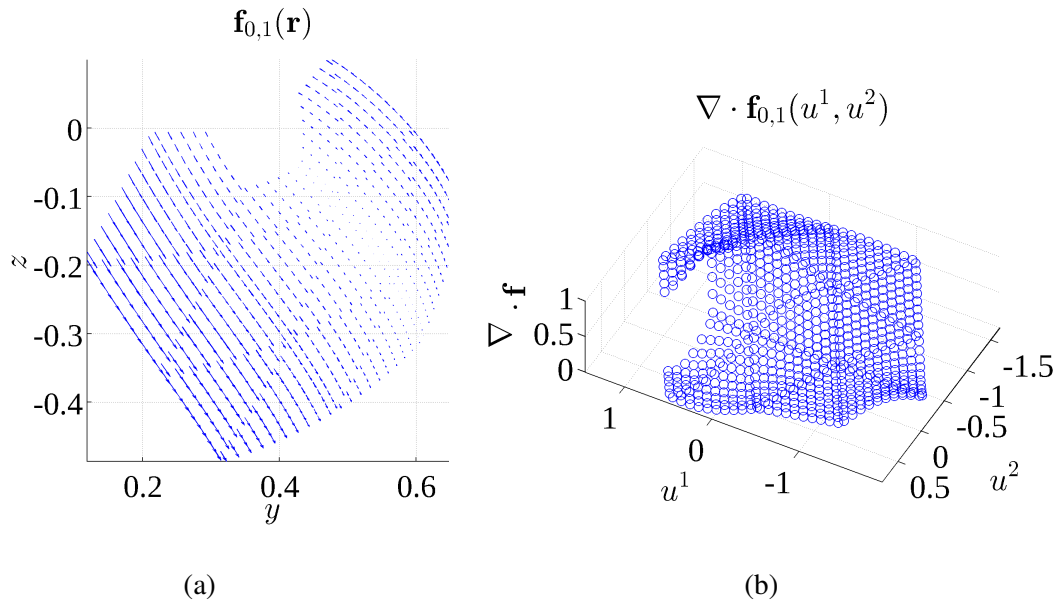


Figure 6.18: Basis function and divergence for a merged regular patch.

Helmholtz-decomposition (HD) basis with a total of $N_s = 1736$ GMM unknowns. Figure 6.19(a) shows the bistatic RCS, taken in the $\phi = 0^\circ$ cut, for the MFIE and EFIE compared with the Mie series solution. Good agreement is evident for all cases. Relative l_2 error in RCS for the MFIE result is 3.8×10^{-3} , for the EFIE result is 5.8×10^{-3} and for the CFIE result is 3.1×10^{-3} .

Figure 6.19(b) shows the RCS for the same sphere computed using the MFIE, EFIE, and CFIE ($\alpha = .3$), but with merged patches and a mixture of a $p = 2$ HD bases on irregular patches and a

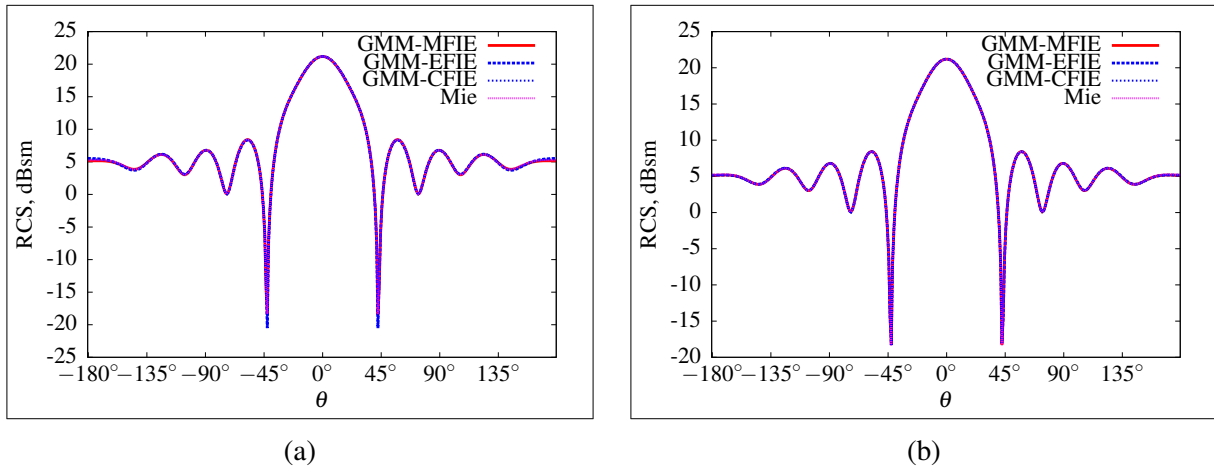


Figure 6.19: (a) RCS for 1λ subdivision sphere ($\phi = 0^\circ$). (b) RCS for 1λ subdivision sphere with merged patches ($\phi = 0^\circ$).

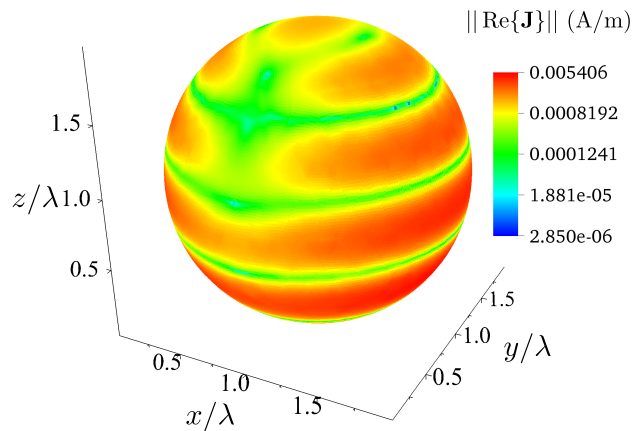


Figure 6.20: Real part of MFIE solution surface currents for 1λ sphere using $h = .5\lambda$ merged patches. Incident plane wave is traveling in $+\hat{z}$ direction.

$p = 2$ Legendre bases on regular merged patches, for a total of $N_s = 2208$ GMM unknowns. The maximum merged patch diameter is set to $h = .5\lambda$. Again, the results show good agreement, with the l_2 relative error in this case 1.9×10^{-3} for the EFIE result, 1.8×10^{-3} for the MFIE result, and 1.9×10^{-3} for the CFIE result. Fig. 6.20 shows the real part of the currents for the merged MFIE result. The smoothness of the currents everywhere indicates that the blending of functions between patches of different valences is smooth and well-behaved.

The second result, scattering from a $2\lambda \times 2\lambda$ Chmutov surface, shows the ease with which subdivision can produce higher order surfaces from topologically nontrivial primal meshes. Fig.

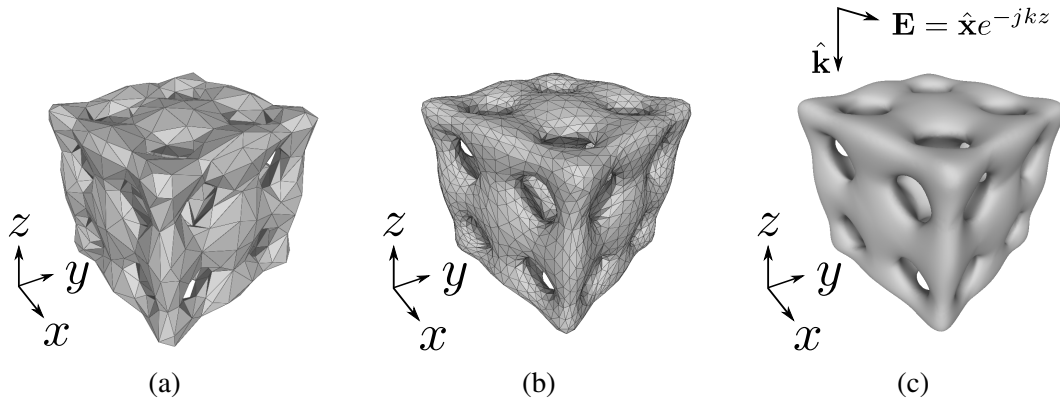


Figure 6.21: Chmutov surface (a) Coarse primal mesh. (b) Mesh after one subdivision. (b) Limit surface.

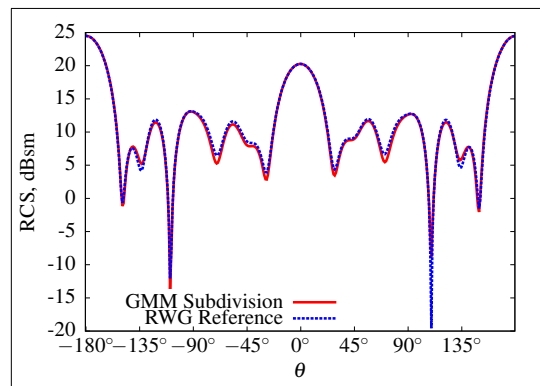


Figure 6.22: Bistatic RCS for 2λ Chmutov geometry ($\phi = 0^\circ$).

6.21 shows the primal mesh, the $k = 1$ mesh, and the limit surface for the Chmutov, as well as the incident plane wave. Despite the coarseness (and therefore sparseness) of the primal mesh representation, the subdivision process yields a smooth limit surface suitable for discretization with GMM. The Chmutov was discretized with a $p = 1$ mixed HD/Legendre GMM basis on $h = .3\lambda$ patches using the CFIE with $\alpha = .1$. Fig. 6.22 shows the RCS compared with a reference first order RWG CFIE implementation constructed on the $k = 1$ mesh. The results match well.

Finally, the scheme is applied to a shape deformation problem, scattering from a 2λ torus that is deformed by twisting. Figure 6.23 shows the $k = 1$ mesh for the original torus and the smooth subdivision representation of the twisted mesh, as well as the incident wave direction. The RCS for the untwisted torus is shown in fig. 6.24a for a $p = 2$ mixed basis discretization with patches

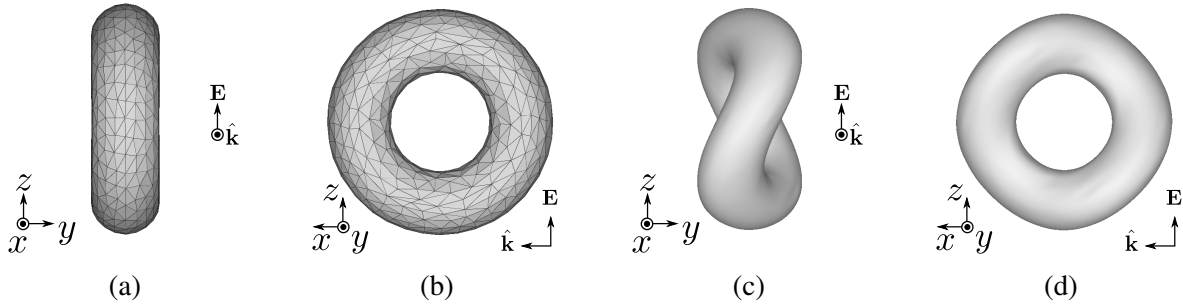


Figure 6.23: Torus mesh (a) front view, (b) side view, and twisted torus limit surface (c) front view, (d) side view.

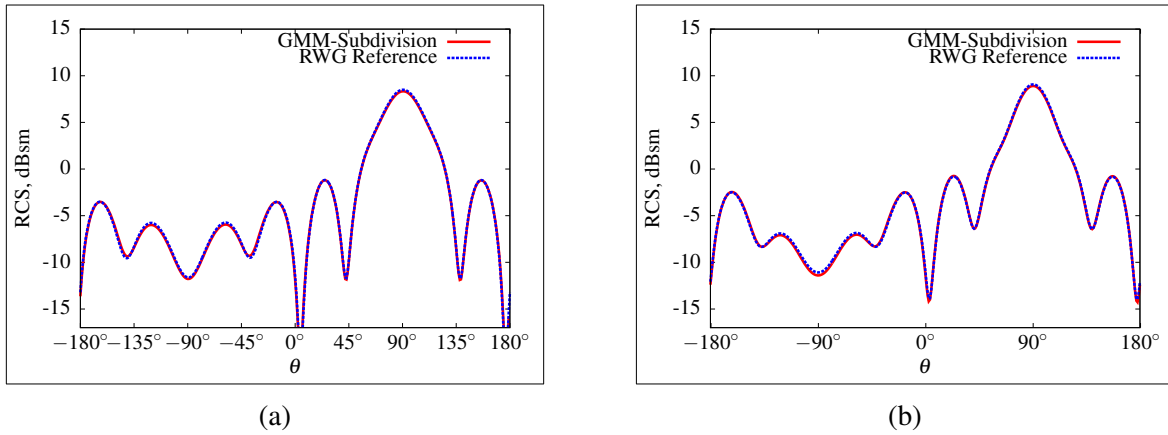


Figure 6.24: Bistatic RCS ($\phi = 0^\circ$ cut) for (a) torus and (b) twisted torus geometries.

merged up to $h = .5\lambda$ and an MFIE solution. The reference solution uses an RWG basis on a low order triangular mesh. To obtain the high-order representation of the twisted torus, only the primal mesh vertices were transformed; this is in contrast to traditional higher order representations in which all interpolation points must be properly transformed to obtain a well-behaved surface. It is also more efficient than previous GMM higher order polynomial geometry representations which relied on re-interpolation of the surface after any deformation. The ease with which the GMM subdivision surfaces may be deformed, coupled with the accelerated solution method of Chapter 3, provides a promising framework for tailoring electromagnetic response of scatterers using rapid geometry optimization. Figure 6.24b compares the twisted torus RCS for the two solution methods; subdivision exhibits good matching with the reference solution.

6.7 Discussion and Conclusions

This chapter has given a prescription for the construction of a GMM discretization on subdivision surfaces, with a specific implementation of Loop subdivision, although other subdivision surfaces could also be easily handled. The resulting GMM algorithm has several advantages: the surface description is always smooth and single-valued, the partition of unity is simple and easily integrated, and integration domains are well-defined. A chief challenge of defining a well-behaved integral equation discretization on subdivision surfaces is the handling of irregular vertices due to the singular nature of subdivision tangent vectors near irregular vertices. In this work this difficulty was solved by using a local characteristic map parameterization of the subdivision surface and defining basis functions using gradients of scalar functions, which are invariant under reparameterization. Results furnished demonstrate the use of the subdivision-based scheme on a variety of surfaces, and show that subdivision is a viable representation for a GMM discretization of electromagnetic boundary integral equations. Although the scattering geometries shown in the results section are all smooth, sharp tips, edges, and creases can be readily included in the subdivision surface description [119]. These capabilities and corresponding modifications to the GMM discretization will be explored in future work.

Several features of GMM on subdivision surfaces make it attractive for an array of targeted applications. Since subdivision is built upon a refinement of an initial coarse mesh into successively finer meshes, and because the mesh at any level of refinement converges to the same limit surface, subdivision induces a natural h -adaptivity that can be exploited in refining solutions. Since the support of GMM basis functions extends over multiple triangles, the method can easily handle meshes containing triangles with poor aspect ratios or with multiple length scales driven by geometrical meshing constraints. Furthermore, due to the global smoothness of the subdivision surface, it is possible to decouple the support of the basis functions from the support of faces in the generating mesh. The ease with which subdivision surfaces can be deformed makes subdivision-based integral equations attractive for uncertainty quantification and optimization applications in which electromagnetic response is tailored via shape deformation. Finally, the method may be

readily extended to traditional moment method discretizations by using a hybrid approach with isolated GMM patches about regular vertices and traditional basis sets everywhere else. All of these avenues will be subjects of future research.

APPENDIX

EIGENVALUES OF THE GMM INTERIOR PENALTY SYSTEM.

This appendix gives the full derivations of equations (4.13) and (4.14) that underlie the spectral analysis section of Chapter 4. Analytical expressions for the eigenspectra of the compensated and uncompensated GMM operators are derived; the two eigenspectra are compared to deduce the effect of the addition of the penalty term to the GMM system.

Under the assumptions that the basis set is shift invariant and that each patch supports a single basis function, patch indices may be identified with basis function indices such that $l \rightarrow n$, $n = 1, \dots, N_s$ for source functions and $k \rightarrow m$, $m = 1, \dots, N_s$ for testing functions, with N_s the total number of functions on the cylinder. The total current is then expanded as

$$\mathbf{J}_\phi(\boldsymbol{\rho}) = \sum_{n=1}^{N_s} a_n \boldsymbol{\psi}_n(\boldsymbol{\rho}) f_n(\boldsymbol{\rho}) \sum_{n=1}^{N_s} a_n \boldsymbol{\psi}_n(\phi - n\phi_0) f_n(\phi - n\phi_0). \quad (28)$$

The source and testing functions are expanded into Fourier series as

$$f_n(\phi) = f_n(\phi - n\phi) = \sum_{p=-\infty}^{\infty} F_p e^{jq\phi} e^{-jpn\phi_0}, \quad (29)$$

$$t_m(\phi) = t(\phi - m\phi) = \sum_{p=-\infty}^{\infty} T_p e^{jq\phi} e^{-jpm\phi_0}, \quad (30)$$

where F_p and T_p are the Fourier coefficients of $f(\phi)$ and $t(\phi)$, respectively, and the two dimensional Green's function is expanded using the addition theorem for Hankel functions,

$$H_0^{(2)}(k||\boldsymbol{\rho} - \boldsymbol{\rho}'||) = \sum_{p=-\infty}^{\infty} J_p(k\rho') H_p^{(2)}(k\rho') e^{-jp(\phi - \phi')}. \quad (31)$$

Using (29), (30), and (31), a spectral representation of the moment method matrix elements may be obtained as [87]:

$$Z_{mn} = \frac{2\pi\eta_0ka}{2N_s} \sum_{p=-\infty}^{\infty} J_p'(ka) H_p^{(2)'}(ka) T_{-p} F_p e^{-jq(m\phi_0 - n\phi_0)}. \quad (32)$$

Here $J_p'(ka)$ and $H_p^{(2)'}(ka)$ are the derivatives of a first kind Bessel and second kind Hankel Function, respectively, and T_{-p} , F_p are the Fourier coefficients For a circular cylinder, the impedance

matrix is an $N_s \times N_s$ circulant matrix, and therefore has eigenvectors given by $e^{jl\phi_0}$, $l = 0, \dots, N_s - 1$.

1. The eigenvalues of a circulant matrix are given by the Fourier coefficients of the discrete Fourier transform of the first row,

$$\lambda_q = \sum_{n=0}^{N_s-1} Z_{0n} e^{-jqn\phi_0}, \quad (33)$$

which, upon substitution of the expression (32) yields

$$\lambda_q = \sum_{n=0}^{N_s-1} e^{-jqn\phi_0} \frac{2\pi\eta_0ka}{2N_s} \sum_{p=-\infty}^{\infty} J'_p(ka) H_p^{(2)'}(ka) T_{-p} F_p e^{jpn\phi_0}. \quad (34)$$

Rearranging summations, one obtains

$$\lambda_q = \frac{2\pi\eta_0ka}{2N_s} \sum_{p=-\infty}^{\infty} J'_p(ka) H_p^{(2)'}(ka) T_{-p} F_p \sum_{n=0}^{N_s-1} e^{-jqn\phi_0} e^{jpn\phi_0}. \quad (35)$$

The rightmost term in (35) may be simplified as:

$$\sum_{n=0}^{N_s-1} e^{-jqn\phi_0} e^{jpn\phi_0} = \begin{cases} (-1)^l N_s, & q - p = lN, l \in \mathbb{Z} \\ 0, & \text{O.W.} \end{cases} \quad (36)$$

Reindexing (35), the eigenvalues of the Z matrix are therefore given by:

$$\lambda_q = \frac{2\pi\eta_0ka}{2N_s} \sum_{l=-\infty}^{\infty} J'_{q+lN_s}(ka) H_{q+lN_s}^{(2)'}(ka) T_{-q-lN_s} F_{q+lN_s} \quad (37)$$

This equation matches that in [87], which was obtained by slightly different means.

The addition of the penalty function adds another matrix to the system as

$$\tilde{Z} = Z^{MoM} + Z^P. \quad (38)$$

By virtue of the definition of the penalty function as a local operator that only operates on equispaced neighboring patches, the matrix Z^P is circulant, with nonzero entries only in the i th, $(i-1)$ th, and $(i+1)$ th slots of row i (where the arithmetic is taken modulo N_s). Entries of Z^P are given ex-

explicitly by:

$$Z_{m,n}^p = \begin{cases} \int_0^{2\pi} P_n^+(\phi)t(\phi - n\phi_0)f(\phi - n\phi_0)d\phi + \int_0^{2\pi} P_n^-(\phi)t(\phi - n\phi_0)f(\phi - n\phi_0)d\phi, & m = n \\ -\int_0^{2\pi} P_n^+(\phi)t(\phi - (n-1)\phi_0)f(\phi - n\phi_0)d\phi, & m = n + 1 \\ -\int_0^{2\pi} P_n^-(\phi)t(\phi - n\phi_0)f(\phi - (n+1)\phi_0)d\phi, & m = n - 1 \\ 0, & \text{O.W.} \end{cases} \quad (39)$$

where $P_n^\pm(\phi) = P(\phi - (n \pm 1/2)\phi_0)$ is a pulse function that restricts the integration to either $\gamma_{n,n-1}$ or $\gamma_{n,n+1}$ depending on the sign, and the arithmetic $m = \pm 1$ is understood to be modulo $N_s - 1$. ($\gamma_{l,k}$ is the overlap between patches Ω_l and Ω_k). Making use of the identity $P_n^\pm(\phi) = (P_n^\pm(\phi))^2$ and expanding Fourier series of the products yields

$$\begin{aligned} P_n^\pm(\phi)f(\phi - (n \pm 1)\phi_0) &= \sum_{p=-\infty}^{\infty} \tilde{F}_p^\pm e^{jq\phi} e^{-jq(n \pm 1)\phi_0} \\ P_n^\pm(\phi)t(\phi - (n \pm 1)\phi_0) &= \sum_{p=-\infty}^{\infty} \tilde{T}_p^\pm e^{jq\phi} e^{-jq(n \pm 1)\phi_0}, \end{aligned} \quad (40)$$

where \tilde{F}_p^\pm and \tilde{T}_p^\pm are understood to be the Fourier coefficients of the product of the pulse and basis or testing function. Rewriting (39) using these expansions, one obtains

$$Z_{m,n}^p = \begin{cases} 4\pi a \sum_p \tilde{T}_{-p} \tilde{F}_p, & m = n \\ -2\pi a \sum_p \tilde{T}_{-p} \tilde{F}_p e^{jq\phi_0}, & m = n + 1 \\ -2\pi a \sum_p \tilde{T}_{-p} \tilde{F}_p e^{-jq\phi_0}, & m = n - 1 \\ 0, & \text{O.W.} \end{cases} \quad (41)$$

Note that the \pm superscript is dropped in (41) because the phase factors of the pulse functions implicitly cancel under integration. These expansions may now be used to define the eigenvalues by a process analogous to those of Z^{MoM} via the DFT. In this case, since there are only three nonzero terms in the first row of Z^p , the DFT expression becomes

$$\lambda_q = 2\pi a \sum_{p=-\infty}^{\infty} \tilde{T}_{-p} \tilde{F}_p (2 - e^{-j(q+p)\phi_0} - e^{j(q(N_s-1)+p)\phi_0}), \quad (42)$$

where the phase of $(q - (N_s - 1))\phi_0$ comes from the fact that in the first row of the circulant matrix Z^p , the only nonzero terms are $n = 0, 1, N_s - 1$. Further manipulations yield

$$\begin{aligned}
\lambda_q &= 2\pi a \sum_{p=-\infty}^{\infty} \tilde{T}_{-p} \tilde{F}_p (2 - e^{-jp\frac{N_s}{2}} (e^{-j(q(\frac{N_s}{2}+1)+p)\phi_0} - e^{j(q(\frac{N_s}{2}+1)+p)\phi_0})) \\
&= 2\pi a \sum_{p=-\infty}^{\infty} \tilde{T}_{-p} \tilde{F}_p (2 - e^{-jp\frac{N_s}{2}} \cos\left(\left(q\left(\frac{N_s}{2} + 1\right) + p\right)\phi_0\right)) \\
&= 4\pi a \sum_{p=-\infty}^{\infty} \tilde{T}_{-p} \tilde{F}_p \left[1 - (-1)^q \cos\left((q+p)\phi_0 + q\pi\right)\right].
\end{aligned} \tag{43}$$

The definition of $\phi_0 = 2\pi/N_s$ gives the ratio $N_s\phi_0/2 = \pi$, and finally,

$$\begin{aligned}
\lambda_q &= 4\pi a \sum_{p=-\infty}^{\infty} \tilde{T}_{-p} \tilde{F}_p \left[1 - (-1)^q \cos\left((q+p)\phi_0\right) \cos(q\pi) - \sin\left((q+p)\phi_0\right) \sin(q\pi)\right] \\
&= 4\pi a \sum_{p=-\infty}^{\infty} \tilde{T}_{-p} \tilde{F}_p \left[1 - \cos\left((q+p)\phi_0\right)\right].
\end{aligned} \tag{44}$$

A few additional manipulations give more insight into the behavior of the eigenvalues λ_q . First, the last line in 44 may be rewritten

$$\begin{aligned}
\lambda_q &= 4\pi a \left\{ \sum_{p=-\infty}^{\infty} \tilde{T}_{-p} \tilde{F}_p - \sum_{p=-\infty}^{\infty} \tilde{T}_{-p} \tilde{F}_p \cos(q\phi_0) \cos(p\phi_0) + \sum_{p=-\infty}^{\infty} \tilde{T}_{-p} \tilde{F}_p \sin(q\phi_0) \sin(p\phi_0) \right\} \\
&= 4\pi a \left\{ \sum_{p=-\infty}^{\infty} \tilde{T}_{-p} \tilde{F}_p - \cos(q\phi_0) \sum_{p=-\infty}^{\infty} \tilde{T}_{-p} \tilde{F}_p \cos(p\phi_0) + \sin(q\phi_0) \sum_{p=-\infty}^{\infty} \tilde{T}_{-p} \tilde{F}_p \sin(p\phi_0) \right\}.
\end{aligned} \tag{45}$$

Under the assumption that both $f(\phi)$ and $t(\phi)$ are purely real so that $\tilde{T}_{-p}\tilde{F}_p = (\tilde{T}_p\tilde{F}_{-p})^*$, then $\tilde{T}_{-p}\tilde{F}_p + \tilde{T}_p\tilde{F}_{-p} = 2\Re\{\tilde{T}_p\tilde{F}_{-p}\}$ and $\tilde{T}_{-p}\tilde{F}_p - \tilde{T}_p\tilde{F}_{-p} = 2j\Im\{\tilde{T}_p\tilde{F}_{-p}\}$. If the usual Galerkin testing is used ($\tilde{T}_p = \tilde{F}_p$), then $\tilde{T}_{-p}\tilde{F}_p + \tilde{T}_p\tilde{F}_{-p} = 2|\tilde{T}_p\tilde{F}_{-p}|^2 = 2|\tilde{T}_{-p}\tilde{F}_p|^2$. Thus, for Galerkin testing all eigenvalues λ_q are real since the sine term vanishes by odd symmetry. The sums over p are independent of q and may be assigned real values C_1, C_2 , so that the final expression for the eigenvalue becomes

$$\begin{aligned}
\lambda_q &= 4\pi a \left\{ C_1 - C_2 \cos(q\phi_0) \right\} \\
&= 4\pi a \left\{ C_1 - C_2 \cos\left(\frac{2\pi q}{N_s}\right) \right\},
\end{aligned} \tag{46}$$

where

$$\begin{aligned} C_1 &= 4\pi a \sum_{p=-\infty}^{\infty} \tilde{T}_{-p} \tilde{F}_p, \\ C_2 &= 4\pi a \sum_{p=-\infty}^{\infty} \tilde{T}_{-p} \tilde{F}_p \cos(p\phi_0). \end{aligned} \tag{47}$$

These are the expressions in (4.14) and (4.15).

BIBLIOGRAPHY

BIBLIOGRAPHY

- [1] T. A. Driscoll, "Algorithm 756: A matlab toolbox for schwarz-christoffel mapping," *ACM Transactions on Mathematical Software (TOMS)*, vol. 22, no. 2, pp. 168–186, 1996.
- [2] R. Harrington, "Origin and development of the method of moments for field computation," *Antennas and Propagation Magazine, IEEE*, vol. 32, no. 3, pp. 31–35, 1990.
- [3] V. Rumsey, "Reaction concept in electromagnetic theory," *Physical Review*, vol. 94, no. 6, p. 1483, 1954.
- [4] G. Arfken and H. Weber, *Mathematical methods for physicists*. Elsevier Acad. Press, 2008.
- [5] J. M. Lee, *Introduction to Smooth Manifolds*, vol. 218. Springer New York, 2003.
- [6] J. Nedelec, "Mixed finite elements in r3," *Numerische Mathematik*, vol. 35, pp. 315–341, 1980.
- [7] J. Wang and J. Webb, "Hierarchical vector boundary elements and p-adaption for 3-d electromagnetic scattering," *Antennas and Propagation, IEEE Transactions on*, vol. 45, no. 12, pp. 1869–1879, 1997.
- [8] R. Graglia, D. Wilton, and A. Peterson, "Higher order interpolatory vector bases for computational electromagnetics," *Antennas and Propagation, IEEE Transactions on*, vol. 45, pp. 329–342, mar 1997.
- [9] A. Peterson and R. Graglia, "Evaluation of hierarchical vector basis functions for quadrilateral cells," *Magnetics, IEEE Transactions on*, vol. 47, no. 5, pp. 1190–1193, 2011.
- [10] B. Notaros, B. Popovic, J. Weem, R. Brown, and Z. Popovic, "Efficient large-domain moment solutions to electrically large practical em problems," *Microwave Theory and Techniques, IEEE Transactions on*, vol. 49, no. 1, pp. 151–159, 2001.
- [11] E. Jorgensen, J. Volakis, P. Meincke, and O. Breinbjerg, "Higher order hierarchical legendre basis functions for electromagnetic modeling," *Antennas and Propagation, IEEE Transactions on*, vol. 52, no. 11, pp. 2985–2995, 2004.
- [12] B. Notaros, "Higher order frequency-domain computational electromagnetics," *Antennas and Propagation, IEEE Transactions on*, vol. 56, pp. 2251–2276, aug. 2008.
- [13] L. P. Zha, Y. Q. Hu, and T. Su, "Efficient surface integral equation using hierarchical vector bases for complex em scattering problems," *Antennas and Propagation, IEEE Transactions on*, vol. 60, no. 2, pp. 952–957, 2012.
- [14] R. Graglia and G. Lombardi, "Singular higher order divergence-conforming bases of additive kind and moments method applications to 3d sharp-wedge structures," *Antennas and Propagation, IEEE Transactions on*, vol. 56, no. 12, pp. 3768–3788, 2008.

- [15] M. Djordjevic and B. Notaros, "Double higher order method of moments for surface integral equation modeling of metallic and dielectric antennas and scatterers," *Antennas and Propagation, IEEE Transactions on*, vol. 52, pp. 2118 – 2129, aug. 2004.
- [16] Z.-L. Liu and J. Yang, "Analysis of electromagnetic scattering with higher-order moment method and nurbs model," *Progress In Electromagnetics Research*, vol. 96, pp. 83–100, 2009.
- [17] H. Yuan, N. Wang, and C. Liang, "Combining the higher order method of moments with geometric modeling by nurbs surfaces," *Antennas and Propagation, IEEE Transactions on*, vol. 57, no. 11, pp. 3558–3563, 2009.
- [18] I. Babuska and J. M. Melenk, "The partition of unity method," *International Journal for Numerical Methods in Engineering*, vol. 40, no. 4, pp. 727–758, 1997.
- [19] C. Duarte, I. Babuska, and J. Oden, "Generalized finite element methods for three-dimensional structural mechanics problems," *Computers & Structures*, vol. 77, no. 2, pp. 215 – 232, 2000.
- [20] J. Oden, C. Duarte, and O. Zienkiewicz, "A new cloud-based hp finite element method," *Computer Methods in Applied Mechanics and Engineering*, vol. 153, no. 1–2, pp. 117 – 126, 1998.
- [21] T. Strouboulis, I. Babuska, and K. Copps, "The design and analysis of the generalized finite element method," *Computer Methods in Applied Mechanics and Engineering*, vol. 181, no. 1–3, pp. 43 – 69, 2000.
- [22] I. Babuska, U. Banerjee, and J. E. Osborn, "Survey of meshless and generalized finite element methods: A unified approach," *Acta Numerica*, vol. 12, pp. 1–125, 4 2003.
- [23] C. Duarte, D.-J. Kim, and D. Quaresma, "Arbitrarily smooth generalized finite element approximations," *Computer Methods in Applied Mechanics and Engineering*, vol. 196, no. 1–3, pp. 33 – 56, 2006.
- [24] E. Perrey-Debain, J. Trevelyan, and P. Bettess, "Plane wave interpolation in direct collocation boundary element method for radiation and wave scattering: numerical aspects and applications," *Journal of Sound and Vibration*, vol. 261, no. 5, pp. 839 – 858, 2003.
- [25] H. Beriot, E. Perrey-Debain, M. B. Tahar, and C. Vayssade, "Plane wave basis in galerkin bem for bidimensional wave scattering," *Engineering Analysis with Boundary Elements*, vol. 34, no. 2, pp. 130 – 143, 2010.
- [26] M. Peake, J. Trevelyan, and G. Coates, "Novel basis functions for the partition of unity boundary element method for helmholtz problems," *International Journal for Numerical Methods in Engineering*, vol. 93, no. 9, pp. 905–918, 2013.
- [27] E. Perrey-Debain, O. Laghrouche, P. Bettess, and J. Trevelyan, "Plane-wave basis finite elements and boundary elements for three-dimensional wave scattering," *Philosophical Transactions of the Royal Society of London. Series A:Mathematical, Physical and Engineering Sciences*, vol. 362, no. 1816, pp. 561–577, 2004.

- [28] O. Bruno, “Fast, high-order, high-frequency integral methods for computational acoustics and electromagnetics,” in *Topics in Computational Wave Propagation* (M. Ainsworth, P. Davies, D. Duncan, B. Rynne, and P. Martin, eds.), vol. 31 of *Lecture Notes in Computational Science and Engineering*, pp. 43–82, Springer Berlin Heidelberg, 2003.
- [29] O. P. Bruno and C. A. Geuzaine, “An integration scheme for three-dimensional surface scattering problems,” *Journal of Computational and Applied Mathematics*, vol. 204, no. 2, pp. 463 – 476, 2007. <ce:title>Special Issue: The Seventh International Conference on Mathematical and Numerical Aspects of Waves (WAVES’05)</ce:title>.
- [30] T. Belytschko, Y. Krongauz, D. Organ, M. Fleming, and P. Krysl, “Meshless methods: An overview and recent developments,” *Computer Methods in Applied Mechanics and Engineering*, vol. 139, no. 1–4, pp. 3 – 47, 1996.
- [31] G. Liu, *Meshfree Methods: Moving Beyond the Finite Element Method, Second Edition*. Taylor & Francis, 2010.
- [32] V. Cingoski, N. Miyamoto, and H. Yamashita, “Element-free galerkin method for electromagnetic field computations,” *Magnetics, IEEE Transactions on*, vol. 34, no. 5, pp. 3236–3239, 1998.
- [33] L. Xuan, Z. Zeng, B. Shanker, and L. Udupa, “Element-free galerkin method for static and quasi-static electromagnetic field computation,” *Magnetics, IEEE Transactions on*, vol. 40, no. 1, pp. 12–20, 2004.
- [34] O. Bottauscio, M. Chiampì, and A. Manzin, “Element-free galerkin method in eddy-current problems with ferromagnetic media,” *Magnetics, IEEE Transactions on*, vol. 42, no. 5, pp. 1577–1584, 2006.
- [35] C. Lu and B. Shanker, “Hybrid boundary integral-generalized (partition of unity) finite-element solvers for the scalar helmholtz equation,” *Magnetics, IEEE Transactions on*, vol. 43, no. 3, pp. 1002–1012, 2007.
- [36] O. Tuncer, C. Lu, N. Nair, B. Shanker, and L. Kempel, “Further development of vector generalized finite element method and its hybridization with boundary integrals,” *Antennas and Propagation, IEEE Transactions on*, vol. 58, no. 3, pp. 887–899, 2010.
- [37] W. Nicomedes, R. Mesquita, and F. Moreira, “A local boundary integral equation (lbie) method in 2d electromagnetic wave scattering, and a meshless discretization approach,” in *Microwave and Optoelectronics Conference (IMOC), 2009 SBMO/IEEE MTT-S International*, pp. 133–137, 2009.
- [38] W. Nicomedes, R. Mesquita, and F. Moreira, “A meshless local boundary integral equation method for three dimensional scalar problems,” in *Electromagnetic Field Computation (CEFC), 2010 14th Biennial IEEE Conference on*, pp. 1–1, 2010.
- [39] M. S. Tong and W. C. Chew, “A novel meshless scheme for solving surface integral equations with flat integral domains,” *Antennas and Propagation, IEEE Transactions on*, vol. 60, no. 7, pp. 3285–3293, 2012.

- [40] N. Nair and B. Shanker, “Generalized method of moments: A novel discretization technique for integral equations,” *Antennas and Propagation, IEEE Transactions on*, vol. 59, pp. 2280–2293, June 2011.
- [41] N. V. Nair and B. Shanker, “Generalized method of moments: a framework for analyzing scattering from homogeneous dielectric bodies,” *J. Opt. Soc. Am. A*, vol. 28, pp. 328–340, Mar 2011.
- [42] N. Nair, *The Generalized Method of Moments: A novel discretization technique for integral equations*. PhD thesis, Michigan State University, 2010.
- [43] N. V. Nair, B. Shanker, and L. Kempel, “Generalized method of moments: A boundary integral framework for adaptive analysis of acoustic scattering,” *The Journal of the Acoustical Society of America*, vol. 132, no. 3, pp. 1261–1270, 2012.
- [44] N. Nair, B. Shanker, and L. Kempel, “Generalized method of moments: A flexible discretization scheme for integral equations using locally smooth surface approximations,” in *Microwaves, Communications, Antennas and Electronics Systems (COMCAS), 2011 IEEE International Conference on*, pp. 1–4, Nov. 2011.
- [45] N. Nair, B. Shanker, and L. Kempel, “A discretization framework for scalar integral equations using the generalized method of moments and locally smooth surface approximations,” in *Antennas and Propagation (APSURSI), 2011 IEEE International Symposium on*, pp. 3193–3196, July 2011.
- [46] D. Dault, N. Nair, B. Shanker, and L. Kempel, “A flexible framework for the solution to surface scattering problems using integral equations,” in *Electromagnetics in Advanced Applications (ICEAA), 2012 International Conference on*, pp. 148–151, Sept. 2012.
- [47] J. M. Song and W. C. Chew, “Multilevel fast-multipole algorithm for solving combined field integral equations of electromagnetic scattering,” *Microwave and Optical Technology Letters*, vol. 10, no. 1, pp. 14–19, 1995.
- [48] H. Hoppe, T. DeRose, T. Duchamp, J. McDonald, and W. Stuetzle, *Surface reconstruction from unorganized points*, vol. 26(2). ACM, 1992.
- [49] D. Shepard, “A two-dimensional interpolation function for irregularly-spaced data,” in *Proceedings of the 1968 23rd ACM national conference*, ACM ’68, (New York, NY, USA), pp. 517–524, ACM, 1968.
- [50] N. Nair, M. Vikram, and B. Shanker, “Analysis of scattering from complex, electrically large structures using the generalized method of moments,” in *Antennas and Propagation Society International Symposium (APSURSI), 2012 IEEE*, pp. 1–2, July 2012.
- [51] A. F. Peterson, “Mapped vector basis functions for electromagnetic integral equations,” *Synthesis Lectures on Computational Electromagnetics*, vol. 1, no. 1, pp. 1–124, 2006.
- [52] J. Song and W. Chew, “Moment method solutions using parametric geometry,” *Journal of Electromagnetic Waves and Applications*, vol. 9, no. 1-2, pp. 71–83, 1995.

- [53] S. Rao, D. Wilton, and A. Glisson, "Electromagnetic scattering by surfaces of arbitrary shape," *Antennas and Propagation, IEEE Transactions on*, vol. 30, no. 3, pp. 409–418, 1982.
- [54] Z. Peng, X.-C. Wang, and J. F. Lee, "Integral equation based domain decomposition method for solving electromagnetic wave scattering from non-penetrable objects," *Antennas and Propagation, IEEE Transactions on*, vol. 59, no. 9, pp. 3328–3338, 2011.
- [55] M.-K. Li, W. C. Chew, and L. J. Jiang, "A domain decomposition scheme based on equivalence theorem," *Microwave and Optical Technology Letters*, vol. 48, no. 9, pp. 1853–1857, 2006.
- [56] D. Dault, N. Nair, J. Li, and B. Shanker, "The generalized method of moments for electromagnetic boundary integral equations," *Antennas and Propagation, IEEE Transactions on*, vol. 62, pp. 3174–3188, June 2014.
- [57] V. Rokhlin, "Diagonal forms of translation operators for the helmholtz equation in three dimensions," *Applied and Computational Harmonic Analysis*, vol. 1, no. 1, pp. 82 – 93, 1993.
- [58] T. Eibert, "A diagonalized multilevel fast multipole method with spherical harmonics expansion of the k-space integrals," *Antennas and Propagation, IEEE Transactions on*, vol. 53, no. 2, pp. 814–817, 2005.
- [59] I. Ismatullah and T. Eibert, "Surface integral equation solutions by hierarchical vector basis functions and spherical harmonics based multilevel fast multipole method," *Antennas and Propagation, IEEE Transactions on*, vol. 57, no. 7, pp. 2084–2093, 2009.
- [60] I. Ismatullah and T. Eibert, "Higher order surface integral equation solutions employing spherical harmonics based multilevel fast multipole method," in *Antennas and Propagation Society International Symposium, 2009. APSURSI '09. IEEE*, pp. 1–4, 2009.
- [61] O. Borries, P. Meincke, E. Jorgensen, and P. Hansen, "Multi-level fast multipole method for higher-order discretizations," *Antennas and Propagation, IEEE Transactions on*, vol. PP, no. 99, pp. 1–1, 2014.
- [62] B. Kolundzija and D. Sumic, "Multilevel fast multipole method for higher order basis functions implemented in wipl-d pro," in *Antennas and Propagation, 2009. EuCAP 2009. 3rd European Conference on*, pp. 2136–2140, 2009.
- [63] X. Pan, L. Cai, and X. Sheng, "An efficient high order multilevel fast multipole algorithm for electromagnetic scattering analysis," *Progress In Electromagnetics Research*, vol. 126, pp. 85–100, 2012.
- [64] K. Donepudi, J. Song, J.-M. Jin, G. Kang, and W. C. Chew, "A novel implementation of multilevel fast multipole algorithm for higher order galerkin's method," *Antennas and Propagation, IEEE Transactions on*, vol. 48, no. 8, pp. 1192–1197, 2000.

- [65] K. Donepudi, J.-M. Jin, S. Velamparambil, J. Song, and W. C. Chew, "A higher order parallelized multilevel fast multipole algorithm for 3-d scattering," *Antennas and Propagation, IEEE Transactions on*, vol. 49, no. 7, pp. 1069–1078, 2001.
- [66] K. Donepudi, J.-M. Jin, and W. C. Chew, "A higher order multilevel fast multipole algorithm for scattering from mixed conducting/dielectric bodies," *Antennas and Propagation, IEEE Transactions on*, vol. 51, no. 10, pp. 2814–2821, 2003.
- [67] M. He, J. Liu, and K. Zhang, "Improving the spherical harmonics expansion-based multilevel fast multipole algorithm (se-mlfma)," *Antennas and Wireless Propagation Letters, IEEE*, vol. 12, pp. 551–554, 2013.
- [68] B. Kolundzija, M. Pavlovic, and B. Mrdakovic, "Optimum choice of currents' expansion order in mlfmm algorithm for electromagnetic scattering," in *Antennas and Propagation Society International Symposium, 2009. APSURSI '09. IEEE*, pp. 1–4, 2009.
- [69] D. Schobert and T. Eibert, "Fast integral equation solution by multilevel green's function interpolation combined with multilevel fast multipole method," *Antennas and Propagation, IEEE Transactions on*, vol. 60, pp. 4458–4463, Sept 2012.
- [70] L. Jiang and W. Chew, "Low-frequency fast inhomogeneous plane-wave algorithm (lf-fipwa)," *Microwave and Optical Technology Letters*, vol. 40, no. 2, pp. 117–122, 2004.
- [71] B. Shanker and H. Huang, "Accelerated cartesian expansions — a fast method for computing of potentials of the form $\frac{1}{|\mathbf{r} - \mathbf{r}'|}$ for all real \mathbf{r} ," *Journal of Computational Physics*, vol. 226, no. 1, pp. 732 – 753, 2007.
- [72] J. Song and W. C. Chew, "Error analysis for the truncation of multipole expansion of vector green's functions [em scattering]," *Microwave and Wireless Components Letters, IEEE*, vol. 11, no. 7, pp. 311–313, 2001.
- [73] Y. Saad, "A flexible inner-outer preconditioned gmres algorithm," *SIAM Journal on Scientific Computing*, vol. 14, no. 2, pp. 461–469, 1993.
- [74] B. Carpentieri, I. Duff, L. Giraud, and G. Sylvand, "Combining fast multipole techniques and an approximate inverse preconditioner for large electromagnetism calculations," *SIAM Journal on Scientific Computing*, vol. 27, no. 3, pp. 774–792, 2005.
- [75] D. Ding, R. shan Chen, Z. Fan, and P. Rui, "A novel hierarchical two-level spectral preconditioning technique for electromagnetic wave scattering," *Antennas and Propagation, IEEE Transactions on*, vol. 56, pp. 1122–1132, April 2008.
- [76] D. Arnold, F. Brezzi, B. Cockburn, and L. Marini, "Unified analysis of discontinuous galerkin methods for elliptic problems," *SIAM Journal on Numerical Analysis*, vol. 39, no. 5, pp. 1749–1779, 2002.
- [77] I. Babuška, "The finite element method with lagrangian multipliers," *Numerische Mathematik*, vol. 20, no. 3, pp. 179–192, 1973.

- [78] F. Brezzi, "On the existence, uniqueness and approximation of saddle-point problems arising from lagrangian multipliers," *ESAIM: Mathematical Modelling and Numerical Analysis - Modélisation Mathématique et Analyse Numérique*, vol. 8, no. R2, pp. 129–151, 1974.
- [79] M. Healey and N. Heuer, "Mortar boundary elements," *SIAM Journal on Numerical Analysis*, vol. 48, no. 4, pp. 1395–1418, 2010.
- [80] H. N. Chouly, F., "A nitsche-based domain decomposition method for hypersingular integral equations," in *Conf. Presentation*, 2012.
- [81] Z. Peng, K.-H. Lim, and J.-F. Lee, "A discontinuous galerkin surface integral equation method for electromagnetic wave scattering from nonpenetrable targets," *Antennas and Propagation, IEEE Transactions on*, vol. 61, no. 7, pp. 3617–3628, 2013.
- [82] K. Cools, "Mortar boundary elements for the efie applied to the analysis of scattering by pec junctions," in *Electromagnetic Compatibility (APEMC), 2012 Asia-Pacific Symposium on*, pp. 165–168, May 2012.
- [83] J.-C. Nédélec, *Acoustic and electromagnetic equations : integral representations for harmonic problems*. Applied mathematical sciences, New York: Springer, 2001.
- [84] A. Buffa and S. Christiansen, "The electric field integral equation on lipschitz screens: definitions and numerical approximation," *Numerische Mathematik*, vol. 94, no. 2, pp. 229–267, 2003.
- [85] A. Peterson, D. Wilton, and R. Jorgenson, "Variational nature of galerkin and non-galerkin moment method solutions," *Antennas and Propagation, IEEE Transactions on*, vol. 44, pp. 500–503, Apr 1996.
- [86] J. Ma, V. Rokhlin, and S. Wandzura, "Generalized gaussian quadrature rules for systems of arbitrary functions," *SIAM Journal on Numerical Analysis*, vol. 33, no. 3, pp. 971–996, 1996.
- [87] K. Warnick, *Numerical Analysis for Electromagnetic Integral Equations*. Artech House Electromagnetic Analysis, Artech House, 2008.
- [88] T. A. Driscoll and L. N. Trefethen, *Schwarz-Christoffel Mapping*. No. 8, Cambridge University Press, 2002.
- [89] L. N. Trefethen, "Numerical computation of the schwarz-christoffel transformation," *SIAM Journal on Scientific and Statistical Computing*, vol. 1, no. 1, pp. 82–102, 1980.
- [90] H. M. Oloomi and V. Badii, "Computer solution of electrostatics problems using schwarz-christoffel mapping technique," *Computer Applications in Engineering Education*, vol. 3, no. 4, pp. 241–244, 1995.
- [91] L. Trefethen, "Analysis and design of polygonal resistors by conformal mapping," *Zeitschrift für angewandte Mathematik und Physik ZAMP*, vol. 35, no. 5, pp. 692–704, 1984.

- [92] R. Davis, "Numerical methods for coordinate generation based on schwarz-christoffel transformations," in *Computational Fluid Dynamics Conference*, vol. 1, pp. 180–194, 1979.
- [93] K. Sridhar and R. Davis, "A schwarz-christoffel method for generating two-dimensional flow grids," *Journal of Fluids Engineering*, vol. 107, no. 3, pp. 330–337, 1985.
- [94] A. R. Elcrat and L. N. Trefethen, "Classical free-streamline flow over a polygonal obstacle," *Journal of Computational and Applied Mathematics*, vol. 14, no. 1, pp. 251–265, 1986.
- [95] S. Natarajan, S. Bordas, and D. Roy Mahapatra, "Numerical integration over arbitrary polygonal domains based on schwarz-christoffel conformal mapping," *International Journal for Numerical Methods in Engineering*, vol. 80, no. 1, pp. 103–134, 2009.
- [96] S. Natarajan, D. R. Mahapatra, and S. P. A. Bordas, "Integrating strong and weak discontinuities without integration subcells and example applications in an xfm/gfm framework," *International Journal for Numerical Methods in Engineering*, vol. 83, no. 3, pp. 269–294, 2010.
- [97] J. Bremer, Z. Gimbutas, and V. Rokhlin, "A nonlinear optimization procedure for generalized gaussian quadratures," *SIAM Journal on Scientific Computing*, vol. 32, no. 4, pp. 1761–1788, 2010.
- [98] S. E. Mousavi, H. Xiao, and N. Sukumar, "Generalized gaussian quadrature rules on arbitrary polygons," *International Journal for Numerical Methods in Engineering*, vol. 82, no. 1, pp. 99–113, 2010.
- [99] M. Khayat and D. Wilton, "Numerical evaluation of singular and near-singular potential integrals," *Antennas and Propagation, IEEE Transactions on*, vol. 53, no. 10, pp. 3180–3190, 2005.
- [100] N. Nair, A. Pray, J. Villa-Giron, B. Shanker, and D. Wilton, "A singularity cancellation technique for weakly singular integrals on higher order surface descriptions," *Antennas and Propagation, IEEE Transactions on*, vol. 61, no. 4, pp. 2347–2352, 2013.
- [101] H. Rathod, K. Nagaraja, and B. Venkatesudu, "Gauss legendre quadrature over a triangle," *acharya nagarjuna int, J. Math. Inform. Technol*, vol. 1, no. 1, pp. 33–52, 2004.
- [102] F. Cirak, M. Ortiz, and P. Schroder, "Subdivision surfaces: a new paradigm for thin-shell finite-element analysis," *International Journal for Numerical Methods in Engineering*, vol. 47, no. 12, pp. 2039–2072, 2000.
- [103] A. P. Spann, H. Zhao, and E. S. G. Shaqfeh, "Loop subdivision surface boundary integral method simulations of vesicles at low reduced volume ratio in shear and extensional flow," *Physics of Fluids (1994-present)*, vol. 26, no. 3, pp. –, 2014.
- [104] C. Loop, "Smooth subdivision surfaces based on triangles," department of mathematics, University of Utah, Utah, USA, Aug. 1987.
- [105] E. Catmull and J. Clark, "Recursively generated b-spline surfaces on arbitrary topological meshes," *Computer-aided design*, vol. 10, no. 6, pp. 350–355, 1978.

- [106] D. Doo and M. Sabin, “Behaviour of recursive division surfaces near extraordinary points,” *Computer-Aided Design*, vol. 10, no. 6, pp. 356 – 360, 1978.
- [107] D. Zorin, P. Schröder, and W. Sweldens, “Interpolating subdivision for meshes with arbitrary topology,” in *Proceedings of the 23rd Annual Conference on Computer Graphics and Interactive Techniques*, SIGGRAPH ’96, (New York, NY, USA), pp. 189–192, ACM, 1996.
- [108] S. Lin, F. You, X. Luo, and Z. Li, “Deducing interpolating subdivision schemes from approximating subdivision schemes,” *ACM Trans. Graph.*, vol. 27, pp. 146:1–146:7, Dec. 2008.
- [109] N. Litke, A. Levin, and P. Schröder, “Fitting subdivision surfaces,” in *Proceedings of the Conference on Visualization ’01*, VIS ’01, (Washington, DC, USA), pp. 319–324, IEEE Computer Society, 2001.
- [110] K.-S. Cheng, W. Wang, H. Qin, K.-Y. Wong, H. Yang, and Y. Liu, “Fitting subdivision surfaces to unorganized point data using sdm,” in *Computer Graphics and Applications, 2004. PG 2004. Proceedings. 12th Pacific Conference on*, pp. 16–24, Oct 2004.
- [111] J. Stam, “Evaluation of loop subdivision surface,” *Proceedings CD of SIGGRAPH*, vol. 98, 1998.
- [112] U. Reif, “A unified approach to subdivision algorithms near extraordinary vertices,” *Computer Aided Geometric Design*, vol. 12, no. 2, pp. 153 – 174, 1995.
- [113] D. Zorin, “Constructing curvature-continuous surfaces by blending,” in *Proceedings of the fourth Eurographics symposium on Geometry processing*, pp. 31–40, Eurographics Association, 2006.
- [114] T. Duchamp, A. Certain, A. Derosé, and W. Stuetzle, “Hierarchical computation of pl harmonic embeddings,” tech. rep., 1997.
- [115] G. Umlauf, “Analyzing the characteristic map of triangular subdivision schemes,” *Constructive Approximation*, vol. 16, no. 1, pp. 145–155, 2000.
- [116] D. Zorin, “Smoothness of stationary subdivision on irregular meshes,” *Constructive Approximation*, vol. 16, no. 3, pp. 359–397, 2000.
- [117] I. Boier-Martin and D. Zorin, “Differentiable parameterization of catmull-clark subdivision surfaces,” in *Proceedings of the 2004 Eurographics/ACM SIGGRAPH Symposium on Geometry Processing*, SGP ’04, (New York, NY, USA), pp. 155–164, ACM, 2004.
- [118] A. Levin, “Modified subdivision surfaces with continuous curvature,” *ACM Trans. Graph.*, vol. 25, pp. 1035–1040, July 2006.
- [119] H. Biermann, A. Levin, and D. Zorin, “Piecewise smooth subdivision surfaces with normal control,” in *Proceedings of the 27th annual conference on Computer graphics and interactive techniques*, pp. 113–120, ACM Press/Addison-Wesley Publishing Co., 2000.